Numerical Investigation of Cross-Flow Tidal Turbine Hydrodynamics

Stringer, Robert

Award date:
2018

Awarding institution:
University of Bath

Numerical Investigation of Cross-Flow Tidal Turbine Hydrodynamics

submitted by

Robert M. Stringer

for the degree of Doctor of Philosophy

of the

University of Bath

Department of Architecture & Civil Engineering

2018

Acknowledgements

First and foremost, I wish to express my sincere gratitude to my Ph.D. supervisor Dr Andrew Hillis for his continuous encouragement, patience, wisdom and steadfast belief in my research. I was incredibly fortunate to find myself with such an outstanding mentor working on some brilliantly challenging projects and will always look back with fond memories of days spent in the workshop building rigs and narrowly avoiding hydraulic oil.

I would like to thank academics Dr Jun Zang and Dr Michael Patterson for their guidance and expertise. Their support paved the way to finding my eventual topic and afforded me some unforgettable experiences presenting my research around the world. A huge thank you to William Bazeley for his practical wisdom and his brilliant sense of humour that made experimenting and teaching in the laboratory a delight.

Many thanks to my viva examiners Dr Michael Wilson and Dr Yong Ming Dai for such an exciting and rewarding experience, their insight and feedback was gratefully received and the final handshake a momentous moment I will always remember.

I would like to acknowledge Dr Ross McAdam, University of Oxford, and Kepler Energy Ltd who generously shared data from a program of experimental tests developing their own novel cross-flow tidal turbine. The data provided essential validation of my methods from which I could build my ideas and ultimately construct a successful contribution to the field.

A special thanks to Dave Jones, my manager at Dyson, who endured my mammoth quest of writing up my thesis while in full time employment. His patience, encouragement and generous support gave me the freedom to focus on my write-up on countless occasions.

To my family and friends many thanks for your encouragement and lifelong love and support, you can all relax, it is finished.

The final thank you goes to my partner Dr Jennifer Jones for her gentle encouragement, patience and brilliant maths skills, she always understood.

This research was funded by the Engineering and Physical Sciences Research Council (EPSRC).

Abstract

The challenge of tackling global climate change and our increasing reliance on power means that new and diverse renewable energy generation technologies are a necessity for the future. From a number of technologies reviewed at the outset, the cross-flow tidal turbine was chosen as the focus of the research. The numerical investigation begins by choosing to model flow around a circular cylinder as a challenging benchmarking and evaluation case to compare two potential solvers for the ongoing research, ANSYS CFX and OpenFOAM. A number of meshing strategies and solver limitations are extracted, forming a detailed guide on the topic of cylinder lift, drag and Strouhal frequency prediction in its own right. An introduction to cross-flow turbines follows, setting out turbine performance coefficients and a strategy to develop a robust numerical modelling environment with which to capture and evaluate hydrodynamic phenomena. The validation of a numerical model is undertaken by comparison with an experimentally tested lab scale turbine. The resultant numerical model is used to explore turbine performance with varying Reynolds number, concluding with a recommended minimum value for development purposes of $Re = 350 \times 10^3$ to avoid scalability errors. Based on this limit a large scale numerical simulation of the turbine is conducted and evaluated in detail, in particular, a local flow sampling method is proposed and presented. The method captures flow conditions ahead of the turbine blade at all positions of motion allowing local velocities and angles of attack to be interrogated. The sampled flow conditions are used in the final chapter to construct a novel blade pitching strategy. The result is a highly effective optimisation method which increases peak turbine power coefficient by 20% for only two further case iterations of the numerical solution.

Contents

List of Figures

List of Tables

Nomenclature

Roman Symbols

A	Rotor swept area (2D plane)
b	Blockage ratio
c	Chord/characteristic length
C_D	Coefficient of drag
C_L	Coefficient of lift
C_M	Coefficient of moment
C_N	Coefficient of distributed normal (blade) force
C_P	Coefficient of power
C_p	Coefficient of pressure
C_Q	Coefficient of torque
C_T	Coefficient of thrust
D	Drag force
I	Turbulence intensity
L	Lift force
N	Number of turbine blades
P	Power
p	Pressure
r	Radius
Re	Reynolds Number
St	Strouhal number
t	Time

U	Velocity
U_∞	Freestream velocity
U_t	Tangential velocity

Greek Symbols

α	Angle of attack
α_{lim}	Stall limit angle
λ	Tip speed ratio (TSR)
μ	Dynamic viscosity
ν	Kinematic viscosity
ω	Angular velocity
ϕ	Downstream blade path velocity loss percentage
ψ	Active blade pitch demand angle
ρ	Density
σ	Solidity
θ	Angular position of turbine
ξ	Effective angle of attack (from active pitch)

Subscripts

∞	Freestream value
$Blade$	Single turbine blade value
$local$	Numerically sampled local value

Superscripts

$\overline{var}$	(overline) Mean value for one turbine rotation

Chapter 1

Introduction

Over 70% of the Earth's surface is covered by water, almost all of which is subject to wave or tidal action. In every wave and tidal flow, energy can be found in abundance. Waves collect energy from prevailing winds, while tides are driven by the gravitational interaction of the Earth, Moon and Sun. Together they provide an expansive and inexhaustible amount of free energy, the extraction of which has been collectively named marine renewable energy.

There is currently a huge range of marine energy converters in development and undoubtedly many more to come in the future. With increasing pressure to realise the potential of the devices, and a finite value of investment, it is essential that the technology is developed in a timely and cost effective manner. To achieve this, the emerging marine technology industry is looking to employ the most advanced and effective engineering tools available. Numerical modelling offers a range of such tools, including hydrodynamic analysis, statistical optimisation and structural loading, as well as a host of complimentary features. This research focuses on the application of Computational Fluid Dynamics (CFD), a numerical method that has been a key aerodynamic and hydrodynamic design method in the aerospace and ship industries for decades. Its potential is greater than ever due to low cost high performance computers and the increasing availability and accuracy of software. The focus of the thesis is on a chosen technology, the cross-flow tidal turbine. This type of marine energy device has gathered increasing interest in the last decade due to an advancing knowledge on the potential benefits of the technology over conventional axial turbines, such as form factor, scalability, and in the right format, efficiency. The cross-flow turbine concept will be explained and explored over the coming chapters and revealed to be a serious contender in the marine energy industry of the future.

1.1 Outline of Thesis

The objectives of the thesis is to establish a robust numerical methodology for modelling cross-flow tidal turbines and then exploit the resultant methods to explore a range of hydrodynamic characteristics. The knowledge acquired from the modelling directly informs the development and proposal of new methods to increase turbine efficiency and hence increase the potential of the technology for commercial viability.

Chapter 1: At the outset of the research all types of marine renewable energy technology were considered as a focus for the numerical study. This is reflected in this chapter in which the motivation behind the drive for renewable energy is briefly explored followed by an account of the natural resources and study of technologies for both wave and tidal power.

Chapter 2: A numerical test case is presented in which two solvers, ANSYS CFX 13.0 and OpenFOAM 1.7.1 are tasked with modelling a circular cylinder in a tidal flow. The study, and thesis in general, assumes that the reader has a sound understanding of CFD, offering a comparison of solver architectures, implementation methods and available capabilities. While exploring and establishing numerical practices using an unsteady RANS model, the study of circular cylinders is undertaken as a research focus in its own right with the aim of offering a guide for modelling flow around structural elements in the marine environment. The selection of a solver and a high degree of numerical awareness is extracted from the study.

Chapter 3: The cross-flow turbine is introduced, including a detailed account of the principles of operation and definition of performance. The chapter draws upon a range of literary sources to explain established parametric relationships and cross-flow turbine phenomena. Finally, a review of selected publications related to numerical modelling of cross-flow turbines is presented. For completeness, references from both pre and post the dates between which this research was conducted are included.

Chapter 4: In preparation for the simulation of a full turbine, a detailed validation study of an isolated turbine blade is undertaken. To start, a general outline of aerofoil performance is discussed with the study beginning with a wide ranging exploration of numerical meshing effects at high Reynolds number. With the knowledge that an experimental cross-flow turbine operating at low blade chord Reynolds numbers will be used for validation in the next chapter, specific attention is then paid to ensuring a suitable numerical environment is developed. The limitations of the resultant numerical method are established and discussed at the close of the chapter.

Chapter 5: A laboratory tested cross-flow turbine is used as the basis for the development of a corresponding numerical model. The model is fully transient using a multi-domain approach to model the rotation of the three-bladed design. The chapter provides full details on the numerical technique, numerical accuracy, and validation against experimental performance metrics. The chapter concludes by considering the effect Reynolds number has on scaling laboratory size turbines up to potential commercial geometries.

Chapter 6: Based on the evidence provided by Chapter 5, a large cross-flow turbine case is constructed in a numerical model which operates at higher blade chord Reynolds numbers. The turbine is solved over a range of tip speed ratios and dissected to closely analyse the hydrodynamic interaction of the device with the flow field. Furthermore, a novel 'local flow' sampling is proposed and implemented in the numerical environment to give a new perspective on the flow conditions experienced by individual blades. The study uses the collected data to inform a new method of efficiency improvement conducted in the next chapter.

Chapter 7: Two novel methods of optimising an active pitch cross-flow turbine are proposed and numerically tested. Both methods attempt to prevent blade stall and maintain an optimal turbine blade angle of attack to the resolved flow. The first method required an iterative parameter study while the second takes advantage of the data collected from the local sampling method in the previous chapter. The two techniques are compared with each other alongside the original fixed pitch turbine to gauge success and future potential.

Chapter 8: A summary of the thesis findings, concluding remarks and potential for further work is presented in this chapter.

1.2 Research Motivation

1.2.1 Climate Change

In recent decades global climate change has become universally acknowledged among the world's leading scientists. In 1988 the United Nations formed the Intergovernmental Panel on Climate Change (IPCC) to provide an objective scientific view on climate change and it's impacts. The IPCC have produced five assessment reports to date, covering "the scientific, technical and socio-economic information relevant to understanding the scientific basis of risk of human-induced climate change, its potential impacts and options for adaptation and mitigation." The fifth report, which was written and edited by 831 scientists and experts, concludes that;

"*human influence on the climate system is clear and growing, with impacts observed across all continents and oceans. [...] the more human activities disrupt the climate, the greater the risks of severe, pervasive and irreversible impacts for people and ecosystems, and long-lasting changes in all components of the climate system [...] the longer we wait to take action, the more it will cost and the greater the technological, economic, social and institutional challenges we will face.*" (IPCC, 2014).

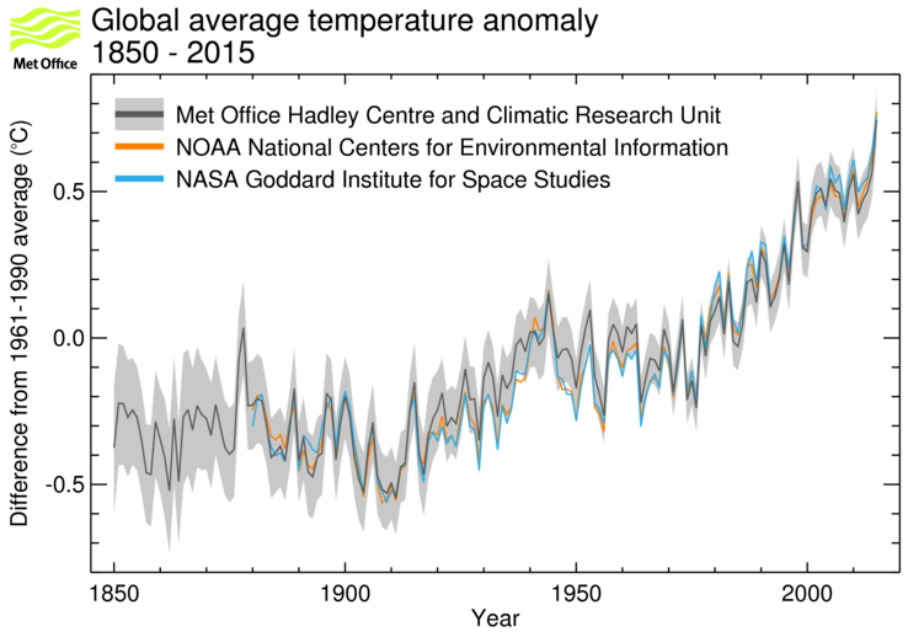

Figure 1-1: Observed annual global average near-surface temperatures for 1850–2013 relative to 1961–90 for three datasets. Grey shading shows 95% confidence range for HadCRUT4 (The Met Office, 2014)

There are many records of the unprecedented increase in global temperature, one such example is the graph shown in Figure 1-1, which has been jointly compiled by the Climatic Research Unit at the University of East Anglia and the UK Met Office. The cause of such a significant trend in global temperatures can be closely compared to the rise in greenhouse gas emissions towards the end of the 20th century. The mechanism of the "the greenhouse effect" is widely understood; in simple terms radiation from the sun is prevented from escaping Earth's atmosphere by the presence of greenhouse gasses, the greater the level of greenhouse gasses, the greater the effect. Having established that global warming is indeed a reality, experts have made many predictions for the consequences if no immediate action is taken;

"If no action is taken to reduce emissions, the concentration of greenhouse gases in the atmosphere could reach double its pre-industrial level as early as 2035, virtually committing us to a global average temperature rise of over 2°C. In the longer term,

there would be more than a 50% chance that the temperature rise would exceed 5°C. This rise would be very dangerous indeed; it is equivalent to the change in average temperatures from the last ice age to today. Such a radical change in the physical geography of the world must lead to major changes in the human geography – where people live and how they live their lives." (Stern, 2007)

Stern has since said of the report that he "underestimated" the threat (Adam, 2008). The specifics of these predicted effects are vast, with major changes in weather systems and sea levels being at the core of the disruption, giving rise to famine, flooding and disease in many parts of the world. Renewable energy can contribute significantly to tackling climate change by replacing ageing fossil fuel power generation, with many technologies such as wind, hydro-power and biomass already making a notable contribution to world energy production. In the last 10 years a new force in the renewable energy industry has emerged that promises to form a significant part of the future of renewable energy, that of Marine Renewable Energy.

1.3 Marine Energy

Marine energy is typically split into two types; wave energy converters (WECs) and tidal stream energy converters. The technology in both fields is still in its infancy and a wide range of potential solutions are still being developed. The search for the ultimate solution is comparable to the wind industry of the 1980's where research in wind turbines was at its height with many types of multi-bladed, vertical and horizontal axis machines were vying to prove their superiority. Owing to a complex interaction with marine forces and huge number of siting possibilities, there is presently little evidence to suggest which technologies may prevail and become the marine industry's equivalent of the familiar three bladed horizontal axis turbine of the wind industry. Logically there is likely to be more than one ubiquitous solution, rather a number of optima to suit various types of geographical and environmental setting. The task of evaluating and developing such diverse and numerous technologies presents a huge engineering challenge. If the potential gains from marine sources of energy are to be realised in the near future then methods of rapid and accurate design development is a necessity. Numerical modelling is one tool that can empower engineers in the industry with the ability to assess and optimise the hydrodynamic performance of an existing or new device before it has even become a physical reality. In this section, the availability of energy in the marine environment is discussed, followed by a review of existing prototype marine energy converter technologies and their operation.

1.3.1 2.1 Ocean Resources

1.3.2 Wave Energy

The worldwide wave energy resource has been estimated to be roughly 10TW, with around 1TW available on coastlines alone (Ross, 1995). However, only a certain amount of this energy is practical to harvest; estimated at some 2000–4000 TWh/year (Callaghan and Boud, 2006). The UK is ideally situated to benefit from wave power with the Atlantic Ocean and associated air currents hitting its western shores. By far the most common source of waves is prevailing winds, with smaller contributors including tides, submarine earthquakes and storm winds. Wind generated waves are a function of wind speed, fetch, duration and water depth, the greater these factors, the more energy the resulting waves will absorb. The UK wave energy resource for practical conversion is estimated to be 50TWh/year for offshore devices, 7.8 TWh/year for near shore and 0.2 TWh/year for shoreline (ETSU, 1985; Arup Energy, 2005). When one considers that in 2016 the total electricity supplied in the UK was 357 TWh, the contribution of wave power alone could be highly significant *(Department for Business, Energy & Industrial Strategy, 2017).*

One of the resourcing difficulties faced by wave power is the seasonal influence on available waves. In the winter waves are abundant with an estimated 45% of yearly energy being available between December and February; in contrast only 12% is available between May and August (Ferro, 2006). Secondly, much of the resource, some 58%, is considered 'offshore' and lies a large distance from the shoreline requiring long power transmission systems (Westwood, 2004). These resource related challenges are just part of the picture for this new and developing technology. A study of renewable resources funded by the Department for Business Enterprise & Regulatory Reform (BERR) (disbanded) was completed in 2008. Figure 1-2 shows results for the yearly averaged wave resource around the UK.

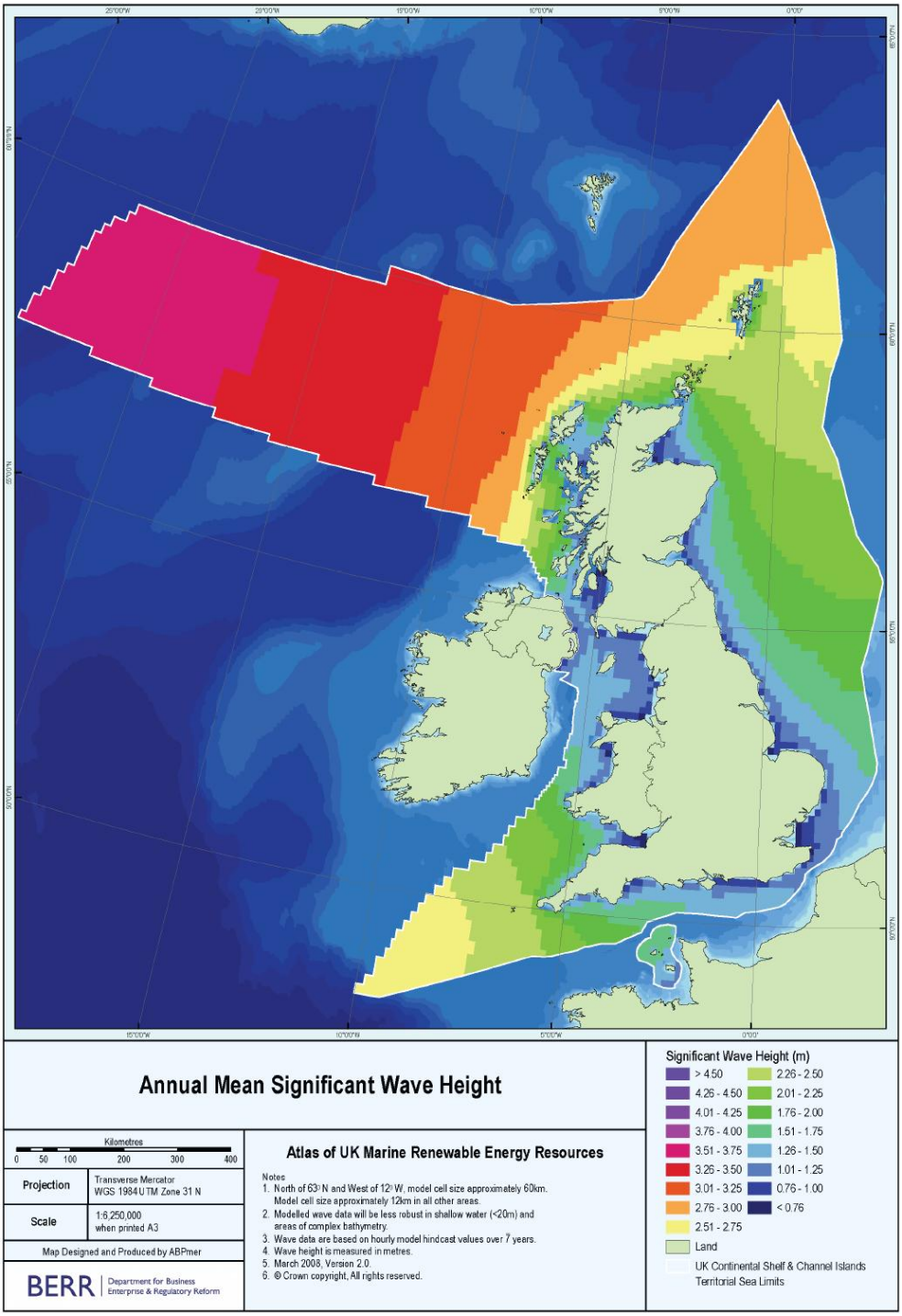

Figure 1-2: Annual mean significant wave height around the UK (ABP Marine Environmental Research, 2008)

1.3.3 Tidal Energy

Tides are driven by gravitational interaction of the Earth, Moon and Sun, with each imparting an attractive force to the huge bodies of water that surround the earth. Its range, direction and velocity are a complex mix of gravitational forces, plus global position, local bathymetry, coastal profile, sub-sea topology and weather. Despite this array of factors, predicting the tides is a highly developed science. In the UK, tables are produced by the National Oceanography Centre up to 20 years in advance for around 700 sites around the UK plus more in international locations. Technically extractable tidal energy around the UK has been estimated in a Carbon Trust report to be approximately 18TWh/y, however only 12TWh/y has been deemed economically extractable (Black & Veatch, 2005b). An evaluation of the tidal resource as a function of velocity and depth ranges is shown in Table 1.1.

	Extractable & Available Annual Energy (% of total)					
Depth Range (m)	Velocity Range (m/s)					Total
	<2.5	2.5 - 3.5	3.5 - 4.5	4.5 - 5.5	>5.5	
< 25	0.2	3.4	0.9	0.0	0.0	4.5
25 - 30	0.1	2.3	0.0	0.0	0.0	2.4
30 - 40	8.8	17.5	3.5	0.0	0.0	29.8
> 40	11.1	3.3	10.7	10.4	27.8	63.3
Total	20.2	26.5	15.1	10.4	27.8	100

Table 1.1: Available Annual Energy Breakdown Black & Veatch (2005a).

The results shown in Table 1.1, published by The Carbon Trust, were generated as part of a study that considered the readiness of existing technologies and the feasibility of deployment at given sites throughout the UK. With the overwhelming majority of energy available in sites above 30 meters, the study concluded;

"*approximately 20% of the UK resource is within sites of depth 30-40m that have Vmsp between 2.5-4.5 m/s. This site range has often been considered to be the most (economically) attractive type of site for near term developments using seabed-standing (e.g. monopole) devices; velocities are not too high, the water is not so deep as to prevent realistic installation but deep enough to allow reasonable large device size*" (Black & Veatch, 2005b)

The UK tidal resource is identified as being 10-15% of the known extractable energy worldwide. However, these figures are currently very conservative, with new studies and technologies one would expect these quantities to grow significantly.

1.4 Marine Technology

1.4.1 Wave Devices

A large array of WECs are currently in development throughout the world. Each device is designed to operate from specific combinations of wave motion and energy extraction mechanism. Various means of categorisation have been adapted by many authors relating to orientation, motion, structure, location, conversion mechanism, and generator type, examples can be found in the following references Duckers (1994); Katofsky (2008); The Watt Committee on Energy (2005); de O.Falcao (2010). The reality is that there are many combinations of factors, each valid depending on use, therefore it may be suitable to devise structures based on audience. For example, from an installation perspective one may divide the devices into mooring types i.e. tethered, gravity and pinned. However, as this research is focussed primarily on hydrodynamic and structural analysis, the following categories are aimed at classification with fluid interaction as a key divisor.

1.4.1.1 Categorisation

The categorisation is primarily based on that adopted by the European Marine Energy Centre (EMEC) website (EMEC, ndb) due to its focus on wave interaction.

Type 1: Attenuator

The principle operation of an attenuator is to exploit the relative heights of wave crests and troughs, over multiple wavelengths, at a given instance of time. Previously leading technologies, such as Palamis, achieve energy capture by means of series of floating segments that are hinged together, and orientated in parallel to wave direction; see image Figure 1-3 A. As waves propagate past the device the segments become pitched relative to one another due to their comparative positions along the wavelength, and hence wave amplitude. A power take off system, such as a hydraulic piston, is retracted and extended by the motion which pressurises a fluid. As with many types of WEC, a pressurised fluid is converted into a rotary torque via a hydraulic motor in order to drive the electrical generator. The example, Pelamis Wave Power, went into administration in 2014, but by this time it had become the first offshore wave power device to supply power to the UK grid, and the first UK wave power company to be purchased by a utility company (E.ON).

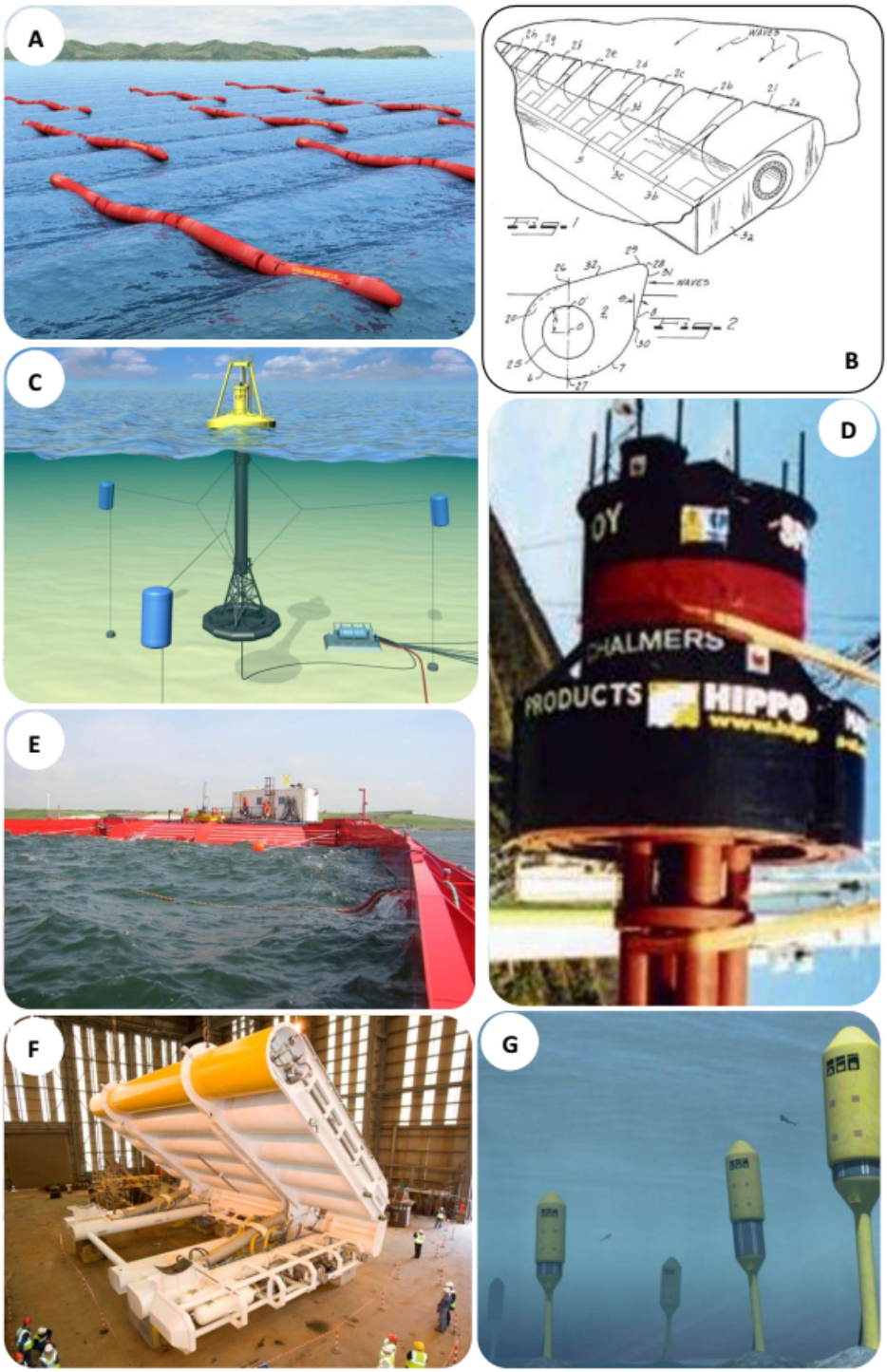

Figure 1-3: Image gallery of wave device types A: Example of an attenuator WEC, 'Pelamis' (EMEC, nda); B: Image of a terminator, from Stephen Salter's 1975 US patent (Salter, 1975); C: Image of a point absorber, the OPT PowerBuoy (FERC, 2010); D: Image of 1/5th scale Sperboy OWC (Embley Energy Ltd, nd); E: In the jaws of the Wavedragon overtopping device (Wave Dragon, nd); F: Aquamarine Power's surge generator 'Oyster' mk1, ready for deployment (Miller, nd); G: Artists impression of AWS Ocean Energy's Archimedes Wave Swing (Harris, 2016)

Type 2: Terminator

Terminators operate using a combination of wave height and the interception of surface and near surface flow velocities developed within the wave. It is a directional device with a hinged mechanism normal to the wave direction. Salter's Duck is perhaps the most prevalent of terminator technology; see image Figure 1-3 B. Its design includes a number of external bodies that are able to rotate about an integral secondary component; this is fixed in pitch by connection to an external structure (spine) or a method of counterbalance. As the wave crest rises, the force on the water acts upon a specially shaped external body, both at the surface and below, causing it to rotate about the central spine. The rotated part then returns through potential energy as the succeeding trough passes. Energy is absorbed from both the up and down rotation by a mechanism interfacing between the moving and stationary parts, for example a ring-cam pump.

Type 3: Point Absorber

A point absorber is a device that converts the heaving motion of waves into useful energy through buoyancy forces. It differs from the attenuator as the device's footprint is small, less than half a wavelength. This allows the device to accept waves from any direction. Existing point absorber designs are particularly varied, the most established is that used by the OPT PowerBuoy; see image Figure 1-3 C. The device has a fixed, seabed mounted part, in this case a weighted base; and an upper floating section, the Buoy. A hydraulic piston is connected between the fixed base and floating upper section. The wave causes the floating section to rise and lower, actuating the piston.

Type 4: Oscillating Water Column (OWC)

The principle of the oscillating water column is to isolate part of a heaving wave and a portion of air above it within a column (or similar). As the water in the column rises and lowers, the air above it is compressed and decompressed, this oscillatory pressure differential is exploited. An example of an existing OWC design is the SperBoy; see image Figure 1-3 D**.** Energy is extracted from the air by allowing it to flow to and from the surrounding atmosphere via an air driven turbine. Due to the oscillatory air flow experienced, the OWC presents a challenge to conventional turbines which expect a uni-directional flow. One solution to this is the Wells Turbine, an axial turbine with symmetrical blades able to accept flow from both directions. OWCs have been proposed for both floating and shoreline deployment.

Type 5: Overtopping

An overtopping device operates by firstly collecting sea water that has been elevated by wave action into a reservoir. The potential energy contained within the fluid is then converted into power as it is released back to the lower level of the surrounding sea. The Wave Dragon is one example of an overtopping device; see image Figure 1-3 E. To maximise its effectiveness the design includes two large curved reflectors which concentrate the wave front to a central ramp. The water flows up the ramp and into the raised reservoir where it is fed into low head turbines before returning to the sea. This type of design is often referred to as a TAPCHAN, short for 'tapered channel'. Overtopping devices have been considered extensively for both offshore and shoreline application.

Type 6: Wave surge converter

This device interacts with the surface and subsurface currents developed by passing waves. As a crest passes there is a net flow of water, or surge, in the same direction as wave propagation, this is followed by a reverse flow as the trough passes. The oscillatory forward and backward surge of water is exploited by the device. An example of this type of device is the Oyster, a seabed mounted device designed for near shore use; see image Figure 1-3 F. The energy of the oscillating flow is captured by a large flap hinged at the seabed. The flap is large enough to cover a fair width and is surface piecing to capture the larger surge forces generated there. The oscillatory motion is used to drive a hydraulic piston system adopted by many of the previous wave devices discussed.

Type 7: Pressure differential

A pressure differential device lies beneath the surface and exploits the changes in water pressure created by the waves as crests and troughs pass overhead. The Archimedes wave swing (AWS) is an existing device currently being developed; see image Figure 1-3 G. Its design has many similarities in terms of motion and footprint to that found in a point absorber, however, water pressure rather than buoyancy is used as the driving force. It is constructed from an upper air-filled cylindrical chamber, and a base fixed to the seabed. As a wave crest passes over the device, the depth of the water is effectively increased, thus increasing water pressure throughout the column of water below it. This creates in increased pressure difference between the air in the cylinder and surround sea water resulting in the compression of the air, its volume is reduced causing the cylinder to slide down a central shaft. As a trough passes over the device a reverse of the process

occurs giving the AWS the necessary oscillatory motion. For this particular device a novel power take-off has be adopted, a linear generator.

1.4.1.2 Power Take-off and Optimisation

When considering the hydrodynamic design and optimisation of a wave device, it is essential to consider how one can effectively and efficiently convert the resultant mechanical output into electricity. The power take-off system provides the means for this conversion. In many cases the output of a wave device is unsurprisingly an oscillatory motion, with the exception of a linear generator, all legacy generators are high speed rotary machines. In the case of the rotary generator, it is immediately compatible with a limited number of concepts such as the overtopping device and oscillating water column both of which use a rotating turbine. However these machines do face a number of issues, including low pressure heads, reciprocating fluid flow, cavitation and abrasive particles (Drew et al., 2009). Various studies have been conducted in order to improve the efficiency of these power take-off systems. For most reciprocating WEC systems a hydraulic fluid take-off is the most popular. This allows the oscillatory motion of a piston to be easily converted into rotary by a suitable hydraulic motor. Further systems are usually added including a rectifying system, so both the outward and inward stroke of the piston can be utilised, and an accumulator, to store and deliver the pressure evenly to the hydraulic motor. Optimising the take-off system as a whole is a complex task. One has to consider the non-linear damping the system will generate and 'tune' it to match the kinematics of the WEC or vice versa. Another issue is the inconsistency of wave frequency. One method proposed to tackle this issue is the use of 'latching'. Latching involves holding the buoy at its extremes of motion (peak and trough), allowing the wave to pass until there is suitable wave force for maximum energy extraction.

1.4.2 Tidal Devices

In terms of hydrodynamic design, current tidal technologies have taken inspiration from various concepts in the wind industry. This includes the conventional axial configuration and the less usual vertical axis turbine conceived by Darrieus in 1931. Although the majority of developers are focussing on these designs, or a derivative thereof, a few have ventured into revolutionary mechanisms for energy extraction. Despite this link with wind energy, tidal power presents a new set of challenges more closely associated with conventional marine hydrodynamics. This includes greater pressure variation, cavitation, high Reynolds number conditions, particulates and potentially the growth of marine life and many more besides. The world's first commercial scale tidal turbine was produced by UK developer, Marine Current Turbines Ltd. Named 'Seagen', the twin axial rotor machine was located in the narrows of Strangford Lough in Northern Ireland and was rated at 1.2MW. The company has since been acquired by Atlantis and SeaGen is due to be decommissioned this year, the turbines generated 10GWh during their lifetime. Atlantis have said lessons learned from SeaGen have been used in the development of the next generation SeaGen 1MW tidal turbine (reNews, 2016).

1.4.2.1 Categorisation

Fluid motion in tides is much simpler than waves and can be considered as a body of fluid travelling in uniform direction and velocity. Any changes in velocity or direction occur slowly; around the UK one tidal cycle takes on average 12 hours 25 minutes. Therefore, for the purposes of modelling, flow conditions can be considered quasi-steady. In reality there is likely to be turbulence and possibly some wave interaction, however, devices in a uniform flow are well understood and already have many optima for various applications. The two main types include:

- Axial – where flow direction is parallel to the device's axis of rotation
- Cross-flow – where flow direction is normal to the device's axis of rotation

While the vast majority of tidal devices are rotating, a few alternatives propose reciprocating motion. To maintain good resolution of the existing tidal devices, all variants of axial and cross-flow turbines are sectioned into individual categories based on their hydrodynamic individuality and their principle of energy extraction.

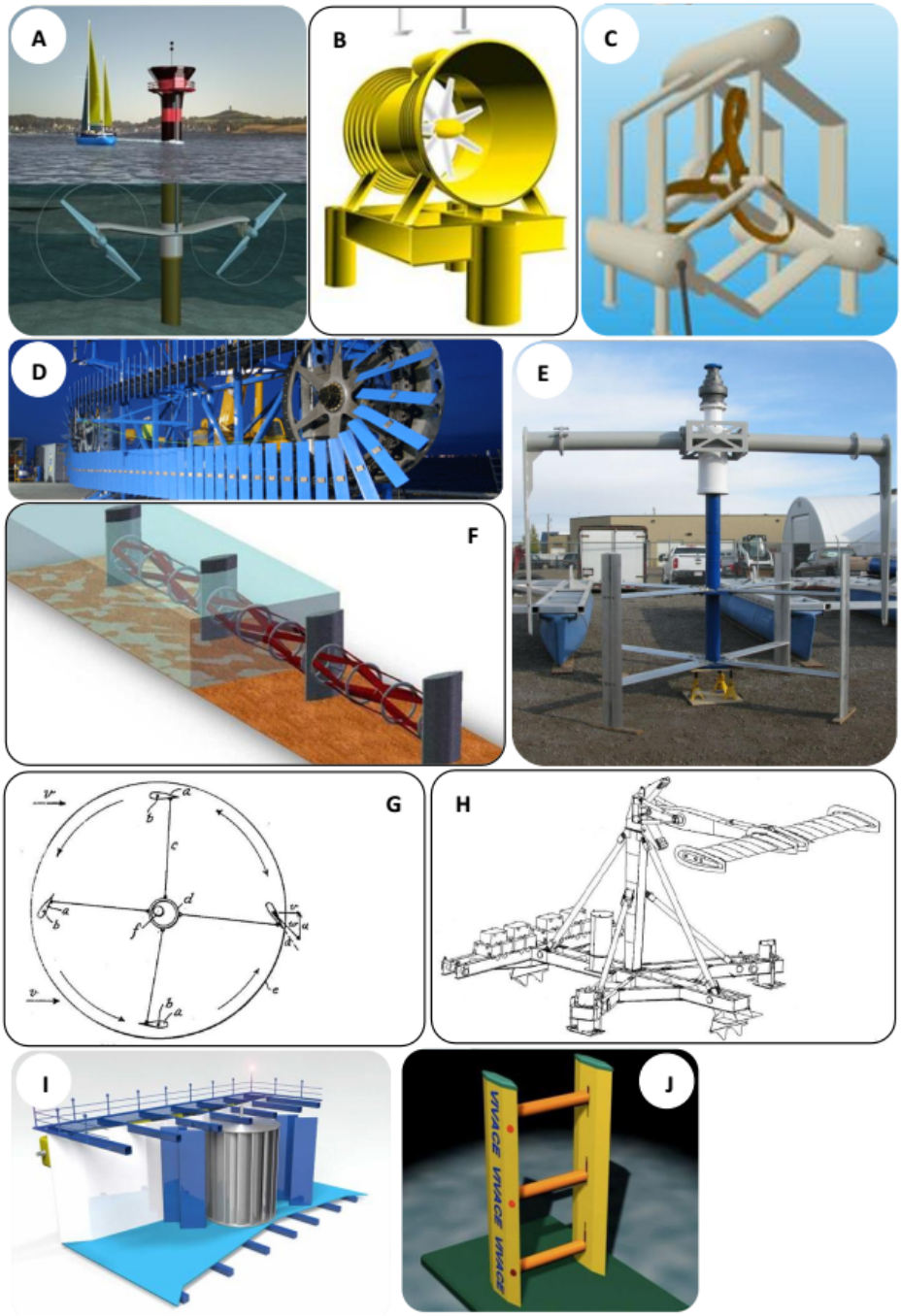

Figure 1-4: Image gallery of tidal devices A: Artist's impression of the Seagen tidal turbine (CBC News, 2009); B: Lunar Energy's Venturi tidal turbine (Lunar Energy Power Ltd., nd); C: Loopwing tidal turbine (Patel, 2011); D: 'Nereus' chain axial turbine (Miller, 2009); E: Example of a fixed pitch cross-flow turbine, EnCurrent turbine (New Energy Corporation Inc., nd); F: THAWT cross-flow turbine (Kepler Energy, nd); G: Variable-Pitch turbine proposed in Darrieus' patent (Darrieus, 1931); H: Drawing of the Stingray, Engineering Business Ltd (Engineering Business Ltd., nd); I: Proteus Mk III Venturi cross-flow turbine (Neptune Renewable Energy, 2010); J: CAD drawing of the VIVACE tidal energy converter (Karin, 2009)

Type 1: Conventional axial turbine

The axial turbine is identical in concept to the ubiquitous wind turbine. Hydrofoil blades are arranged as to rotate about an axis which is in parallel to flow direction. The blades act in the same manner as aerofoils; fluid is accelerated over one side of the blade causing a low pressure region. The pressure difference between blade surfaces gives rise to lift force, pushing the blade towards the low pressure and rotating the turbine. The SeaGen tidal turbine is an example of an axial turbine; see image Figure 1-4 A. This type of turbine is often referred to as a 'horizontal axis turbine', a term born in the wind industry. However, unlike the wind industry the device types in the marine setting are potentially more diverse with alternative turbines including a horizontal axis, but which receive the flow perpendicular to the axis of rotation. Hence the term 'axial' has been deemed more accurate for categorisation. In order to achieve good efficiency over a range of flow speeds the blades of an axial turbine may include the ability to mechanically alter their angle of attack to the oncoming flow by rotation about their own axis. The decision whether to include this feature is a matter of debate, a trade-off between conversion efficiency and simplicity being at the root. Designs include both floating devices, such as the Evopod (Ocean Flow Energy, nd) and fixed, including the aforementioned Seagen, which is secured to the seabed via a monopole. Efficiency of the first generation SeaGen turbines is claimed to be above 48% (Fraenkel, 2010). There are a few unusual variants of axial turbine, including openhydro's open-centre turbine. The turbine differs because it has a much higher blade number and an annular ring connects the blades at their tips. The effect of an open centre is unjustified in terms of efficiency; instead its purpose appears to be environmental, i.e. as a way for sea creatures to pass through the turbine unharmed.

Type 2: Venturi axial

This axial turbine operates in much the same manner as the conventional axial turbine but with an added shroud. The shroud's purpose is to accelerate the flow by taking advantage of the Venturi effect. An axial turbine is placed within the accelerated flow section of the shroud, allowing a more conventional high speed blade profile and the ability to operate at relatively slower ambient tidal flow speeds. See image Figure 1-4 B.

Type 3: Loopwing axial

The loop-wing concept originates from Japan and stemmed from the company's original wind turbine product. The loopwing consist of blades that extend radially, which then curve around and reconnect to the axis at a displaced position; see image Figure 1-4 C. Although most of the analysis is presented on the wind turbine variant, one would assume similar attributes are present in the tidal version (ReNew, 2007). The loopwing design has a significantly reduced tip vortex and high efficiency at low tip speed ratios compared to conventional turbines. These attributes are highly desirable for tidal flows where drag and cavitation are significant barriers for high tip speed devices.

Type 4: Chain axial

This 400kW turbine was successfully trialled by Atlantis Resources Corporation and is currently grid connected in Australia. Much like the drive chain of a bicycle, the turbine consists of two hubs linked by a chain. Numerous hydrofoils are mounted on the chain, taking a linear path back and forth between the hubs and rounding the corner at each end; see image Figure 1-4 D. The turbine has some rather obvious advantages including its geometry and blade number, allowing it to operate in relatively shallow water and develop significant torque compared to conventional axial turbines. There are also some drawbacks, the current prototype appears to have fixed pitch blades and will only accept flow from one direction. These issues should be surmountable however and future designs could prove very effective.

Type 5: Fixed Pitch cross-flow

The cross-flow concept originates from the Darrieus wind turbine design. The turbine is orientated with the axis of rotation normal to the flow, and can either be mounted vertically or horizontally. A vertically mounted example is shown in Figure 1-4 E. The cross-flow turbine exhibits an array of advantages and disadvantages over the axial design. The advantage of the cross flow turbine is that all of blade length is held at a fixed distance from the axis of rotation, this means the experienced flow velocities are constant across the blade, which is in contrast to axial turbines where load is spread unevenly along blade length. The disadvantage is power is cyclic as the blades travel in and out of optimum angles of attack, also the downstream orbit of the blades is subject to turbulence from the upstream blade interaction. The fixed blade type is also not self starting and has a low efficiency compared to axial turbines.

Type 6: Helical cross-flow

This turbine is powered by the same hydrodynamic mechanism as the previous cross-flow turbines, this difference is that the blades are bent around the central axis in a helical fashion. The term helical is used loosely as some devices have essentially straight blades which are angled to achieve the same effect. The purpose of the blade geometry is to smooth out the torque curve for each rotation of the device. This eases the task of converting the output into a usable constant velocity which is required for effective power generation. One example is the Transverse Horizontal Axis Water Turbine (THAWT) developed by Oxford University Engineering Department, a project which has now been formed into the spin-off company Kepler Energy; see image Figure 1-4 F.

Type 7: Variable-Pitch cross-flow

As the name suggests, this type of marine turbine is a hybrid of the fixed-pitch. As the blades rotate about the central axis, they are also rotated about their own axis, often in a sinusoidal motion or similar. As with all of the turbines discussed so far, the included blades are hydrofoils that convert the flux of energy into lift force. By oscillating the blades about their own axis one can delay separation and reduce drag of the blades from various positions of rotation about the central axis. This concept of variable pitching can also be credited to Darrieus as it is also proposed in his 1931 patent (Darrieus, 1931); see image Figure 1-4 G. Interestingly, in the same year Ernst Schneider, while working for J. M. Voith, patented what is now known as the Voith-Schneider Propeller (VSP) (Scheider et al., 1931), which is essentially the same concept, however it was designed for use in water as a propulsion device. One can look at the design as a variable-pitch Darrieus in water, or a reverse VSP. Oscillation of the blades can be achieved either mechanically or passively. An example of a mechanically pitched concept is the cycloidal turbine investigated in 1994 by QinetiQ under funding from the DTI (QinetiQ Ltd., 1994). Alternatively, the Kobold turbine being developed by Ponte di Archimede International S.p.A, used a combination of hydrodynamic and centrifugal forces to regulate blade pitch, although little information is available about the specifics of the system. Both controlled and passive pitch blades have their advantages, one would assume controlled blades could be highly optimised and unaffected by environmental factors such as turbulence and debris, however the passive is potentially a simpler design in terms of components and maintenance.

Type 8: Reciprocating hydrofoil

The reciprocating hydrofoil concept consists of hydrofoil blades attached to pivoting arms. The blades move up and down by altering their angle of attack to the oncoming flow. Much like wave devices the energy is used to drive hydraulic rams, pumping fluid to turn an electrical generator. The design has the advantage of having a small profile height compared to many other technologies, making it easy to deploy a high power output device in comparatively shallow water. Examples of reciprocating hydrofoil based devices include the Pulse-Stream 100 and the Stingray (Fischer et al., 2016). An image of the Stingray device is shown in Figure 1-4 H.

Type 9: Venturi cross-flow

The turbine uses the same principles as the venture axial turbine, but applied to a cross-flow turbine. One example is The Neptune Proteus NP1000, shown in Figure 1-4 I. This turbine is particularly interesting as it introduces the use of guide vanes to improve the angle of incidence of the incoming flow. The turbine rotor itself also has a noticeably higher solidity. It is claimed that the design "generates 30% more electricity per unit channel width than circular turbines" (Neptune Renewable Energy, 2010).

Type 10: Vortex induced vibration

The vortex induced vibration tidal device was invented by Professor Michael Bernitsas at the University of Michigan. The device has been named VIVACE, which stands for Vortex Induced Vibration Aquatic Clean Energy; an image is shown in Figure 1-4 J. The principle of the device is to use the natural phenomenon of vortex generation, in this case by circular cylinders. The process of vortex shedding was first described by Hungarian physicist Theodore von Kármán, and thus is aptly named the von Kármán vortex street. Within certain ranges of Reynolds number, and with reasonably laminar flow conditions, vortex streets can generate large alternating lift forces on circular cylinders (although other shapes may also experience this). The VIVACE allows these forces to vertically push the cylinders up and down, actuating linear generators at each end of the cylinder.

The prototype device has successfully produced electricity, however there are a large number of issues which present themselves for this device. Firstly there is the issue of scale; one would assume the cylinders used in the device are scaled according to the flow speed to achieve the Reynolds number for optimum vortex street generation. Increasing cylinder size to suit industrial scale generation would

not be possible as the Reynolds number would be altered, leaving only the option of using thousands of devices. Secondly, when tidal flow speeds are out of the vortex inducing range the device is incapable of producing energy, while alternative devices may still be generating even at a somewhat lower output.

1.4.3 Technology Summary

Many exciting and innovative designs have been identified in both the wave and tidal fields, each with a diverse mix of advantages and disadvantages. At this stage it is impossible to conclude which are the "best" designs, with a lack of statistical data, design optimisation and long term trials being common issues facing the developers and industry as a whole. If any of the designs are to become successful forms of renewable energy, they will continue to require development and optimisation from a number of disciplines. Most notably is their ability to produce electricity, consistently, efficiently and cost effectively. Secondly, and of equal importance, the devices need to have unparalleled survivability within the hostile environment of the open ocean.

From a fluids perspective the modelling of wave devices presents the greatest challenge for computational methods, particularly as free surface and mesh motion require significant processing power. To provide useful device development, a coupled approach to simulation is almost certainly a requirement for wave devices. Here the motion of a buoy, for example, requires not only its interaction with the wave, but also with the power take-off system. This level of model coupling would enable tuning of the buoy dimensions to suit a take-off system or vice versa. In fact one could go further and include the effects of mooring lines, cable tensions and tidal effects for example.

Looking at the tidal energy challenge independently, the industry has an excellent head start for axial type turbines due to the already highly understood wind turbine being largely applicable to the marine environment after the application of various scaling factors. However, alternative forms, such as cross-flow, hydrofoil and VIV, are much less developed, requiring significant research before they are proven to be hydrodynamically robust. A part of the challenge for coastal engineers is the development of suitable platforms off of which tidal turbines can be deployed. Interaction with supporting structures, directional and cyclic issues of tidal flow, and extreme weather conditions, are just some of the additional factors included in the task.

Chapter 2

Numerical Benchmarking: Circular Cylinder

SUMMARY: In this chapter the fluid flow around a circular cylinder is investigated using numerical methods. The study is used as an opportunity to scrutinise two alternative solvers (ANSYS CFX and OpenFOAM), develop meshing strategies, explore boundary parametrisation and extract post-processing metrics. However, the work is also a comprehensive analysis in its own right, offering guidance to marine energy researchers (or otherwise) where cylindrical structures are under scrutiny. The study is limited to the use of an unsteady RANS numerical method using the SST turbulence closure model due to its predicted applicability to the study of turbine blades in subsequent chapters and due to the constraints of computational resource.

2.1 Introduction

Understanding the flow around a circular cylinder has historically been a fundamental challenge for researchers largely due to the complexity and transient nature of the wake. However, in the last decade desktop computational resources have increased sufficiently such that high resolution solutions for practical engineering have become feasible. In this case, the study of cylindrical geometries was prompted by their inclusion in leading marine turbine technologies such as the SeaGen (Marine Current Turbine Ltd, 2016) and Davis Hydro Turbine, the former having a mono-pile construction and the latter having a central shaft. Analysis of circular cylinders for the offshore market has traditionally been conducted to assess structural loading caused by vortex shedding. This phenomenon, also known as vortex induced vibration (VIV), has influenced new offshore technologies

Re **range**	**Flow regime**
$Re < 1$	Creeping flow
$3 - 5 < Re < 30 - 40$	Steady separation (Föppl vortices)
$30 - 40 < Re < 150 - 300$	Laminar periodic shedding
$150 - 200 < Re < 1.4 \times 10^5$	Subcritical
$1.4 \times 10^5 < Re < 1 \times 10^6$	Critical
$1 \times 10^6 < Re < 5 \times 10^6$	Supercritical
$5 \times 10^6 < Re < 8 \times 10^6$	Transcritical
$8 \times 10^6 < Re$	Postcritical

Table 2.1: Flow regimes around a circular cylinder (Raghavan and Bernitsas, 2011)

aimed at reducing the impact of the effect such as riser fairings and platform leg surfacing. While this is also applicable to marine renewables, it is also possible that vortices shed from cylindrical components may reduce device efficiency and cause structural fatigue and therefore require an increased level of resolution in design and development solutions. To address this, this research aims to develop and assess a rigorous numerical methodology for modelling such cases. The flow around cylinders has been extensively investigated through experimentation by notable contributors such as Tritton (1959), Roshko (1955) and Achenbach (1968), amongst many others. One of the key outcomes of this work was to categorise flow by regimes of vortex shedding with Reynolds number (Re). A prominent early paper by Lienhard (1966) proposes an outline of flow characteristics from laminar flow, up to supercritical values $\approx Re = 3.5 \times 10^6$. However, the complexity of the turbulent wake has undergone many new discoveries, with a distinct contribution from advancing numerical modelling. A review by Williamson (1996) considers the wake in detail; highlights include a detailed account of the transition of wakes from 2D to 3D between $180 < Re < 190$, control of the shedding by modification of the cylinder end conditions, and the Direct Numerical Simulation (DNS) of 3D instabilities in landmark detail. The regimes of flow around a cylinder as Reynolds number increases has been refined by numerous researchers, most notably Zdravkovich (1990) with fifteen distinct ranges. A summary of the key stages in flow development are presented in Table 2.1.

The study here considers incremental values of Re from 40 up to a maximum of 10^6. To give perspective on the range, the peak value of Re is equivalent to a 0.5m pile in a 2m/s tidal flow. This velocity range represents 'slack water' up to the peak flow/ebb for many locations around the UK, such as the Severn Estuary (Xia et al., 2010).

2.1.1 Numerical Literature

To simplify the problem many researchers have opted to conduct numerical modelling in 2D, a selection of recent examples are considered here. Beginning with the low Re cases, $Re < 160$, Park et al. (1998) and Dehkordi and Jafari (2009) both show excellent agreement of all parameters using a laminar URANS method; no ill effects from 2D simplification are found. Moving into the subcritical regime, research by Rahman et al. (2008) compares a number of two-equation turbulence models at Re values of 1000 and 3900. Results show a clear improvement in accuracy using the shear stress transport model (SST) over the $k-\epsilon$ and realizable $k-\epsilon$ models. At critical and supercritical Re values of 10^6 and 3.6×10^6, Ong et al. (2009) evaluates the $k-\epsilon$ model with a log law wall function. A limited study of the effect of y^+ is conducted although values are kept in the 5 to 30 region. Results are compared with 2D and 3D Large Eddy Simulation (LES) and experimental data with force and shedding frequencies falling within known limits, however, pressure distribution and shear stress show some divergence. Benim et al. (2007) explores the topic of near wall meshing further by using the commercial code Fluent to compute flow around a cylinder at $Re = 10^4$ using wall models and the standard turbulence model. Results from meshes in the range of y^+ values, from 10 to 1000, yield a large range of drag values. Significantly no discernible plateau is visible. Consequently, the author continues testing without wall functions, switching to the SST turbulence model and adhering to meshes that conform to $y^+ = 1$. It is worth noting that a non-conformal surface grid is used, akin to a body fitted quadtree grid. In parallel with Ong, Benim finds acceptable correlation in the supercritical regime but this rapidly loses accuracy in the critical transition region, under-predicting values quantitatively for both $k-\epsilon$ and, to a lesser extent, SST models. The application of LES to the 2D problem is approached by Tutar and Holdo (2001) where cases are computed in both URANS and LES models at an Re of 1.4×10^5. The results show that a non-linear two-equation $k-\varepsilon$ model gives improvement over the standard form, although both URANS methods under-predict pertinent values. The LES is seen to produce a superior flow field, as expected, but results in over-prediction of force and shedding values compared with experiment. While LES in this case uses a fully resolved boundary layer, the URANS method uses wall models that have previously been shown to be highly mesh dependant. Based on the findings discussed here and additional sources, it can be concluded that the URANS method shows great promise for satisfactory prediction of flow characteristics around circular cylinders. However, the lines of applicability are blurred in terms of Reynolds number range and optimal computational methodology. This paper presents a rigorous methodology to overcome some of these limitations and to maximise the applicability of URANS simulation. The methodology incorporates the SST turbulence model, a fully

Attribute	CFX	OpenFOAM*
Solution method	Fully Coupled	Segregated
Temporal control	Implicit	Implicit/Explicit
Discretisation	Median-Dual Cell-Vertex	Cell-Centred
Variable Storage	Collocated	Collocated
Pressure-Velocity handling	Rhie-Chow (adapted)	PISO

Table 2.2: Comparison of mathematical attributes for CFX and OpenFOAM. *Attributes specific to pisoFoam module

resolved boundary layer at every Re, a dense conformal grid, cell aspect ratio control and adaptive timestepping. Two solvers are used to compare the effects of the two host software packages, particularly as each uses alternative mathematical approaches. The two software packages selected for the study are OpenFOAM 1.7.1 (OpenFOAM) and ANSYS® CFX-13.0 Academic Research (CFX). OpenFOAM is a C++ based open-source software written for the Linux platform, while CFX is a prominent commercial code heavily used in the aerospace and marine industries amongst others. Both OpenFOAM and CFX employ the finite volume method (FVM) to represent and solve the Navier-Stokes equations in algebraic form; Table 2.2 gives a basic outline of the contrasting approaches taken by the two solvers.

OpenFOAM has numerous FVM solvers depending on application, for incompressible transient problems the pisoFoam solver is most suitable. As the title suggests, pisoFoam uses the Pressure Implicit with Splitting of Operators method for pressure-velocity coupling proposed by Issa (1986). The method is akin to the SIMPLE (Semi-Implicit Method for Pressure-Linked Equations) algorithm with the addition of a second corrector stage that performs momentum (neighbour) and skewness correction. Note that all future references to OpenFOAM are specifically in regard to the implementation of the pisoFoam solver. As Table 2.2 states, OpenFOAM performs the PISO loop as part of the segregated solution method, while CFX uses a coupled solution, where continuity, momentum and energy are solved simultaneously and hence decoupling is avoided by using Rhie-Chow pressure interpolation. One of the key differences between the two methods is their sensitivity to timestepping. The coupled method in CFX is able to re-solve the governing equations in a pseudo inner timestep, whereas OpenFOAM converges each parameter once, correcting only for pressure and velocity in each timestep. The result is that CFX is relatively insensitive to timestep, while OpenFOAM requires tight control, such as adhering to low Courant numbers. In terms of spatial discretisation, the medium dual-method adopted by CFX divides the original mesh into a new set of polyhedral volumes defined by connecting the face centroids and edge midpoints of all cells that share any one grid node. In contrast, the cell centred method uses the existing cell volumes defined by the input mesh. The result is that CFX includes a greater number of integration points, while

OpenFOAM retains a greater level of flexibility. A comprehensive comparison of the methods is offered by Blazek (2005). The use of turbulence models is used equally for both solvers such that cases considered to be globally low Re cases employ a Laminar model, while turbulent flows, $Re > 150$, implement the Shear Stress Transport turbulence model (SST), as developed by Menter (1994). The model uses a $k-\omega$ model to estimate turbulence in the near wall region and $k-\varepsilon$ outside of the boundary layer; a blending function connects the two models. The SST model has been chosen for the study due to its availability in both solvers and a history of preferable results in high shear conditions, demonstrated by Bardina et al. (1997), over alternative mainstream models. In terms of iterative method and general interpolation of the variables, both solvers have been kept to settings suggested by their accompanying literature. In OpenFOAM this comprises of Gaussian methods for gradient divergence and Laplacian schemes, with second order accuracy throughout. A mix of preconditioned conjugate gradient and bi-conjugate gradient solvers are used for solution of the physical and turbulence parameters as found in example pisoFoam models. CFX uses a proprietary method which is described at length by Gretton (2009). While a comprehensive account of the setup is provided in the next section, any omissions regarding underlying constants should be assumed to be solver default values.

2.2 Numerical Method

In this section a detailed account of the setup is given including boundary and solver constraints, meshing strategy and turbulence modelling. The dimensions of the domain for all cases are given in Figure 2-1. The proportions allow blockage to be negligible; also note that the 3$^{\text{rd}}$ dimension (z) was set to $0.1c$.

2.2.1 Boundary Conditions

The boundary conditions for all cases were defined in OpenFOAM and CFX with similarity a stringent objective. The properties are as follows:

Inlet: A uniform flow is specified at the inlet, calculated by rearrangement of the Reynolds number equation 2.1, for flow velocity U; where ρ is density, c is characteristic length (diameter) and μ is dynamic viscosity.

$$Re = \frac{\rho U c}{\mu} \tag{2.1}$$

Outlet: The outlet is sufficiently downstream such that any vortices are no longer present in the flow stream. In this case a pressure or velocity outlet is applicable

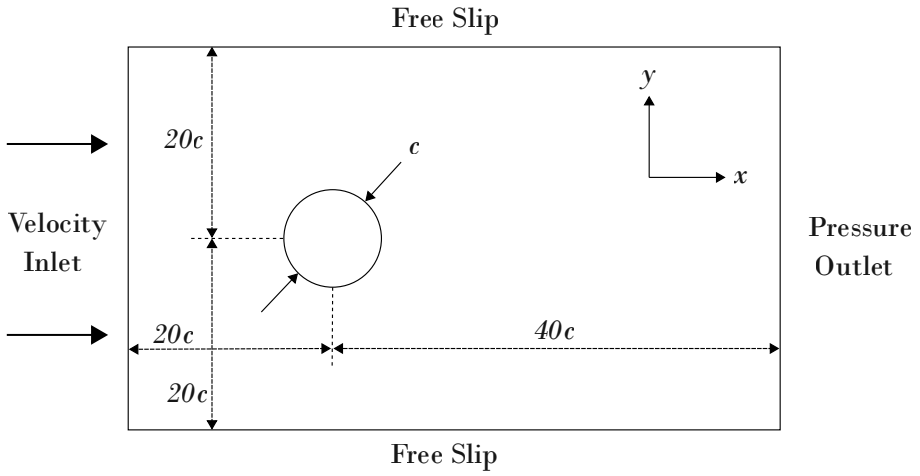

Figure 2-1: Geometry of computer domain (not to scale)

with both showing identical results. For a pressure boundary in CFX the relative pressure is set to zero; $p_{rel} = 0$. In OpenFOAM the equivalent setting used is a 'free stream' pressure outlet.

Free slip edges: The sides assigned as 'free-slip' boundaries, shown in Figure 2-1, allow the fluid velocity component parallel to the wall to remain computed, while velocity normal to the wall and the wall shear stress are set to zero; $U_y = 0, \tau_{wall} = 0$.

Periodic faces: The boundaries in the X-Y plane were set as symmetry planes; here velocities and pressures are assumed equal at both sides of the boundary. With zero spanwise flow in the 2D case, this boundary type provides the illusion of an infinitely long cylinder. CFX employs this technique due to its node centred spacial discretisation, the result being a very narrow 3D calculation, sometimes regarded as '2.5D'. In OpenFOAM a second option exists in the form of an 'empty' boundary condition. In this case the solver performs an effective 2D calculation between cell centres, with a result only existing within a central plane. Tests were conducted in OpenFOAM for both symmetry and empty boundaries, returning a result of negligible difference.

Cylinder surface: The cylinder boundary is set to a no-slip condition, where pressure is set to zero gradient and velocities are set to zero; $U_x = U_y = 0$.

2.2.2 Turbulence Properties

For URANS computation using the SST model, as discussed in Section 2.1.1, values for turbulence kinetic energy k and turbulent frequency ω are required. In CFX it

is standard practice to select a turbulence intensity from which automatic values are calculated, however, in the interests of similarity both solvers are manually set using equations 2.2-2.3. A turbulence intensity I of 2.5% is used throughout; note that turbulence length l is given in equation 2.4 and C_μ is the empirical non-dimensional constant 0.09. Values of k of ω and at the cylinder wall are given in equations 2.5 and 2.6, as proposed by Wilcox (1993), where is kinematic viscosity, $\beta = 0.075$, a non-dimensional constant, and $y_1$is the distance to the first node.

$$k = \frac{2}{3}(U_\infty I)^2 \tag{2.2}$$

$$\omega = \frac{k^{\frac{3}{2}}}{kC_\mu l} \tag{2.3}$$

$$l = 0.07c \tag{2.4}$$

$$k_{wall} = 0 \tag{2.5}$$

$$\omega_{wall} = \frac{60\upsilon}{\beta y_1^2} \tag{2.6}$$

It is important to note that the use of standard logarithmic wall functions for low Re meshes leads to high inaccuracies. Kalitzin et al. (2005) discusses the issues in detail including both methods employed in this work. The CFX solver uses an automatic near-wall treatment in which k is set to zero and the velocities close to the wall are calculated from an alternative formulation of the velocity profile. Additionally the ω term is a blended value of sublayer and logarithmic components. The SST model available for pisoFoam in the employed version of OpenFOAM forces the implementation of a wall model and does not offer an advanced solution as found in CFX. However, it is possible to gain an effective solution by replacing the standard logarithmic model with a continuous wall formulation; in this case Spalding's solution to the 'law of the wall' is used (Spalding, 1961).

2.2.3 Meshing

To assure a high level of grid independence a low-Re approach to meshing is taken. The term 'low-Re' is not to be confused with global Reynolds number, but indicates the low turbulent Reynolds number that exists in the viscous sublayer. The y^+ value represents a non-dimensional distance of the first node from a no-slip wall. It links the node distance to shear stress τ_ω, by non-dimensionalising the value with the fluid properties density and viscosity; refer to equation 2.7. In order to utilise low-Re boundary properties it is generally accepted that the mesh must achieve first layer cell thicknesses equivalent to a $y^+ < 1$ for most solvers, see ANSYS® (2010) and Benim et al. (2007). However, a study of hull forms in comparably high Re marine flows by Jagadeesh and Murali (2009), concludes that a mesh of $y^+ < 2$ with 5 cells in the boundary layer was sufficient for accurate solution of a number of two-equation turbulence models.

$$y^+ = \frac{\sqrt{\frac{\tau_\omega}{\rho}} y_1}{\nu} \tag{2.7}$$

To achieve a mesh within the constraints identified, a commonly employed empirical calculation based on flat plate theory is initially used to estimate a first layer height, as shown in equation 2.8.

$$y_1 = cy^+ \sqrt{74} Re_L^{-13/14} \tag{2.8}$$

Initial tests were conducted using the predicted values and post processed to acquire boundary layer thicknesses using velocity at $0.99U_\infty$. The result was a clear over-prediction for thickness y_1, particularly at walls adjacent to the maximum flow velocities. Therefore a second round of meshing was completed which ensured that a minimum 5 cells were located in the boundary layer; for the majority of the cylinder surface this number was higher. To assess and correct the inflated hexahedral mesh layers, equations were derived to link total height (of boundary layer) h, number of layers j, expansion ratio r and first cell height y_1. Equations 2.9-2.11 represent the derivation of the total thickness, and equations 2.12-2.13 are rearrangements for post processing the number of layers and establishing a replacement first cell thickness respectively. Note that the final meshes conformed

to a maximum value of $0.5 < y^+ < 1.5$ on post-processing.

$$h = y_1 + y_1 r + y_1 r^2 + y_1 r^3 + \cdots + y_1 r^{j-1} \tag{2.9}$$

$$h = \sum_{0}^{j-1} y_1 r^j \tag{2.10}$$

$$h = y_1 \left(\frac{r^j - 1}{r - 1} \right) \tag{2.11}$$

$$j = \frac{\ln \left(\frac{h(r-1)+y_1}{y_1} \right)}{\ln r} \tag{2.12}$$

$$y_1 = h \left(\frac{r - 1}{r^j - 1} \right) \tag{2.13}$$

An exact mesh match between the two solvers was maintained by generating all meshes in ANSYS® Meshing 13.0 then converting into OpenFOAM format for each Reynolds number. The mesh template consists of a body fitted hexahedral region surrounding the cylinder with unstructured wedges filling the remaining far field domain. A typical mesh in the near field of the cylinder is shown in Figure 2-2 (Left). The lack of any symmetry is theoretically unimportant given sufficient grid resolution, a positive aspect being that it aids the development of vortex shedding. Iaccarino et al. (2003) conducted a URANS simulation of a square cylinder in an external flow, reporting that for a symmetrical grid a user induced flow velocity perturbation was required to induce shedding. Figure 2-2 (Right) shows the body fitted region of the mesh in more detail; an expansion ratio of 1.1 is used with a total of 30 layers. Furthermore, the aspect ratio of wall cell circumferential width to cell height y_1 is kept below 20:1 for all cases, the single exception was $Re = 10^6$ where the ratio is extended to 100:1, a value that still offers exceptional resolution at this Re.

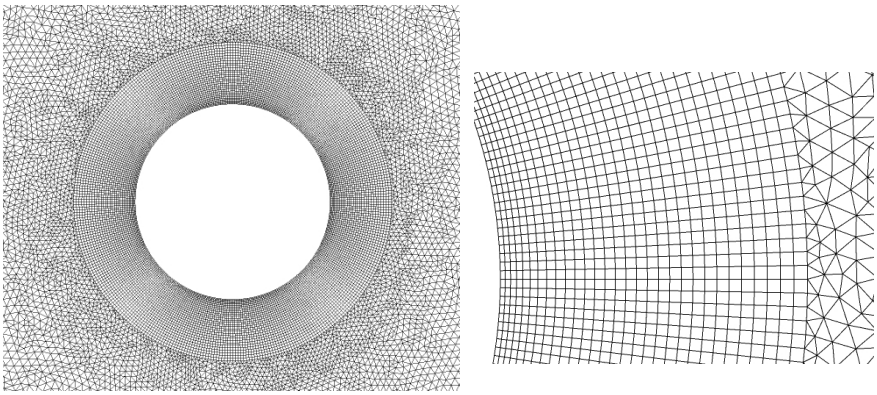

Figure 2-2: Images of a typical mesh ($Re = 1000$ shown); Left: Image showing near and far field meshes from the cylinder, Right: Detail of inflated hexahedral mesh at the cylinder boundary

2.2.4 Solver Control

Both CFX and OpenFOAM are implicit solvers; however, the pisoFoam solver does not include outer loop corrections, i.e. full recalculation of the N-S equations at any given timestep. The result is that a low Courant number is required to maintain numerical stability, calculation of which is given in equation 2.14, where Δt is the timestep and Δx is the minimum cell width. As a consequence the timestep decreases significantly as the mesh is refined for greater Reynolds numbers and hence processing time increases disproportionally. It should be noted that pisoFoam does not include Courant controlled timestepping by default; therefore modifications to the source code are required according to equation 2.14.

$$Cr = \frac{U\Delta t}{\Delta x} \tag{2.14}$$

The second important aspect of solver control is the convergence criteria. Both CFX and OpenFOAM include residual calculation for the solution variables; mass, momentum and turbulence parameters in the case of CFX and pressure, velocity and turbulence in the case of OpenFOAM. The recommended value for both CFX and the pisoFoam solver in accompanying guidance notes is 10^{-6} for tight convergence; this value is selected for all cases, as well as solving all parameters to double precision. The specified total time is calculated from a non-dimensional

time value t^* as given in equation 2.15. All simulations are solved to 150 non-dimensional time units.

$$t^* = \frac{tU}{c} \tag{2.15}$$

2.2.5 Post-Processing

Data from CFX and OpenFOAM were post-processed using ANSYS CFD-Post 13.0 and ParaView 3.12.0-RC2 respectively. Instantaneous values of drag coefficient C_D and root mean square of lift coefficient C_{Lrms} are calculated using equations 2.16 and 2.17, where F_D and F_L are the corresponding unit forces. The Strouhal number, St, represents a normalised value of shedding frequency; see equation 2.18, where f is the shedding frequency in Hertz. The coefficient of pressure C_p is calculated by equation 2.19, where p is the static pressure, and where all values with the subscript infinity denote free-stream values taken 0.1m from the inlet in the x-axis and at the centreline of the cylinder in the y-axis.

$$C_D = \frac{F_D}{\frac{1}{2}\rho U^2 c} \tag{2.16}$$

$$C_{Lrms} = \frac{\sqrt{\frac{1}{n}\left(F_{L_1}^2 + F_{L_2}^2 + ...F_{L_n}^2\right)}}{\frac{1}{2}\rho U^2 c} \tag{2.17}$$

$$St = \frac{fc}{U} \tag{2.18}$$

$$C_p = \frac{p - p_\infty}{\frac{1}{2}\rho_\infty U_\infty^2} \tag{2.19}$$

2.3 Results

To represent the full range of conditions expected in the case of a cylinder in tidal flow, computations have been performed at $Re = 40, 100, 10^3, 10^4, 10^5$ and

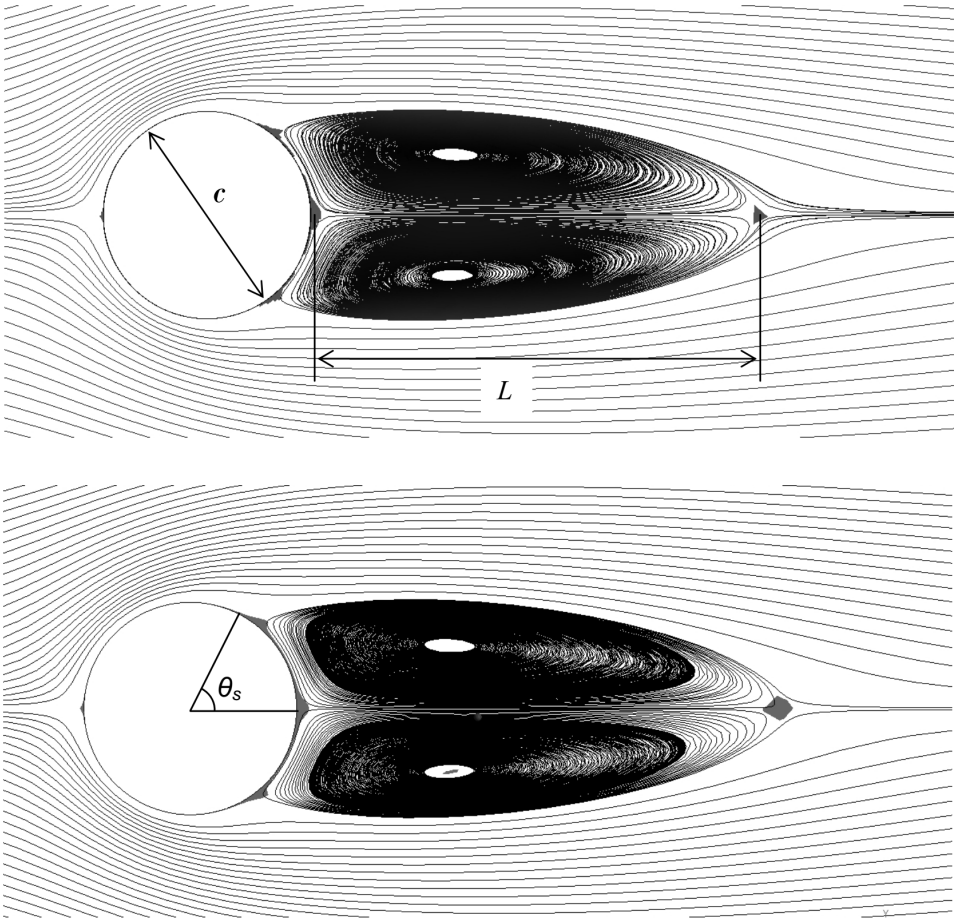

Figure 2-3: Streamline and stagnation point images at $Re = 40$ after 150 non-dimensional seconds, top: OpenFOAM, bottom: CFX

10^6 . The following results serve to evaluate a number of objectives, namely, the performance of URANS simulation using the Menter SST turbulence model combined with low-Re meshing, and the comparability of the commercial code ANSYS® CFX 13.0 with the open-source code OpenFOAM (using the pisoFoam solver), given nominally identical cases. A number of key parameters have been identified for presentation and discussion.

2.3.1 Calibration Testing Re = 40

Testing initially at a low Reynolds number using a laminar model was conducted to provide validation of the boundary setup strategy outlined throughout Section 2.2.1 (excluding turbulence), and to evaluate the success of the modified pisoFoam solver to include Courant timestepping control. The Courant number is initially defined as 0.8. The images in Figure 2-3 show the visible similarity between the Föppl vortices computed by OpenFOAM and CFX at $Re = 40$.

	C_D	C_{D_p}	C_{D_f}	L/c	θs
Experimental	1.6	0.935	-	2.1-2.19	53-53.4
Numerical	1.51-1.54	0.99-1.02	0.51-0.54	2.15-2.345	53.6-53.8
CFX	1.55	1.01	0.54	2.25	54
OpenFOAM	1.55	1.01	0.54	2.17	54

Table 2.3: Lift, drag and separation measurements for $Re = 40$. Experimental: Tritton (1959); Taneda (1956); Coutanceau and Bouard (1977); Grove et al. (1964); Numerical: Dehkordi and Jafari (2009), Park et al. (1998), Dennis and Chang (1970)

The images were generated by independent post-processing software; (a) ParaView and (b) ANSYS® 13.0 CFD-Post. Comparing the results quantitatively at $t^* = 150$, shown in Table 2.3, the components of drag, wake length to cylinder diameter ratio (L/c) and separation angle (θs) are all within minor tolerances between CFX, OpenFOAM and experimental values.

Although the tests were continued up to $t^* = 150$, the results of both CFX and OpenFOAM had effectively reached a steady state around $t^* = 30$, with the majority of the wake growth occurring below $t^* = 12$. Figure 2-4 displays the time histories of wake growth for both the computed cases and those from literature. For both CFX and OpenFOAM the wake growth is almost identical to that computed by Rosenfeld, and only marginally less than experimental values at 12 seconds. The agreement of the present study calculations of both CFX and OpenFOAM against published data indicates that the cases are appropriately defined and that the Courant number value of 0.8 is an acceptable initial value for time accurate computation. Using this information the remaining tests were defined, including one further laminar shedding case at $Re = 100$, and a number of turbulent cases using the SST turbulence model from $Re = 10^3$ to 10^6. The results of these tests are graphically represented and discussed in terms of forces and flow features henceforth.

2.3.2 Coefficient of Drag

The results for drag coefficient averaged over $t^* = 140$ to 150 for both solvers are plotted in Figure 2-5 against published work by Zdravkovich (1990), Massey (1989) and the Engineering Sciences Data Unit (ESDU (1980)). The three reference plots are considered to be an infinitely long smooth cylinder. The discrepancy between the plots in the critical region, around $10^5 < Re < 3.5 \times 10^6$, is demonstrative of the flow instability in this region with experimental values varying significantly between many authors. The plot by Massey is largely similar to Wieselsberger et al. (1923), while Zdravkovich identifies the large variance by including boundaries of

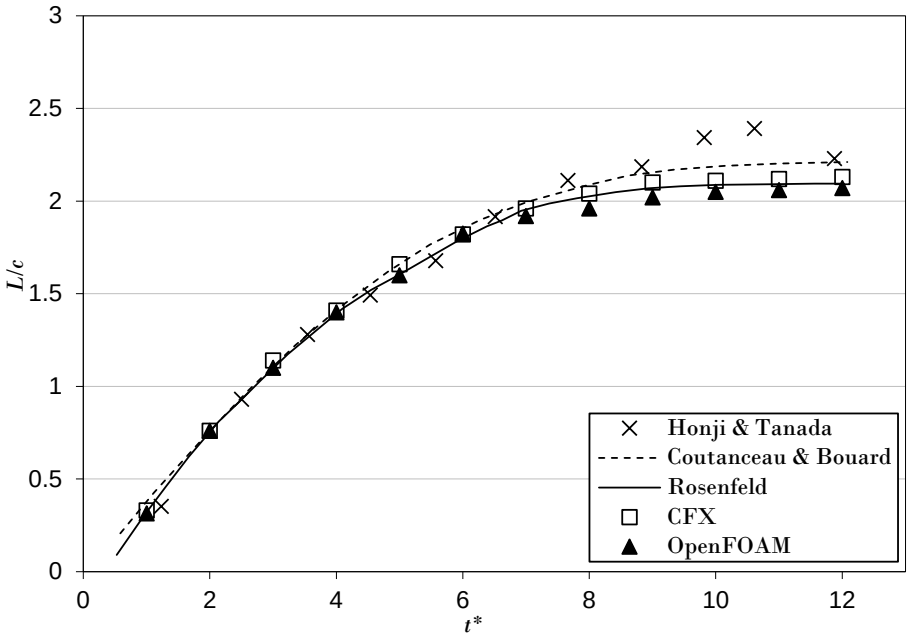

Figure 2-4: Development of vortex length with respect to non-dimensional time. Experimental: Honji and Taneda (1969); Coutanceau and Bouard (1977); Numerical: Rosenfeld and Kwak (1988).

possible results, such as that presented by Shih et al. (1993). The ESDU source largely affirms Massey and Zdravkovich's findings.

The present results from CFX and OpenFOAM are clearly in agreement at low Re values, in fact, OpenFOAM continues to give values within $0.1C_D$ of experimental values up to $Re = 10^4$. CFX over-predicts CD at Re values of10^3 and 10^4, but shows some recovery in the critical region, that of $Re > 10^5$, with values close to, or within, known regions of high variability. In the same region OpenFOAM suffers a sharp drop in drag; to investigate this, a breakdown of the result into pressure and viscous components is presented in Figure 2-6.

Considering firstly the viscous element of drag, values are generally under-predicted by both solvers, with values above $Re = 10^3$ becoming negligible compared to total drag. The comparative importance of pressure drag is clearly visible, which in the CFX results, shows good correlation with experimental for all Re values although quantitatively reaches a maximum error $\approx 30\%$ at $Re = 10^4$. OpenFOAM displays similar characteristics up to $Re = 10^4$ where the maximum error is half at approximately 15%. Above this Re the OpenFOAM result clearly shows the extensive under-prediction of pressure drag.

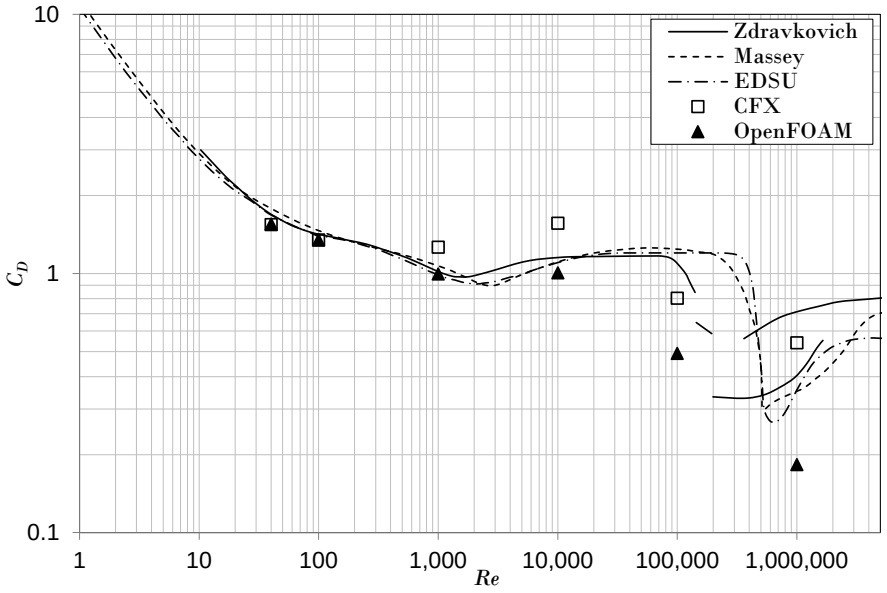

Figure 2-5: Drag coefficient versus Reynolds number; correlation between experimental and numerical results. Published values for smooth cylinder: Zdravkovich (1990); Massey (1989); ESDU (1980).

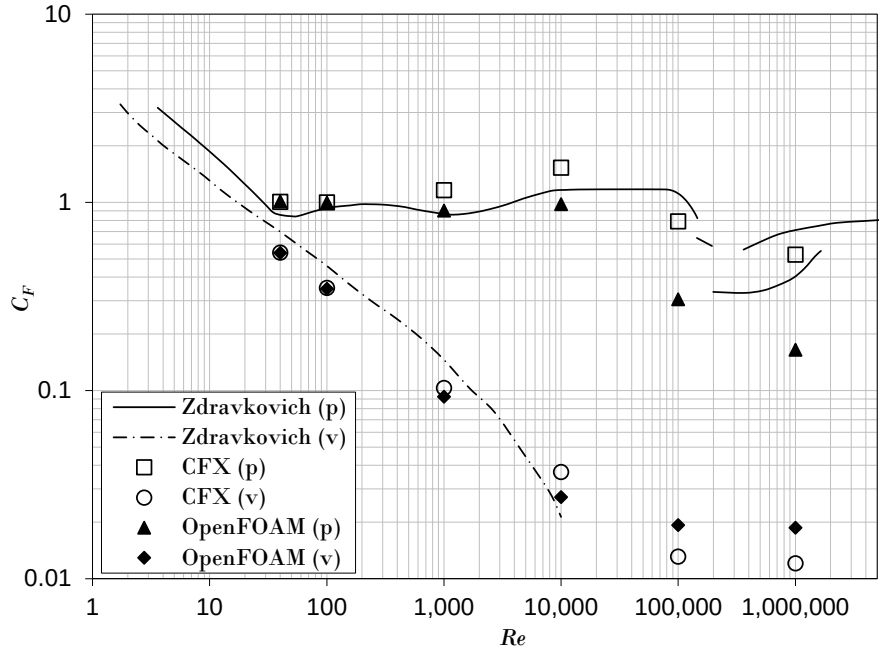

Figure 2-6: Pressure and viscous components of drag coefficient versus Reynolds number. Published values for smooth cylinder: Zdravkovich (1990)

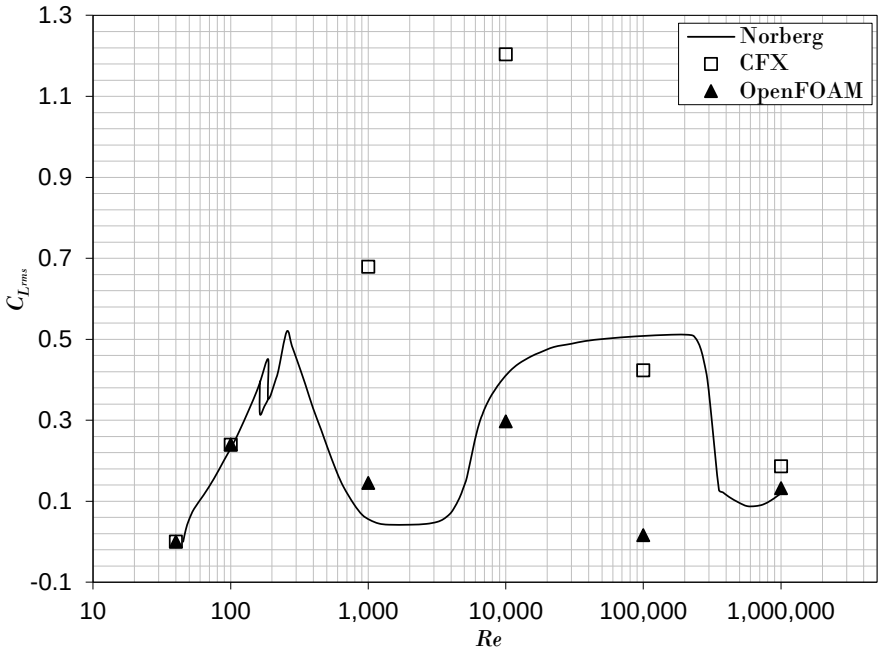

Figure 2-7: Graph of rms value of lift coefficient with Reynolds number. Published experimental data: Norberg (2003)

2.3.3 Coefficient of Lift

A significant contribution to the distribution of pressure driven forces is that of vortex shedding, an expected feature of the flow at the Reynolds numbers tested (with the exception of 40). The fluctuating lift coefficient, $C_{L'}$, provides an accessible record of vortex shedding. Taking a root mean squared (rms) of values for time $t* = 140$ to 150, see equation 2.17, results are plotted alongside a best fit curve based on an experimental review by Norberg (2003) in Figure 2-7. In parallel to the trends in C_D, OpenFOAM performs reasonably up to $Re = 10^4$ with results falling within the scatter of the original data points presented by Norberg (not shown in Figure 2-7). At $Re = 10^5$ OpenFOAM is seen to generate zero lift, suggesting the absence of shedding, followed by a final value at $Re = 10^6$ recovering to closely match Norberg's result. The CFX results differ significantly from OpenFOAM in the subcritical region with highly over predicted values at $Re = 10^3$ and $Re = 10^4$. At high Re the CFX results for C_{Lrms} return to values with less than a 15% error from Norberg's result. This unusual behaviour in the critical Re range can be investigated further by considering the lift oscillation, represented by the Strouhal shedding frequency.

2.3.4 Strouhal Number

The final part of the analysis considers the Strouhal number of captured vortex shedding. The Strouhal number is an important indicator of the transient accuracy of the simulation. The results in Figure 2-8 for CFX and OpenFOAM are compared with an experimental 'best fit' curve from Norberg (2003) and experimental results at high Re from Achenbach and Heinecke (1981). Success in the laminar range continues as the Strouhal number is accurately captured by both codes to 3.d.p. of accuracy. Both codes are within $\pm 9\%$ of findings by Norberg at $Re = 1000$, above this point the CFX simulations begin to shed at steadily increasing rates, failing to predict the drop at intermediate Re values. OpenFOAM provides a matching Strouhal frequency at $Re = 10^4$, before a distinct drop at 10^5 and failure to shed at 10^6. With both solvers failing to predict the sharp rise in the supercritical region, it is clear that the SST model is no longer able to produce a realistic flow field. The sharp rise indicates the transition of the boundary layer to a turbulent state, this dramatically reduces the length scale of eddies below the resolution of URANS method. However, although the shedding can no longer be realistically captured, we have previously seen the drag and lift coefficients being predicted with satisfactory accuracy by CFX. One may postulate that the URANS averaging of the more highly turbulent flow is more suited to the CFX model than the structured shedding at lower Re values. Paradoxically OpenFOAM fails to shed, with the previous C_{Lrms} value at 10^6 being accurate by chance rather than realistic flow conditions.

2.3.5 Pressure coefficient

The variance between the two solvers can be visualised by considering the pressure distribution in the wake. Figure 2-9 displays contours of instantaneous pressure coefficient for the CFX and OpenFOAM results at $Re = 10^4$. While the general structure of the wake is well matched between plots, the minimum pressure is significantly different. The general range of pressure coefficient is from 1, at regions of stagnation, to 0 at values equal to the free stream pressure, to values <1 for regions of low pressure. With a peak low pressure coefficient of -2.4, CFX predicts pressures 65% lower than OpenFOAM at vortex centres. This difference is inherently connected to the level of vorticity and in turn to shear profile. The pressure variance explains why the lift coefficient is significantly higher for CFX particularly in the sub-critical region. A possible cause of the extreme values is that this region in prone to strongly 3D wakes with distinct laminar shedding modes and transverse flows. This reasoning is supported by Norberg (2003), in which Re is plotted against axial correlation length normalised with the diameter . The plot reveals a peak in spanwise flow at $Re \approx 5 \times 10^3$, reducing from this point

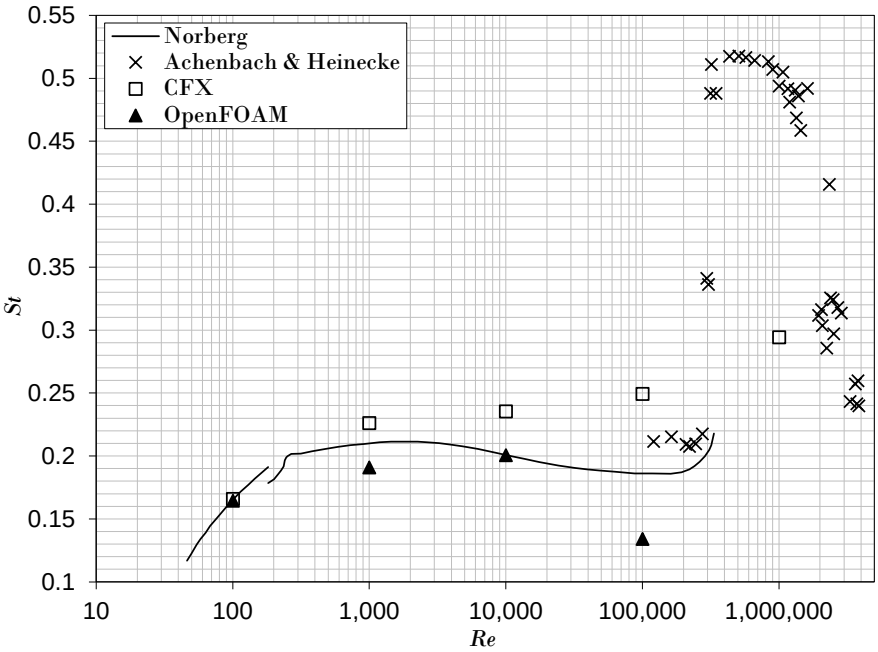

Figure 2-8: Graph of Strouhal number with Reynolds number. Experimental data: Norberg (2003); Achenbach and Heinecke (1981)

as Re increases. This theory opposes the satisfactory results from OpenFOAM both in terms of forces and shedding frequency. However, a number of reasons may explain this disparity, including but not limited to; solver specific minimum turbulence levels, density of integration points or variation in the wall handling (see Section 2.2.2).

2.3.6 Boundary Layer

With boundary layer thickness not known a priori, iterative meshing is required in order to satisfy established values of y^+ and cell count at the non-slip surface. Figure 2-10 plots the non-dimensional value of 99% velocity boundary layer thickness (δ_U) divided by cylinder diameter (c), against Reynolds number. While results differ slightly between solvers, the results show a consistent rate of decay in velocity boundary layer thickness with increasing Re; this relationship was confirmed by solving two other cylinder diameters. Using a trend line approximation a power law can be established to describe the link between Re and δ_U/c, see equation 2.20. The approximation tracks the OpenFOAM result more closely due to the higher solution accuracy produced at sub-critical values, and is proposed as guidance for numerical modelling of smooth circular cylinders.

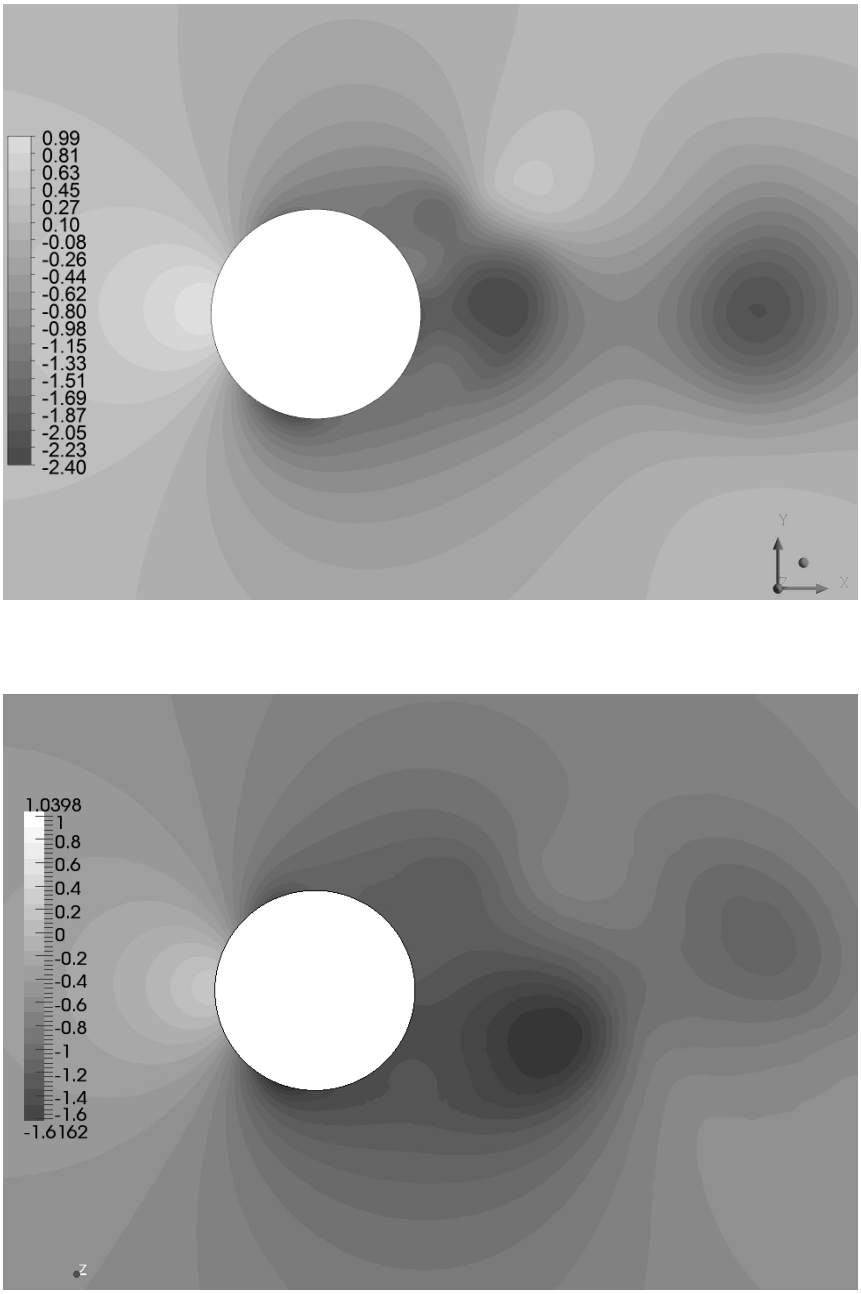

Figure 2-9: Contour plots of pressure coefficient for $Re = 10^4$; top: CFX, bottom: OpenFOAM

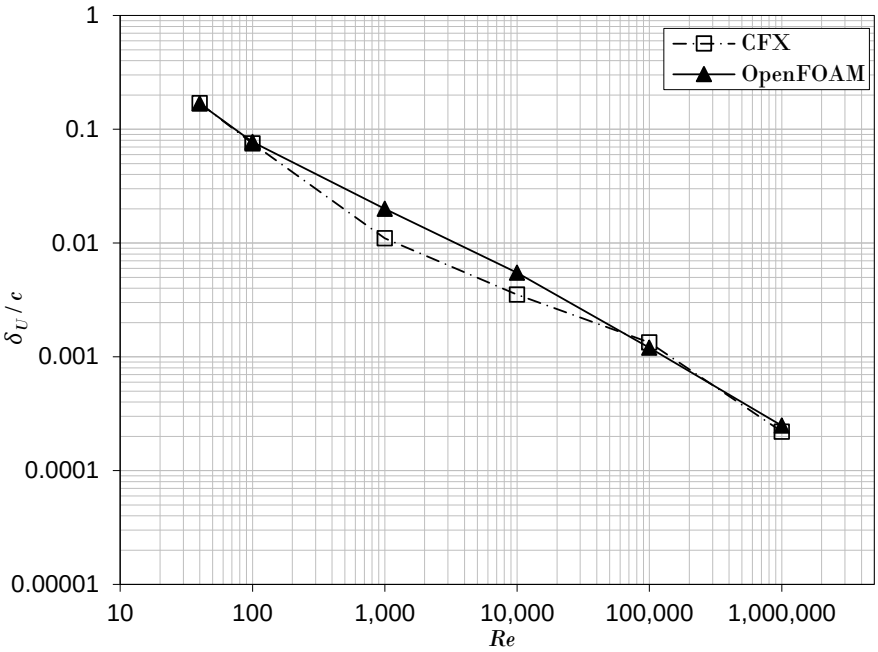

Figure 2-10: Graph of non-dimensional minimum boundary layer thickness versus Reynolds number.

$$\frac{\delta_U}{c} \approx 1.5Re^{-0.625} \tag{2.20}$$

2.4 Discussion

The aim of the research presented was to perform a robust assessment of the URANS method over a wide range of Reynolds numbers within the limits of a 2D simplification. Success is judged by comparison of forces and transient flow field parameters with literary experimental values. Two finite volume solvers have been employed and compared; ANSYS® CFX-13.0 and OpenFOAM® 1.7.1. To extract the best possible outcome for the circular cylinder case, a high resolution methodology was established with regard to geometric, numerical and discretisation practices which were applied to all cases. Specifically this includes:

- Application of URANS calculation using SST turbulence model
- Domain size/Cylinder ratio chosen to avoid blockage effects
- Surface meshing to specified y^+ and cell count in boundary layer
- Cell aspect ratio conformity and far field size limitation

- Utilising fully adaptive Courant controlled timestepping
- Maintaining maximum commonality between solvers

Although previous studies have found successful application of the URANS method for some of the Reynolds numbers considered here, a clear methodology for all flow cases has not previously been proposed and evaluated. For low Reynolds numbers, the method developed is highly accurate. At subcritical Reynolds numbers, the findings are less conclusive. Using two solvers has exposed fundamental differences despite closely matched definitions. While the differences and possible causes have been discussed in the results section of this chapter, further work is required to establish exact root causes. However, despite the unavoidable subtle differences between the two setups, and the fact that the results correlate well enough for engineering purposes, mean that OpenFOAM cannot be dismissed as a useful tool for subcritical flows. At the onset of boundary layer transition and beyond, CFX agrees with findings from published work, such as Ong et al. (2009), achieving good correlation with experimental values for forces, but failing to capture a realistic wake. For engineering purposes it is believed that for high Re, the URANS method in CFX is satisfactory for force prediction. The pisoFoam solver does not follow this trend, failing to shed at critical Re values. Further work has already included reducing timestep to a Courant of 0.1 in order to reduce any instability which may result from the absence of under-relaxation. However, this provided no change to the result pointing to a possible issue with the accumulation of numerical truncation errors or the like. The implementation of an Algebraic Multi-Grid (AMG), or solution using pimpleFoam, a solver capable of outer loop timestepping, may improve high Re convergence in OpenFOAM. The plot of non-dimensional velocity boundary layer thickness versus Re, and associated relationship given in equation 2.20, is given to assist further numerical studies in RANS and LES where resolution of the boundary layer down to sublayer accuracy is desired. Having formed differing conclusions for each solver tested, it is clear that individual benchmarking of software is an essential step for any simulation, a requirement heightened in this case with increasing boundary layer and wake turbulence.

2.5 Conclusion

The fundamental study of flow around a circular cylinder provides a range of information relevant to the next stage of this research. In terms of software, both CFX and OpenFOAM displayed advantages for differing physical parameters. However, it is known that the forthcoming turbine simulations are certain to include a greatly varying flow in terms of both Reynolds and Courant numbers, therefore the stability offered by CFX is highly desirable. In addition, the current

version of OpenFOAM does not possess all of the boundary handling mathematical models to enable the envisaged sliding interfaces and rotating motion. Although CFX achieved a result that was not as quantitatively accurate as OpenFOAM in both C_D and C_{Lrms}, the circular cylinder was a challenging case for RANS computations and a more robust capability is widely acknowledged for unstalled blade profiles, the topic of the next chapter. In addition to solver analysis, the study highlights the formulation of turbulence variables, attention to mesh control such as y^+, control of boundaries, and transient sensitivities. This information directly informs the numerical environment and test strategy in the isolated blade study and beyond.

Chapter 3

The Cross-Flow Turbine

SUMMARY: In this section the fundamentals of cross-flow turbine operation are presented and discussed. This includes the definition of established key parameters that define design techniques, flow features, evaluation techniques and performance metrics.

3.1 Cross-Flow Origins

The earliest recorded example of a cross-flow turbine is the sail-driven Panemone, or 'Persian windmill', dating to 500-900 A.D. (Dodge, 2001). The Panemone and other interpretations remained simple drag-driven devices in which the advancing sail (moving toward the wind) would either be shielded from the flow, or allowed to luff, to allow energy extraction from the downwind sail. It is unclear exactly when bucket turbines arose, those with rigid curved scoops, but by 1887 Scottish professor James Blyth was the first to generate electricity using a cross-flow device of this type (Todkar et al., 2017). The scoop type turbine remained unchanged until 1922 when S. J. Savonius proposed an improved bucketed system which subsequently appeared in a US patent (Savonius, 1929). The 'Savonius' rotor uses two half-cylinder buckets which overlap (shown in figure 3-1) allowing some of the airflow from the retreating blade (from the wind direction) to flow into the bucket of the advancing blade. The result of this mechanism is a reduction of the drag created by the advancing bucket due to a more advantageous pressure differential across the bucket and a reduction in tip vortices. Beyond a well crafted Savonius design little advancement in efficiency has been possible with a drag-driven cross flow turbine partially due to the turbine being inherently limited to speeds below that of the oncoming flow.

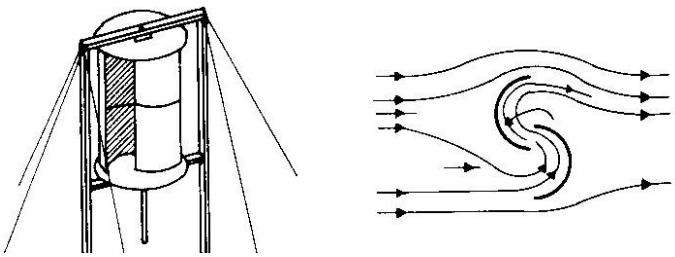

Figure 3-1: Diagram of a Savonius rotor and principle airflow, reproduced from Khammas (2007)

The next advancement in cross-flow technology was proposed by G. J. M. Darrieus' in his 1931 patent for a transverse turbine (Darrieus, 1931), shown in Figure 3-2. The patent describes a lift driven mechanism with aerofoil shaped blades, principally much the same as the majority of designs today both in wind and water devices. The invention remained unexplored until 1968 when P. South and R. S. Rangi, two scientists with the National Research Council of Canada, independently re-invented the concept as part of a Canadian wind energy program. During their research they discovered Darrieus' patent and promptly credited him with the concept (South and Rangi, 1971). The lift-driven design is the basis for the research presented in this thesis, an introduction to the principle of operation and numerical literature review is provided in this chapter.

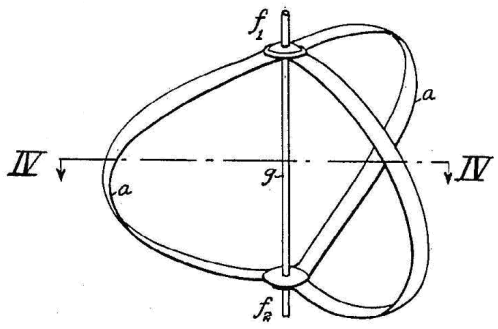

Figure 3-2: Image of a Darrieus rotor, reproduced from US patent 1,835,018 (Darrieus, 1931)

3.2 Basis of Operation

The principle of operation of a lift-driven cross-flow turbine is to extract power by turning at a speed as to present a set of aerofoils with favourable angles of attack throughout each rotation. The process can be described using Figure 3-3 which depicts a cross-section of a three bladed cross-flow turbine where the circular line

is the blade's flight path around rotational axis z. The direction of rotation is anti-clockwise at angular velocity ω, the blade is located at radius r, the multiplication of which results in a blade tangential velocity U_t, see equation 3.1. Components of the oncoming free-stream velocity vector U_∞ and U_t are resolved to give a local velocity U, as shown in equation 3.2, with the average value for one revolution $\overline{U}$ given in equation 3.3. Assuming zero losses at the downstream side of the turbine (omitting any momentum or wake losses), a perceived angle of attack, α, can be calculated using equation 3.4, where θ is the azimuthal position of the blade as shown in Figure 3-3. The angle of attack induces a lift L and drag D, the vector sum of which gives resultant force F_R, this force can, it turn, be decomposed into a torque acting tangentially to the flight path Q and a radial force F_N.

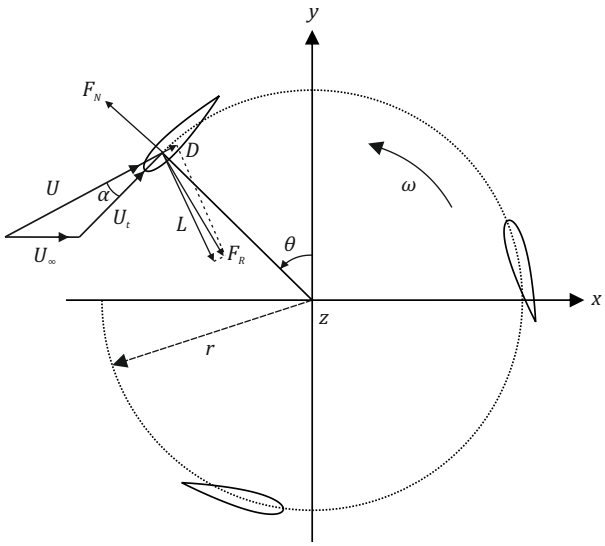

Figure 3-3: Diagram of a cross-flow turbine

$$U_t = r\omega \tag{3.1}$$

$$U = \sqrt{(U_\infty sin\theta)^2 + (U_\infty cos\theta + U_t)^2} = \frac{U_\infty sin\theta}{sin\alpha} \tag{3.2}$$

where U_∞ is a function of depth (h)

$$\overline{U} = \frac{1}{360}\int_0^{360} U d\theta \tag{3.3}$$

$$\alpha = tan^{-1}\frac{U_\infty sin\theta}{U_\infty cos\theta + U_t} \equiv tan^{-1}\frac{sin\theta}{cos\theta + \lambda} \tag{3.4}$$

$$TSR = \lambda = \frac{U_t}{U_\infty} \tag{3.5}$$

$$Re = \frac{\rho U c}{\mu} \tag{3.6}$$

$$\overline{Re} = \frac{\rho \overline{U} c}{\mu} \tag{3.7}$$

A key relationship in turbine design, linking free-stream and rotation velocities, is the tip speed ratio (TSR) or λ, as calculated by equation 3.5 (note that the two terms, TSR and λ, are used interchangeably throughout the thesis). This relationship is shown in Figure 3-4, where α is plotted with increasing θ for tip speed ratio values of 2, 3, 4 and 5. The plot reveals that as λ is increased, peak α is decreased and vice versa. Looking at α in Figure 3-3 it is possible to envisage that if α becomes too small then resultant force F_R will switch from a positive torque to a negative torque slowing the turbine down. However, if α is too large then the blade will stall; the result is that TSR must achieve a balance to maximise power output. In addition to angle of attack, the TSR influences blade velocity U which is plotted in figure 3-5 for TSRs of 2 to 5. The top plot shows how the velocity ratio U/U_∞ fluctuates with azimuth angle θ and is shifted to higher velocities as TSR increases. However, the bottom plot shows that as a percentage of peak blade velocity, U_{max}, the lower the TSR, the higher the fluctuation. Local velocity U determines the blade chord Reynolds number Re, as calculated by equation 3.6; where ρ is fluid density, μ is dynamic viscosity and c is blade chord length. Reynolds number is a non-dimensional value representing the relative contributions of inertial and viscous forces acting on the blade, the result of which determines its lift and drag curves. With both absolute and relative values of lift and drag being the primary factors in total turbine performance, Reynolds number provides an important factor against which tidal turbines can be characterised. Equation 3.7 provides the most suitable value for this purpose, representing an average Reynolds number for a single turbine rotation.

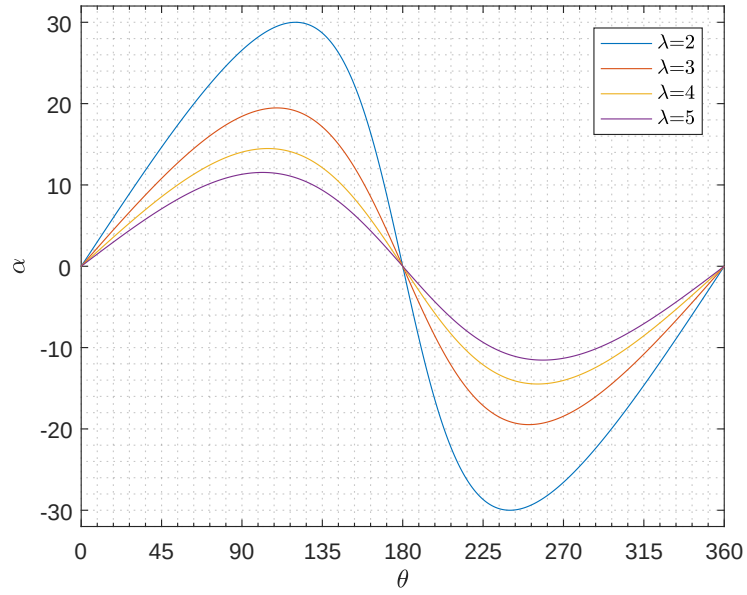

Figure 3-4: Plot of effective angle of attack with azimuth for three TSRs

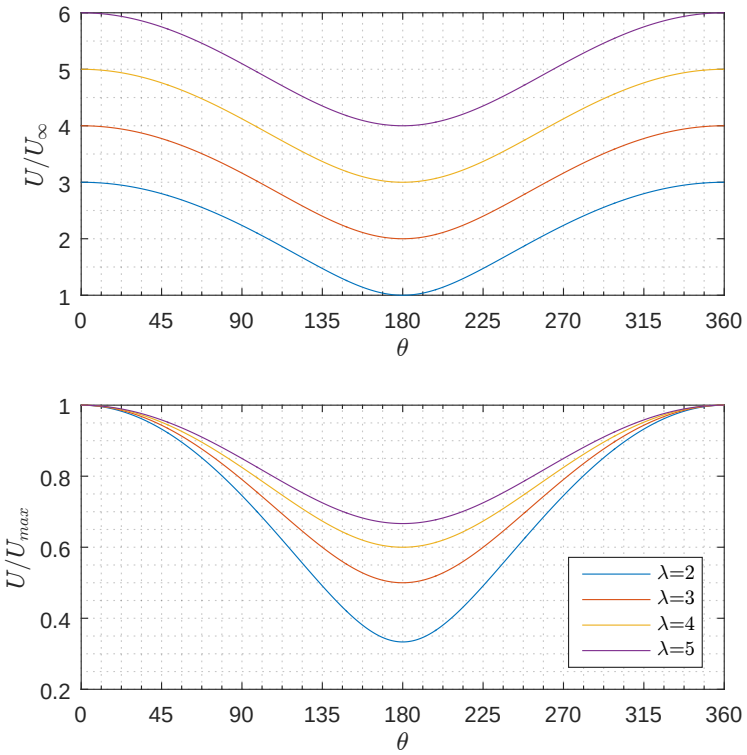

Figure 3-5: Plot of non-dimensionalised velocities with azimuth for three TSRs; top: local to free-stream ratio, bottom: local to peak local ratio

3.2.1 Performance Metrics

The performance of a turbine is characterised by coefficients of power P, torque Q and thrust T, denoted as C_P, C_Q and C_T respectively. Both power and torque are based upon the available kinetic energy within the limits of the rotor, calculated using equations 3.8, 3.9, where A is the swept area of the rotor seen by the flow, and U_r is the mean flow velocity (within rotor area A). Thrust is a force acting in a streamwise direction, positive facing upstream, and can be considered as a resistance to the oncoming flow, see equation 3.10.

$$C_P = \frac{P}{\frac{1}{2}\rho A U_r^3} \quad where, \; P = Q\omega \tag{3.8}$$

$$C_Q = \frac{C_P}{\lambda} \tag{3.9}$$

$$C_T = \frac{T}{\frac{1}{2}\rho A U_r^2} \tag{3.10}$$

Average values are the commonly plotted throughout the thesis is which power, torque and thrust are averaged over a single turbine rotation. Rotationally averaged values are identified by an overbar, as shown in equations 3.11, 3.12 and 3.13.

$$\overline{C_P} = \frac{\overline{P}}{\frac{1}{2}\rho A U_r^3} \tag{3.11}$$

$$\overline{C_Q} = \frac{\overline{C_P}}{\lambda} \tag{3.12}$$

$$\overline{C_T} = \frac{\overline{T}}{\frac{1}{2}\rho A U_r^2} \tag{3.13}$$

3.2.1.1 Betz limit

The Betz limit, see Betz (1920), theorises that the maximum extractable energy (C_P) by a turbine is 59.3%. The value comes from the application of continuity, conservation of axial momentum and Bernoulli's equation to locations upstream and downstream of the rotor. The result is equation 3.14, setting the axial induction factor a between 0 and 1 the maximum of 59.3% can be shown. The Betz limit, although valid for wind turbines, can be exceeded by tidal turbines due to the addition of potential energy acting on the fluid.

$$C_P = 4a(1-a)^2, \; where \; a \equiv \frac{U_1 - U_2}{U_1} \tag{3.14}$$

3.2.2 Geometric Parameters

A number of non-dimensionalisations are made to relate turbine components and the environment. The first of these is 'blockage' or 'blockage ratio' calculated as ratio of the diameter of the turbine to channel depth, given in equation 3.15. The blockage ratio is known to be highly influential on turbine performance. An early attempt to quantify the effect of blockage was published by Garrett and Cummins (2007) in which the authors propose an increase over the Lanchester-Betz limit by a factor of $\left(1 - \frac{A}{A_c}\right)^{-2}$ where A is turbine area and A_c is channel area. However, the method and subsequent improvements such as Whelan et al. (2009) and later Schluntz and Willden (2015) are all based on horizontal axis type turbines where applicability to cross-flow turbines has not been determined. Cross-flow turbines have been specifically addressed by Consul et al. (2013) using a unsteady RANS numerical method. The study includes tests at blockage ratios of 12.5%, 25% and 50% which are solved with both a free-surface and rigid lid, more details are given in Table 3.1. The results showed that by increasing blockage ratio the power coefficient can be increased. However, the increase in C_P is non-linear, with the difference between 12.5% and 25% being much smaller than between 25% and 50%. The result of the study suggests that commercial turbines should aim to reach high blockage ratios where possible to increase yield.

$$b = \frac{2r}{h} \tag{3.15}$$

A second parameter, solidity, is defined as the ratio of total blade to turbine circumference, see equation 3.16. The effect of solidity for cross-flow tidal turbines

was studied by Consul (2011) using 2D CFD. Solidity was varied by solving three cases with 2, 3 and 4 blades with solidities of 0.019, 0.029 and 0.038 respectively. The study found that peak power coefficient increased alongside solidity, however, the peak also became more narrow losing performance at higher TSRs. A wider range of solidities, 0-0.14, were studied by Grylls et al. (1978) experimentally on a vertical axis wind turbine. An upper limit of performance is found at a solidity of ∼0.04, above which turbine performance declines. Both sources agree that the higher the solidity the lower the TSR at which peak coefficient of power occurs. The mechanisms for the effects of solidity share a number of similarities with blockage, such as the change in momentum loss both upstream and downstream and hence lift and stall conditions experienced by the turbine blades. Although a number of trends can inform an expected behaviour, none are universal, and each new configuration of cross-flow turbine requires independent analysis to find new limits of performance.

$$\sigma = \frac{Nc}{2\pi r} \tag{3.16}$$

3.3 Turbine Phenomena

3.3.1 Virtual camber effect

The virtual camber effect originates from research conducted by Migliore et al. (1980). The observation is that a straight blade travelling in a curved path receives a range of flows depending on radius which can be equated to a cambered aerofoil in straight flow. Figure 3-6 visualises the effect in which a curvilinear flow is mapped to produce a cambered aerofoil with lift generation in the direction of the turbine axis. The strength of the effect is determined by the chord to radius ratio, where the smaller the ratio the lower the effect due to a decreasing relative curvature of the flow. The effect is automatically captured by fully resolved CFD methods, however, a number of authors have proposed statistical adaptions to momentum based methods in order to account for the effect, such as Bianchini et al. (2011).

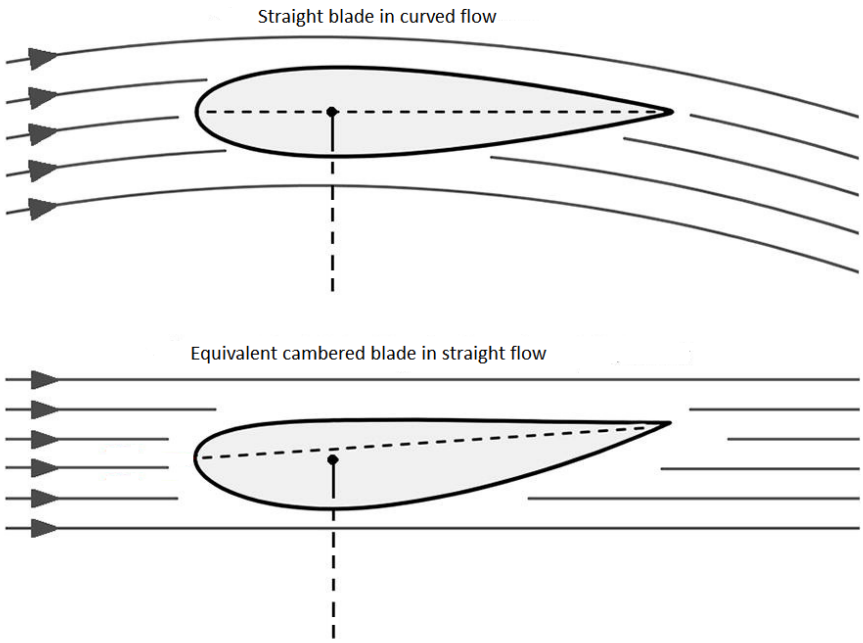

Figure 3-6: Diagram to show the mechanism of the virtual camber effect

3.3.2 Dynamic stall

Dynamic stall is a state caused by a rapid change in angle of attack resulting in the generation of a leading edge vortex that can travel along low pressure surface of the aerofoil before detaching into the flow. A number of researchers have focussed on capturing and quantifying the effects of dynamic stall in regard to cross-flow turbines, examples include Brochier et al. (1986), Kim and Xie (2016) and Ferreira et al. (2007). The effect can be significant to the performance of some turbines although this is not always the case. With the study being limited to RANS turbulence modelling due to computational resource, it is known that dynamic stall cannot be captured with any certainty. Therefore, should these conditions occur in the cases investigated in this thesis it is accepted that the results will incur some error and will be evaluated as such.

3.4 Turbine Numerical Modelling

The number of published articles in which numerical modelling techniques are used to study cross-flow turbines has expanded significantly in the last decade due to both climate concerns and the rise of computational power. Many of the techniques now used for cross-flow tidal turbines were first proposed by researchers in the field of wind turbines of the same type. Numerical modelling can be split into

two categories, statistically driven momentum-based models such as streamtube, cascade and vortex models, or fully resolved flow field methods generally termed Computational Fluid Dynamics (CFD) methods.

3.4.1 Momentum Models

The streamtube modelling method was originally conceived as a method of predicting the performance of Darrieus type wind turbines by Templin (1974) consisting of a single disk, akin to actuator disk theory. The method was refined by Strickland and Department (1975) by the addition of multiple actuator disks, each representing a 'streamtube' of flow able to account for varying induced velocities. The method has been expanded by numerous authors and continues to be so, most notably by Paraschivoiu (1988) who developed the double multiple streamtube (DMS) in which the turbine is split into independent upstream and downstream streamtube groups. The basis of the proposed method for cross-flow turbines (mostly wind applications at present) involves the discretisation of the flow field into 'streamtubes' in which changes in momentum are tracked, by means of an axial induction factor, through an upstream and downstream actuator disk. At each actuator disk the resultant velocities and associated angles of attack are converted into blade forces and thrust by means a of lookup table. The thrust, or streamwise force, is calculated individually from both the conservation of momentum and the aerodynamic coefficients, the two are then compared, if they match the solution is converged, if not the algorithm continues to iterate through induction factors until the two balance; see Beri and Yao (2011) for further detail. The method has been increasing in capability as additional corrections have been added by succeeding researchers, including flow curvature, dynamic stall and tip stall. The expansion of the flow due to high blockage has been additionally accounted for by Soraghan et al. (2013) in the redistribution of the streamtubes. The method is in the early stages of being used in tidal applications; an example can be found by Zhang et al. (2004).

Alternatives to the DMS method include the cascade method, proposed by Hirsch and Mandal (1987), which is essentially a reworking of the DMS method to improve convergence. Finally, vortex models have been attempted for cross-flow applications by Strickland et al. (1981), finding good agreement between experiment and a 3D model. Although the method is fast, using simple vortex lines to perturb the flow, it replies on a lookup table of static lift and drag coefficients for the selected aerofoil. This limitation is common across all momentum models causing inaccuracies relating to virtual camber, wake interactions, dynamic stall and turbulence. While these effects have been accounted for in a number of situations by different authors, general solutions that can account for all blade

types and turbine geometries verges on the impossible. A review of all analysis types has been conducted by Dai et al. (2011) in which cascade, DMS and vortex models are compared to experimental test data. While the DMS method is identified as the best performing, the results show that none of the methods are particularly close to the test data over the full envelope parameters. A 2D CFD model is also computed which does not improve on the accuracy, however, the author concludes that additional resolution is required and the success of CFD methods has been proven by a number of researchers.

3.4.2 CFD

The modelling of cross-flow tidal turbines using CFD has rapidly converged towards a ubiquitous methodology. This trend is highlighted in Table 3.1 in which a selection of highly cited publications has been compiled detailing key turbine attributes and numerical approach characteristics. The examples in Table 3.1 will be used to dissect the similarities and variations to the CFD treatment of a cross-flow turbine in the following sections.

3.4.2.1 Turbine Geometry

The design of cross-flow tidal turbines has been heavily influenced by their wind turbine counterparts in which symmetrical aerofoil sections are common. Due to the increased density of water versus air, tidal turbines typically turn at slower speeds than wind turbines and therefore thicker aerofoil sections are required to reduce stall as larger angles of attack are experienced by the blades. This condition is reflected by the chosen sections with the NACA 0018 being the most popular found in current research.

3.4.2.2 Computational Framework

One of the first tasks in modelling the cross-flow geometry is to assemble a computational framework that enables the blades to rotate within a fixed channel. The standard method, used by all studies in Table 3.1, is to split the computational domain into a fixed domain, and a single of multiple rotating domains that are connected by sliding interfaces. The multi-domain approach, as opposed to a deforming mesh technique, allows carefully constructed meshes to maintain their quality, taking advantage of interface algorithms such as a general grid interface (GGI). Some of the earliest examples of the method applied to cross-flow tidal turbines include Dai and Lam (2009) and Hwang et al. (2009) for a fixed pitch case and a variable pitch case respectively. The multi-domain approach for fixed

pitch cases usually consists of a rotating annulus containing all three blades with fixed domains external to and in the centre of the annulus. Alternatively, variable pitch cases include circular domains around each blade to allow for local pitch control, this technique is sometimes used for fixed pitch cases in order to provide a locally high quality mesh around the blade such as Consul et al. (2013).

3.4.2.3 Solver Setup

The vast majority of past researchers have chosen to use unsteady RANS methods with 2 or 4-equation turbulence closure models and stick to 2-dimensional representations of the turbine geometry. Ultimately this combination of geometry and solver method is often selected due to the current state of computational power. At this level of resolution turbine blade forces can be sufficiently captured and allows for fully transient simulation of the turbine for a number of rotations until quasi-steady convergence in reached. Out of the available RANS turbulence models the $k-\omega$ SST method is the most frequently used due to its proven ability to handle adverse pressure and can be relied upon to produce stable results for a range of surface mesh resolutions, see Table 3.1.

3.4.3 Variable Pitch

Variable, or active pitching of the blades has been shown to significantly increase cross-flow tidal turbine performance by a number of researchers. The challenge of determining an optimum pitching function has been approached in a number of ways. Three examples are shown in Table 3.1 the first of which, by Hwang et al. (2009), uses a genetic algorithm driven optimisation method. Although one of the most advanced methods, the study required 1700 numerical solutions per optimal curve which was repeated 4 times per TSR to reach a final solution. Due to the high number of solutions required the solution used only a coarse mesh and the $k-\epsilon$ turbulence model to make the computational resource requirement feasible. The result was a 25% improvement in peak turbine power. The second and third optimisations by Gorle et al. (2014) and Paillard et al. (2015), use analytical estimations and iterative refinement respectively. Both methods achieve significant improvements in performance, although, as with the previous method both rely upon estimation and numerous test cases to reach an uncertain optimum. Active pitch control, if fully harnessed, can offer a number of benefits such as:

- Increasing turbine performance in a wide range of conditions
- Regulation of power output

Source	Type	Wind/Tidal	Profile	N	$\overline{Re}$	Test Methods
Dai and Lam (2009)	Fixed Pitch	Tidal	NACA 0018/0025	3	-	Experiment, CFD, DMS
Lain and Osorio (2010)	Fixed Pitch	Tidal	NACA 0025	3	-	CFD
Beri and Yao (2011)	Fixed Pitch	Wind	NACA 0018	3	-	DMS, CFD
Lain et al. (2012)	Fixed Pitch	Tidal	NACA 0025	3	-	CFD
Consul et al. (2013)	Fixed Pitch	Tidal	NACA 0015	3	$4e^5 - 3e^6$	CFD
Maître et al. (2013)	Fixed Pitch	Tidal	NACA 0018 (wrapped)	3	$1.2e^5$	Experiment, CFD
Hwang et al. (2009)	Variable	Tidal	NACA 0012/0018	3	-	Experiment, CFD
Gorle et al. (2014)	Variable	Tidal	NACA 0015	4	-	CFD
Paillard et al. (2015)	Variable	Tidal/Wind	NACA 0012/0018	2	$3.8e^4 - 4e^4$	CFD

Model 2D/3D	Turbulence Model	Software	Focus
2D	$k-\omega$ SST	ANSYS CFX	Method comparison, performance prediction
2D	$k-\omega$ SST	Fluent	Validation exercise for 2D method
2D	$k-\epsilon$	Fluent	Comparison of numerical methods
3D	$k-\omega$ SST	ANSYS CFX	Validation exercise for 3D model
2D	$k-\omega$ SST	Fluent	Study of the effect of blockage ratio
2D	$k-\omega$ SST	Fluent	Effect of wall grid refinement
2D	$k-\epsilon$	STAR CCM+	Genetic algorithm based pitch optimisation
2D	$k-\omega$ SST	STAR CCM+	Potential flow / Couchet theory based pitching
2D	$k-\omega$ SST	ANSYS CFX	Multi-harmonic sinusoidal pitching using a deforming mesh

Table 3.1: Summary of numerical research publications in the field of cross-flow turbines

- Load balancing or limiting of structural loads
- Self-starting
- Emergency braking
- Reversibility depending on flow direction

3.5 Notes on ANSYS CFX

The chosen analysis software used for the remainder of this thesis is the ANSYS® suite, this was updated to version 14.0 for Chapters 4 and 5, and finally to version 17.0 in Chapters 6 and 7. Included are Workbench, a project management utility including a CAD package which is used for geometry definition, CFX-Mesh, used to spatially discretise the geometry into finite blocks, and CFX, a CFD package which comprises a pre-processor, solver and post-processor. In the following sections relevant attributes of the software shall be briefly outlined.

3.5.1 Mesh generation

The CFX-Mesh meshing tool includes both hexahedral and tetrahedral options. Edge, surface and volume spacing can be strictly controlled with the addition of inflation layers, used to generate superior body fitted meshes, and localised mesh tightening, for capturing wakes and alike.

3.5.2 Solver attributes

The CFX solver is based on the Navier-Stokes equations in their conservation form. The equations were developed in the early 1800's and are essentially an extension of the Euler equations to include viscous effects. They describe a moving fluid in terms of velocity, pressure, temperature and density by the application of three laws; conservation of mass, conservation of momentum and conservation of energy. This form of the Navier-Stokes equations is well documented and form the basis for most modern CFD codes, extensive descriptions and derivation are available from references (Blazek, 2005; Peyret, 1996; Anderson, 1995). The following list includes defining aspects of the CFX solver, it is not designed to be exhaustive as solver architecture is a very broad and complex topic. However, aspects that prove relevant in testing shall be discussed at the relevant section of the thesis.

- Spatial discretisation is done using a median-dual cell-vertex finite volume method (FVM).

- Temporal discretisation is achieved using an implicit scheme, employing an iterative dual-timestepping approach.
- Solution values are stored at node points in a collocated approach.
- Approximation of the solution gradients within cells is done using finite-element shape functions.
- An algebraic multigrid (AMG) method is used by default to accelerate the incomplete lower upper (ILU) factorisation technique employed to solve the linearised governing equations.

3.5.2.1 Turbulence

One of the most defining factors of CFD computation is the handling of chaotic flow, that of turbulence. A commonly quoted understanding of turbulence is the statistical model developed by Russian mathematician Andrey Kolmogorov in 1941. The theory, subsequently dubbed the "Kolmogorov cascade" describes how large eddies transfer their energy to smaller eddies, and those pass their energy to even smaller eddies, the process being repeated until the eddies are small enough for viscosity to dissipate the remaining energy as heat. Kolmogorov concludes that eddies can be categorised into size ranges with eddies in each range dissipating energy at predictable levels, further description can be found in Jimenez (2010). Turbulence is addressed in CFD by the following main methods:

- Direct Numerical Simulation (DNS) – all eddies are solved
- Large Eddy Simulation (LES) – large eddies are solved, small are approximated by a sub-grid scale (SGS) turbulence model
- Detached Eddy Simulation (DES) – a combination of RANS (SST) boundary layer modelling and LES for heavily separated/turbulent regions
- Reynolds Averaged Navier-Stokes (RANS) – all eddy length scales are modelled

The CFX solver offers LES, DES and RANS solution types, with the focus in this thesis being RANS methods. In order to solve the Navier-Stokes equations in a RANS model a turbulence model is required to close the set. Further details of turbulence closure models and their abilities are discussed at suitable stages of the thesis in the context of their application.

3.5.2.2 Solver Control

The solver includes the ability to select a scheme for advective and transient properties independently. The advection scheme offers methods which are used to predict integration point values of the transport terms, the resulting algebraic equation can then be solved iteratively. In a similar fashion the transient term also requires discretisation and prediction is made by similar schemes. The options for advection scheme are based upon the turbulence model selected, for the SST model a "high resolution" method is selected, a hybrid function based work by Barth and Jesperson (1989). The transient scheme chosen is a second order backward Euler option. The use of this scheme can be further controlled by various methods to yield the initial conditions for each succeeding timestep. Options include previous timestep, extrapolation, or a combination of the two based on Courant number filtering. The combination mode "automatic" is selected as it allows the more computationally expensive extrapolation to be used only when necessary. One of the features of the CFX solver is its dual timestepping approach. At each timestep a quasi-steady solution is reached by using an iterative pseudo-timestep approach. The iterative process is a feature of implementing ILU factorisation, the calculation steps of which are referred to as coefficient loops in CFX; these can be limited to a maximum number. For turbulent flow fields resolution of early timestep will require considerable iterations, therefore a large value for maximum timesteps will be used to account for this. The continuation to requiring large numbers of coefficient loops as time progresses is an indicator that the physical timestep discussed earlier is likely to be too aggressive. The final aspect of convergence control is the residual target. In the CFX code a residual is calculated from the difference of the left (LHS) and right hand sides (RHS) of the linearised mass and momentum equations. The exact method of calculation can differ from code to code, because of this CFX supplies a guide to residual targets. It states that the RMS residual of the whole domain should range from $1e^{-4}$ to $1e^{-6}$, the former providing loose convergence, and the latter providing exceptional convergence.

3.6 Conclusion

An introduction into the operation and performance metrics has been provided in this chapter for reference throughout the thesis. A study of existing methods has yielded a methodology which has been growing in prevalence during the course of this study. The methods, including multi-domain approach, turbulence model choice and limitations are used to inform the strategy taken in the next chapter.

Chapter 4

Isolated Blade Analysis

SUMMARY: In this chapter a numerical study is undertaken in order to explore and validate the prediction of hydrodynamic forces acting upon an isolated turbine blade. The blade is studied at three Reynolds numbers, representing three scales of turbine, employing a numerical environment built upon the knowledge gained from the circular cylinder case in Chapter 2. Information from literature and parametric testing are combined to improve quantitative accuracy, particularly at low Reynolds number conditions. The results highlight the benefits and limitations of using a RANS numerical method and provide a robust validation of blade force prediction for use in subsequent chapters.

4.1 Introduction

As with many complex numerical scenarios it is beneficial to validate isolatable components in order to gain confidence in results generated by an assembled system. The same approach is taken in this chapter, in which an individual turbine blade is numerical modelled in order to ascertain validity of quantitative lift and drag forces against published data sets in preparation for use in a full turbine model. Three Reynolds numbers are computed representing small, medium and large scale devices, roughly approximating laboratory, river and ocean conditions respectively. The profile of the blade itself is a key element in the performance of any lift-driven tidal turbine leading to many researchers choosing to work with tried and tested profiles originating from the aeronautical industry.

4.1.1 Terminology & Background

The design and performance of aerofoils in a continuous flow is a well understood science. Starting with a simple aerofoil, Figure 4-1 outlines the common naming convention; note that the chord length (c) is the distance in a straight line between leading and trailing edges, the camber line marks the mid position between upper and lower surfaces and that the lift and drag act perpendicularly and tangentially to the flow direction respectively. Lift and drag are normally the forces for which an aerofoil is optimised, lift being driven by a pressure difference between upper and lower surfaces, and drag being a function of skin friction (due to viscosity) and form drag (influenced by shape and angle of attack).

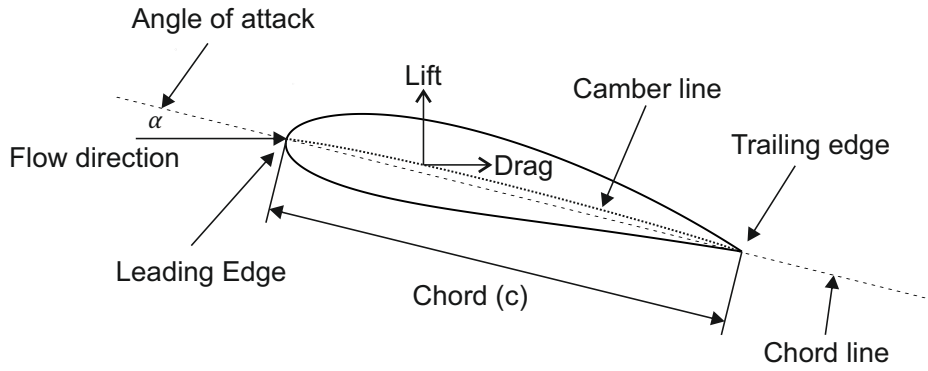

Figure 4-1: Features of a typical aerofoil

The topic of lift and drag as a fundamental science is extensive, with continued theories still arising in recent years. One of the most highly regarded contributions on the theory of aerofoils was made by Abbott and Von Doenhoff (1959) entitled 'The Theory of Wing Sections'. Newer explanations have been subsequently offered, the most recent of which originating from professor Babinsky of the University of Cambridge who credits the induced curvature of the air with driving the pressure difference on the two surfaces (Babinsky, 2003). In addition to lift and drag, a third metric, known as pitching moment, is often given as part of an aerofoil's characteristic. The pitching moment is the torque measured about the aerofoil's aerodynamic centre, a point that is commonly found at a $\frac{1}{4}$ chord distance from the leading edge for symmetrical aerofoils. In the same manner as the cylinder in Chapter 2, components of profile lift, drag and additionally moment, are non-dimensionalised into coefficients using equations 4.1 , 4.2 and 4.3 respectively. For profile (or 2D) coefficients, it is assumed that the blades are one unit in length, i.e. the chord is multiplied by a length of 1. This balances the

equations by ensuring the denominator, composed of dynamic pressure $\frac{1}{2}\rho U^2$ and chord length c results in a force or moment for unit cancellation of the lift, drag or pitching moment.

$$C_L = \frac{L}{\frac{1}{2}\rho U^2 c} \tag{4.1}$$

$$C_D = \frac{D}{\frac{1}{2}\rho U^2 c} \tag{4.2}$$

$$C_M = \frac{M}{\frac{1}{2}\rho U^2 c^2} \tag{4.3}$$

4.1.2 The Boundary Layer

The generation of forces is determined largely by the fluid behaviour in the boundary layer of the blade and thus it is of great importance to our numerical study. An example of boundary layer flow around an aerofoil is shown in Figure 4-2. The example depicts what would be considered a low Reynolds number case in which a laminar flow region extends from the leading edge along the surface of the blade until approximately the 50% chord position. At this point transition occurs leading to a turbulent downstream half of the blade and early separation of the flow. If Reynolds number were to be gradually increased on the example, the turbulent boundary layer would move further towards the leading edge until eventually enveloping the entire blade . In addition, the separation point would move backwards due to an increase in the turbulent energy of the fluid as well as a decrease in the thickness of the boundary layer. The extent to which the boundary layer influences blade performance is discussed in terms of Reynolds number in the following section; an extensive account of boundary layer theory can be found in Schlichting and Gersten (2016).

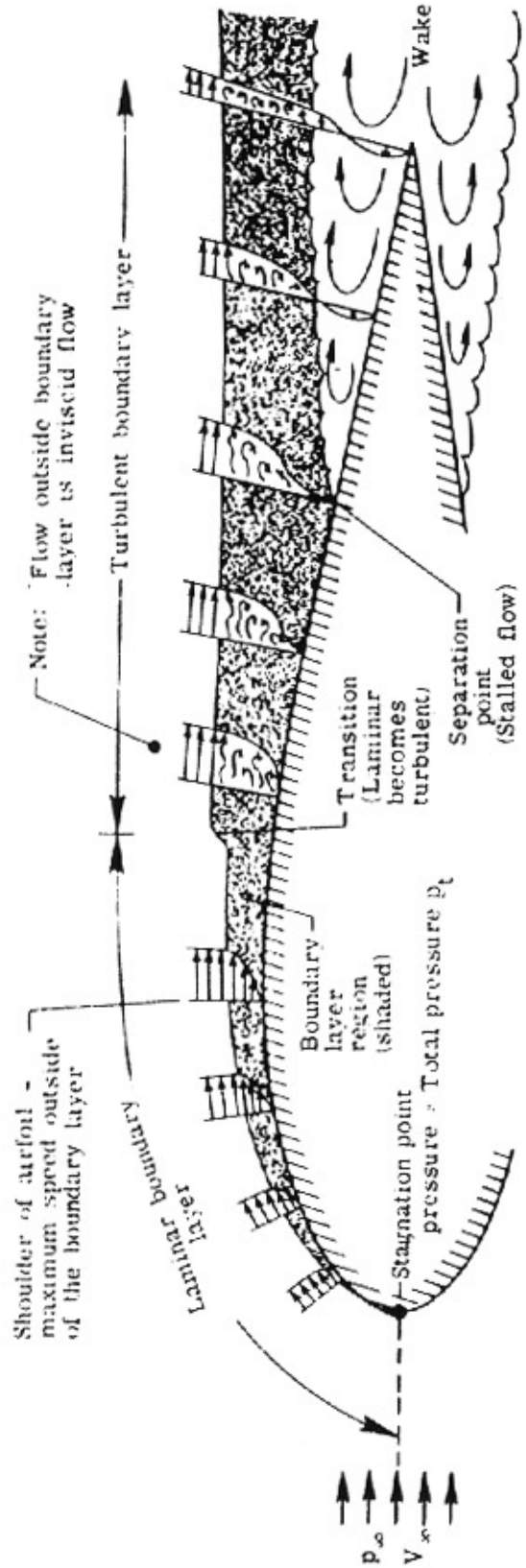

Figure 4-2: Boundary layer flow around an aerofoil
Image reproduced from NASA (2017)

4.1.3 Reynolds Number Characteristics

The blade chord Reynolds number, given in equation 4.4, is an essential part of classifying the performance of a blade profile. In the same manner as the circular cylinder, it provides a non-dimensional value against which a blade's performance can be characterised independent of fluid velocity, viscosity, density and blade size.

$$Re = \frac{\rho U c}{\mu} \tag{4.4}$$

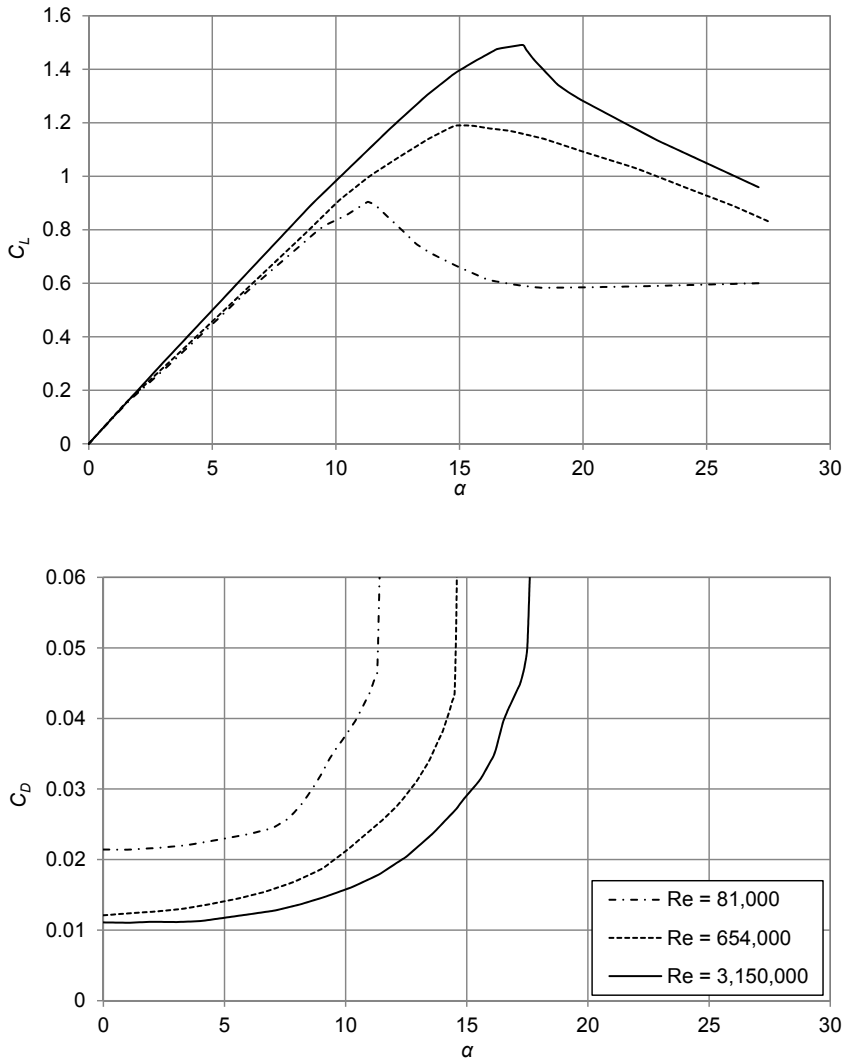

Figure 4-3: Plot showing coefficient of lift (top) and drag (bottom) for a NACA 0018 over a range of angles of attack at three Reynolds numbers. Data from (Jacobs et al., 1933; Jacobs and Sherman, 1937)

Due to the increased complexity of boundary layer flow at low Reynolds numbers, a greater focus has been given to aerofoil performance in this region of operation in a review of current literature. In particular, at a nominal λ of 3, a University of Oxford experimental test of a cross-flow tidal turbine (later used as a validation case in this report) operates in an approximate Reynolds number range of 35,000 – 80,000, with the lower and higher boundaries representing rotation away from, and towards, the incoming free stream flow respectively. This Reynolds number range is characterised by a highly transitional boundary layer, laminar separation, and often the formation of a laminar separation bubble (Hain et al., 2009; Selig et al., 1996). The result is an overall poor performance in terms of lift and drag coefficients; Figure 4-3 illustrates this by comparing lift and drag coefficients at three progressively increasing Re for an infinite (or 2D) 0018 NACA profile blade. Examining Figure 4-3, lift coefficient is seen to increase with Reynolds number, and stall is delayed until higher angles of attack. Similarly, the drag coefficient is higher for low Reynolds number cases, decreasing and extending to higher α as Re increases. A combination of these properties results in a poorer lift to drag ratio. This issue is illustrated by Mcmasters and Henderson (1979), shown in Figure 4-4, where a Reynolds number value of approximately 10^5 is identified as an average transition point for many aerofoils from a mixed boundary layer to one that is fully turbulent.

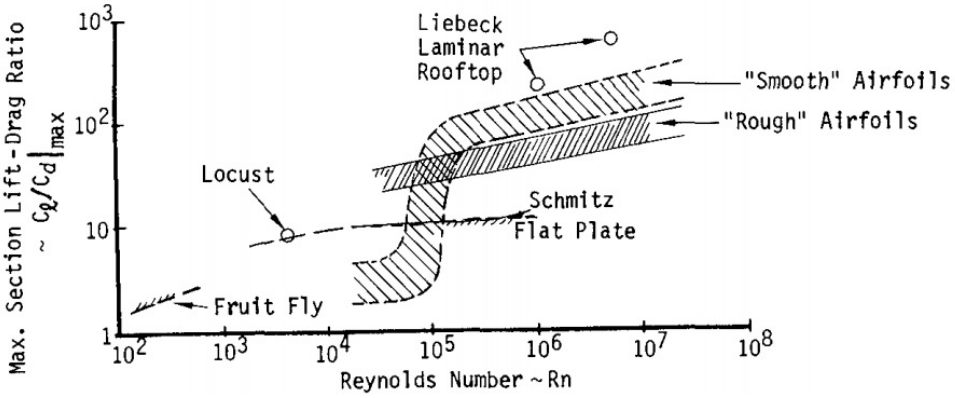

Figure 4-4: Generalised lift to drag ratio behaviour of aerofoils with Reynolds number. Image from Mcmasters and Henderson (1979)

The boundary layer in the subcritical range, where the University of Oxford laboratory test falls, is explored experimentally by Yarusevych et al. (2009) at a Reynolds number range of 55,000 – 210,000 at 0, 5 and 10 degrees α. Testing with a NACA 0025, two types of boundary layer were observed; at Reynolds numbers below 135,000 separations without reattachment occur, for values above, the turbulence generated in the shear layer is sufficient to promote reattachment forming a separation bubble. A variant of vortex shedding is also

observed throughout the range tested, a phenomenon specific to low Reynolds number conditions that is attributed to Kelvin-Helmholts and Tollmien-Schlichting instabilities (Lin and Pauley, 1996; Brinkerhoff and Yaras, 2011). Depending on Reynolds number, these factors invariably contribute to the reduction in performance previously identified. However, the situation becomes further complicated by the effect of free stream turbulence, an issue experimentally studied by Devinant et al. (2002) for aerofoils in Reynolds number flows of 100,000 to 700,000. A superior lift and drag performance is observed as turbulence is increased due to delay of boundary separation. In a similar manner the surface roughness of the aerofoil can also influence the lift and drag by increasing boundary layer turbulence and thus increasing lift in subcritical flow conditions (Mcmasters and Henderson, 1979; Santhanakrishnan et al., 2005).

4.1.4 Numerical Studies of Aerofoils

Many studies have been conducted to assess and improve and the suitability of common numerical methods at low Reynolds number. The most robust of these is Direct Numerical Simulation (DNS) such as that conducted by Shan et al. (2005) and Alam and Sandham (2000), however, the mesh densities and timestepping resolution required exclude this method from practical engineering studies (Coleman and Sandberg, 2010). Large Eddy Simulation (LES) is a less computationally expensive method and has been used by Uranga Cabrera (2010) and Catalano and Tognaccini (2011), amongst others, to successfully predict pressure and friction distributions as well as vortex instabilities. In addition, Kim and Xie (2016) use LES to successfully predict an enhanced lift and drag performance with the presence of an increased free stream turbulence level as seen experimentally. However, evidence of a superior performance over RANS methods is not explicitly established, particularly for values of C_L and C_D, as demonstrated by Yuan et al. (2006). While RANS cannot offer the temporal and boundary resolution of the previous methods, the reduced computational effort makes it the most feasible for current research activities. A number of publications consider various turbulence models and their suitability to capture both transition and/or lift and drag values. In particular, Windte et al. (2006) and Tang (2008) both attempt solutions for the SD7003, a low-Re aerofoil, finding the Menter-baseline (BSL) and the Spalart-Allmaras (S-A) models superior respectively. Rumsey and Spalart (2009) compare the S-A model with the Shear Stress Transport (SST) models for a NACA 0012 for $Re = 100,000$. Both models are shown to perform similarly, displaying varying uncertainty with regard to transition onset.

With the SST model proving to be robust at higher Reynolds numbers, as shown by Douvi et al. (2012) and Menter (1994), adaptions to account for transition

have been attempted to make the 2-equation model more widely applicable. A prominent example for general-purpose applications is the SST $\gamma - Re\theta$ transition model developed by Menter et al. (2006a). The model adds an intermittency term, γ, and transition momentum thickness Reynolds number, $Re\theta$, to the transport equations of the SST model. The model has been empirically calibrated through experimental comparison and integrated into ANSYS CFX software as described in a paper by Menter et al. (2006b). The results of validation studies by Counsil and Boulama (2012) and Langtry et al. (2006) show that a significant improvement is achieved over the SST in terms surface friction, and to a lesser extent the pressure distribution due to good baseline performance from the SST formulation. Furthermore, the computation of a T106 turbine blade at $Re \approx 91,000$ by Langtry et al. (2006) compares steady and unsteady application of the SST $\gamma - Re\theta$ model, finding little variance between the two for pressure distribution.

Predictably, the more computationally intensive numerical methods, such as LES and DNS, provide increased capabilities, particularly the ability to capture the transitional boundary layers and a greater range of turbulent length scale associated with low Reynolds number conditions. However, provided that heavy stall is avoided, RANS models can deliver an accurate prediction of lift and drag forces comparable with the higher resolution models. This conclusion led to the selection of a RANS methodology for ongoing application in this research, with test cases being built to optimise the SST result and consideration of the SST $\gamma - Re\theta$ model for comparison at low Reynolds number.

4.2 Numerical Method

4.2.1 Turbine Blade Geometry

The turbine blade selected for use in this research is the National Advisory Committee for Aeronautics (NACA) 0018 profile. This blade design has been used by a number researchers in cross-flow tidal turbine development due to its high resistance to stall compared to low thickness variants used in wind turbines. In addition, it is the profile chosen by the experimental work later used in this thesis to validate full turbine CFD. The NACA 0018 is part of the NACA four-digit wing section series that are defined in Cartesian coordinates by equation 4.5. A Matlab code was developed to generate a point grid of the upper and lower surfaces which could be interpolated into 2D geometries by CAD software, see appendix A.1 for details. A example plot of the resultant blade coordinates is shown in Figure 4-5 using 50 points each, to define the upper and lower surfaces. The

coordinates were fitted by the CAD software package Rhino®3D and imported into ANSYS®Workbench

$$y = 5tc\left[0.2969\sqrt{\frac{x}{c}} + (-0.1260)\left(\frac{x}{c}\right) + (-0.3516)\left(\frac{x}{c}\right)^2 + 0.2843\left(\frac{x}{c}\right)^3 + (-0.1015)\left(\frac{x}{c}\right)^4\right] \tag{4.5}$$

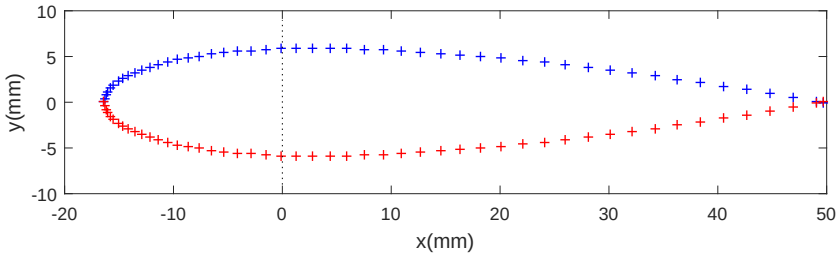

Figure 4-5: NACA 0018 generated profile coordinates

4.2.2 Multi-Domain Definition

The physical domain consisted of a rectangular far-field domain (Fixed Domain) with circular sub-domain (Blade Domain) in which the blade is contained, see Figure 4-6. The two domains are linked via a sliding mesh that uses a General Grid Interface (GGI) to mathematically resolve the fluxes across the interface (Galpin et al., 1995). This arrangement allows the blade domain to pitch the aerofoil without re-meshing and provides a region for enhanced grid refinement. In similar fashion to the circular cylinder test case (see Section 2.2) the fixed domain is sized to ensure that blockage is negligible. Due to the solution method of chosen CFD software requiring volumes, a third dimension must be present in the z-direction, perpendicular to the plane depicted in Figure (4-6). Domain thickness z was set to 0.005mm in order to achieve acceptable cell aspect ratios close to the blade's surfaces. The result is a mesh made of hexahedra and triangular prisms, differing from the customary tetrahedral cells that would have been created in a conventional unstructured 3D model.

4.2.3 Boundaries

Dimensionally, the computational domain is sufficiently large to negate blockage errors with the $\frac{1}{4}$ chord point of the aerofoil located at the centroid of both domains. With reference to Figure 4-6 the boundary conditions are as follows:

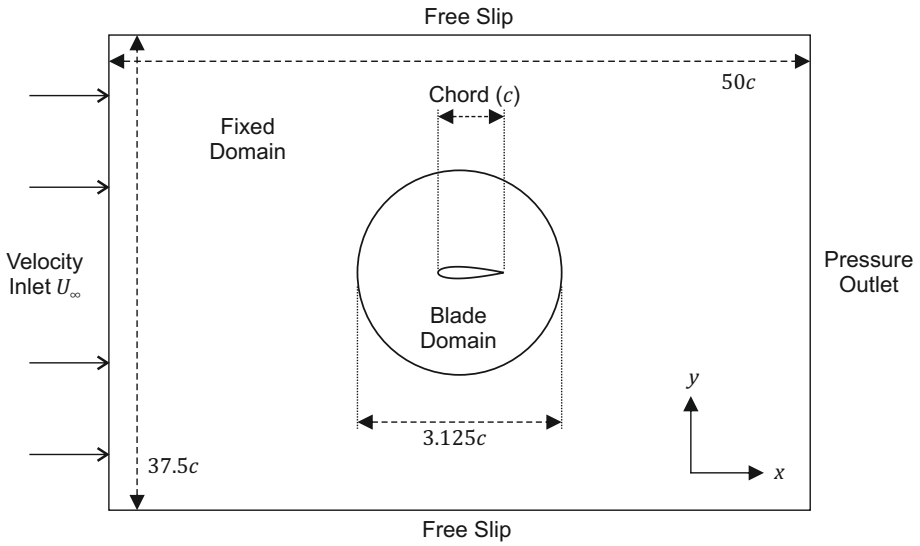

Figure 4-6: Diagram of numerical domain (not to scale)

Inlet: A uniform flow is specified, calculated by rearrangement of the Reynolds number for flow velocity U, see equation 3.6. As discussed in Section 2.2.2 of the circular cylinder case, the turbulent properties of the flow are controlled by specifying a turbulence intensity value I; for the purposes of calibration testing, this was set to 1%.

Outlet: This is set as an 'opening' with a relative static pressure of zero; $p_{rel} = 0$.

Top and bottom: Boundaries of the fixed domain, these are assigned to a 'free-slip' condition.

Periodic faces: All boundaries in the x-y plane are set as 'symmetry planes'.

Blade surfaces: Set to a 'no-slip'condition.

4.2.4 Meshing

The Fixed Domain contains a structured hexahedral mesh that only deforms at the interface with the Blade Domain. The interface was divided into 360 cells at both sides allowing for 1:1 cell alignment when the Blade Domain is rotated by 1 degree increments. The Blade Domain, shown in Figure 4-7, is a mixed mesh consisting of a body fitted hexahedral mesh at the blade surface, with the remaining domain filled with wedges. Figure 4-8 displays the mesh surrounding the blade in more detail, the resolution of the mesh has been significantly reduced to provide a clear reference for the parameters listed in Table 4.1.

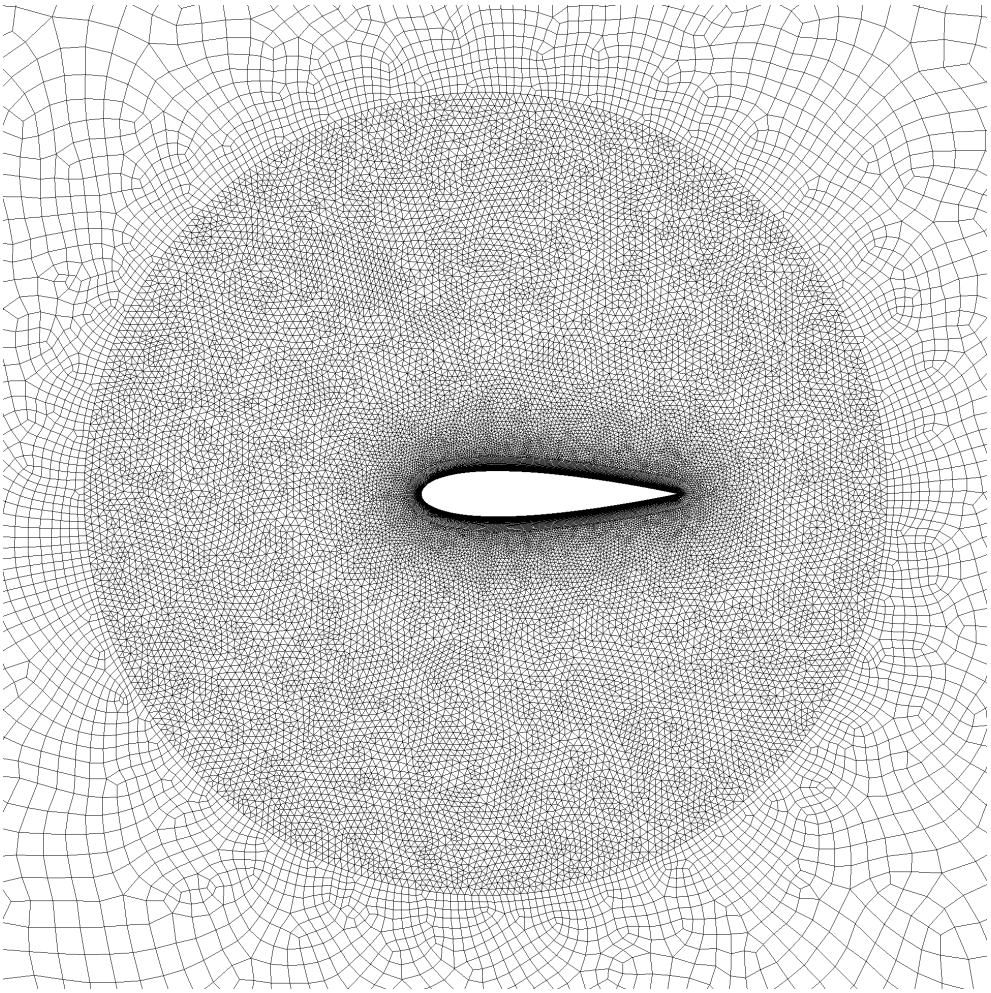

Figure 4-7: Image of multi-domain mesh (focus on Blade Domain)

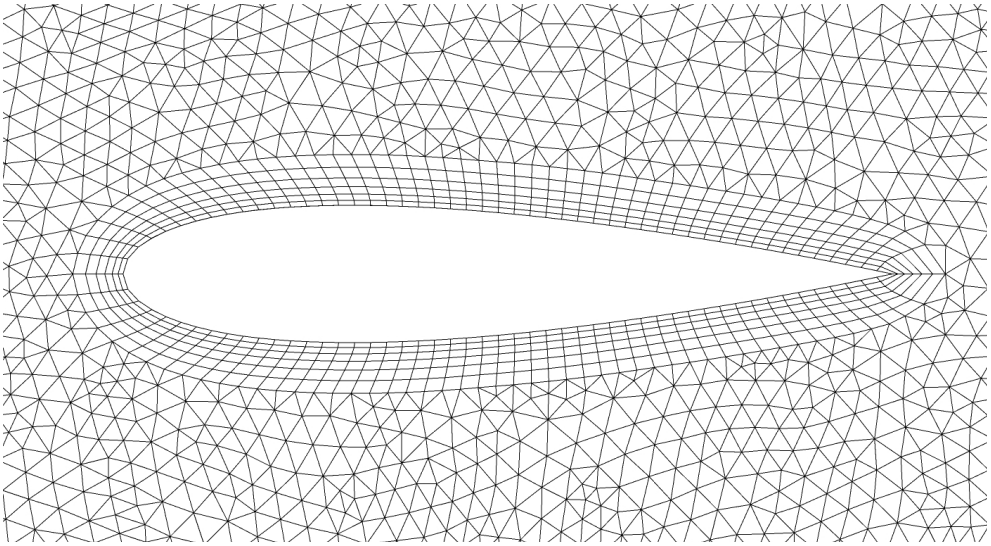

Figure 4-8: Near-field blade mesh - cell sizing has been enlarged for illustrative purposes

Mesh Parameter	Description
First Layer Height (y_1)	the distance of the first cell row from the blade's surface (first cell height). As discussed in Section 2.2.3, selection of the first layer height is used to control the surface y^+ value and hence the boundary layer calculation numerics (example shows 1mm).
Number of Layers	the total number of hexahedral rows wrapping around the blade (example shows 6 layers)
Layer Growth Ratio	the ratio of cell height for each row compared to the previous, moving outwards from the blade surface (example shows 1.2)
Surface Divisions	the number of cells that the blade's upper and lower surfaces are each divided (example shows 50)
Surface Bias	this bias allows the user to weight the cells on the blades surface such that the leading and trailing edge are assigned smaller cell widths than at the 1/2 chord position. A bias of 1 specifies uniform widths, while a bias of 2 specifies that the leading and trailing edges must have cells half the size than the 1/2 chord point. (example shows 1)
Mesh Growth Ratio	similar to the layer growth ratio, this parameter controls the ratio of the wedges as they expand in size beyond the conformal layer zone
Max Element Size	this is the maximum edge length allowable for any cell within the blade domain and hence is a main contributor to mesh density

Table 4.1: Mesh parameters

4.2.5 Solver Control

The solutions were completed to a residual target of 1×10^{-5} for mass and momentum terms and the cases are solved using a SST turbulence model unless otherwise stated. To prevent numerical divergence and accelerate the solving process, the fluid within the domain is given a set of initial conditions. In this case all the fluid in the domain is initialised with flow conditions equal in magnitude and direction to that of the inlet.

4.3 Test Planning

A numerical study of isolated blades was conducted at Reynolds numbers of 3.15×10^6, 1×10^6, and 81×10^3. Using the highest Re case a scoping study was conducted, guided by literary sources and Chapter 2, in order to find a set of nominal meshing parameters. From this, a sensitivity study of the mesh was conducted for all parameters listed in Table 4.1. Each parameter was independently varied from

the nominal case with each design point being solved at 0, 4, 8, 12, 16 and 20 degrees angle of attack. Using multiple angles of attack for each design point meant that the accuracy of the entire lift and drag curve was scrutinised. The result of the parameter study was used to inform the next stage of the study in which an individual blade was computed from 0-25 degrees at the three selected Reynolds numbers. Once a strategy was established for the meshing parameters, the study continues by exploring the effect of y^+ in more detail for each of the Reynolds numbers.

4.3.1 Panel Code

Due to only a small number of sources reporting experimental data for aerofoil performance at Reynolds numbers of interest in this study, a well documented panel code solver was also used as part of the validation process. The solver, named XFOIL, uses a vortex-panel potential flow method with an integral e^n boundary layer formulation which is designed to produce predictions for the lift and drag performance of subsonic aerofoils. Full details and derivation are presented in the originating paper by Drela (1989). The panel method it employs combines well developed methods that have been extensively published in the aeronautical field with Drela's code being well recognised for its accuracy (Selig, 2003). XFOIL has been compared to experimental results and RANS methods in papers by Morgado et al. (2016) and Kirk et al. (2014) who find a high degree of correlation between all methods for aerofoils at Reynolds numbers of 200×10^3 and 1.3×10^6 respectively; values which are similar in magnitude to those explored here. All results generated in this chapter were done with viscosity effects included, a total of 200 panels to represent the aerofoil, and an Ncrit value set to 2.622 (equal to a turbulence intensity of 1%).

4.4 Results

4.4.1 High Re case: $Re = 3.15 \times 10^6$

The results section is presented in chronological order beginning with the mesh parameter study. The results of the parameter study were processed by calculating a percentage error from experimental data digitally extracted from plots published in Jacobs et al. (1933), page 305. The experimental data was corrected by the source authors to infinite aspect ratio (or profile) values, allowing direct comparison with the numerical result. For each design point the numerical results for C_L and C_D were divided by equivalent experimental values in order to obtain the percentage error; the largest of these was used to represent the accuracy of the

design point as a whole. This method was selected above taking an average for the angles tested due to equal weighting of non-linear correlation and curve shift errors providing equivalent error percentages. However, 0 and 20 degree test angles were subsequently removed from the process due to the sensitivity of very small values of C_L causing unrepresentative large percentages, and the onset of stall causing unstable solutions, respectively. A full table of results can be found in the appendix (A.2).

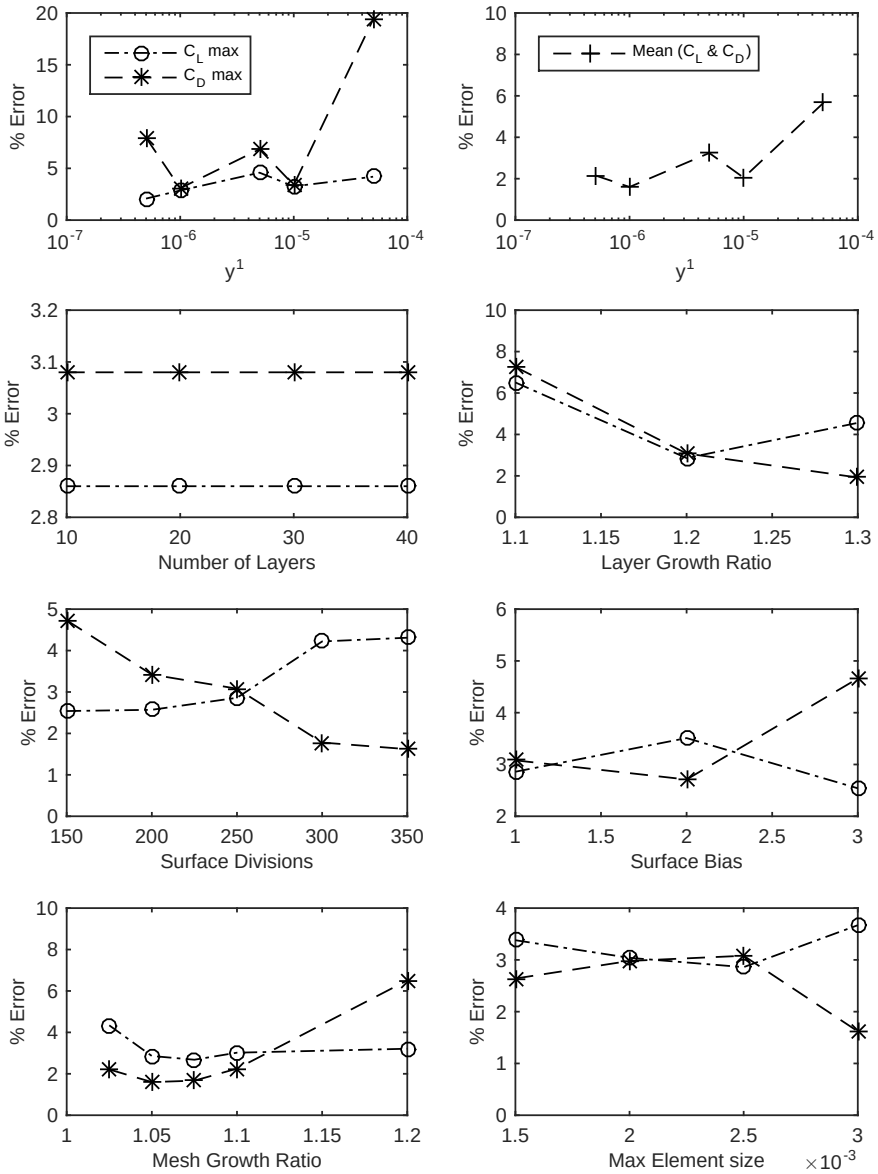

Figure 4-9: Graphs showing percentage error of lift and drag coefficients from experimental benchmark

The results of the parameter study are presented in Figure (4-9) in which each mesh parameter is plotted against percentage error for C_L and C_D. An analysis of each parameter is given in the following list:

- First layer height: two plots are shown, one for C_L and C_D independently, and one in which they are combined into a mean. Initially a mean of the two errors was considered for the analysis of all results, however, the independent plots of C_L and C_D show that significant information would be lost; a highly varying C_D versus a relatively stable C_L. Due to this, all further plots are made with independent error values of C_L and C_D. Both plots display a general trend towards increasing accuracy with decreasing first cell height. The exceptions to this include the C_D at the lowest y^1, and a rise of both values at 5×10^{-6}. Closer inspection of the raw data reveals that the high C_D at low y^1 occurs at an angle of attack of 16, the diverging accuracy can therefore be attributed to the instability of the solution as at 16 degrees the blade begins transition to stall. Both values diverging at 5×10^{-6} coincides with the buffer layer, a region traditionally avoided by numerical methods, however, the scalable wall function employed by CFX means that both parameters vary by <5% error from adjacent first layer heights. The range of first cell heights modelled are equivalent to a maximum y^+ ranges (due to angle of attack) of ∼1-2.5 to ∼100-250. This range covers all physical boundary layer conditions; from within the viscous sublayer to deep into the logarithmic region. All other points plotted in Figure 4-9 are plotted using a first layer height of 1×10^{-6}.

- Number of layers: the error for both parameters remains constant over the range of layers chosen, this suggests 10 layers was sufficient to capture all boundary layer behaviour for the nominal first cell height case. However, further scrutiny suggests that despite the settings being correct at the time of the study, the mesh sizes are identical and therefore it is suspected that the re-meshing by ANSYS-meshing may not have been attempted due to a software bug. A mesh sensitivity study conducted later in this research ensures this error is superseded. At alternative first layer heights the number of layers may vary, therefore close attention is paid to future meshes with reference to boundary layer methodologies developed in Section (2.2.3) of Chapter (2).

- Layer growth ratio: both C_L and C_D are shown to be worse at a low growth ratio, this is potentially an usual result as a lower growth ratio would conventionally be associated with higher accuracy. One potential explanation, if we assume the experiment is ideal, is that the computational cells in the inflated boundary no longer reach the edge of the boundary layer,

thus requiring a greater number of layers. With 1.2 being the conventional value for growth layer, the result shows no advantage to differ either side of this value.

- Surface divisions: the number of surface divisions influences the numerical accuracy in two ways; the resolution of the aerofoil shape, and the length scale of eddy that the model is able to capture close to the blade's surface. Both of these benefits are particularity desirable in the case of a cross-flow tidal turbine where flows rapidly change angle and stall is possible at regular intervals. The scoping study showed value in high numbers of surface divisions, therefore a test range of 150 - 350 was chosen. The result shows opposing behaviour for C_L and C_D, with C_L losing accuracy and C_D gaining accuracy as surface divisions are increased. The two trends cross at 250 divisions which is selected for further work.

- Surface bias: increasing surface bias displays little discernible improvement over an equally spaced mesh. The result is unsurprising as the high number of surface divisions ensures that the leading and trailing edges are already captured to a high resolution. For cases in which high resolution is less feasible, such as 3D models, surface bias would become an increasingly important factor and may be used in conjunction with curvature normal angle to ensure sufficient mesh quality in critical regions of flow.

- Mesh growth rate: depending on the extents of the conformal layers, the near-field unstructured mesh may be required to resolve a proportion of the logarithmic layer. In addition, any turbulent structures produced at the blades surface are likely to pass though this region and therefore a conservative growth rate would be considered to be advantageous. The results show a roughly consistent error in C_L across the range of ratios, while C_D shows a more distinct loss in accuracy at the highest ratio. The lowest error occurs at a growth ratio of 1.075.

- Max element size: the range of maximum element size was chosen to fall either side of the element length generated by cutting the circumference of the blade domain into 360 elements; the calculation gives a section length of 1.8mm. The result shows no strong correlation within the lengths set, therefore 1.8mm is selected for generation of the high Re lift and drag curve slopes to maintain the 360 element edge.

The final mesh controls resulting from the parameter study are presented in Table 4.2. The resulting numerical model, labelled 'current CFD', was solved at the test Reynolds number of 3.15m and plotted against the XFOIL and digitally extracted 'infinite aspect ratio' experimental values from Jacobs et al. (1933) in Figure 4-10.

Parameter	Value
First layer height	1×10^{-6}mm (max Re = 5)
Number of layers	30
Layer growth ratio	1.2
Surface divisions	250
Surface bias	1
Mesh growth rate	1.075
Max element size	domain edge/360 (1.8mm)

Table 4.2: Optimum mesh control parameters

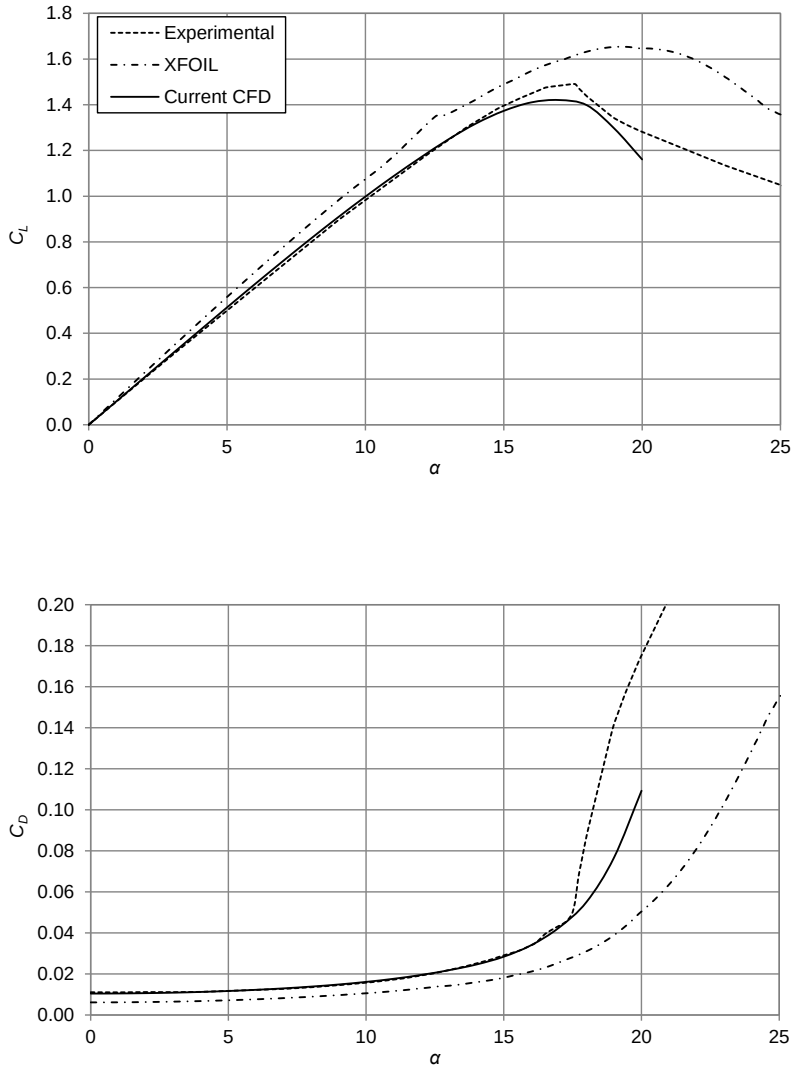

Figure 4-10: Comparison of lift and drag curves for experimental, XFOIL and current CFD values at $Re = 3.15 \times 10^6$; top: coefficient of lift; bottom: coefficient of drag. Experimental data from Jacobs et al. (1933)

Comparing the numerical result and the experimental result for both coefficient of lift and coefficient of drag an exceptional agreement is found up to an angle of attack of 15° with errors significantly less that 1%. Above 15° the coefficient of lift continues to have close correlation although slightly under predicts the peak which occurs at 17.5°. The numerical coefficient of drag remains almost identical up to 17.5° at which point the experimental value displays a sharp stall and increases in drag much faster than the CFD. The XFOIL result is shown to over-predict the coefficient of lift by approximately 5% across most of the range, and under predict the coefficient of drag by 25% increasing in error with angle of attack. Based on the positive reviews of the accuracy of XFOIL the variances are greater than expected, however, additional sources of experimental data have not been found to corroborate either data set. Overall, the numerical result is as close as practically possible using a RANS method only failing beyond stall which is to be expected. The numerical environment and mesh settings were taken forward for the medium and low Reynolds number tests.

4.4.2 Medium Re case: $Re = 1 \times 10^6$

All the settings from the High Re were used to set-up the medium Re case with the flow velocity being altered to achieve the target Reynolds number. The exception to the mesh parameters is the first layer height which is used to control the y^+ of the solution; the most important mesh based influence on solution accuracy. As discussed in the cylinder modelling, Section 2.2.3, y^+ represents a non-dimensional distance of the first node from a no-slip wall which is fundamental to the wall function based mathematical calculation of shear stresses and turbulence near to the wall. ANSYS CFX uses an automatic near-wall treatment for omega-based models, including the SST model implemented here. The standard 'scalable wall function' model is able to switch between a near wall low-Re (turbulent Reynolds number) formulation and a standard wall function of the viscous sublayer depending on local y^+. The special treatment differs from this by blending approximations between the local velocity u^+ in the viscous sublayer with a separately calculated u^+ for the logarithmic layer. The directly computed velocities are fed into the momentum flux equation replacing the turbulence kinetic energy term k which itself is set to zero. The turbulent frequency ω is treated similarly to u^+ as it is blended between sublayer and logarithmic expressions. The result of the special wall treatment is that the solution is stable over a large range of mesh refinement and offers a seamless improvement in solution accuracy for increasingly refined meshes as additional points are added to the viscous sublayer. A detailed account can be found in the ANSYS help system, see ANSYS® (2011a). The relationship between velocity and distance is presented visibly in Figure 4-11, notice that the linear viscous sublayer ends at a y^+ of 5 and the logarithmic

layer begins at a y^+ of 30. Between these two sits the buffer layer where viscous domination of the forces succumb to turbulent action, the point at which the two cross is a y^+ of 11.06. With the high Re study displaying a mixed picture of accuracy it, and with the knowledge of the wall treatment, it was decided that a series of tests would be conducted to explore the effect of meshing to y^+ values (boundary maximum) from 1 to 30. Testing at y^+ values greater than 30 were omitted as the boundary layer becomes stretched beyond this point and results in gross exaggeration of the drag coefficient as shown in Figure 4-9.

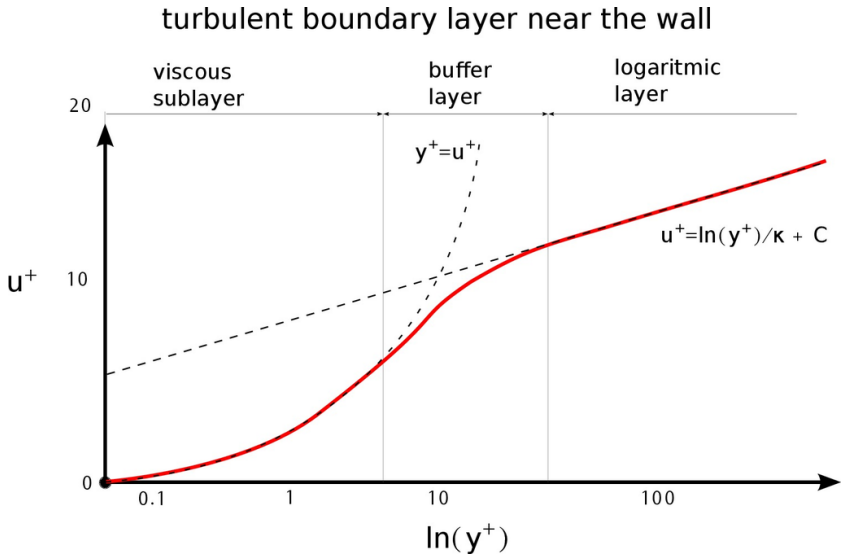

Figure 4-11: Graph showing the relationship between near wall velocity u^+ and non-dimensional distance y^+

The medium Re case was tested at y^+ values of 1, 5, 10, 15 and 30, the results of which are given in Figure 4-12. The numerical results are plotted against experimental values from Jacobs and Sherman (1937) (corrected by the author to sectional values) and computed values from the panel code XFOIL. In this case, a y^+ of 1 is shown to under predict the lift while between a y^+ of 5 and 15 all computed results were very close to experimental values up to stall at around 16 degrees angle of attack. At a y^+ of 30 the numerical result produces the highest prediction of C_L suggesting a progressive divergence from the experimental value. XFOIL displays the same behaviour found in the high Re case, over prediction of C_L and under prediction of C_D. Beyond stall, above 16°, all numerical results above a y^+ of 1 display a level of instability due to an inability to reach a high level of convergence. In summary, the tests show that a mesh resulting in y^+ between 5 and 15 is optimum for pre-stall angles of attack and that stalled conditions will result in poor predictions.

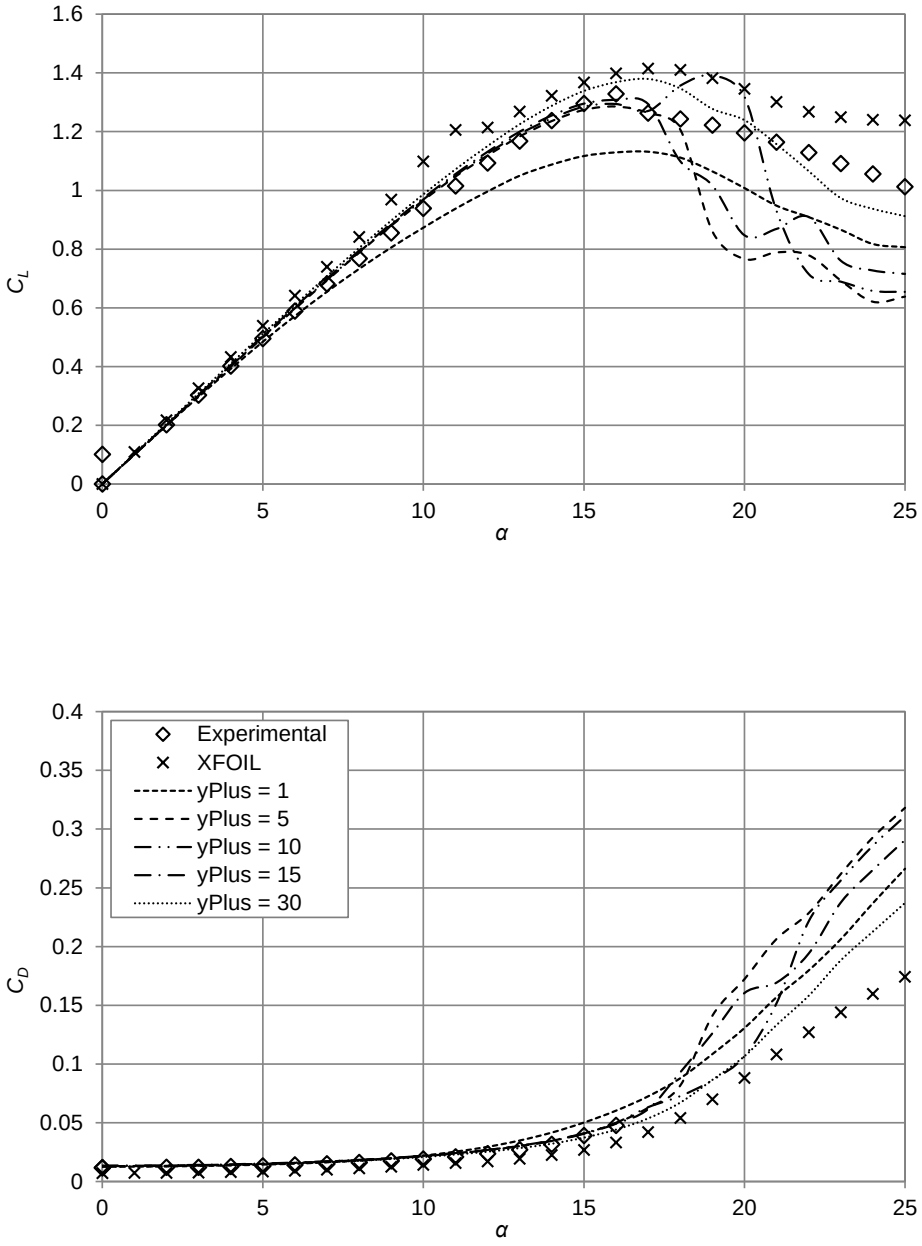

Figure 4-12: Comparison of lift and drag curves for experimental, XFOIL and current CFD values at $Re = 1 \times 10^6$; top: coefficient of lift; bottom: coefficient of drag. Experimental data at $Re = 1.251 \times 10^6$ from Jacobs and Sherman (1937)

4.4.3 Low Re case: $Re = 81 \times 10^3$

Testing at low Reynolds number was conducted over a range of y^+ values in similar fashion to the medium Re tests. Again, the numerical results are plotted in Figure 4-13 alongside experimental data from Jacobs and Sherman (1937) and XFOIL panel code, all three methods were conducted at a Reynolds number of 81×10^3. The two plots display results up to 25° angle of attack, with post-stall angles suffering from fluctuating convergence due to heavy stall. The experimental C_L values are closely matched by all numerical schemes up to the onset of stall at 12°, with a maximum error of ≈5%. The stall point is delayed by the numerical models by +2° to 3° compared to the experimental values, with a range of gradients predicted beyond stall. In terms of drag coefficient, the correlation is very similar, with pre-stall displaying high accuracy and post-stall being shifted up the same margin as the lift coefficient. Considering the effect of y^+ on the results more closely, divergence is seen as α increases. Additionally, as y^+ increases, C_L is increasingly over-predicted near to stall while conversely, C_D is progressively under-predicted. At a y^+ of 30 the solution is beginning to diverge from the experimental values as was seen in the medium Reynolds number modelling. As discussed in Section 4.1.4, capturing the point of stall at low Reynolds number is particularly challenging for a RANS method. This can be observed in the current results by the overestimation of all numerical attempts by 2° to 3° of α, an issue not seen in the medium and high Re cases. The effectiveness of the SST $\gamma - Re\theta$ model was tested to establish if the over-prediction could be improved.

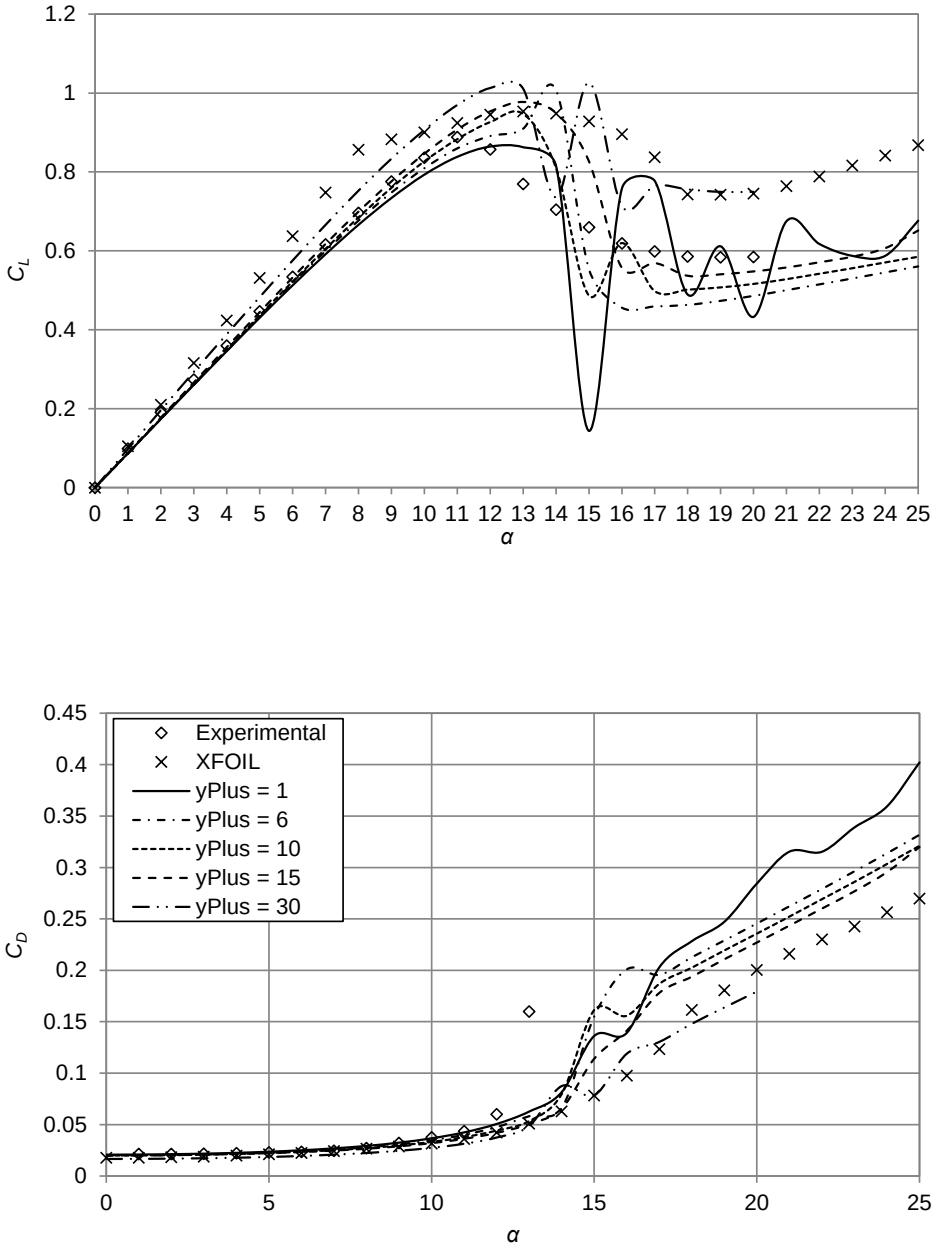

Figure 4-13: Comparison of lift and drag curves for experimental, XFOIL and current CFD values at $Re = 81 \times 10^3$; top: coefficient of lift; bottom: coefficient of drag. Experimental data from Jacobs and Sherman (1937)

4.4.4 Turbulence Transition Model

The SST $\gamma - Re\theta$ model was computed using a mesh achieving a y^+ of 1 at the low Re test value of 81×10^3. A low y^+ mesh is a prerequisite of the model as defined in the ANSYS software. As detailed in Section 4.1.4, the $\gamma - Re\theta$ model is able to trigger the turbulence structures based on adverse pressure gradient, this capability is visible in Figure 4-14 where contour plots of turbulence kinetic energy are displayed for the standard SST model and for the $\gamma - Re\theta$ model. Figure 4-14 shows that the $\gamma - Re\theta$ model results in a delay of boundary layer transition until the 3/4 chord position. A comparison of the C_L and C_D of the $\gamma - Re\theta$ turbulence model is plotted against the standard SST model, experimental and XFOIL results, in Figure 4-15. The model predicts a much steeper increase in C_L over the first 5° which then tails off and stalls at 10°. C_D is around 30% to 50% higher that all other data across the pre-stall range which then rapidly increases at the stall point of 10°. Although a number of additional numerical attempts were made using the $\gamma - Re\theta$ model as a scoping exercise, none displayed sufficient promise to warrant the use of the model above the standard SST.

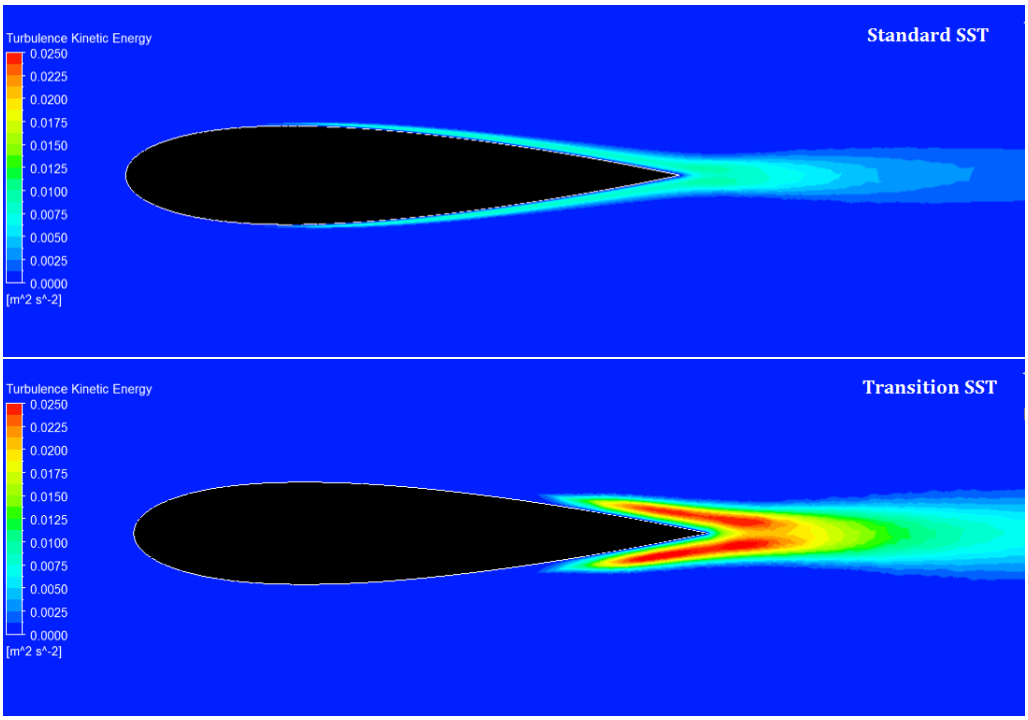

Figure 4-14: Contour plots of turbulence kinetic energy around a low Re turbine blade for two turbulence models; top: standard $k - \omega$ SST; bottom: transitional turbulence model SST $\gamma - Re\theta$

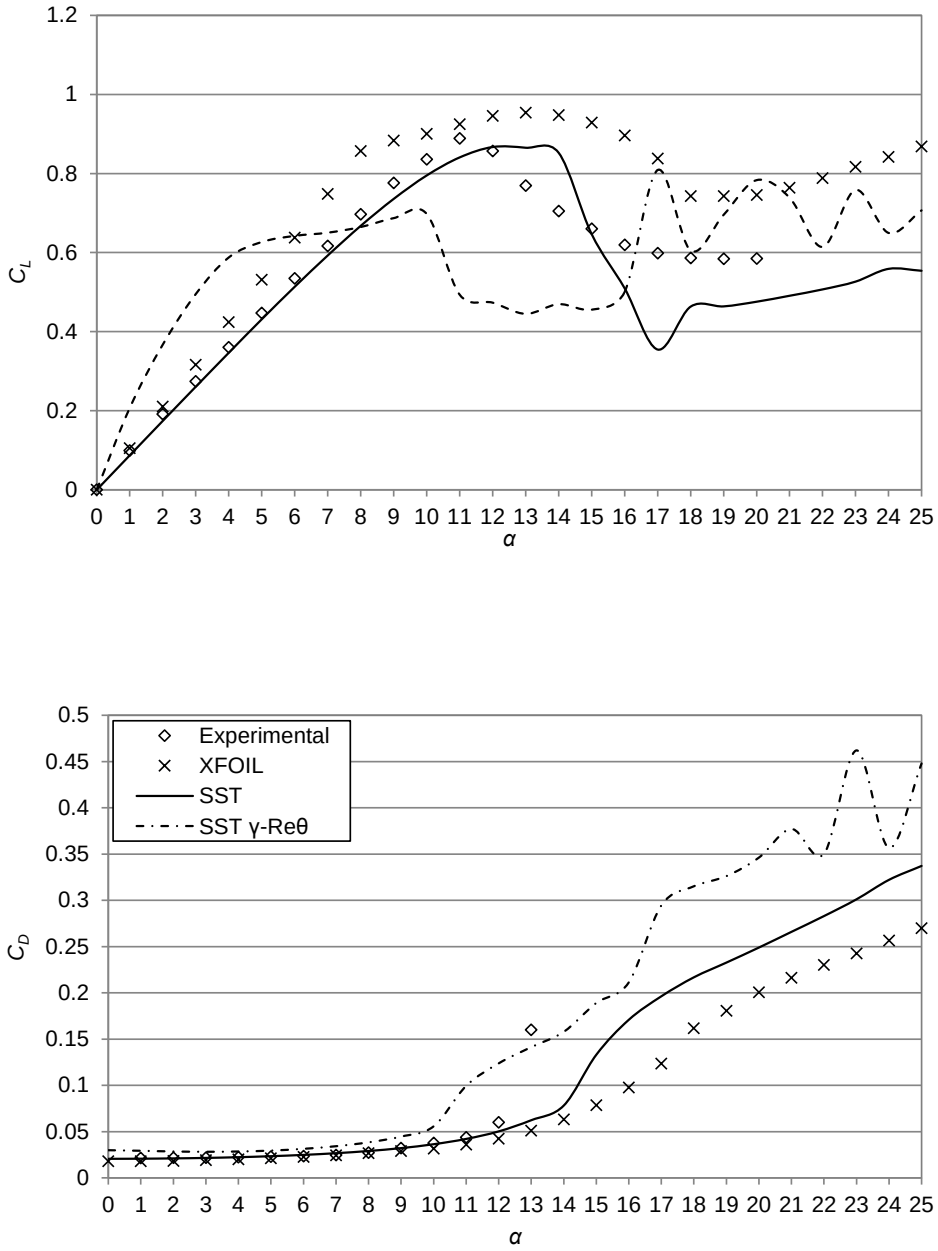

Figure 4-15: Comparison of lift and drag curves for experimental, XFOIL and numerical values with and without a transitional turbulence model at $Re = 81 \times 10^3$; top: coefficient of lift; bottom: coefficient of drag. Experimental data from Jacobs and Sherman (1937)

4.5 Discussion

A detailed consideration of isolated blade modelling has been undertaken in order to independently establish a numerical strategy. A study of prior art suggests that a RANS methodology is both adequately capable and most suitable for turbine research given the availability of computational power at present. As part of this, the two equation turbulence model $k-\omega$ SST was identified due to its proven ability to perform well at resolving adverse pressure gradient conditions along boundaries. Testing at Reynolds numbers of 3.15×10^6, 1×10^6, and 81×10^3 and over a range of y^+ resulted in a number of observed behaviours, namely:

- The parameter study did not offer any firm relationships or dramatic departures from the original model which was scoped using literary sources and the philosophies from the circular cylinder study. The exception was first layer height (determines y^+), which had the effect of increasing C_D as it increased, particularly above a y^+ of 30.
- Pre-stall the numerical set-up (with SST turbulence model) was consistently accurate at predicting lift and drag when compared to experimental values, with an average error for all three models <2% and a maximum error <5%
- Post-stall the method could not achieve a high degree of convergence; residual of 1×10^{-5} for mass and momentum terms not met. This stability issue become worse as Reynolds number decreased.
- At the higher Re test cases the stall angle was predicted correctly, at low Re the stall angle was over predicted by 2° to 3°.
- On average, the most reliable and stable lift and drag predictions were obtained at y^+ values between 5 and 15.
- The transient turbulence $\gamma - Re\theta$ model did not offer a suitable correction in this case. Although some empirical tuning may improve the model's success, such as that performed by Wang et al. (2010),Malan (2009) and Lanzafame et al. (2014), the widely varying conditions of a full turbine would potentially cause unknown out of calibration variances even at low angles of attack.

Reviewing these findings, it can be concluded that a RANS method coupled with a SST turbulence model is a capable method to predict the performance of turbine blades over a wide range of Reynolds numbers within certain limits. The most quantitatively accurate results would be expected in cases where a turbine operates such that local blade stall in avoided. If blades exceed stall by only a few degrees, continued stability and minor error would be expected at high Reynolds numbers, unfortunately the converse is true for blades operating at low Re.

4.5.1 A note on source data accuracy

After the completion of the research a new set of experimental data generated by Timmer (2008) was discovered and it was noted that despite a relatively small difference in Reynolds number the results were markedly different from Jacobs and Sherman (1937) in terms of C_L in particular, as shown in Figure 4-16. Timmer's paper identifies a correction to the stated Reynolds numbers presented by Jacobs and Sherman (1937) to account for a previously unidentified wind tunnel turbulence issue. The information is contained in the latter half of Jacobs and Sherman (1937) but is somewhat ambiguous describing a correction from 'test Reynolds number' to 'effective Reynolds number' or 'flight Reynolds number', it is unclear if the plots already include this correction. If we assume Timmer's interpretation of the data is correct then the results from Jacobs and Sherman (1937) become much closer to Timmer (2008). For example, at 15 degrees α it is estimated that the predicted value of C_L from Jacobs and Sherman (1937) falls from $\sim$1.32 to $\sim$1.1. It is important to note that the error is shown by Timmer (2008) to reduce as Reynolds number decreases, reaching zero at an Reynolds number of 300×10^3. The result is that the low Re case, at 81×10^3, should not be affected by this issue. However, there are a number of options to reach quantitatively more accurate values in future studies using a RANS method. Firstly, Figure 4-16 shows that at a y^+ of 1 the numerical result is much closer to Timmer (2008) for both C_L and C_D which could be employed in full turbine modelling. A second method, presented by Matyushenko and Garbaruk (2016), uses the tuning of the SST model's a_1 coefficient to influence the eddy viscosity equation. The modification alters the 'SST limiter' which exists to prevent over prediction of the shear stress in the boundary layers under adverse pressure gradient. The result is that the a_1 coefficient can be used to control the separation behaviour of the aerofoil and hence advance its stall point. This method can be applied at higher y^+ values leading to a potentially lower cost in computational effort for a equally accurate result.

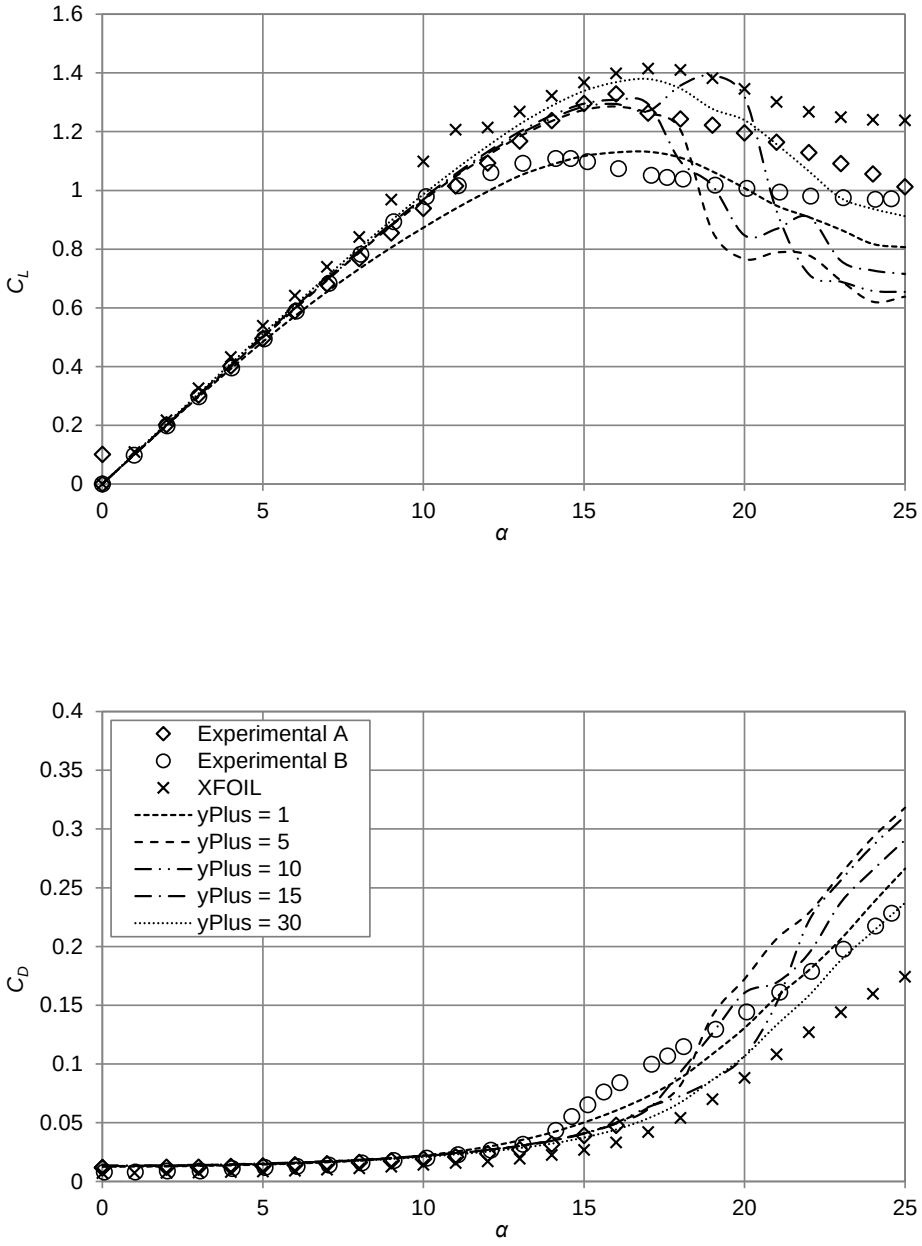

Figure 4-16: Comparison of lift and drag curves for experimental, XFOIL and current CFD values at $Re = 1 \times 10^6$; top: coefficient of lift; bottom: coefficient of drag. 'Experimental A' is at $Re = 1.251 \times 10^6$ from Jacobs and Sherman (1937); 'Experimental B' is at $Re = 1 \times 10^6$ from Timmer (2008)

4.6 Conclusion

The development of a numerical method and meshing strategy for an isolated blade in a circular domain was specifically targeted with individual blade control a future aim of the research. There is no evidence to suggest that the circular domain compromises the accuracy of the force prediction and the multi-domain approach displayed no issues transmitting all flow variables across the GGI interface. The results prove the merits and limits of RANS numerics which can be accommodated or evaluated in subsequent studies. The final mesh and numerical environment is suited to expansion into transient tidal turbine analysis where mesh qualities and solver stability is achievable using the available resources. In the next chapter a full turbine model is assembled, including the isolated blade meshes developed in this chapter, for comparison and validation against an experimental test case.

Chapter 5

Lab Scale Turbine

SUMMARY: The development and validation of a numerical model of a cross-flow turbine is presented in this chapter. The study utilises the blade domains developed in Chapter 4 as part of a fully formed transient model. The study includes spacial and temporal independence tests, which lead to the validation of turbine performance metrics including thrust, torque, power and blade deflection forces against experimental values. Using the resultant numerical methodology, the study continues by exploring the potential of turbine performance scaling based on Reynolds number.

5.1 Introduction

In this chapter the assertion that a quantitatively accurate numerical model of a cross-flow turbine can be accomplished is investigated. From the outset, a numerical model is developed to mimic a laboratory scale physical tidal turbine built and experimentally tested on behalf of Kepler Energy Ltd, a company founded by University of Oxford academics. The experimental device investigated is a straight bladed cross-flow turbine which was tested over a range of tip speed ratios. The numerical objective is to fully resolve all three blades of the turbine which rotate and interact in the simulation as they would on the physical prototype. A single cell thick (2D equivalent) slice of the turbine is used to keep the model computationally practical with accuracy and method validation an aim at all stages. To begin, the experimental turbine is presented, followed by the development of the numerical model and finally presentation of the results.

A second aim of the study is to consider the effect of scale on the performance characteristics of a cross-flow turbine. Scaled physical models are a standard

method for engineers to study a concept in a controlled and cost effective manner. However, in the case of a fluid system, scaling is usually achieved by the non-dimensional relationship described by Reynolds number. For flows with a free surface an additional relationship, which includes the effects of gravity, is also often considered and comes in form of Froude number $Fr = \frac{U}{\sqrt{gc}}$, where U is flow velocity, g is gravitational acceleration and c is characteristic length. Achieving both values after scaling is rarely mathematically feasible and in the case of large changes in scale matching neither is likely. In the development of tidal turbines such large variances are unavoidable leading to the question of whether the scale model is, at the least, exhibiting the same behaviour as its full scale counterpart. With the effects of Froude number being considered negligible for a fully submerged tidal turbine (Lynn, 2013), average blade Reynolds number $\left(\overline{Re}\right)$ is sometimes chosen as a value against which turbine performance is classified. Examples include Bachant and Wosnik (2016), Bogateanu et al. (2014) and Whelan and Stallard (2011) who identify a number of issues including dramatic shifts in mean power output, stall limits and the relationship between performance and tip speed ratio. With cross-flow tidal turbines still being in their infancy, prototypes are typically less than 1 meter in diameter and as such achieve blade chord Reynolds numbers in the $10^4 - 10^5$ range; examples include Hill et al. (2014), Gebreslassie et al. (2016) and McAdam et al. (2013a). This Reynolds number range is far below a commercial scale turbine which would operate upward of 10^6. To investigate any possible changes in behaviour, and to ascertain the possibility of scaling turbine performance with mean Reynolds number, a series of tests are integrated into the numerical modelling test program and analysed at the end of the chapter.

5.2 Experimental Test

The benchmark for the numerical model is a laboratory test of a cross-flow fixed-pitch tidal turbine conducted at Newcastle University in the combined wind, wave and current tank. The experiment, a preliminary stage assessment of a larger research initiative named THAWT (Transverse Horizontal Axis Water Turbine), tested a straight bladed transverse turbine over a range of tip speed ratios. The experimental study was undertaken by Ross McAdam of the University of Oxford in association with Kepler Energy Ltd; a photograph of the turbine in-situ is shown in Figure 5-1. Details required for a numerical replication of the experiment are given in the section, however they are not exhaustive. For full details of the experimental setup reference should be made to publications by McAdam et al. (2013a; 2013b; 2013c); It should be noted that the cited publications present testing from the THAWT rotor, however, the testing equipment and method are identical to that used for the straight-bladed variant presented in this thesis.

Figure 5-1: Experimental setup of a straight bladed cross-flow turbine (Courtesy of Ross McAdam, University of Oxford, and Kepler Energy Ltd)

5.2.1 Device Features

The experimental test was built to be mechanically robust and to capture the performance of the turbine using real-time data logging. The main features of the experimental equipment include:

- Three carbon fibre turbine blades
- Aluminium circular end plates
- Belt driven power take-off coupled to a torque sensor and motor/brake
- Load cell located in a blade to directly measure radially acting force
- A NACA 0018 blade profile, circumferentially mapped such that the chord line falls on the arc of rotation of the blade
- Inclusion of a constriction to allow for the belt drive and instrumentation to be isolated from the flow

5.2.2 Geometry

The major dimensions of the combined wind, wave and current tank working section are shown in Figure 5-2. The Figure is plan view, showing the turbine transversely mounted 5.25m from the inlet (to its central axis). In order to

incorporate a power take-off belt (visible in Figure 5-1) and instrumentation, two partitions either end of the turbine were attached to the wall of the flume causing a localised constriction. The partitions occupy the full depth of the flume, see appendix B.1 for geometric details. The flume was >1m in height allowing a water depth of 1m to be set for the testing. A summary of the geometric attributes of the experiment are given in Table 5.1.

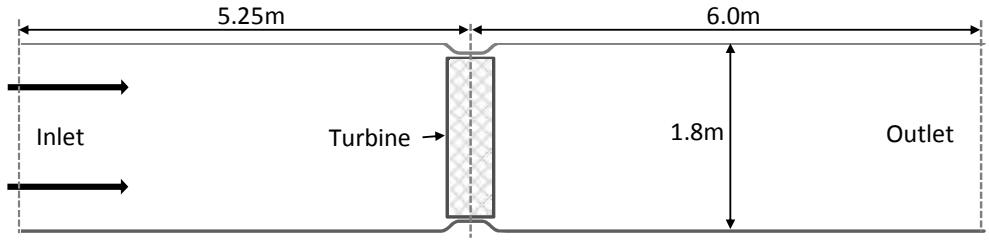

Figure 5-2: Diagram of the experimental flume, plan view

5.2.3 Blade Profile

The turbine blade used in the experiment was modified from a standard NACA 0018 by circumferentially 'wrapping' its profile such that its chord line coincides with the arc of rotation of the blade. The wrapping was achieved using equations 5.1 and 5.2 to recalculate the defining coordinates, see Figure 5-3 for an illustration of the process. The 'wrapping' was found to increase efficiency during experimental testing by Consul (2008) who reasons that the mechanism of the improvement is due to the elimination of the virtual camber effect resulting in the delay of stall. Further details of blade sizing is given in Table 5.1.

$$x' = (r + y)\sin\left(\frac{x}{r}\right) \tag{5.1}$$

$$y' = (r + y)\cos\left(\frac{x}{r}\right) \tag{5.2}$$

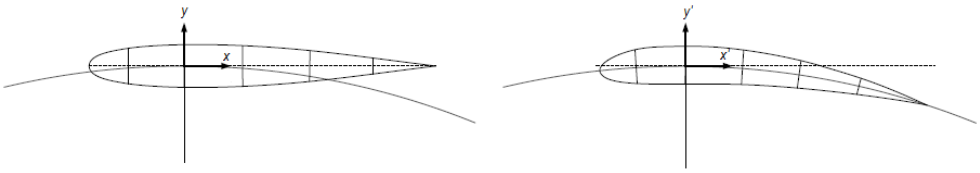

Figure 5-3: Images of blade wrapping; left - straight blade, right - wrapped blade

5.2.4 Current Profile

The current profile of the Newcastle test tank is unusual due to the inlet location being beneath a set a wave paddles close to the floor of the tank. Therefore, as part of the experimental test an ADCP (Acoustic Doppler Current Profiler) was used to analyse the current flow at a number of pump power ratings. Readings were taken at the centreline of the turbine at 10mm depth intervals for the full water height. The profile itself, given in Figure 5-4, shows a high level of shear in the flow ranging from 0.363 m/s at the lower boundary of the turbine to 0.275 m/s at the higher, a variance of 25%. Turbulence intensity in the experimental flume immediately upstream of the rotor was measured but later found to be erroneous, therefore is has been estimated to be ∼1% (from personal correspondence with McAdam et al. (2013a)).

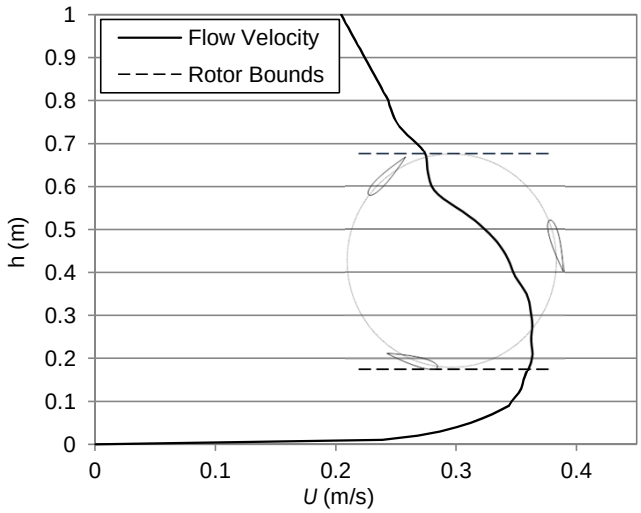

Figure 5-4: Velocity profile of unimpeded flow in the experimental current tank

5.2.5 Data Processing

The experimental data was collected by gradual ramping of the turbine rotation from zero up to a TSR of 5 and back to zero during which torque and force

sensors recorded the turbine's responses. Due to the cyclic delivery of the torque, the collected data was smoothed using re-sampling (see McAdam et al. (2013a)). The ramping experimental methodology produced a slight variation in the results between the rising and falling data due to the reaction time of the motor/brake; therefore an average of the two plots has been taken to produce values of power, torque and thrust. All three performance metrics are corrected to values per unit length by multiplication of 1/experimental blade length. In order to convert the corrected values of power and torque into coefficients, the available kinetic energy in the flow must be calculated. This shown by the denominater in equation 3.8, in which U_r is the mean velocity and A is the area within the bounds of the rotor shown in Figure 5-4. The same values are used in the denominator of equation 3.10 for the conversion of raw thrust into a coefficient. The raw data and corrected values are contained in appendix B.3.

5.2.6 Summary

Although an account of the experimental setup and conditions have been provided here, it should be noted that all values are subject to calibration limits and error bounds as given in McAdam et al. (2013a). In addition, the inclusion of a narrows to house instrumentation makes the case difficult to interpret into a 2-dimensional model, this issue is discussed in Section 5.3.3.1. A summary of pertinent attributes of the experimental setup is provided in Table 5.1.

Parameter	Symbol	Unit	Value
Flume width	b_C	m	1.8
Constriction width	b_T	m	1.61
Flow depth	h	m	1.0
Height of rotor axis above flume base	h_r	m	0.425
Rotor radius	r	m	0.25
Blade length	L_b	m	1.528
Chord length	c	mm	65.45
Endplate thickness	-	mm	10
Endplate diameter	-	mm	540
Mean channel velocity	$\overline{U_\infty}$	m/s	0.298
Mean velocity within rotor bounds	U_r	m/s	0.3698
Swept area of rotor (per unit length)	A	mˆ2	0.5

Table 5.1: Summary of experimental flume and turbine geometries

5.3 Numerical Model

To enable the capture of the flow field in full, an objective stated in the introduction, the numerical model is based upon a multi-domain method as used in the isolated blade. The model differs however, due the requirement of a transient rotation model for the blade and rotating domains. The ANSYS solver achieves this by inclusion of a GGI based method termed Multiple Frames of Reference (MRF) which is designed to permit situations where one domain is rotating relative to another (described in ANSYS® (2011b)). In simple terms, the solver transmits the fluid fluxes from a stationary to a rotating domain in which the velocity of the bodies (blades in our case) is accounted for by the addition of the rotational velocity field to the fluid itself. This allows the correct forces to be calculated on the blades with the MRF handling the tracking of the rotation and the crossing of the fluxes over the frame-change interface. The MRF is automatically activated at any affected interfaces by selection of the 'Transient Rotor-Stator' model. Based on the use of this method the geometry and meshing are assembled with the inclusion of non-overlapping sliding interfaces with conformal meshing to minimise any errors of the MRF. The effects of the MRF are most clearly seen in the post-processor in which two velocity and pressure fields are available to view, a stationary frame and a rotational frame.

5.3.1 Geometry

The geometry of the numerical tank, shown in Figure 5-5, represents a centre section through the xy plane of the experiment, with turbine dimensions being identical and numerical flume height being equal to water depth. The inlet is shortened as the velocity profile and turbulence conditions are not required to develop and can be directly specified in the model. The outlet distance has been shortened to 2.5m to save on computational resources as the wake is not the target of the study and therefore will not be resolved in detail.

Using a similar multi-domain approach to the isolated blade tests, the model consists of 3 Blade Domains, a Rotating Domain, and an outer Fixed Domain, as shown in Figure 5-5. The blade domain is directly imported in its optimised state from the isolated blade study, while the Fixed and Rotating domains were drawn using ANSYS Workbench v14.0.

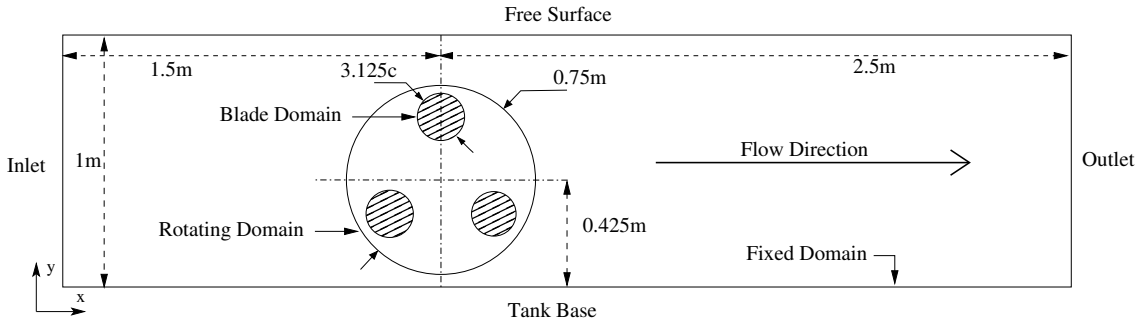

Figure 5-5: Geometry of the numerical tank

5.3.2 Meshing

The purpose of the isolated blade optimisation was to supply a validated blade meshing methodology for use in the full turbine model. To employ the methodology the Reynolds number of a blade must first be estimated so that the optimal y^+ range can be achieved during the solve. An estimation of Reynolds number was generated using a code written in MATLAB that was able to account for the change in velocity profile with depth as determined by equation 3.3. A nominal mesh was constructed following a scoping exercise, the result of which is detailed in Table 5.2 and displayed in Figure 5-6. From this reference point, a structured mesh independence study was constructed to confirm the findings of the scoping work, the full details and result are given in Section 5.4.1. As with the previous chapters, the model was limited to a single cell depth in order to maintain achievable solve times, as described in Section 2.2.1.

Domain	Mesh Type	Nodes	Elements	Max Element Size (mm)	Growth Rate	Interface Constraints
Fixed	Hexahedral / wedges	16592	7916	25	1.1	Fixed to Rotating: 360 edges.
Rotating	Wedges	30652	29666	5.14	1.2	Rotating to Fixed: 360 edges. Rotating to Blade: 180 edges.
Blade (1 of 3)	Hexahedral Inflation layer / wedges	33954	26974	5.14	1.05	Blade to Rotating: 180 edges. Upper and Lower blade: 150 edges each.

Table 5.2: Summary of meshes for laboratory scale model

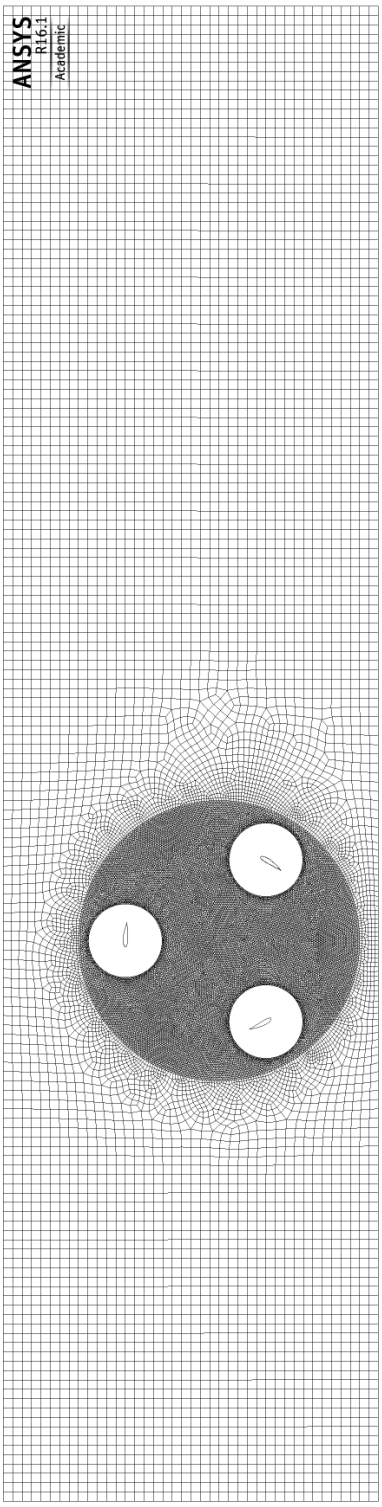

Figure 5-6: Images of lab scale meshes; Fixed and Rotating domains

5.3.3 Boundary Conditions

The full turbine case takes a similar single cell slice methodology as the isolated blade and hence has a number a similarities. Referencing Figure 5-5 for boundary names, the boundary conditions are as follows:

Inlet – The experimental inlet velocity distribution was achieved by creating a 'User Function' in the solver pre-processor. The function contains a lookup table of values of velocity versus depth that is interpolated to set the boundary values. The velocity profile itself was modified to take into account the experimental narrows, a detailed explanation is given in Section 5.3.3.1.

Outlet – This is set as an 'opening' with a relative static pressure of zero; $p_{rel} = 0$.

Free Surface – The model also excludes a free surface, instead using a 'free slip' condition at the upper boundary, where $U_y = 0$,$\tau_{wall} = 0$. These simplifications have been previously shown to have little effect on the numerical result for overall turbine torque, see Consul and Willden (2011).

Tank Base – The base is set as a 'no-slip' boundary.

Periodic faces – All boundaries in the x-y plane are set as symmetry planes; where normal velocities and advection gradients are set to zero.

Blade surfaces – These surfaces are set to 'no-slip', where pressure is set to zero gradient and velocities are set to zero; $U_x = U_y = 0$.

5.3.3.1 3D to 2D Conversion

To convert the 3D experimental case into a 2D equivalent, the experimental channel constriction described in Section 5.2.2 has to be addressed. Figure 5-7 depicts the constriction more clearly, where L_b is turbine blade length, b_T is test width, and b_C is channel width. Assuming water depth change is negligible through the constriction, continuity dictates that the velocity must increase equal to the ratio of area lost, i.e. b_C/b_T or 1.8/1.61. The resulting corrected inlet velocity used in the numerical model is plotted alongside the experimental profile in Figure 5-8 (see appendix B.2 for values). In the experimental case the rotor region (hashed area on Figure 5-7) is aligned centrally within the constriction resulting in the narrowing and then widening of the constriction occurring inside of the rotor's upstream and downstream extremities respectively. The position of these constriction changes, and hence velocity, are problematic for the 2D model, therefore it is assumed that the whole turbine is subject to the velocity increase and that TSR is maintained for the upstream half of the rotor, i.e. rotational velocity is calculated from the increased mean inlet velocity.

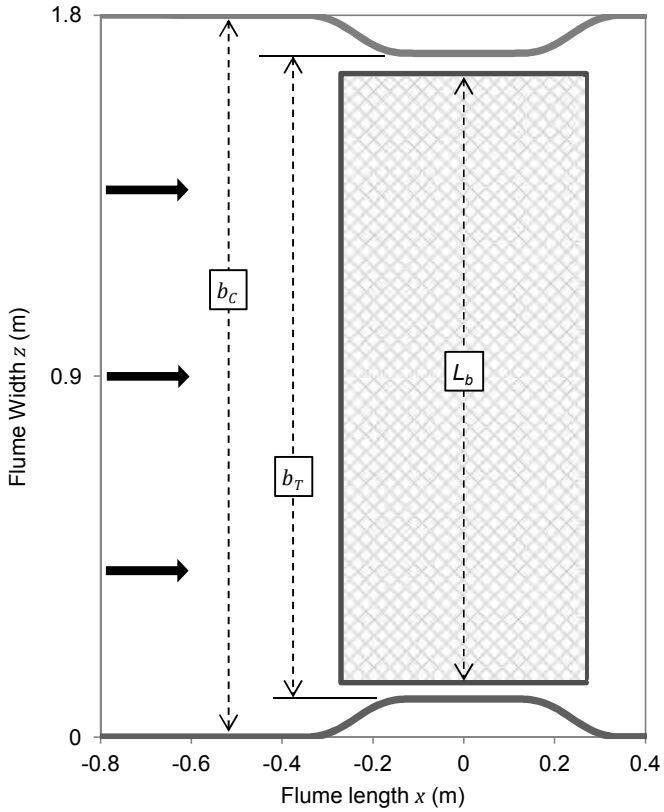

Figure 5-7: Diagram of experimental flume geometry, plan view

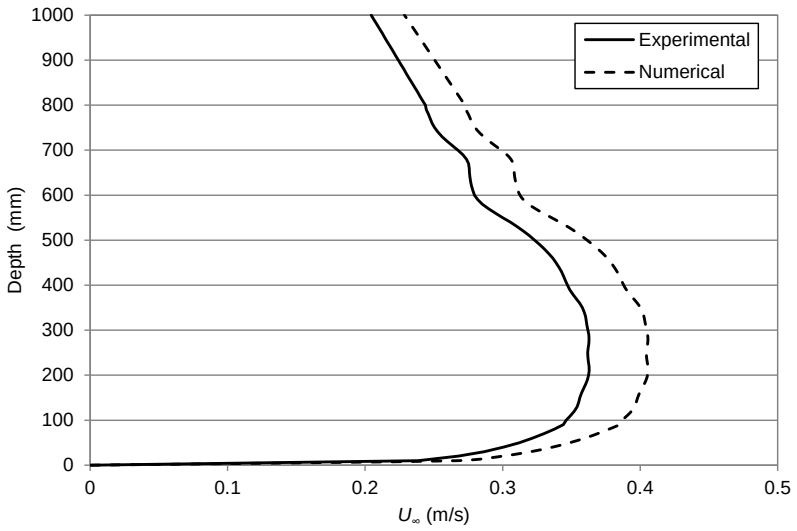

Figure 5-8: Plot showing experimental and numerical velocity profiles

5.3.4 Setup Summary

A summary of the numerical environment is detailed in Table 5.3. Notable features include the change to a transient timestepping scheme, interpolated flow velocity distribution at the inlet and the turbine angular velocity which is determined by tip speed ratio.

Type	Parameter	Symbol	Unit	Value
Time Discretisation	Analysis type	-	-	Transient
	Step angle	θ_s		Various
	Timestep	Δt	s	$\Delta t = \frac{\theta_s}{\omega}$
	Courant number	Cr	-	Uncontrolled
	Total time	t_{tot}	s	$t_{tot} = \frac{\theta_{tot}}{\omega}$
Fluid Properties	Fluid model	-	-	Pure water (custom)
	Molar mass	M	$kg/kmol$	18.02
	Density	ρ	kg/m^3	1000
	Specific heat capacity	$[c]$	$J/kg/K$	4181.7
	Dynamic viscosity	μ	$Pa \cdot s$	$11.3774e-4$
	Temperature	T	C	15
	Heat transfer model	-	-	None
Boundary Conditions	Inlet velocity	U_∞	m/s	Interpolated distribution
	Inlet turbulence intensity	I_∞	%	1
	Outlet pressure	p_{out}	Pa	0
Initial Conditions (full model)	Fluid velocity (x-direction only)	-	-	Interpolated distribution
Rotating Domain Motion	Angular velocity	ω	rad/s	$\omega = \frac{U_\infty \lambda}{r}$
	Frame change model	-	-	Transient rotor stator
Solver Control	Advection scheme	-	-	High resolution
	Transient scheme	-	-	Second order backward Euler
	Turbulence Model	-	-	Shear Stress Transport (SST)
	Turbulence numerics	-	-	High resolution
	Max. coefficient loops	-	-	15
	Residual target	-	-	$1e-5$(RMS)

Table 5.3: Setup parameters for cross-flow turbine numerical model

5.3.5 Post-Processing

A similar mean is calculated for torque Q and thrust T from the numerical result by averaging each value over a single 360° rotation of the turbine, see Section 3.2.1 for relevant equations. All mean values, averaged for a single rotation, are denoted by an overline in the form $\overline{P}$, $\overline{Q}$ and $\overline{T}$. Simulations were computed on the University of Bath 'Aquila' high performance computer taking an average of 48 hours on 4 processors (due to licensing limitations) to complete.

5.4 Numerical Accuracy

In the same manner as the circular cylinder and isolated blade studies, the entire model, now including fixed and rotating domains, are assessed for numerical accuracy. The study tests for numerical error due to both mesh and time discretisation which are presented in detail in this section. The simulation is now transient (unsteady RANS) with solutions running until a quasi-steady result was observed, i.e. solution variables varying with equal magnitude with each revolution. The result was considered to be converged when the average torque for 1 revolution deviated from the previous revolution by <1%, this took between 5 and 6 revolutions.

5.4.1 Mesh Independence

Having established a blade domain meshing strategy in Chapter 4, the independence of the numerical solution from mesh density is now tested for the new domains required for the full turbine simulation. This was achieved by approximately halving and doubling the mesh refinement of the fixed and rotating domains from the nominal 'medium' case to generate three test cases. The cases were numerically computed using the environment detailed earlier in this chapter with the turbine running at a tip speed ratio of 3, for 5 revolutions. The node counts for the three resulting meshes are shown in Table 5.4, along with the resultant power, torque and thrust, averaged over the final rotation. Comparing coefficients of power and torque, the values are seen to vary from the medium case by only 0.4% for the coarse case and -1% for the fine case, with the thrust varying by even less. These small errors, despite large mesh variances, suggest that the flow structure through the turbine has developed into a similar state in all three cases and adds confidence that the mesh is sufficiently refined.

Parameter	Symbol	Coarse	Medium	Fine
Fixed domain nodes	-	8230	16592	36696
Rotating domain nodes	-	15416	30652	61106
Blade domain nodes (1 of 3)	-	33954	33954	33954
Mean power coefficient	$\overline{C_P}$	0.4724	0.4706	0.4659
Mean torque coefficient	$\overline{C_Q}$	0.1575	0.1569	0.1553
Mean thrust coefficient	$\overline{C_T}$	1.5494	1.5396	1.532

Table 5.4: Results of the lab scale turbine mesh independence study

The results of mesh independence is investigated further by the capture of transient variants of C_P, these are plotted in Figure 5-9.

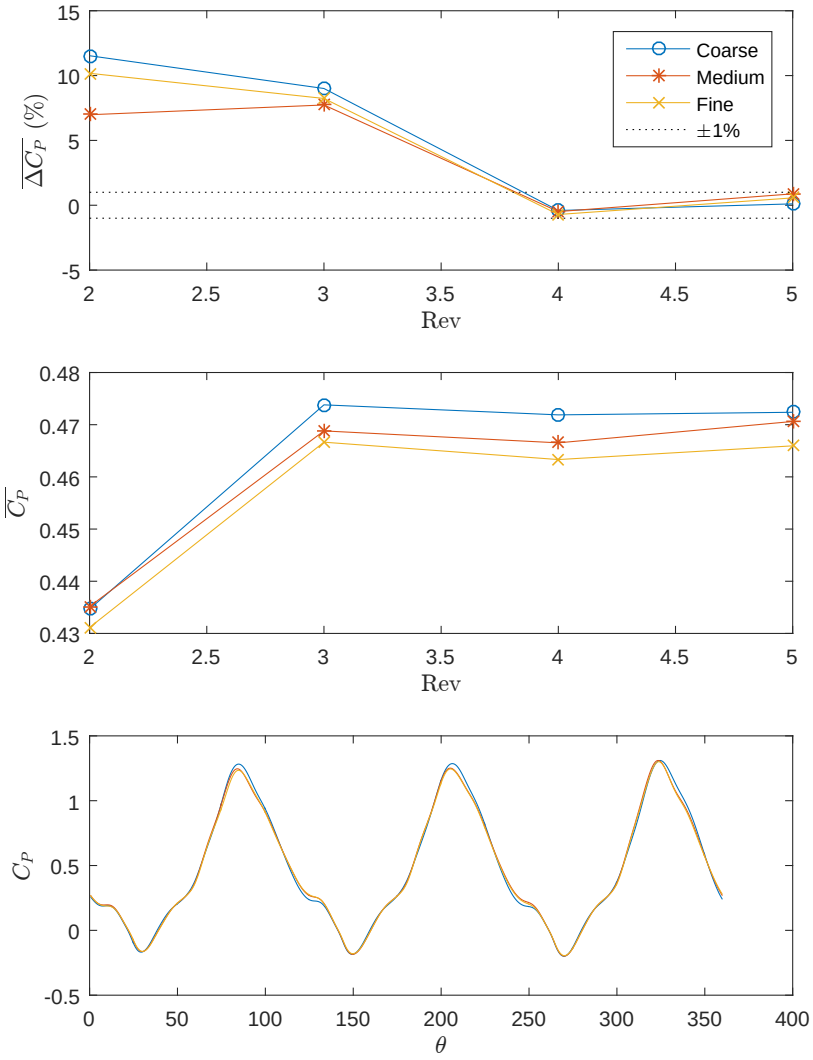

Figure 5-9: Graphs of transient Cp variants for analysis of mesh independence

The top graph shows the % change of mean coefficient of power, $\triangle\overline{C_P}$, for each full rotation of the turbine compared to the previous, as given in equation 5.3 where n is revolution number. The graph shows that for all three meshes the result converges to a change in power coefficient of less that 1% by revolution 4 which continues to remain low after 5 rotations. This convergence can also be clearly seen in the middle graph which shows the absolute values of $\overline{C_P}$ for rotation 2 - 5. The transient values of C_P are plotted against rotation angle in the bottom graph for the final revolution of the simulation. All three meshes display only minor differences adding further confidence to the conclusion that the flow field has reached a similar state in all cases and that the accuracy of the turbine simulation is dominated by the quality of the mesh close the turbine blades.

$$\triangle\overline{C_P} = \frac{\overline{C_P}^{(n)}}{\overline{C_P}^{(n-1)}} \tag{5.3}$$

5.4.2 Time Independence

Due to the implicit RANS solution method, stable convergence can be achieved at high Courant numbers. This provided an opportunity to solve with a timestep size equivalent a selected azimuthal angles, this gives the advantage of simplifying data handling at the post-processing stage. A series of tests were devised with computational timesteps equivalent to azimuthal step angles ($\theta_{\Delta t}$) of 0.25°, 0.5°, 1°, 2° and 4°, and solved until quasi-steady as described in Section 5.4.1. Examining Figure 5-10, a plot of power coefficient against azimuth angle, it is evident that the angle change per timestep has a significant influence on solution resolution. The result shows that larger timesteps result in an increasing overshoot at both peaks and troughs of turbine power output. The effect on mean power coefficient, plotted in Figure 5-11 (top), is an incremental decrease as timestep is increased. In the bottom graph of Figure 5-11 the smallest step angle is assumed to be the most accurate (as it offers the highest resolution) from which differential errors are calculated for all other step angles. The graph provides a clear proportionality to the variance in $\overline{Cp}$, with 0.5° showing very little change, 1° falling just outside the 1% error line and 2° and 4° showing significantly larger errors. Due to these findings, it can be concluded that small changes in timestep have a large influence over solution accuracy and that subsequent research in this paper will be conducted at a nominal azimuthal step angle of 0.5° and a maximum of 1°.

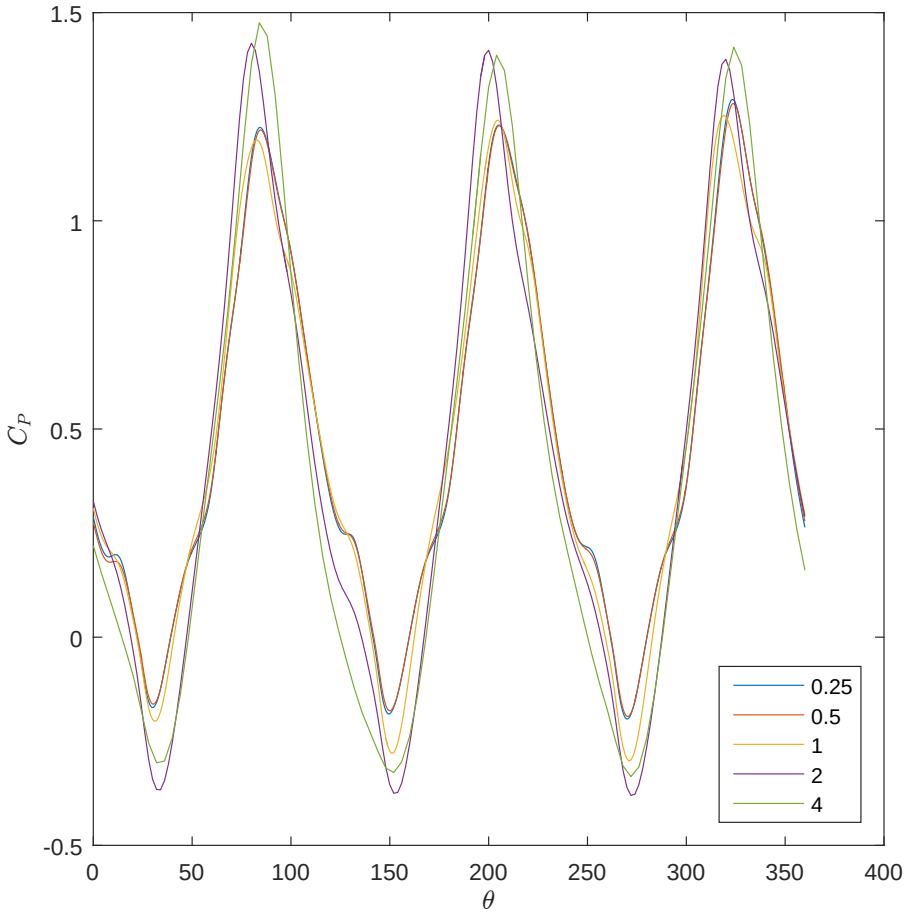

Figure 5-10: Graph of turbine coefficient of power versus azimuth angle for multiple solution step angles

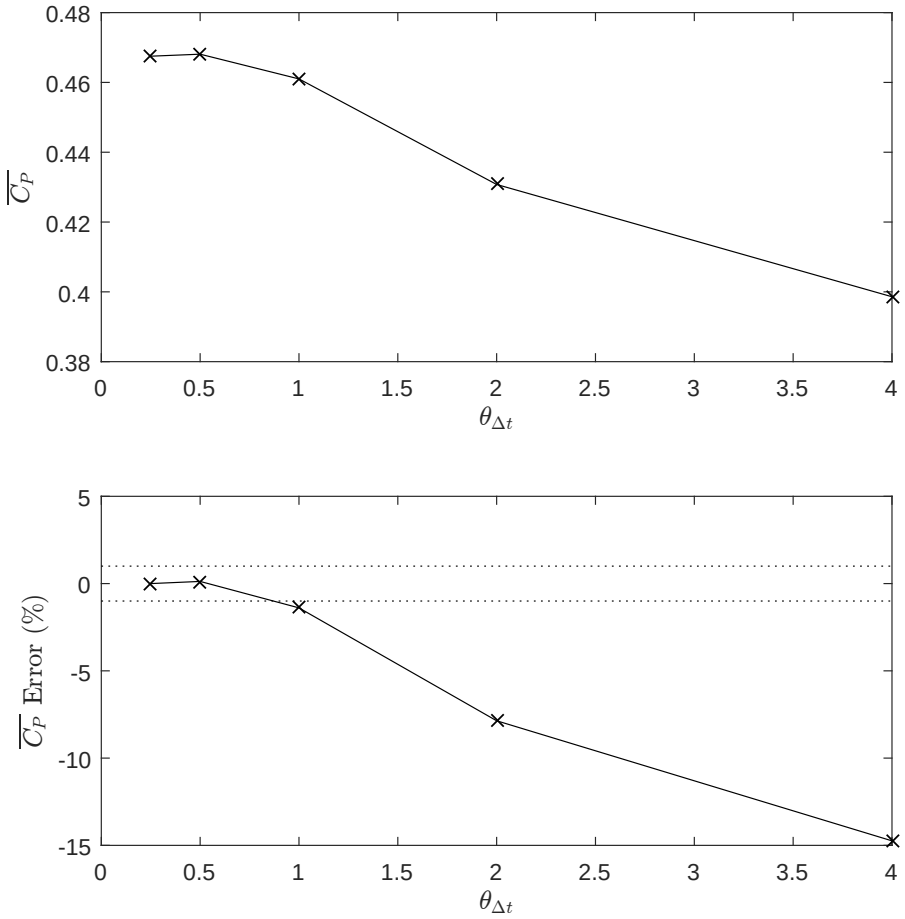

Figure 5-11: Mean power coefficient (top) and percentage delta from the 0.25° result (bottom) are plotted for multiple azimuthal step angles

5.4.2.1 Solution Convergence

Having established a timestep limit in regard to quality, it is useful to explore the computational efficiency at the various levels of time accuracy. As the mesh size is the same for all time independent test cases then the computational time for single mathematical iteration can be assumed to be approximately equal. Therefore, the relative computational cost can be measured by logging the number of iterations required to resolve each timestep for each of the cases. Table 5.5 displays the results from the 5 time independence tests, where iterations per timestep (Iter/Δt) is calculated as the mean number of iterations per timestep over the final 360 degree rotation of the turbine. From this value we can simply divide by timestep angle $\theta_{\triangle t}$ to give non-dimensional time t_c per degree computed. Taking the smallest timestep as a benchmark, the relative speed-up of the solution can be calculated which is presented alongside the comparative temporal resolution. The result shows a typical numerical outcome in which the compromise in resolution does not offer an equivalent speed-up of the solution, i.e. the largest step size is 1/16th of the quality but would result in a speed-up of only 4.4 times. This behaviour is due to the solution having to reach convergence at each timestep, the larger the timestep the greater the differential. A peak trade-off between solution speed and temporal accuracy is often found when the solution requires between 2 and 5 inner loop iterations. In the case of the turbine model it has already been established that a maximum of 1° $\theta_{\triangle t}$ is required to reach an acceptable quality so the data is presented purely as a point of interest.

$\theta_{\Delta t}$	Iter/Δt	t_c/degree	Speed-up	Resolution
0.25	3.98	15.90	×1	1
0.5	6.06	12.11	×1.3	1/2
1	8.25	8.25	×1.9	1/4
2	11.78	5.89	×2.7	1/8
4	14.54	3.63	×4.4	1/16

Table 5.5: Table of full turbine solution convergence values

5.4.3 Blade yPlus

Based on the low Reynolds number results from the isolated blade study the blades surfaces should experience a peak flow shear consistent with a $1 < y^+ < 15$ in order to maximise the accuracy of the surface pressure field, and hence body forces, around each blade. Using the medium meshes from the mesh independence study, a full turbine simulation was run at a number of tip speed ratios from 2 to 5. Figure 5-12 displays a trace of y^+ for a single blade over a 360° rotation for each of the tip speed ratios. The graph shows that the y^+ remains well within the defined

limits for accuracy with an azimuthal y^+ variance of 2.5 and a tip speed ratio y^+ shift of approximately 0.75 per step.

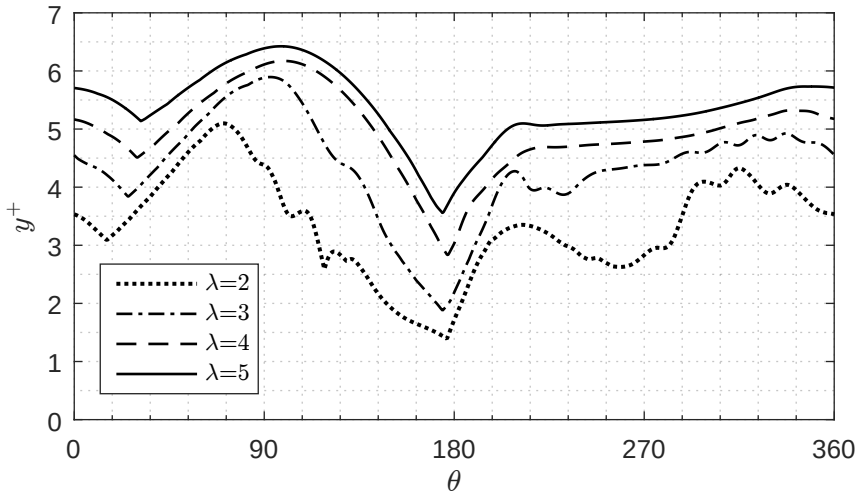

Figure 5-12: Graph of single blade y^+ for a full rotation of the numerical turbine

5.4.4 Empty Flume Validation

In order to test for the successful advection of the inlet flow distribution and turbulence levels to the location of the turbine, a numerical flume of the same dimensions described in Section 5.3.1 was constructed. The numerical model is built with a 'medium' mesh quality from Table 5.4 and solved using the settings specified in Table 5.3. The results, plotted in Figure 5-13, present data profiles where depth is positioned on the y-axis; note that a depth of zero coincides with the centre of the turbine in the numerical model. The velocity profile, shown on the left graph, exhibits a near perfect transmission through the flume with only a minor deviation at the base. The error at the base is due to the shear effect of the non-slip boundary, an error that has been exaggerated due to a coarse mesh in the region (shown in Figure 5-6), however, as it is significantly outside the rotor region it was considered to be negligible. The turbulence intensity (I), plotted in the right-hand graph, confirms the 1% level set at the inlet but also that the numerics are generally dissipative with the turbulence level dropping to approximately 0.3% at the turbine centre. By increasing the turbulence levels at the inlet to improve this discrepancy it was found that the velocity profile was compromised. With the absolute values of turbulence being generally low the discrepancy is not expected to negatively influence the outcome and therefore the model was fixed at the original settings ($I = 1\%$) for further modelling. This behaviour is typical of many two equation turbulence models which should be quantified and accounted for particularly in flows with more significant levels of turbulence.

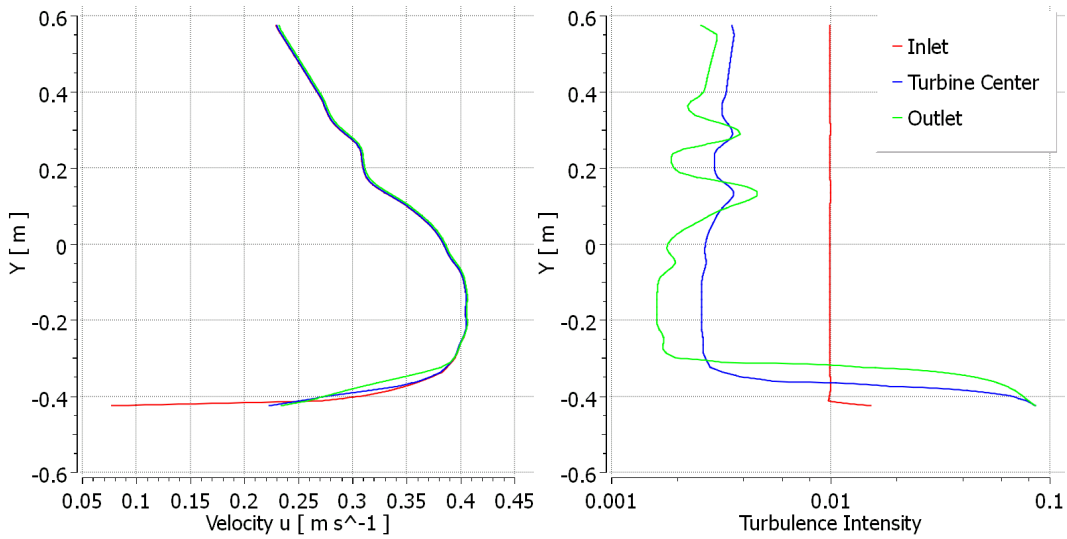

Figure 5-13: Plots of channel velocity and turbulence intensity for an empty numerical flume

5.4.5 Summary

The transient turbine model has been scrutinised for numerical robustness for a number of typical solver characteristics. A summary of the outcomes includes:

- Mesh quality of the fixed and rotating domain had only a small effect on numerical predictions within the limits of the study. To ensure potentially more challenging flow fields are not poorly predicted a level of conservatism is taken with the 'medium' mesh being selected for subsequent models.
- The timestep was shown to have a significant effect on the resolution of the solution with a significant jump in error for timestep angles above 1°. With almost zero error from the smallest timestep angle and with a model solve time still practical, the 0.5° ($\theta_{\Delta t}$) was selected for the next study.
- The y^+ variance of the turbine blade remained well within the $1 < y^+ < 15$ limits established in the isolated blade modelling for all tip speed ratios and azimuthal locations. The result means that a single blade mesh can be used across the full range of testing of the lab scale simulations.
- Advection of the velocity profile was highly accurate with negligible variance between inlet and turbine centroid. Turbulence intensity suffered from some diffusion but due to the low initial levels this change was deemed to be negligible.

5.5 Numerical Test Plan

The fully transient turbine model was solved for TSRs between 2 and 5 for comparison with the experimental turbine values. To investigate scale, further solutions are generated at a TSR of 3 for turbines up to a 10 metre diameter. In order to test the consistency of turbine behaviour with scale additional solutions are run including at an TSR of 4, and for a uniform velocity profile. Table 5.6 details the numerical tests conducted, where the velocity profile is split into experimental (Exp.) or uniform flows, and $\overline{U_\infty}$ and U_r are mean velocities for the full channel depth and across the rotor respectively (see Figure 5-4). Note that all turbine models above laboratory scale (0.5m) were re-meshed in accordance with the methodology outline in Chapter 4 to achieve target y^+ values.

Test ID	Velocity Profile	$\overline{U_\infty}$ (m/s)	U_r (m/s)	λ	$2r$ (m)	$\overline{Re}$
1	Exp.	0.333	0.3698	2	0.5	45,250
2				2.5		55,333
3				3		65,605
4				3.5		75,984
5				4		86,428
6				4.5		96,915
7				5		107,433
8				3	1	131,210
9					2.5	328,026
10					5	656,052
11					10	1,312,104
12				4	1	172,856
13					2.5	432,139
14					5	864,277
15					10	1,728,555
16	Uniform		0.333	3	0.5	59,112
17					1	118,224
18					2.5	295,560
19					5	591,120
20					10	1,182,241

Table 5.6: Numerical modelling test scheme

5.6 Results

5.6.1 Lab Scale

All three parameters given in equations 3.8-3.10 are plotted in Figure 5-14 for experimental and numerical methods. Comparing the two results for $\overline{C_P}$ shown in Figure 5-14 (top), it is clear that the numerical model achieves high correlation with the experiment. At close inspection the numerical result slightly under predicts $\overline{C_P}$ below a TSR of 3, changing to over prediction by a maximum of ∼10% at a TSR of 4. Qualitatively the numerical result matches the experimental values, showing a rising value of up to a TSR of 4, before losing efficiency and falling as TSR rises to 5. Identical trends for both mean torque coefficient plotted in Figure 5-14 (middle), and mean thrust coefficient in Figure 5-14 (bottom), where the crossing points between numerical and experimental values also fall at a TSR of 3, with peak torque falling at the lower TSR of ∼3.6 as would be expected.

The quantitative error of the numerical model can be attributed to a number of limitations. At low TSR the reduced accuracy and marginal under-prediction of forces of the SST model at post-stall angles of attack, as shown in Figure 3-4, would explain the lower than expected values. Above a TSR of 3, the over prediction is more significantly influenced by the required simplification of the 3D constriction of the flume into a 2D model. To achieve this the correction requires an increased angular velocity employed in the numerical model to maintain TSR with the corrected inlet velocity, as detailed in Section 5.3.3.1, and therefore may result in the over prediction of turbine performance. Despite the limitations imposed by the low Re conditions, the simplified numerical model has accurately predicted trends and quantitative values within a peak error of ±10% for all coefficients. It is worth noting that all numerical results fall into the extremities of the experimental raw data (example shown in McAdam et al. (2013a)), with the experiment itself being subject to range of instrumentation and experimental error tolerances.

To explore the accuracy of the simulation further, Figure 5-15 shows the coefficient of distributed normal load C_N, given in equation 5.4, for experimental and numerical results for TSRs of 2, 3 and 4; where N is the distributed normal load. For clarity, the load given is acting radially, where positive values are acting away from the turbine axis (see (McAdam et al., 2013b)).

$$C_N = \frac{N}{\frac{1}{2}\rho U_r^2 c} \tag{5.4}$$

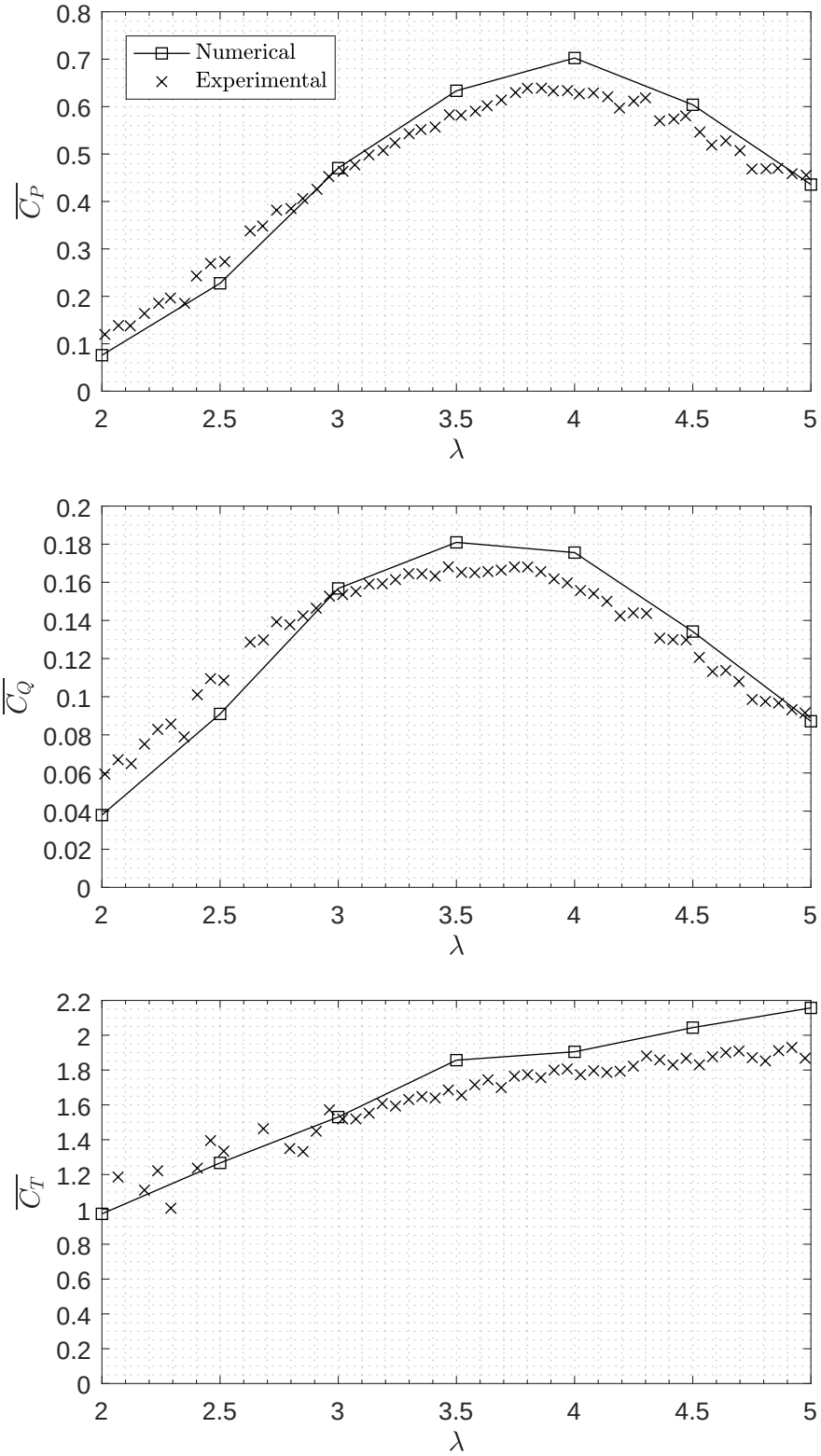

Figure 5-14: Plots comparing experimental and numerical results for coefficients against tip speed ratio for; top: power; middle: torque; bottom: thrust. Experimental results courtesy of Kepler Energy Ltd.

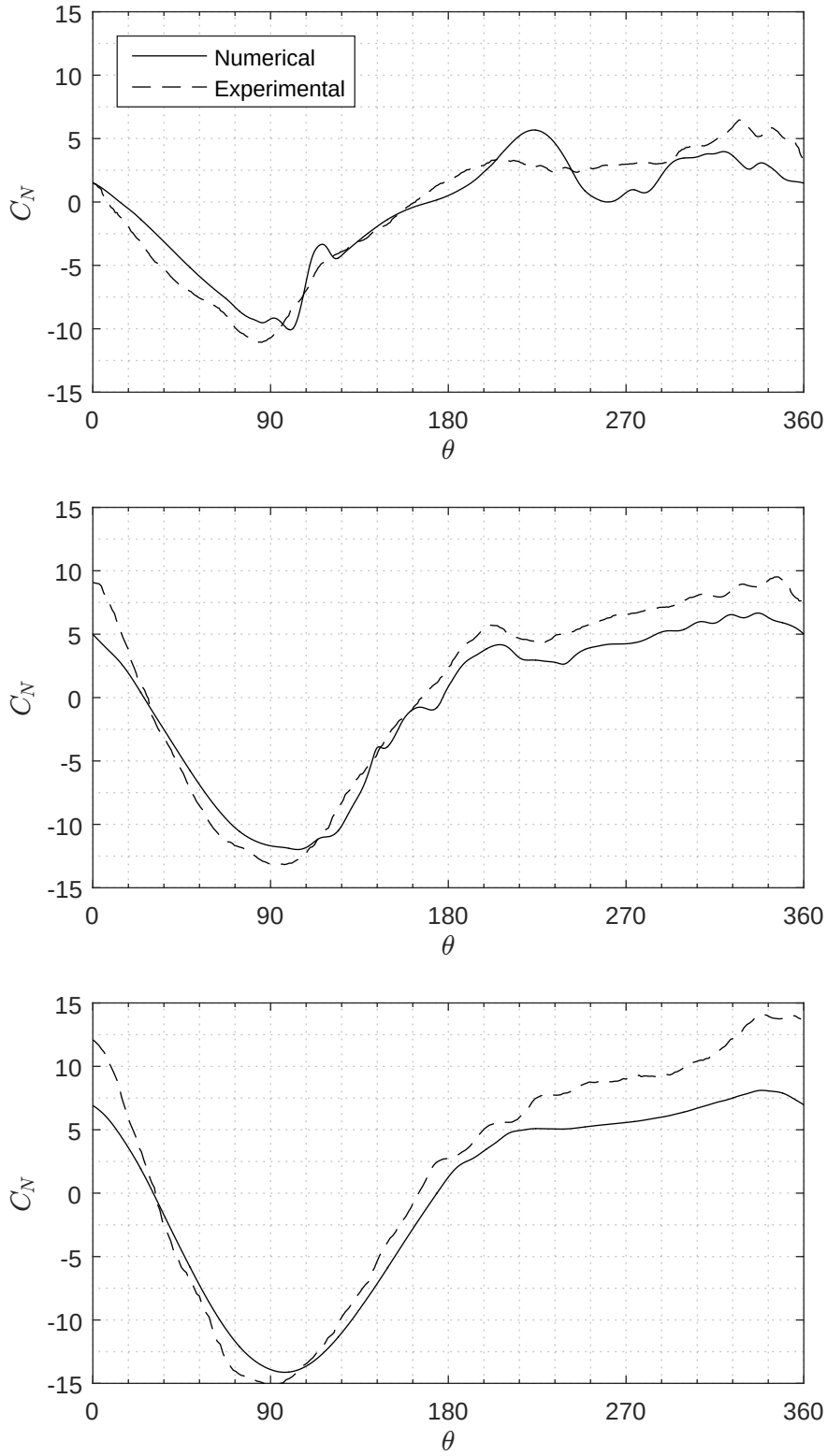

Figure 5-15: Coefficients of blade force normal to chord line against azimuth angle for three tip speed ratios; top: λ=2; middle: λ=3; bottom: λ=4. Experimental results courtesy of Kepler Energy Ltd.

Considering the slowest spinning turbine case, at a TSR of 2, Figure 5-15 (top) shows that the numerical simulation achieves broad correlation with experiment, but with diverging force oscillations visible in the 180-360 degree region. Referring to Figure 3-3, at rotation angles (θ) below 180 degrees the blades are upstream, and above 180 degrees they are downstream. In the downstream region, due to the low TSR and velocity shadow induced by the upstream wake, the blades experience the lowest blade chord Reynolds numbers modelled in this research, resulting in heavy stall of the downstream blades. In such conditions the unsteady RANS method is unable to accurately resolve the flow shear around the blades resulting in a poor match in this region.

At a TSR of 3, Figure 5-15 (middle) shows an improved correlation with the experimental readings compared to a TSR of 2. The positives include a qualitatively high match, with almost all of the peaks and troughs captured by the numerical model. In particular, the downstream values suggest that the generation and advection of shear flows is taking place with consummate accuracy. The origins of the load force fluctuations are highlighted in Figure 5-16 which presents a contour plot of the flow field velocities for the same numerical result. The velocities have been limited to values from 0.125 to 0.625 in order to visually capture the advection of velocity fluctuations generated by the upstream blade wake. By comparing Figure 5-15 (middle) and Figure 5-16 it is possible to correlate the fluctuations in force between θ positions of 170° and 250° to the dynamic vortex shedding shown in the contour plot. Similarly, the wake fluctuations passing the downstream blade between the 270° and 350° positions are also visible in both the force prediction and the contour plot. Quantitatively the zero degree value and the downstream values are below expected. Causes include possible free surface effects for values close to zero degrees and the inability of the 2D model to capture the effect of the diverging flume side walls as shown in Fig. 10.

Examining the bottom plot in Figure 5-15, the results at a TSR of 4 contain similar attributes to those at a TSR of 3. The upstream quantitative values are particularly well matched with the extreme loading predicted within 5% of the experimental value. Downstream the result diverges more significantly from experimental values and appears as a smoother line.

The reduced forces numerically predicted at the downstream positions for TSRs of 3 and 4 suggest that there is unexpected loss in flow velocity between upstream and downstream locations. Along with the issues raised already in the discussion, this discrepancy may also be a symptom of a higher free stream turbulence than was estimated for the experiment, causing faster wake recovery. Additionally, the influence of the velocity correction to account for the constriction may result in an increased blade efficiency at the upstream position and hence result in a lower flow speed downstream. It should be noted that the experimental plot is

an instantaneous result, demonstrated by the 0° and 360° differing in all plots in Figure 5-15, and therefore is subject to variances which may not reflect the exact average of the force acting on the turbine blade.

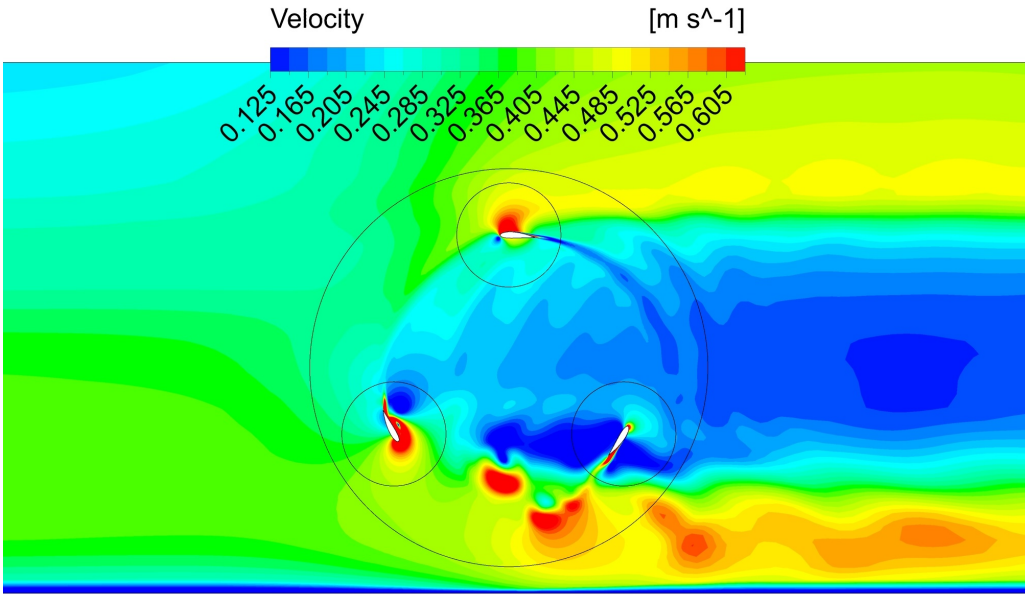

Figure 5-16: Contour plot of velocity for a numerical turbine at a TSR of 3

5.6.2 Turbine Scaling

To explore the effect of Reynolds number scaling on turbine performance a series of simulations were performed at turbine diameters of 0.5m, 1m, 2.5m, 5m and 10m, with 0.5m being the lab scale model. Each test includes a velocity profile equivalent to the lab scale inlet that has been stretched depth-wise such that the overall resolved flow velocities and directions experienced by the blade are equal at all scales. The study includes three sets of results (S1, S2 and S3), referring to Table 5.6, S1 comprises of tests 3, 8-11, S2 from 5, 12-15, and S3 from tests 16-20. The three sets represent three alternative turbine operating conditions, TSR 3 and TSR 4 in the experimental velocity profile, and TSR 3 in uniform flow conditions.

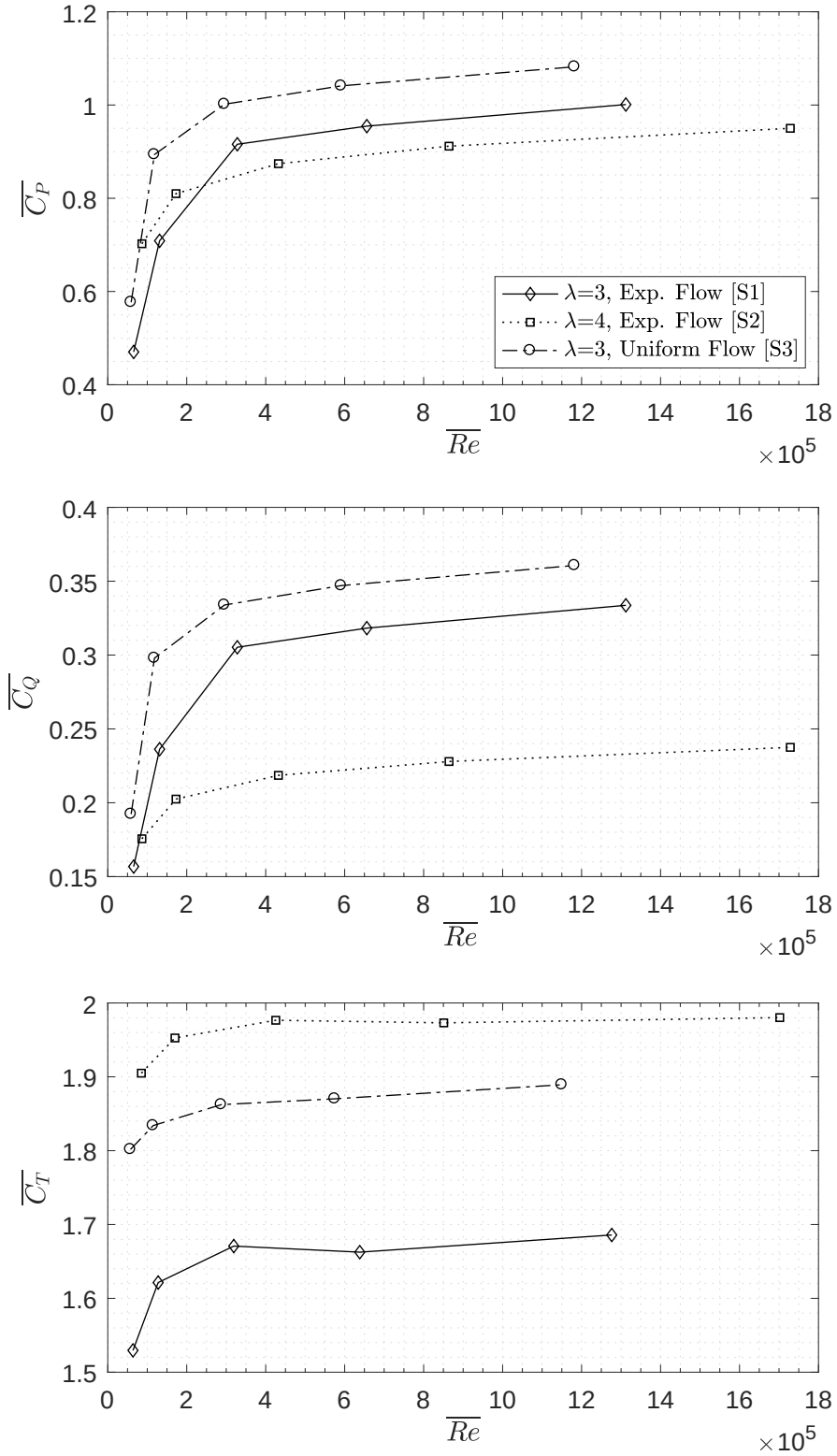

Figure 5-17: Numerical predictions for increasing scale represented by plotting coefficients against increasing mean blade chord Reynolds number for; top: power; middle: torque; bottom: thrust

The results for the scaling tests are shown in Figure 5-17, where all results are plotted against $\overline{Re}$. Starting with the mean coefficient of power in Figure 5-17 (top), the three scaling tests are plotted with each marker representing a result at each increment of geometric scaling; the result for test set S1 is labelled as an example. A number of significant findings can be observed, firstly, the power coefficient increases significantly from low $\overline{Re}$, lab scale conditions, up to the full scale equivalent. For example, S1 increases by over 200% from the experimental lab scale, for a rotor experiencing a mean blade chord Reynolds number 20 times higher. Secondly, the rate of increase is non-linear, with all three test cases displaying a decaying increase in $\overline{C_P}$. Additionally, the three test cases show little correlation with each other. For example, at low $\overline{Re}$, equivalent to lab scale, S2 gives the highest $\overline{C_P}$, S3 medium value, and S1 the lowest. At high $\overline{Re}$ values of $> 10^6$, equivalent to a full scale turbine, the order of performance is altered such that S3 provides the highest $\overline{C_P}$, S1 medium, and S2 the lowest performing turbine. However, at an $\overline{Re}$ of approximately 350,000 the power coefficients of all three cases rise with equal gradients signifying that the effects of low $\overline{Re}$ conditions are diminishing, with the solution converging towards an asymptote.

Figure 5-17 (middle) shows the change in mean torque coefficient, $\overline{C_Q}$, with $\overline{Re}$. Unlike the plot for $\overline{C_P}$ the three test results do not cross, but display an otherwise equivalent behaviour. The final plot, Figure 5-17 (bottom), shows mean thrust coefficient against $\overline{Re}$. All three sets experience a lower relative thrust at lab scale than would be expected at full scale. In parallel to the $\overline{C_P}$, the thrust becomes increasingly constant at an $\overline{Re}$ of $\sim$350,000 and above.

5.7 Discussion

An experimental test has been used as a basis to develop and validate a numerical model of a three bladed variant of a cross-flow turbine. The resultant model has been adapted to explore performance at increased scales and identify relationships and limitations in both the experimental and numerical methods. The results of the numerical modelling of the laboratory scale turbine confirm that a URANS methodology with 2D simplification is capable of providing accurate hydrodynamic performance predictions for cross-flow turbines. For all practical turbine operation speeds the maximum quantitative error for $\overline{C_P}$ was 8%, with positive qualitative agreement achieved for all variables (see Figure 5-14). Investigating local forces on the blades showed that the numerical model is capturing not only global averages, but also advecting realistic turbulent structures through the turbine in cases where deep stall is avoided. The most prominent example of this is shown in Figure 5-15 (middle), supported by Figure 5-16, where the numerical results capture the downstream fluctuation of C_N due to the generated upstream wake in parallel

with the experiment. Limitations to the numerical accuracy of the lab scale result include the negation of the flume narrows, velocity correction and turbulence assumptions, and very low Re ω equation performance in the boundary layer.

Scaling of the turbine was approached by focussing on the changes to device performance with mean blade chord Reynolds number $\overline{Re}$. Based on the high validation achieved at lab scale, and the known improvement to blade force prediction using ω based models at increased Reynolds numbers, a purely numerical series of tests were conducted. The scaling tests, detailed in Table 5.6, generated a number of findings including:

- At full scale/high Re the turbine achieves significantly higher power coefficients than an equivalent lab scale model
- The increase in power coefficient with scale is non-linear and varies inconsistently between operating conditions for values of $\overline{Re}$ below ∼350,000.
- Above an $\overline{Re}$ of ∼350,000, the power coefficients of all operating conditions become equally proportional.

The rise in $\overline{C_P}$ at higher Reynolds numbers is expected and supports existing literature. However, the inconsistency of the increase in $\overline{C_P}$ between the three operating conditions shown in Figure 5-17 shows conclusively that tests both numerically or experimentally do not scale consistently when referenced against mean Reynolds number. For example, Set 2, TSR 4 – experimental flow, was the highest performing of all three cases, but by an $\overline{Re}$ ∼250,000 this had fallen to the worst performing. The transition between varying and proportional results falling at ∼350,000 is consistent with the boundary layer transformation of the selected foil from a mixed to a supercritical boundary layer, this change is key to the behaviour demonstrated in the results. Additionally, the boundary layer behaviour has the knock-on effect of triggering dynamic stall with leading and trailing edge vortex generation causing turbulent structures that have a non-trivial effect on upstream and downstream blade performance. For these reasons, the results advocate the use of a minimum $\overline{Re}$ of ∼350,000 for laboratory scale tests in order to avoid low Re effects and provide scalability and proportionality to the acquired turbine performance data. Furthermore, the reduction in uncertainty may also improve the isolation and application of additional corrections such as accounting for Froude number and blockage. For alternative turbine geometries differing $\overline{Re}$ limits are likely to exist and therefore should be considered alongside other known effects when inferring full scale turbine performance from low Re test data.

5.8 Conclusion

The numerical model constructed and implemented in this chapter has proven an ability to successfully capture performance trends and achieve quantitative comparability to an equivalent experimental turbine. The inherently 3D experimental setup, with particular reference to the 'narrows', forced the inclusion of a number of parameter adjustments and assumptions which add some uncertainty to any error between experimental and computational values. To more effectively scrutinise a numerical model future work in the field would include the design and testing of an experimental turbine with two-dimensionality as an objective. The turbine scaling exercise provides an initial insight into a lack of correlation between the performance of a laboratory scale turbine and a full scale counterpart. The result showed that a minimum mean Reynolds number of $\sim$350,000 is required to ensure at least a behavioural equivalence to a commercially viable device. With the assurance gained from the validation exercise and the scaling limits in place the next chapter focusses on understanding turbine-fluid interaction at a larger scale.

Chapter 6

Large Scale Turbine

SUMMARY: In this chapter a large scale turbine based on the proportions of the experimental turbine is proposed and modelled in order to extract further understanding and provide a baseline on which to identify and trial performance enhancement. In addition to a comprehensive analysis of turbine characteristics, a local flow sampling methodology is proposed and included as part of the study.

6.1 Introduction

The results of Chapter 5 indicate a necessity to develop cross-flow turbines at suitable Reynolds numbers to avoid scaling error. Accordingly, a large scale derivation of the University of Oxford cross-flow turbine is constructed such that $\overline{Re} > 350,000$ for all tested cases. The purpose of the chapter is to explore turbine performance in detail, consider flow conditions passing through the turbine, and scrutinise the mechanisms that drive blade boundary flows.

A key challenge in all attempts to optimise the power extraction of a cross-flow turbine is the difficulty of predicting the effective flow conditions experienced by the turbine blades. The flow field is influenced by many factors relating to turbine geometry, environment and function. This makes accurate statistically driven predictions of blade performance for an effectively infinite number of configurations and environments open to many sources of error. In particular, the momentum loss and blade wake caused by the upstream blade path can be complex, especially at low tip speed ratios where greater variances in flow structures are likely. Using fully resolved numerical methods there are a number of common metrics that are captured to enhance fundamental knowledge and refine statistical models, such as torque, thrust, pitching moment and flow field variables. In order to

optimise performance these factors are often explored using brute force sampling to map parameters and form relationships. However, these methods can be computationally costly and may be avoided if it were possible to know accurate local flow conditions of the blade. This challenge is targeted in this chapter in which a novel approach to flow field interrogation close to the turbine blades is proposed. To extract the maximum understanding of both the turbine function and the drivers behind the findings provided by the novel flow sampling, a detailed interrogation of turbine performance, flow structure and blade forces is presented. The novel local flow interrogation method is described herein.

6.1.1 Local Flow Sampling

The understanding and optimisation of a cross-flow tidal turbine can be aided significantly by a knowledge of the effective angle of attack of a turbine blade. For example, this would allow pitch or blade optimisation by mapping against peak lift forces (of lift to drag ratios) established by static experimentation as shown in Chapter 4. Blade attack angle can be estimated using simple vector resolution, as shown in Section 3.2, but this fails to capture any interaction with the turbine blades. To remedy this, it is proposed that the flow angle and velocity immediately ahead of a blade is captured in a numerical model. Conventionally, angle of attack of an aerofoil is measured with reference to the direction of the far field free stream, in the case of a tidal turbine blade this is not possible as there is no such reference. The result is that a compromise is required between sampling too far ahead of the blade where flow may be unrepresentative, or too close to the blade where flow has begun to turn due to a preceeding pressure wave in front of the blade; this is illustrated in Figure 6-1 by the left and right arrows respectively. With the position being unknown, sampling is done at multiple positions on all turbine models. The features of the computational methods to achieve this are now described.

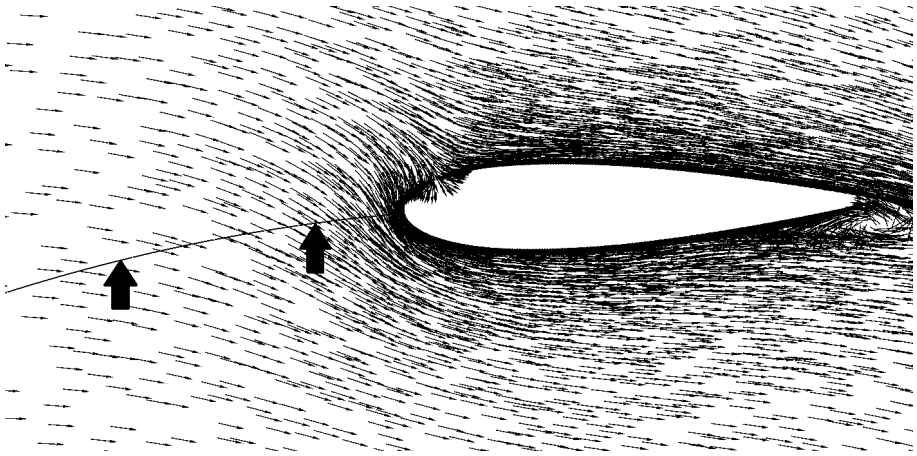

Figure 6-1: Vector plot of the flow field around a turbine blade

6.2 Numerical Model

6.2.1 Geometry

The geometry is based around the lab scale geometry used in the previous chapter but has been scaled up and modified to satisfy a number of constraints and interests. The turbine blades have been changed to non-cambered NACA 0018 profiles in order to represent a more typical setup seen in literature, as shown in Table 3.1. The blade count and chord length have been scaled proportionally to maintain an equal solidity to the lab scale test. The revised turbine has been assigned a diameter of 5m, a size 10 times that of the lab scale. With no known large scale data available, the blockage ratio has been decreased from 1/2 to 1/3 based on the assumption that it represents a more realistic proposition for a prototype early stage commercial turbine operating in near shore operation. The chosen size equates to a kinetic energy potential of 20kW/m at a tidal current of 2m/s. For a 12.5m or 25m span device this equates to a 250kW or 500kW potential yield respectively. In addition, at a minimum TSR of 1.5 and an inflow of 2m/s the lowest local velocity can be estimated by equation 3.2 evaluated at an azimuthal position of 180 degrees. The result is a minimum blade chord Reynolds number of $Re \sim 575,000$, and a zero loss rotation mean of $\overline{Re} \sim 1,920,000$. A summary of the chosen turbine geometry is given in Table 6.1 and the dimensions of the numerical domain is detailed in Figure 6-2.

Parameter	Symbol	Unit	Value
Rotor radius	r	m	2.5
Blade chord	c	m	0.6545
Solidity	σ	-	0.125
Blade count	N	-	3
Blockage ratio	b	-	1/3
Blade profile	-	-	NACA 0018

Table 6.1: Large scale turbine parameters

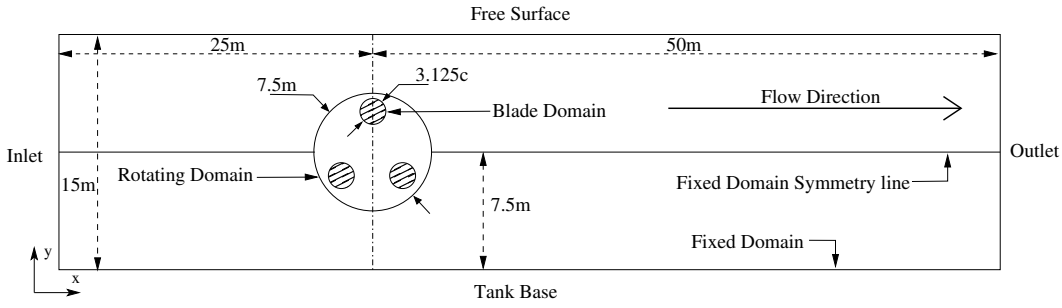

Figure 6-2: Diagram of the large scale turbine numerical domain geometry

6.2.2 Meshing

Meshing of the numerical model was completed to the standards established in the isolated blade case and lab scale testing. In terms of the blade domains, this resulted in a refined mesh at the blades' surfaces to account for the higher Reynolds numbers experienced at the larger scales. The fixed and rotating domains are meshed assuming that the turbulence length scales are proportional to the size of the blade geometry and therefore retain similar node counts to the lab scale model. However, the fixed domain was split into two halves with the upper and lower portions of the domain having symmetrical grid patterns; the symmetry line is shown in Figure 6-2. This enhancement has been implemented to both streamline the meshing process and to minimise any effects grid asymmetry may have on the upper and lower flow fields of the turbine. It should be noted that the two halves were numerically 'glued' meaning that the solver recognises them as one continuous computational grid in which no boundary interface is required. This joining method is reflected in the post-processor in which the symmetry line is no longer visible. A number of authors have additionally implemented rotational symmetry in the rotational domain, however, the homogeneity of the lab scale mesh structure displayed no issues in resolution and was therefore continued in use for the large scale. The resultant mesh is shown in Figure 6-3.

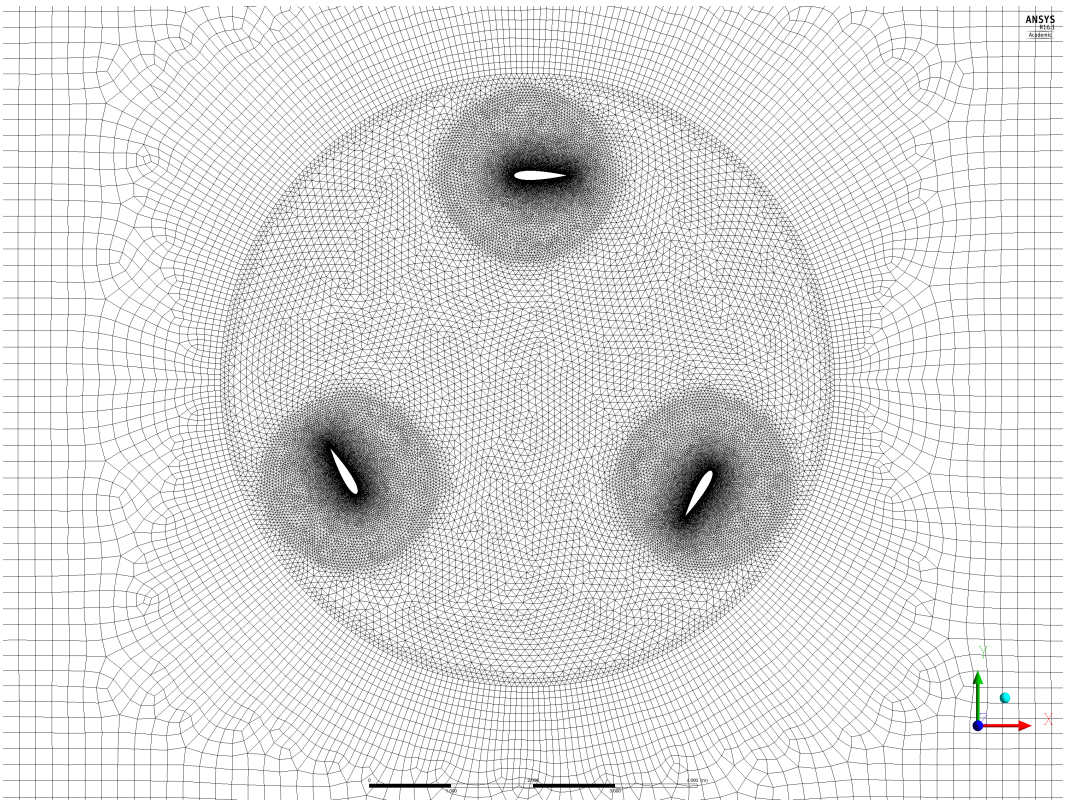

Figure 6-3: Image of large scale turbine mesh

6.2.3 Additional Notes

The boundary conditions remain largely the same as those implemented in the lab scale tests, details are given in Table 5.3. Changes include a uniform inlet velocity profile set to 2m/s and an increased calculation step angle ($\theta_{\Delta t}$) from 0.5° in the lab scale tests up to 1°. The larger step size was chosen because it had already been proved to give equivalent accuracy in Section 5.4.2 and because at the larger blade chord Reynolds numbers the solution has been proven to be more stable. For the numerical study in this chapter the software was updated to ANSYS® 17.0, and the solutions were calculated on a new Linux cluster. Solutions were run on 48 parallel cores each taking 6 hours of wall clock time.

6.2.4 Local Flow Sampling

Local flow sampling was implemented in the solver by setting up four monitor points at increasing distances from the leading edge of the blade. The points lie on the flight path of the blade at 1/4, 1/2, 3/4 and 1 chord length distance from the leading edge which are represented by points a,b,c and d in Figure 6-4 respectively. The monitor points function correctly even when rotation is activated for a number of reasons:

- The sample points are created using an object in ANSYS® CFX called a 'Source Point', these are re-purposed for monitoring by accessing variables at their location using equations written in a solver mathematics code called CFX Expression Language (CEL)
- The source points are placed in a fixed geometric position, one blade was selected and monitored
- The sample points are used to log the flow components in a rotating frame of reference, i.e. the velocity of the rotating domain is mathematically added to the flow field.
- Although the rotating and blade domain meshes are set to rotate, this is achieved by mathematical mapping across the domain interface (using GGI). The result is that while the flow experiences a rotating motion, the geometric location of the mesh and sample points remain fixed.

At each of the sample points flow velocity components u and v, equal in direction to global x and y respectively, were logged and converted into angles of attack and corresponding velocities using equations 6.1 and 6.2. Having attained a 'raw' angle it is clear that the value collected does not correspond to the current angle

of the turbine blade. Referring to Figure 6-5, the delta between current turbine position and a sample point is equal to sample offset angle ψ plus leading edge angle ϕ. The first part of the correction is to align each sample set with a new theta, this is simply the original turbine angle plus the delta, as shown in equation 6.3. A second correction is now required to account for the difference between the reference blade angle and the sample point blade angle. As the blade is a fixed pitch the correction is shown in Figure 6-5 as angle ς, in fact this angle is equal to the θ correction $(\psi + \phi)$ but is identified for completeness.

$$\alpha_{raw} = \arctan\left(v/u\right) \tag{6.1}$$

$$U_{local} = \cos\left(\alpha_{raw} u\right) + \sin\left(\alpha_{raw} v\right) \tag{6.2}$$

$$\theta_{local} = \theta + \psi + \phi \tag{6.3}$$

$$\alpha_{local} = \alpha_{raw} + \varsigma \tag{6.4}$$

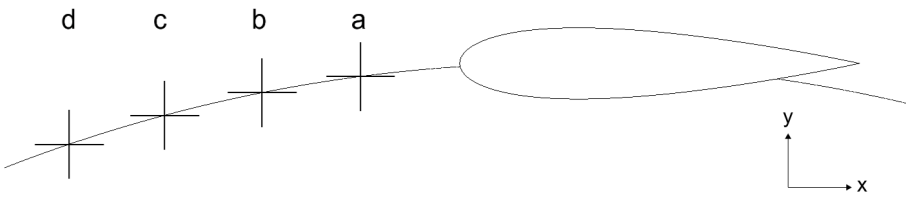

Figure 6-4: Location of local flow monitoring sample points

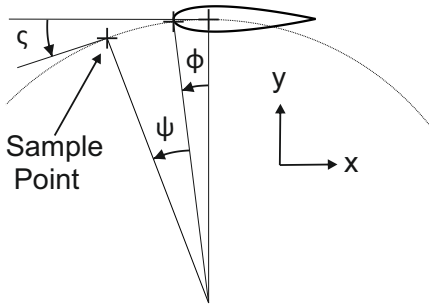

Figure 6-5: Diagram of sample point transformation angles

6.3 Numerical Accuracy

6.3.1 Transient Convergence

In the same fashion as the lab scale numerical study, the convergence of the transient turbine solution was assured by monitoring power coefficient. A mean power coefficient was calculated after each full rotation and divided by the previous rotation mean to give a percentage delta, as shown in equation 5.3. Figure 6-6 shows both the $\overline{C_P}$ and the convergence indicator $\triangle\overline{C_P}$ values plotted against rotation count in the upper and lower plots respectively. Notice that there are two lengths of solver run, this is because TSRs at whole numbers (2,3,4 and 5) were calculated first where it was found that after 6 revolutions $\triangle\overline{C_P}$ was below 1% and therefore the remaining runs were reduced to 6 rotations. The strategy reduced calculation times significantly although at a TSR of 4.5 only a $\triangle\overline{C_P}$ of 5% was reached, however, the was deemed acceptable given its agreement on all performance trends. The plots show that the higher the TSR the slower the transient convergence of the turbine. A probable cause of this trend is the increasing thrust, generated by an increasing TSR, forcing more of the flow to divert around turbine resulting in high flow velocity gradients along the numerical flume. These flows take longer to develop and hence would result in a slower convergence to a quasi-steady state both experimentally and numerically.

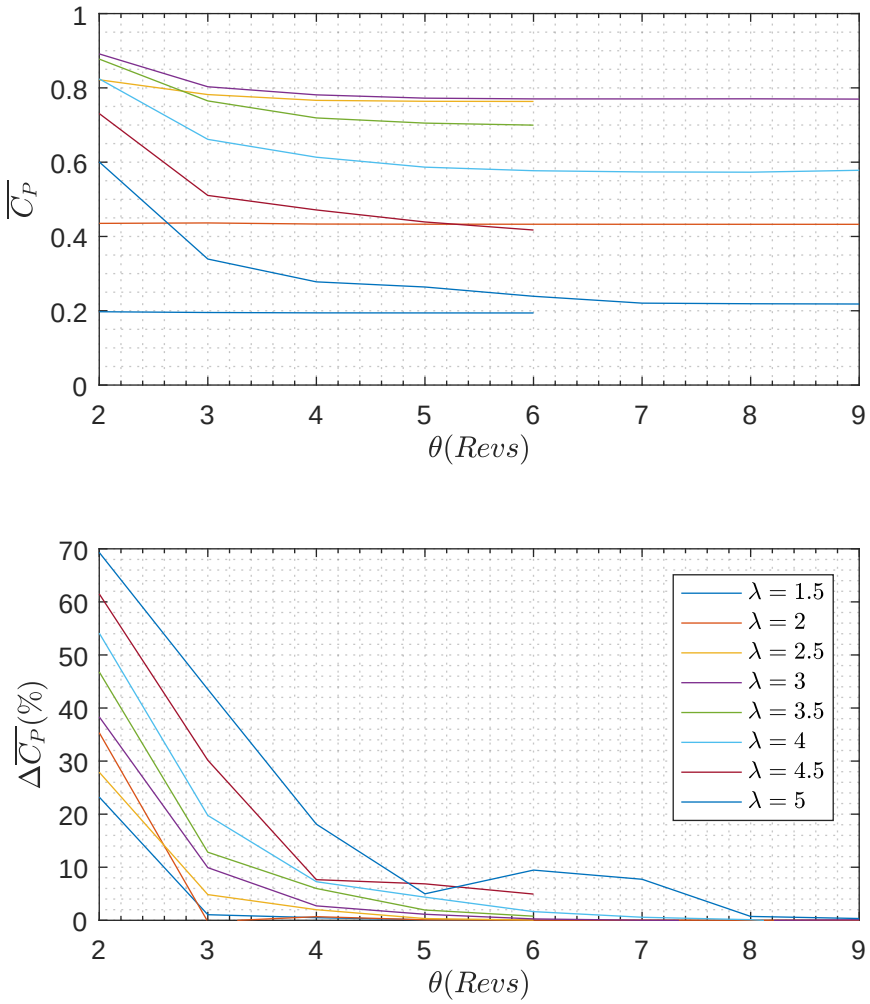

Figure 6-6: Plots depicting the transient convergence of mean power coefficient for TSRs of 1.5 to 5

6.3.2 Confirmation of y^+

A plot of maximum y^+ monitored at the turbine blade's surface is plotted in Figure 6-7 against azimuth angle. The result shows that all y^+ values fall between 5 and 27 with an average of approximately 17. As expected, the highest y^+ come from the highest TSR with all other results falling in order of TSR. The high blade chord Reynolds number of the large scale simulations were found to be more stable up to peak y^+ values of 30 in the isolated blade case, therefore the mesh can be kept constant for all test cases.

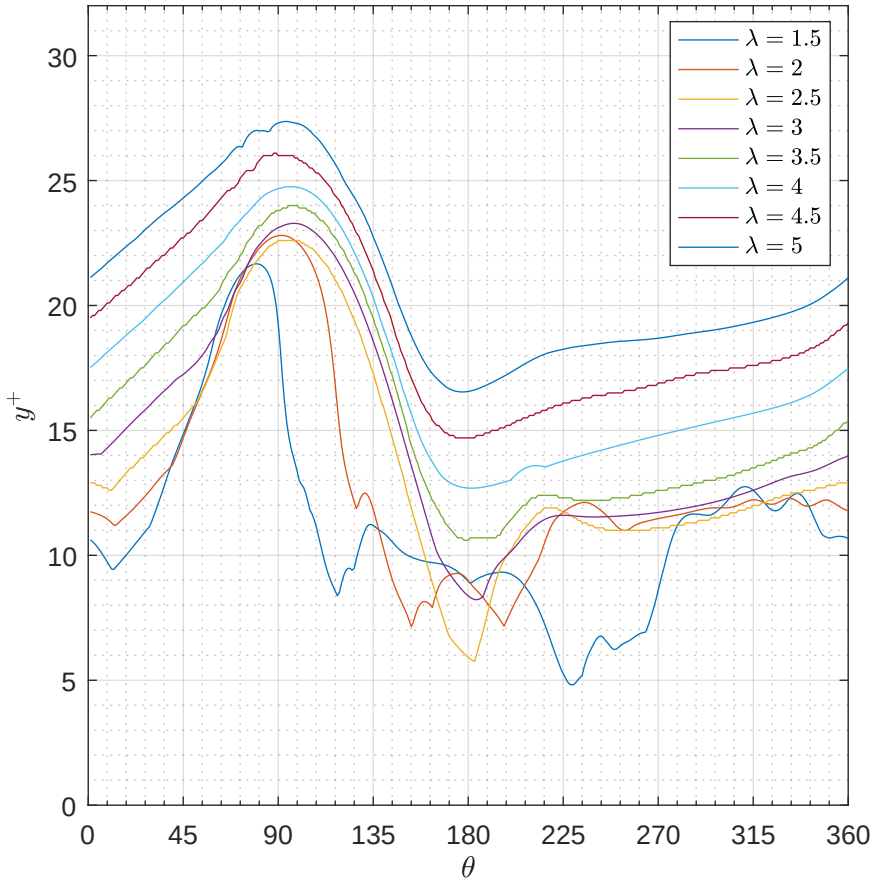

Figure 6-7: Plot of blade surface y^+ maximum vs azimuth angle for TSRs of 1.5 to 5

6.4 Results

6.4.1 Turbine Performance

Simulations were performed at TSRs from 1.5 to 5 at intervals of 0.5. Plots for mean coefficients of power, torque and thrust for all TSRs tested are presented in Figure 6-8. Evaluating the graph of $\overline{C_p}$, a clear shift from a lab scale peak at a λ of 4 (see Figure 5-14) to a peak between 2.5 and 3. This result is indicative of the increase in blade chord Reynolds number offering a delay in stall from an angle of attack of $\sim$ 12 up to $\sim$ 20. Another feature of the large scale $\overline{C_p}$ result is a dramatic drop in power at TSRs below 2.5, this would suggest heavy blade stall conditions at those speeds. The coefficient of torque displays a surprisingly linear rise up to and down from a TSR of 2.5 as TSR increases, something that was not seen in lab scale tests where changes were more progressive. The peak

value of 0.31 is approaching double that of the lab scale device confirming the trend found in the Reynolds scaling study in Section 5.6.2. Despite the increase in power found in the larger scale, the thrust coefficient remains at similar levels to that found in the lab scale test; the result is an increase in the power to thrust ratio. However, it should be noted that comparisons are made only in a qualitative manner as many elements of the turbine have changed, including non-cambered blades, uniform inflow and a reduced blockage.

To explore turbine performance further, instantaneous coefficients of power and torque are plotted in Figure 6-9 for all TSRs. The three bladed turbine configuration means that C_P and C_Q are repeated identically three times over a full rotation, therefore the plots include only a third of a full rotation (120°) to increase clarity. Starting with the low TSR results, 1.5 and 2, the source of the poor performance is visible in the plot of C_P where the output suffers from smaller peaks in both span and amplitude. Achieving the highest power output, TSRs of 2.5 and 3 include the highest peaks and are sinusoidal in nature ranging between a C_P of approximately 0.25 and 1.3. As TSR increases the traces remain sinusoidal but gradually shift downwards towards lower vales of C_P. It is noted that the troughs of C_P reduce much further than the loss in the peak.

Remembering that coefficient of torque for a cross flow turbine is defined as $C_Q = \frac{C_P}{\lambda}$, the visible transformation between power and torque becomes intuitive. The effect is a re-ordering of lowest TSRs resulting in a unblemished trend, as TSR increases peak torque decreases. Akin to the result of C_P, the two lowest TSRs are outliers displaying a significant deficit in the first 40° of rotation although they additionally have the largest ranges of output. The C_P traces of the remaining TSRs continue to be sinusoidal in shape but now include a shift that is uniform across the entire rotation and at consistent intervals of 0.1. These equally spaced shifts between TSRs are the source of the linear drop off in mean torque displayed in Figure 6-8.

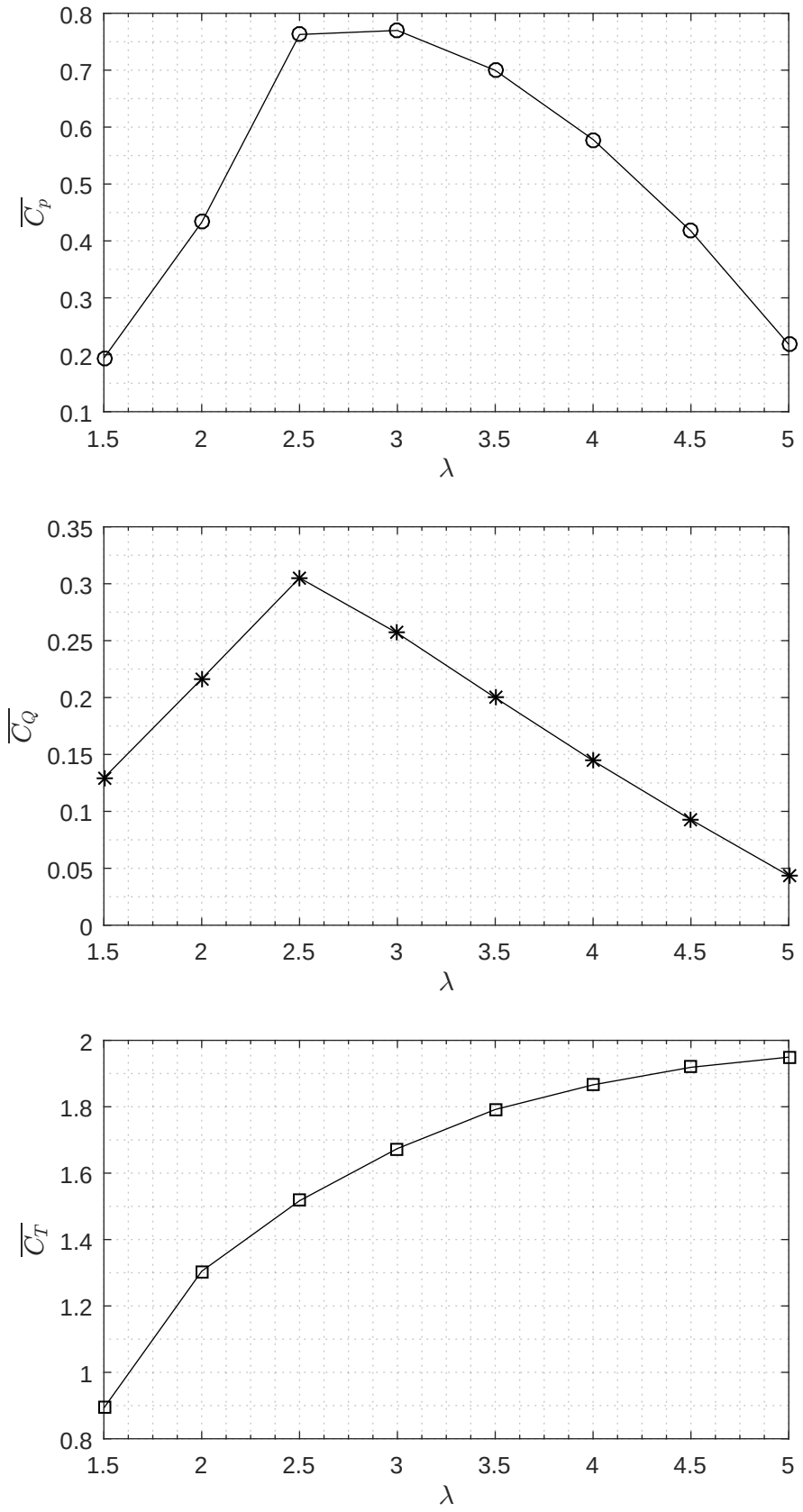

Figure 6-8: Plots of numerical results for mean coefficients versus TSR for; top: power, middle: torque, bottom: thrust

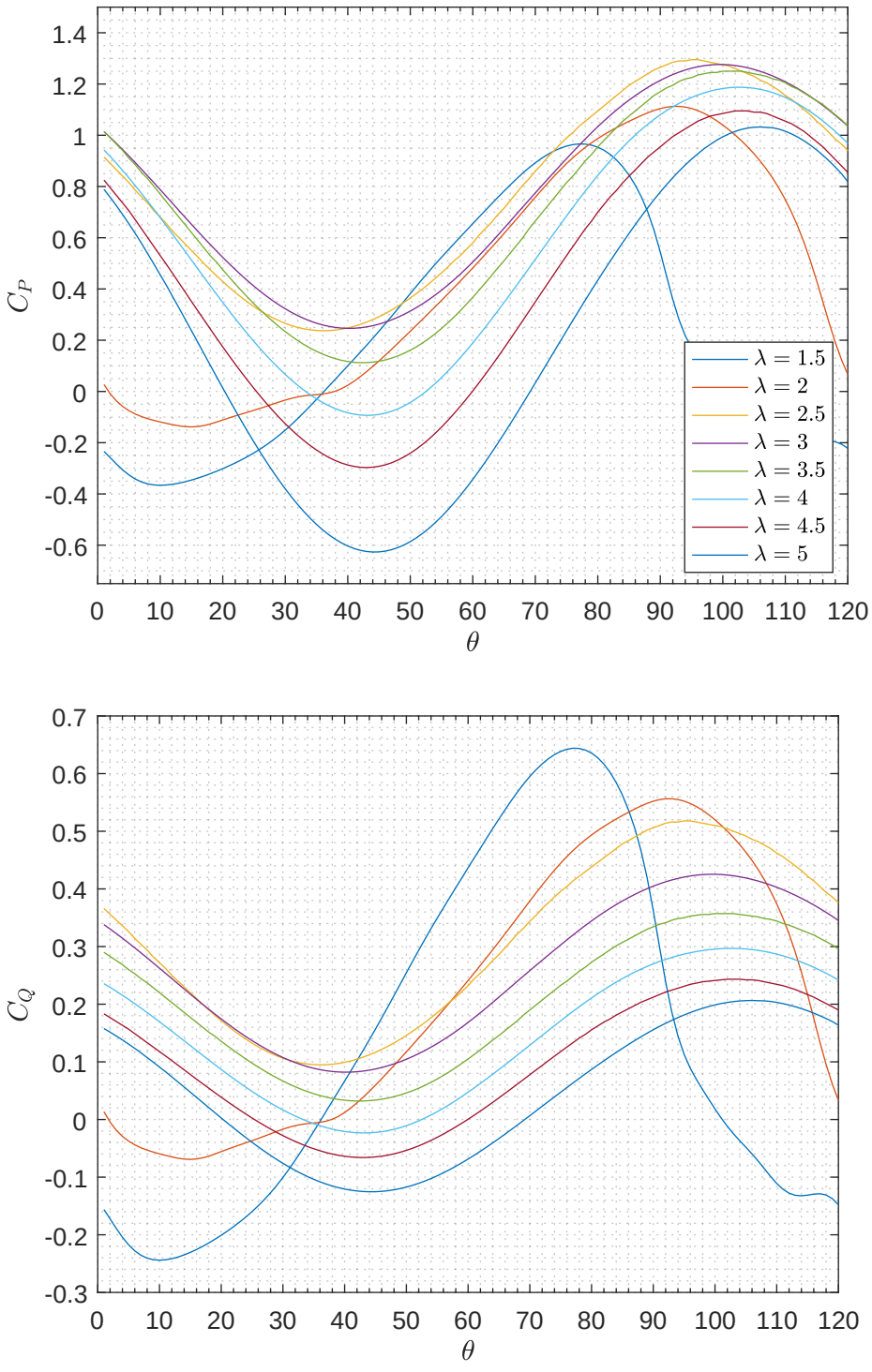

Figure 6-9: Plots of numerical results for transient coefficients versus azimuth angle for TSRs of 1.5 to 5; top: power, bottom: torque

6.4.2 Single Blade Analysis

6.4.2.1 Power and Torque

The contribution of an individual blade (identified by the subscript 'Blade') has been extracted and plotted in Figure 6-10. The plots display the values of power and torque coefficient over time for a full rotation of the turbine. Note that in the range 0°-180° the blade is travelling across the upstream side of the turbine and between 180°-360° the blade in travelling downstream, these terms are used to identify the stated ranges herein. Examining the traces of $C_{P_{Blade}}$, two major features are observed, upstream the peak power increases as TSR increases, and conversely, downstream power decreases as TSR increases. Furthermore, the upstream $C_{P_{Blade}}$ values are all positive, adding power to the turbine, while downstream $C_{P_{Blade}}$ values for all tips speed ratios above 2.5 are increasingly negative. The coefficient of torque, $C_{T_{Blade}}$, displays a reverse order of performance with the highest torque achieved by lowest TSRs and the lowest torque from the highest TSRs (with the exception of $\lambda = 1.5$). These behaviours differ from the full turbine plots shown in Figure 6-9 indicating the effect made by summing three blades.

Expanding on the trends associated with amplitude, the width of the peaks and troughs are key to the average contribution of a blade. The width can be seen as a form of 'duty cycle', inputting and extracting torque over the rotation of the turbine. The duty cycle of upstream power generation in the plot of $C_{P_{Blade}}$ where the upstream peak is seen to gradually widen as TSR increases. Downstream, almost all TSRs are roughly a flat line, either adding a small amount of power at low TSRs, or subtracting power for higher TSRs over the entire 180°-360° range. This observation is embodied in Figure 6-11 where mean coefficients of power and torque have been individually calculated for upstream and downstream ranges and plotted against TSR. The plots clarify the contribution of upstream and downstream blade trajectories, the upstream contributing almost all of the driving torque, $\overline{C_{Q_{Blade}}}$, and the downstream costing an increasing amount of torque as TSR increases. Up to a TSR of 2.5, both upstream and downstream paths contribute positively to turbine toque, above this TSR torque diminishes both upstream and downstream. When rotational velocity is included to get mean power coefficient, $\overline{C_{P_{Blade}}}$, the upstream output continually increases up to a TSR of 4. 5, however, this is more than offset by a steep linear increase in power loss from the downstream rotation.

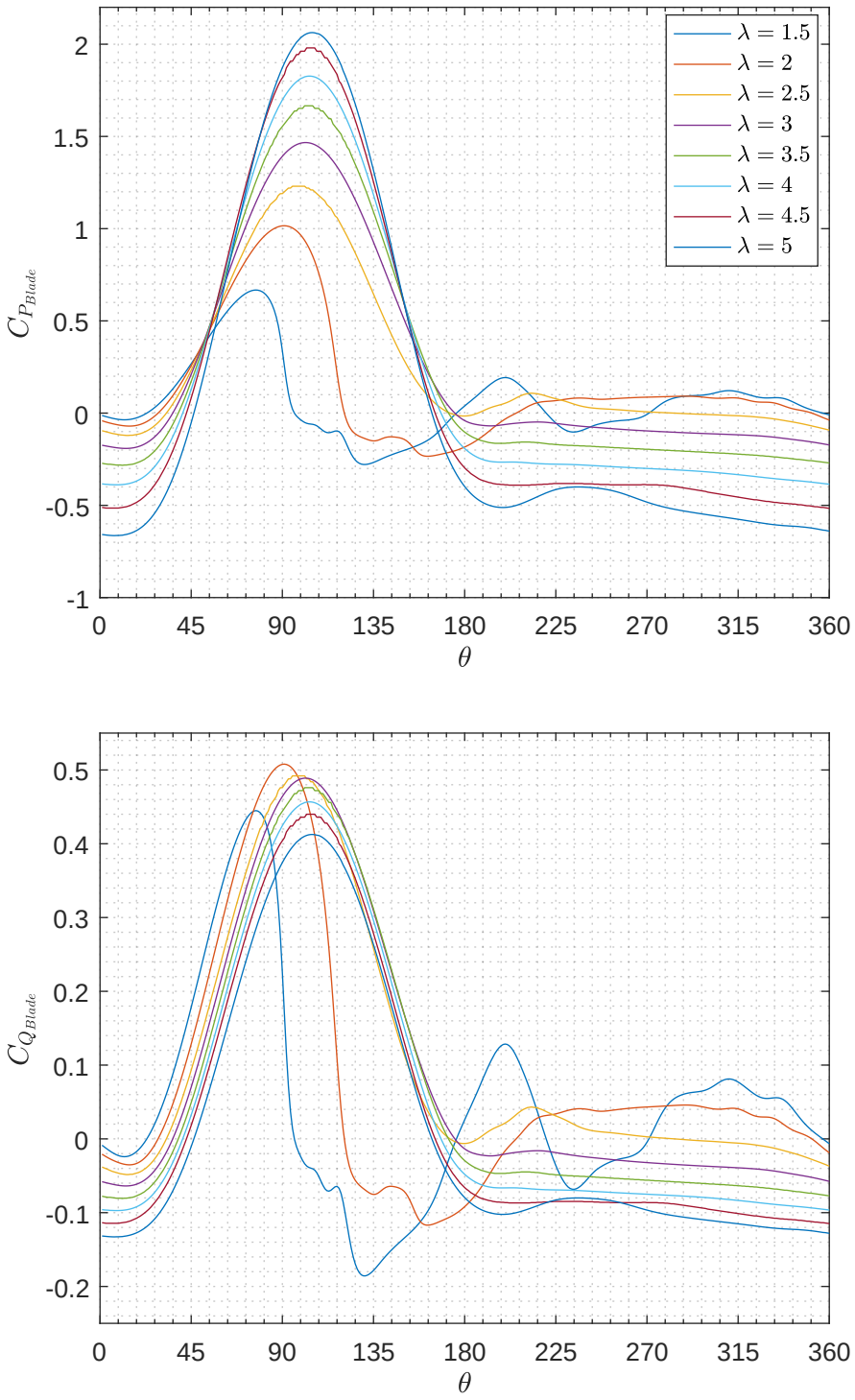

Figure 6-10: Plots of numerical results for transient blade coefficients versus azimuth angle for TSRs of 1.5 to 5; top: power, bottom: torque

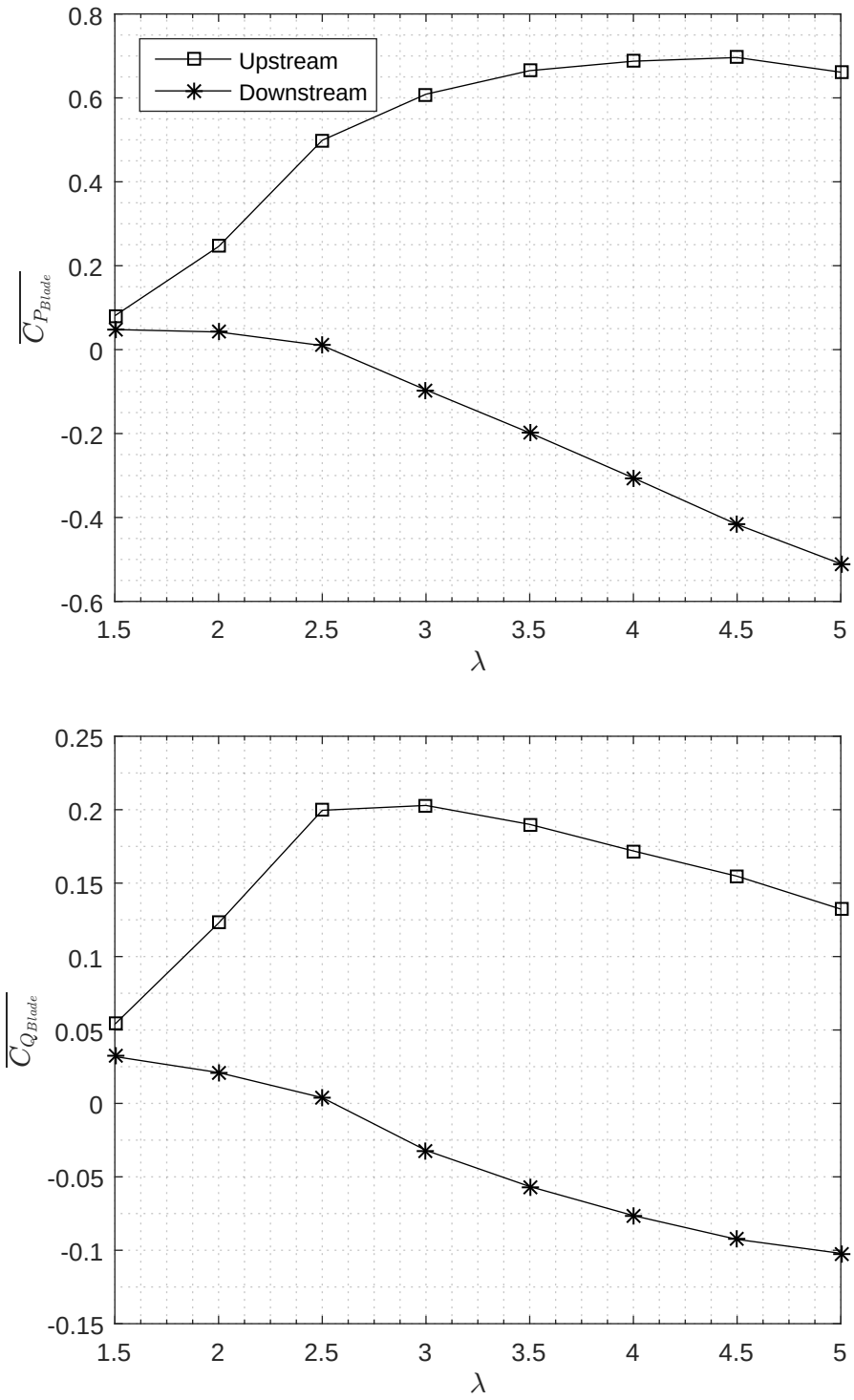

Figure 6-11: Plots of single blade mean coefficients vs TSR; top: power, bottom: torque

6.4.2.2 Normal Load and Pitching Moment

The coefficient of normal load C_N, as plotted for the lab scale turbine in Section 5.6.1, is presented in Figure 6-12 for all tested TSRs; note that positive values indicate a load acting radially outwards and a negative radially inwards. The traces show progressively higher negative values of normal load coefficient as TSR is increased across the full rotation of the turbine. The shape and order of the data is similar (but with a negative sign) to the blade coefficient of power plot in Figure 6-10. This correlation is logical as a higher power output is generated by a greater pressure differential across the blade and hence a higher load would be expected. The radially inward force developed on the upstream side (negative C_N) is expected as the angle of attack would result in the inward facing surface of the blade to be the low pressure side. By the same logic, the downstream half of the rotation would be expected to produce a positive C_N as found in the lab scale turbine. However, only the three lowest TSRs creep into positive values with all higher TSRs remaining negative. The reason for this characteristic is explored henceforth.

The coefficient of pitching moment, C_M, of the blade about its axis (also the blade domain axis) is plotted for all tested TSRs in Figure 6-13. The axis has been located at its aerodynamic centre, a 1/4 chord from the leading edge; note that positive values are anticlockwise. Wind and tidal cross flow turbines are often mounted to a structure at the 1/4 chord position as it is theoretically the point of constant moment where $\frac{\delta C_M}{\delta C_L} = 0$. However, the relationship is true in only ideal conditions which is not the case in the turbine. For TSRs of 1.5 and 2 a rapid drop in pitching moment occurs between 70° and 180° followed by an oscillation, this behaviour is an indication of dynamic stall. The remaining TSRs display the same characteristic shape which are offset by a progressively higher clockwise moment as TSR increases.

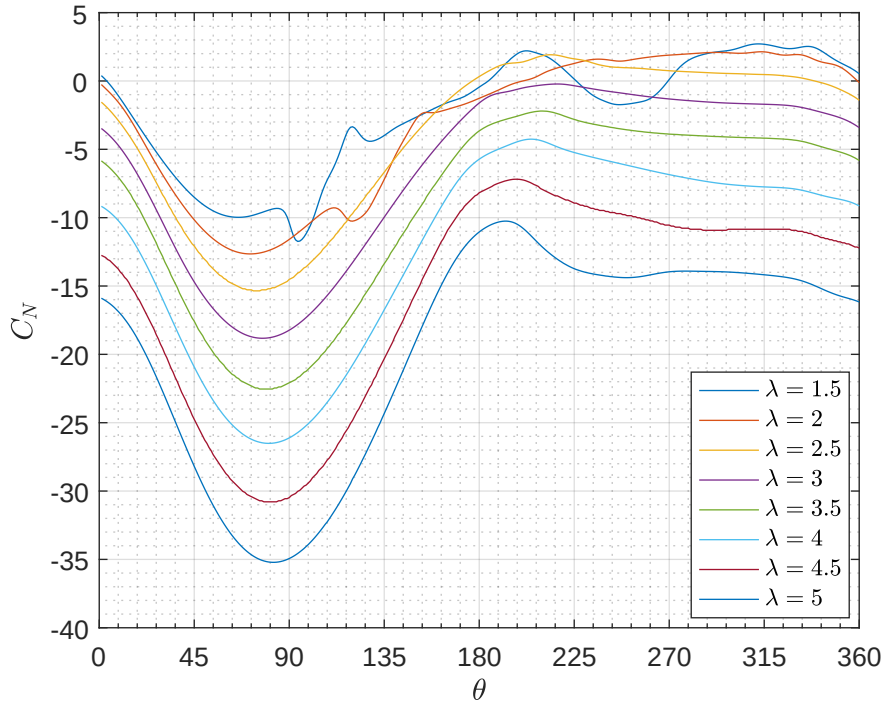

Figure 6-12: Plot of normal load coefficient versus azimuth angle for tip for TSRs of 1.5 to 5

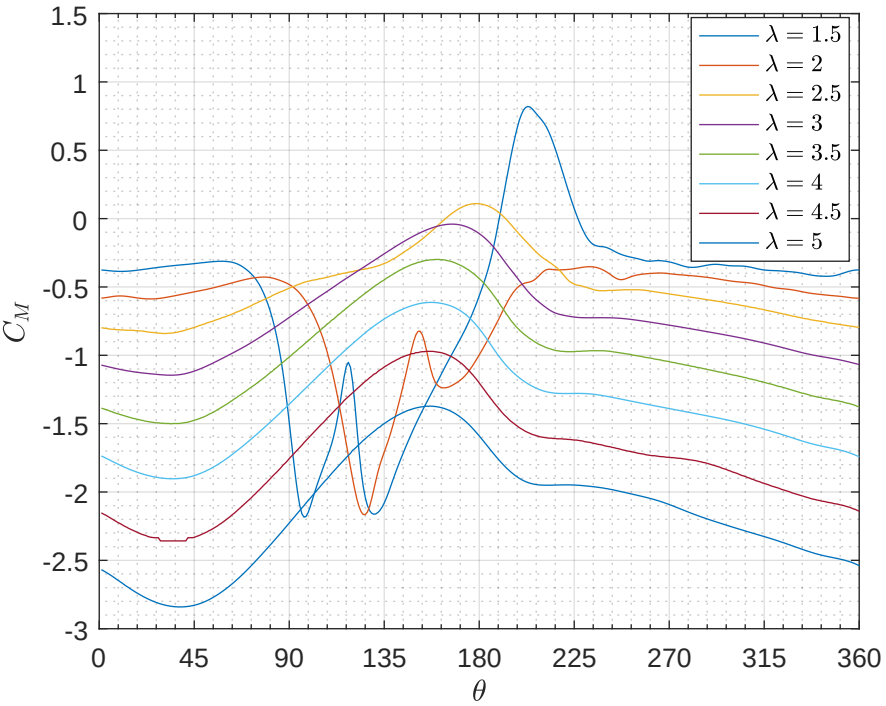

Figure 6-13: Plot of coefficient of pitching moment versus azimuth angle for tip for TSRs of 1.5 to 5

The behaviour of the coefficients of normal load and pitching moment are verified by Figure 6-14 in which static pressure is depicted using a contour plot. The plot shows a cropped view of the turbine blades at the 0°, 120° and 240° azimuthal positions, with 0° vertically upwards and θ increasing in an anticlockwise direction, as shown in Figure 3-3. The pressure contour range has been curtailed at the upper and lower extremities to highlight pressure differentials at the blades surfaces and therefore do not represent the absolute maximum and minimum of the simulations. With flow travelling from left to right, the blade at the 120° position displays a clear low pressure region on the downstream side and a corresponding positive pressure on the upstream side which grows with TSR. In addition, at a TSR of 2 vortices are visible downstream of approximately the 140° position, this is consistent with the hypothesis of dynamic stall indicated by the sudden recovery of normal load and shift in coefficient of moment. Remembering that the blade is pitching about the 1/4 chord position and hence greater leverage is afforded to pressure differential at the trailing end of the blade, the continually negative (clockwise) coefficient of pitching moment is also qualified by the spread of negative pressure extending across most of the blade for TSRs of 2 and 4, and less so for a a TSR of 3 This qualitative analysis matches the trend in Figure 6-13 where TSRs of 2 and 4 are a C_M of approximately -2 and -1 respectively, and only -0.25 a TSR of 3.

For blades at azimuthal positions of 0° and 240° an increasing negative pressure is visible on the radially inward surface. In particular, at 240° the observation is counter intuitive to the zero loss resolution of velocity vectors, and hence angle of attack shown in Figure 3-4, acting on the blades. The explanation is the presence of the virtual camber effect, detailed in Section 3.3.1, which results in the blade being perceived as a cambered aerofoil with the lifting surface on the radially inboard side. The effect is more pronounced toward the rear of the blade as the distance of the trailing edge from the tangential mounting point at the 1/4 chord is further that the leading edge. The result is that the pressure distribution is shifted further backwards toward the trailing edge that would normally be seen from an angled blade in straight flow. A combination of these factors justifies the radially inward normal loads and the negative pitching moment recorded from the computation. Comparing the TSRs, the negative pressure strength acting on the blades at the 0° and 240° positions is visibly increasing with TSR, this confirms the trend shown in Figure 6-12. The reason for this increase is revealed when analysing the channel velocity.

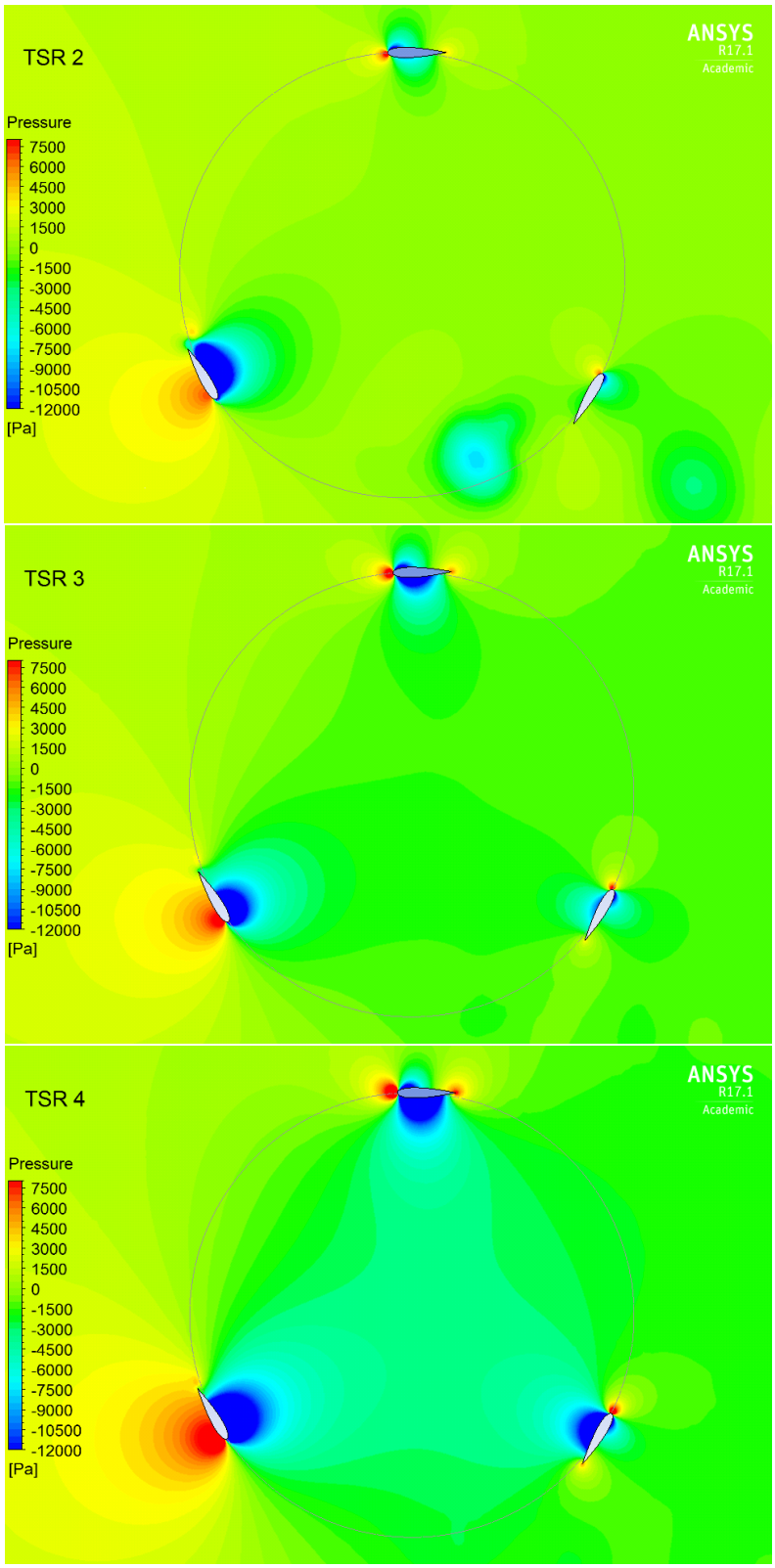

Figure 6-14: Contour plots of static pressure for TSRs of 2,3 and 4.

6.4.3 Channel Velocity

Samples of instantaneous velocity profile were taken from the final timestep of the numerical model. The data represents a sections of the numerical flume at turbine diameters (D) of 0.5, 1 and 2 upstream and downstream of the turbine as well as at the turbine centre, as shown in Figure 6-15. The results are displayed in Figures 6-16, 6-17 and 6-18 for TSRs of 2, 3 and 4 respectively (for all TSRs see appendix C.1). Note that the x-axis is fluid velocity, the y-axis is depth change from the turbine centre ($\triangle h$) and the dashed lines represent the limits of the turbine rotor. Focussing on the result at a TSR of 2, at 2 diameters upstream the flow is steady at 2m/s, at -1D the early initial effects of thrust are detected reducing the velocity at the vertical centreline by approximately 10%. Crucially, the velocity at the centreline, or '0' position, has reduced to ∼1.1m/s or 55% of the input velocity. Further downstream, at +1D and +2D additional velocity is lost suggest wake recovery occurs further downstream beyond the sample limits. As expected, the level of velocity deficit increases with TSR.

The consequence of the velocity deficit between upstream and downstream blade locations can be interpreted as a downstream increase in TSR, λ_{ds}. To highlight the effect of the deficit λ_{ds} has been calculated for velocities extracted from the centre of the turbine, i.e. sample line 'Center' and at $\triangle h = 0$. This sample point is typically at, or close to, the maximum velocity deficit for all TSRs and as such represents the extreme of the effect. The results of the sample calculation, given in Table 6.2, indicate that very large TSRs are generated and that the effect increases rapidly was TSR increases. At high TSR the blade does not achieve a useful angle of attack and acts as solely a drag source, when this is added to camber effect losses the total effect is significantly detrimental to achieving a high turbine performance at high TSRs.

λ	Center Velocity (m/s)	λ_{ds}
1.5	1.36	2.20
2	1.08	3.70
2.5	0.845	5.92
3	0.711	8.44
3.5	0.588	11.90
4	0.479	16.70
4.5	0.378	23.81
5	0.289	34.60

Table 6.2: Effective TSRs calculated from flow velocities taken from the centerline (depth and turbine wise)

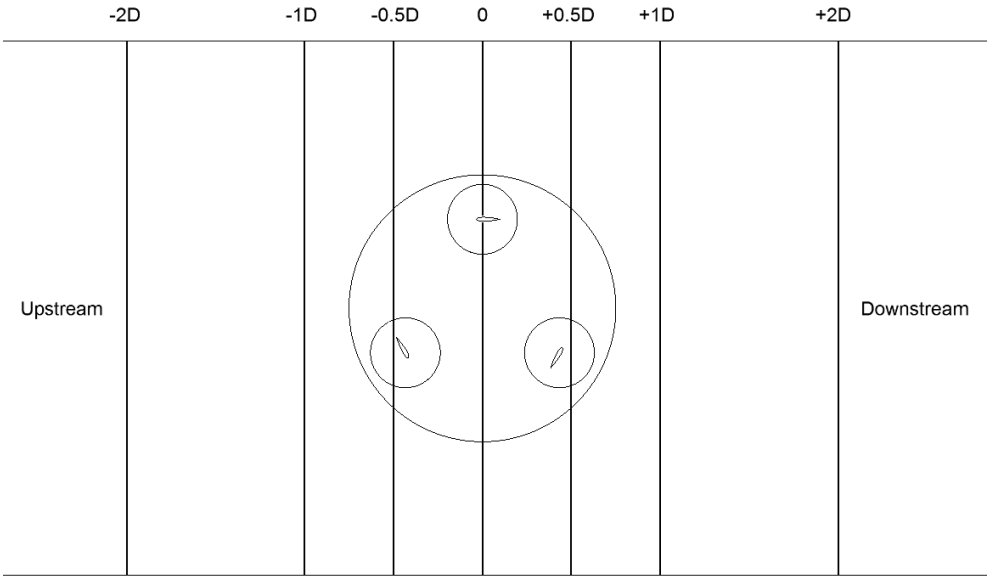

Figure 6-15: Diagram of channel velocity sample lines

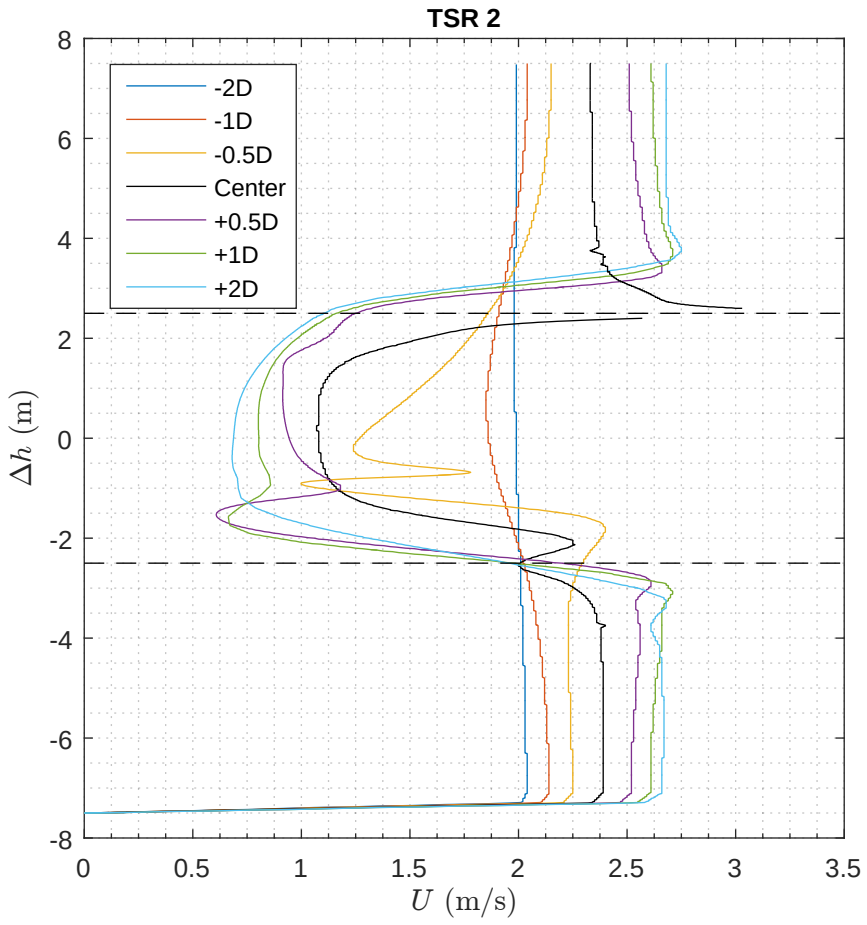

Figure 6-16: Numerical flume velocities profiles with depth at a TSR of 2

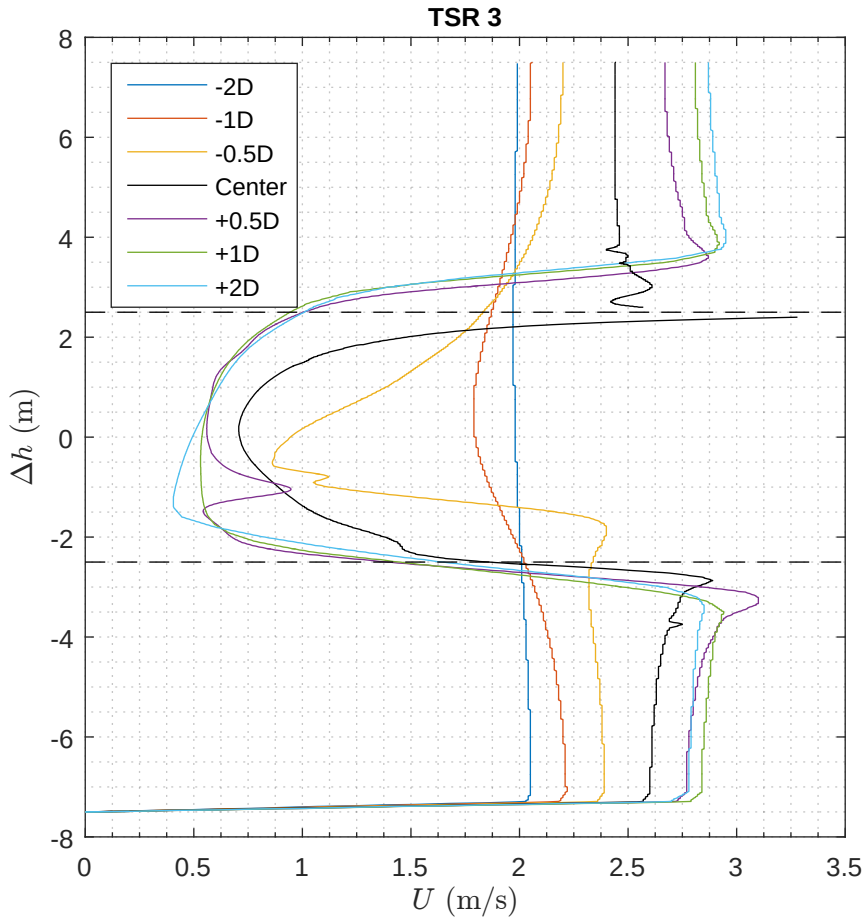

Figure 6-17: Numerical flume velocities profiles with depth at a TSR of 3

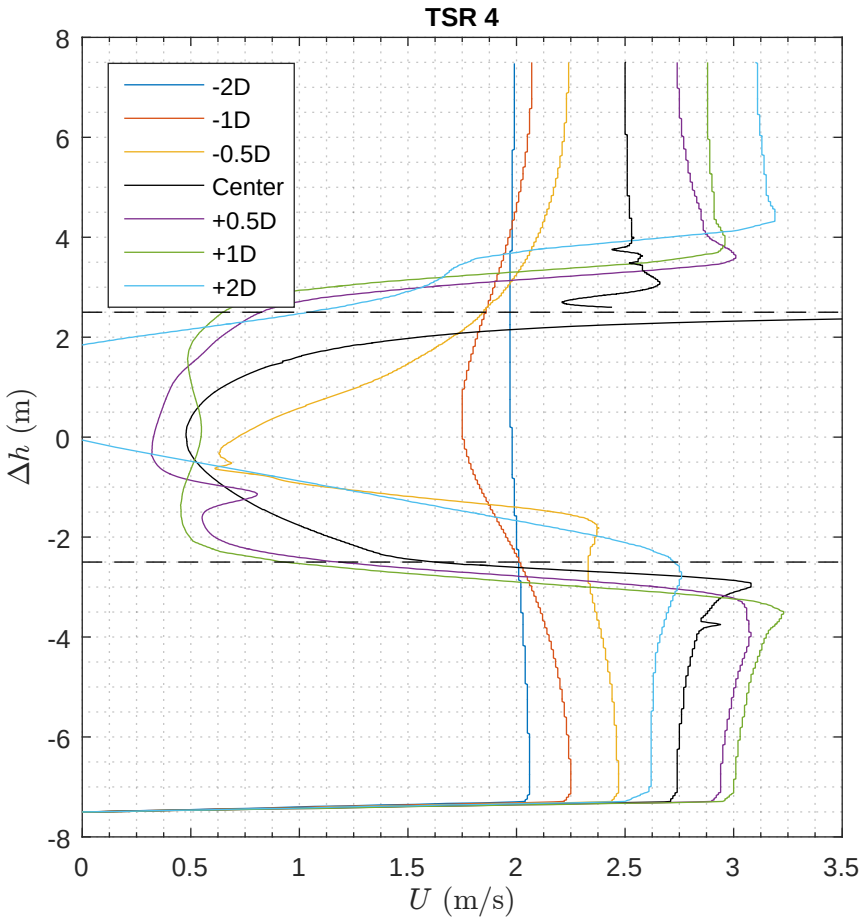

Figure 6-18: Numerical flume velocities profiles with depth at a TSR of 4

6.4.4 Local Sampling

The results from local sampling are presented in this section for points a, b, c and d, representing 1/2, 1/4, 3/4 and 1 chord length in advance of the leading edge respectively, see Figure 6-4. Due to the large quantity of data, results at TSRs or 2, 3 and 4 have been selected for presentation in this chapter, see Figures 6-19, 6-20 and 6-21, the full set of results is available in appendix C.2. The upper plot in each Figure includes local angle or attack (α_{local}) for all sample points alongside 'ideal' α where zero losses are assumed, see equation 3.4. A stall angle has been included which has been set at 17°, a value extracted from the high Reynolds number case ($Re \sim 3 \times 10^6$) reported in Section 4.4.1. This stall angle represents a conservative value of the expected stall angle based on an operating Reynolds number range of $Re \sim 2 \times 10^6$ to $Re \sim 6 \times 10^6$ for the large scale turbine tests. In the middle plot the coefficient of torque for sampled blade, $C_{Q_{Blade}}$, has been plotted, this has been included to enable a cross examination peak and troughs with α_{local}. Finally, the lower plot displays local velocity (U_{local}) for all sample points plus a zero loss velocity line from equation 3.2.

Examining α_{local} the most notable feature is a drop in the angle of attack achieved along the downstream half of the rotation when compared to the zero loss ideal curve. This failure to achieve an angle of attack in the downstream half is exactly as expected and is a direct result of the velocity deficit caused by the upstream energy extraction. The reduced angle of attack is exaggerated as TSR increases, again this correlates with the increasing velocity deficit with TSR. Upstream, results for all TSRs display the same trend, the closer a sample point is to the leading edge of the blade the higher the predicted angle. Secondly, all sample points are qualitatively very similar in form achieving peak and trough maxima and minima at almost identical θ angles. In terms of amplitude, the difference between the closest sample point 'a' and the furthest 'd' is significant, with the closest point predicting an angle approximately double the furthest. The rapid increase in peak α_{local}, particularly sample point 'a', can be attributed to the beginning of the flow bending around the blade itself. It's difference from the 'ideal' prediction is vast which brings its accuracy into question, particularly in the upstream part of the rotation where the ideal curve should be reasonably representative as the flow has not been perturbed by the blades prior to the interaction. In order to establish which sample point may be most representative of the turbine blade's effective angle of attack it is possible to cross-reference the peak torque, shown in middle plot of each figure, with α_{local} to see if the beginning of blade stall correlates to the 17° expected from the static simulations. Applying this method to the upstream peak of $C_{Q_{Blade}}$ on the TSR 2 result the peak occurs at a θ of 91°, this correlates to sample α_{local} values of a=47°, b=37°, c=33°, d=30°. These angles of attack are all higher that the 17° originally predicted to be blade stall and hence the point at which blade torque

would begin to drop. Potential explanations for this behaviour include a dynamic stall condition which may extend useful lift beyond a conventional angle of that the sample angles are prone to error themselves. However, repeating the exercise for the result at a TSR of 3, the peak is significantly closer, where peak $C_{Q_{Blade}}$ correlates to a sample point angle 'd'=20°. Conducting this on the remaining TSRs sampling point 'd' is consistently closest to the expected 17° stall point. Based on the cross-referencing method and in comparison with the ideal case, sample point 'd', or 1 chord length ahead of the turbine blade, could be judged as the most promising position to deliver a representative local angle of attack.

The prediction of local velocity (U_{local}), the lower graph of each figure, displays a much closer agreement between all four sampling points. In addition, the general form of the velocity traces captured by the sampling points are common across all TSRs. The velocity predicted by the sampling is very similar to the ideal prediction for the upstream half of the rotation. At the 180° point all sample points predict a lower dip in velocity followed by a recovery around the 220°, which tails off and remains below the predicted ideal values for the remainder of the rotation. The dip corresponds to an increase in channel velocity around at the base of the turbine which occurs across all TSRs, see -0.5D on Figures 6-16 - 6-18. The deficit in velocity between ∼220° and 360° can be attributed to the bulk flow velocity loss highlighted in the channel analysis.

The analysis of the local sampling identifies location 'd' as being the most likely to be representative of the turbine blade's local flow conditions. Isolating sample point 'd', α_{local}, and U_{local}, are plotted for all TSRs in Figure 6-22. The plot of α_{local} shows the expected increasing peak angles of attack as TSR reduces. However, the traces vary sufficiently to conclude that a trivia non-dimensional collapse is not possible, particularly at low TSRs where the point of inflection begins to shift to a later angle of θ and the downstream exaggerated peaks. An alternative approximation of α_{local} is explored in the next chapter in which a velocity loss is subtracted from the downstream component of the 'ideal' local angle of attack. In contrast to α_{local}, local velocity U_{local} is predicted to be very similar in form across all TSRs with a consistent shift in absolute velocity equal to that calculated by the zero loss equation 3.2.

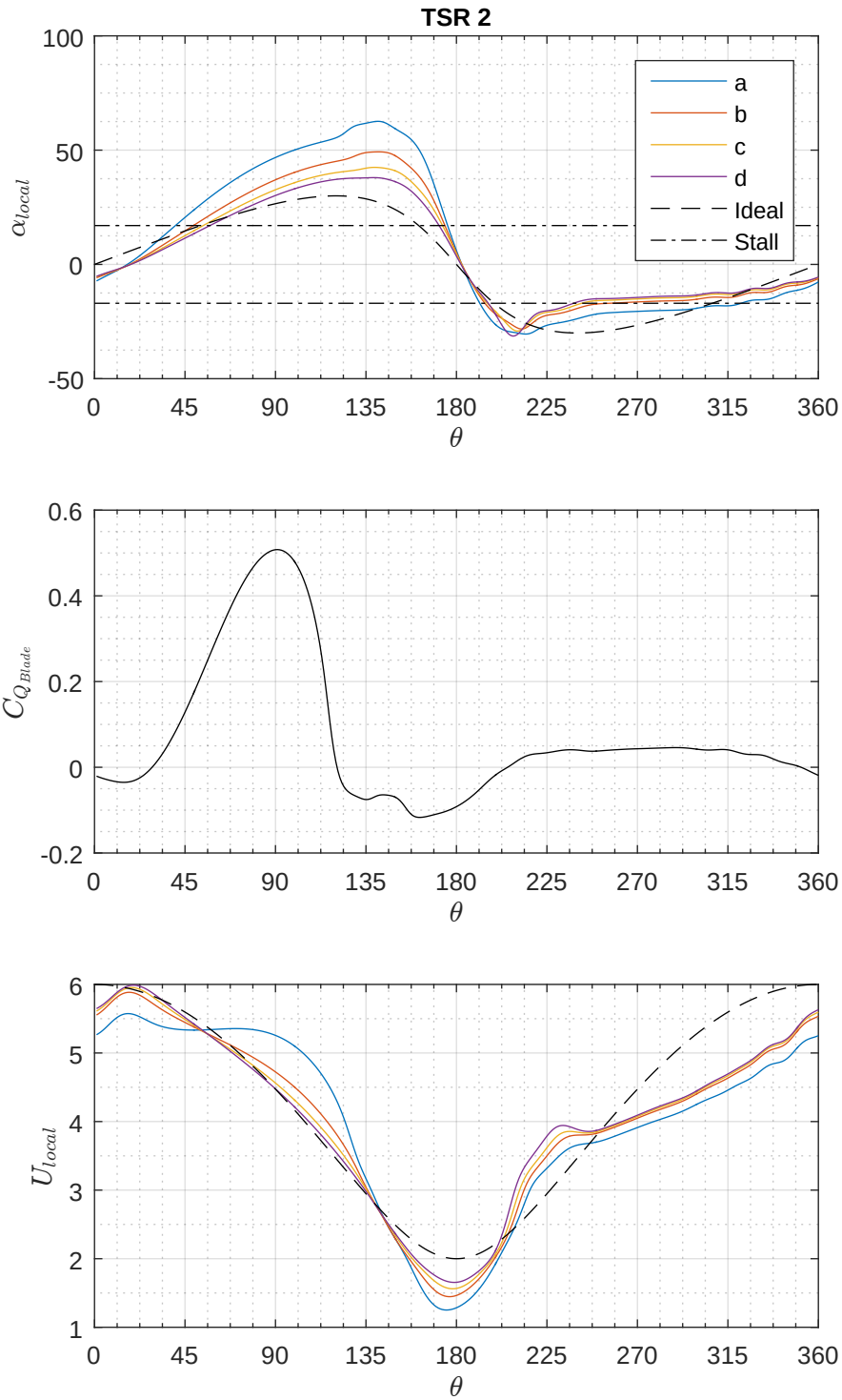

Figure 6-19: Graphs of sample point parameters versus azimuth angle for a single blade, including; top: local angle, middle: coefficient of torque, bottom: local velocity. TSR=2

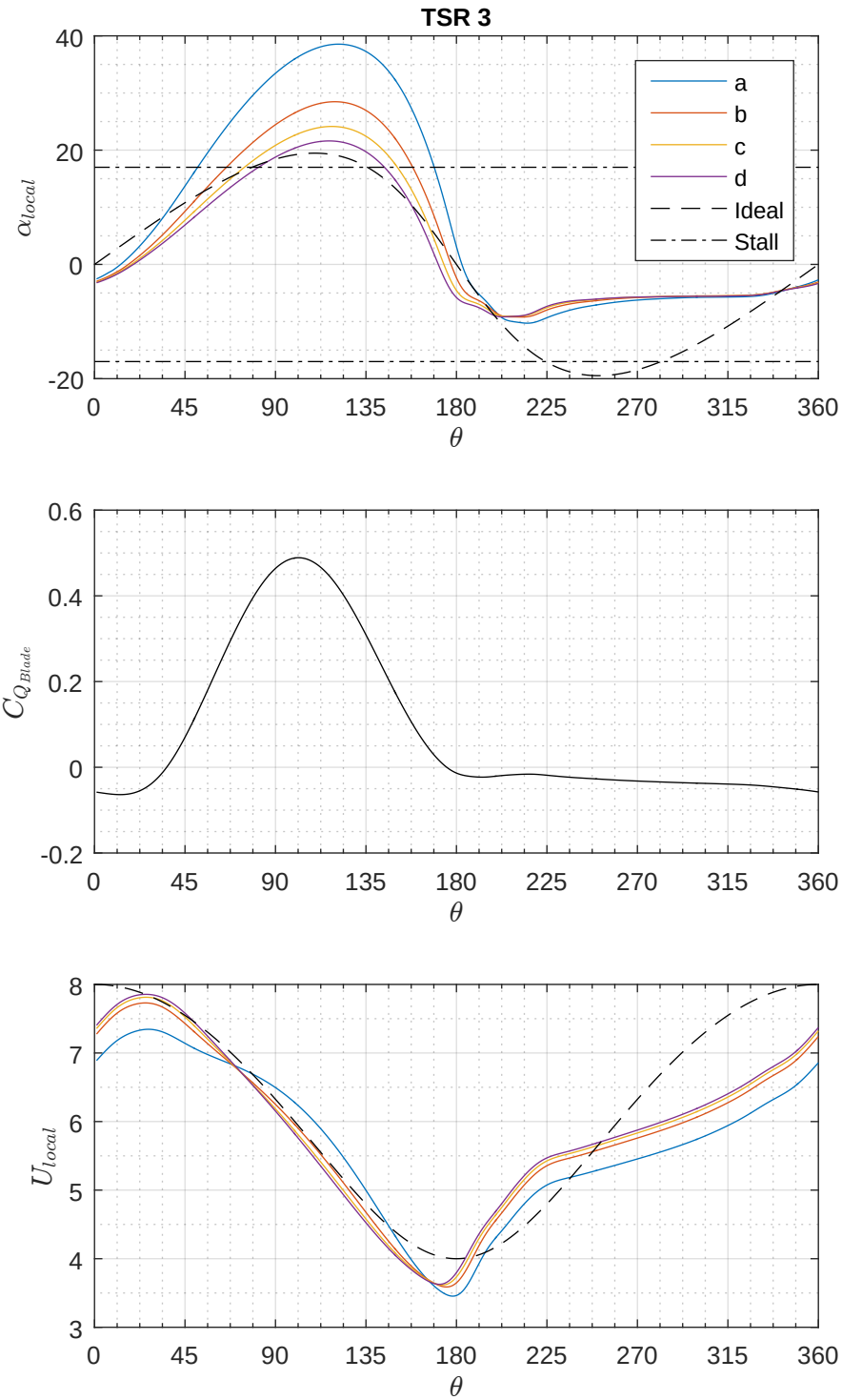

Figure 6-20: Graphs of sample point parameters versus azimuth angle for a single blade, including; top: local angle, middle: coefficient of torque, bottom: local velocity. TSR=3

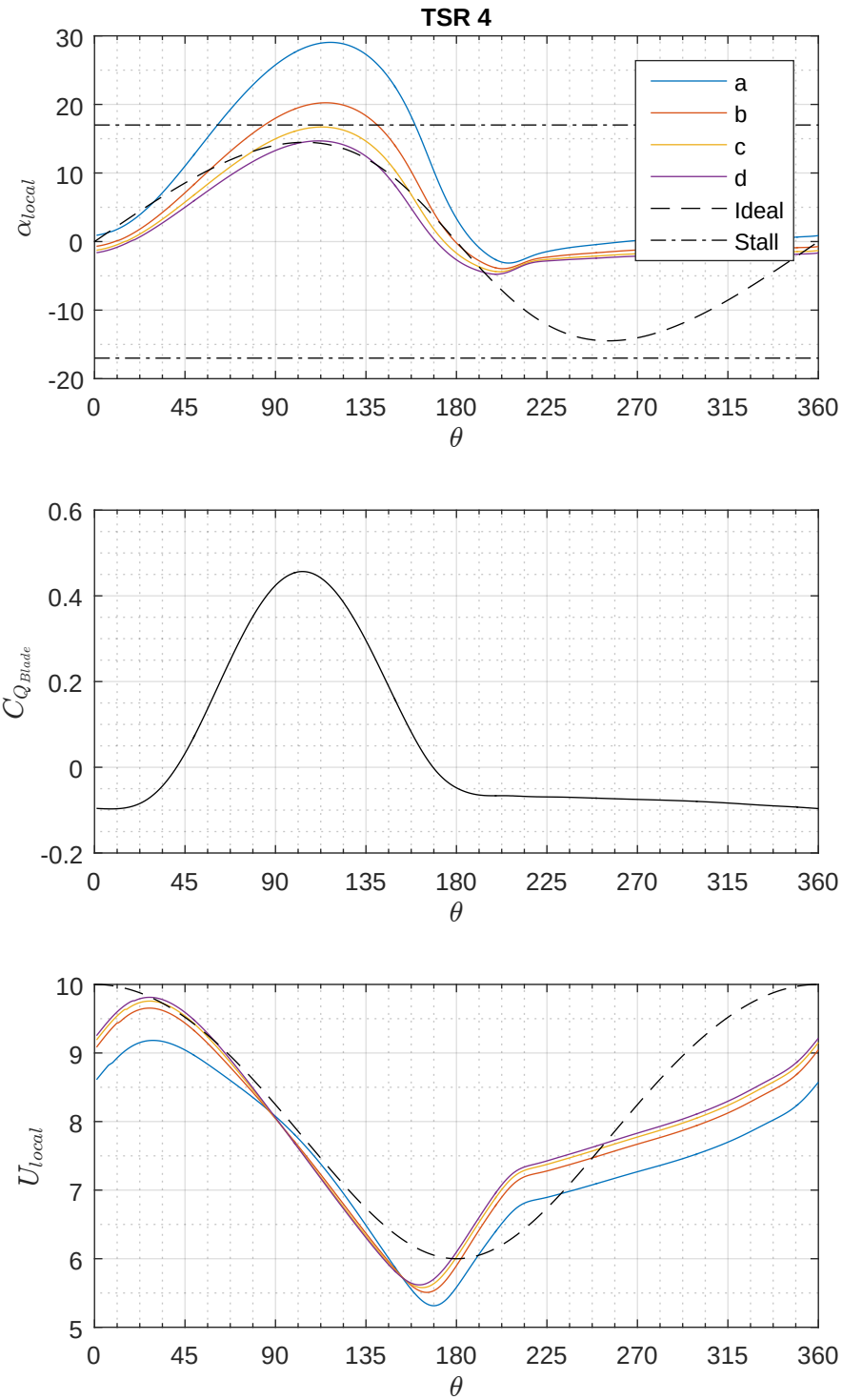

Figure 6-21: Graphs of sample point parameters versus azimuth angle for a single blade, including; top: local angle, middle: coefficient of torque, bottom: local velocity. TSR=4

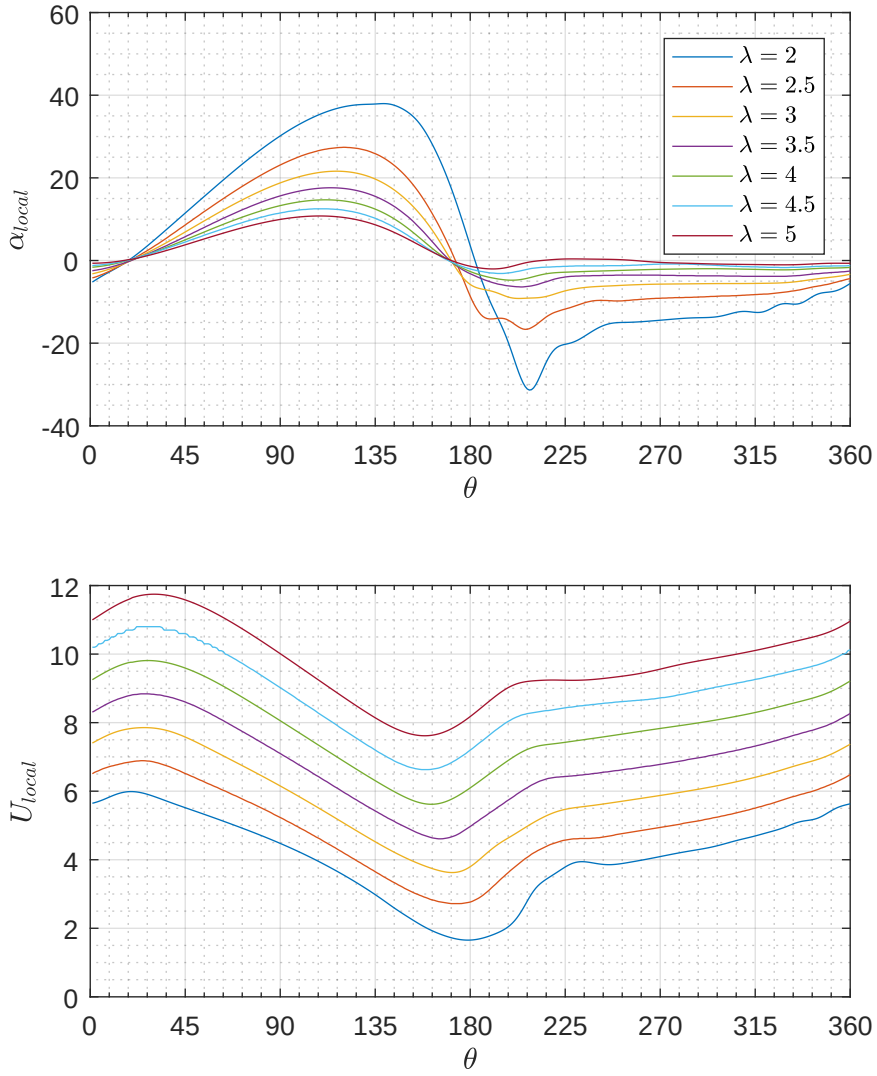

Figure 6-22: Graphs of local angle of attack and local velocity versus azimuth angle collected from sample point 'd' for TSRs of 2 to 5

6.5 Discussion

In this chapter the drivers of cross-flow turbine performance have been dissected in order to acquire an advanced understanding of the hydrodynamic effects taking place and to aid a subsequent optimisation scheme. The numerical accuracy was first confirmed in terms of transient variance and y^+ conformity. The transient result showed that for all but the lowest TSR, case convergence to <5% was achieved within 6 rotations at the higher timestep size ($\theta_{\Delta t}$) of 1°. Analysis of the subsequent results has led to the following findings:

- Peak power and torque occurs at lower TSRs than the small scale turbine, a feature of the shift in blade chord Reynolds number
- The peak torque of an individual blade is inversely proportional to TSR (with the exception of TSR=1.5), a trend which is reversed in order for the single blade coefficient of power. In addition, mean contributions of torque and power coefficient revealed that the upstream flight path of the blade is responsible for generating all of the power in most cases, with the downstream consuming increasing amounts of power as TSR is increased.
- Against expectations the normal load and pitching moment were constantly negative. The cause was a high virtual camber effect, exacerbated by the drop in flow velocity available to the downstream flight path.
- Analysis of the channel velocities revealed large deficits as the flow loses energy to the upstream blade pass. The significance of the loss was emphasised by the calculation of an effective downstream TSR, labelled λ_{ds} in Table 6.2, which displayed a disproportional increase with freestream TSR reaching a maximum $\lambda_{ds} \sim 35$. Using this example, the high downstream TSR means that a local angle of attack would barely reach 2° at its peak which is inadequate to generate any useful power and therefore the blade performance is dominated by the virtual camber effect.
- A novel local sampling method was used to capture angle of attack and velocity at a number of positions ahead of a turbine blade. The local angles and velocities acquired correlate well with the hydrodynamic behaviour evaluated in the preceding results. It was determined though cross-referencing that position 'd', 1 chord length ahead of the blade, was the most likely position to represent the true local flow conditions.

Evaluation of the turbine hydrodynamics has revealed many operational limitations. In the interests of performance improvement a few of these elements stand out. Most notably, high TSRs have proven to be problematic on a number of fronts, including high thrust and hence high loss in momentum between upstream and downstream blades, high susceptibility to virtual camber effect losses, no real advantage on torque fluctuation, all of which has lead to a low overall efficiency. While some of the issues may be improved by custom blade design, the fundamental thrust and downstream flux issues remain. At low TSRs many of the issues are reduced, however, the main drawback is that effective angles of attack exceed the stall angle of the blade. Given the evidence generated by this study, a turbine operating at low TSRs with an anti-stall pitching mechanism is the most attractive option for maximising efficiency and power output.

6.6 Conclusion

The numerical analysis in this chapter was conducted to explore a range of performance and situational characteristics of a turbine at commercial scale. The insight into turbine hydrodynamics provided by the study has led to the conclusion that lower tip speed ratios, between 1.5 and 3, present a greater opportunity for optimisation than those above this range. To achieve these gains it is envisaged that an anti-stall pitching mechanism will be implemented and therefore forms the topic of the next chapter. In addition to the general analysis a novel sampling method has been proposed and conducted in which an effective angle of attack and effective flow velocity, as it would be seen by a turbine blade, are captured using four points ahead of its leading edge. While the output of the novel sampling method are consistent with the available evidence, its accuracy and usefulness are not tested until the next chapter where it will be used to optimise an active pitch turbine alongside alternative methods.

Chapter 7

Active Pitch Control

SUMMARY: The opportunity to maximise the power extraction of a cross flow turbine by means of active blade pitching is the focus of this chapter. The large scale fixed pitch turbine analysed in Chapter 6 is used as a basis and benchmark for the study. Focussing on low tip speed ratios, two novel schemes are proposed, tested and optimised through a series of numerical tests. The premise of both blade pitching schemes is the prevention of blade stall by predicting and controlling the local flow angle experienced by the turbine blade.

7.1 Introduction

A numerical study of the large scale turbine has highlighted the potential for performance optimisation at low tip speed ratios. To pursue this region of interest, the method attempted in this chapter is the implementation of actively pitched blades in order to avoid stall and maintain peak lift whenever possible. The idea of variable pitch has existed since Darrieus' 1931 paper, with many interpretations having been explored in both industrial and academic fields. A number of proposed pitching strategies have been explored using numerical methods, as detailed in Section 3.4.3, with varying success. However, the proposed methods differ from the found literature by the extension of a derived anti-stall pitching control curve to include a downstream loss corrector. A second proposal is a novel custom pitching sequence developed from the newly gathered sample point data. The main objective of the study is to prove the validity of the two methods by quantifying performance gains and comparing with the baseline fixed-pitch case.

The study will consider the following active pitch regimes:

- Sinusoidal: a simple motion strategy selected for numerical environment development and preliminary testing
- α-limit: a pitching demand is calculated by assuming an ideal angle of attack plus a downstream loss corrector
- α_{local}-limit: a pitching demand is calculated directly from the local sampling result

The basis of active blade pitching is to rotate the blade about its axis (1/4 chord) toward the flow to reduce the angle of attack when required to both prevent stall and maximise lift. Figure 7-1 shows the sign convention where ψ is the active pitch angle measured from the tangent of the flight path.

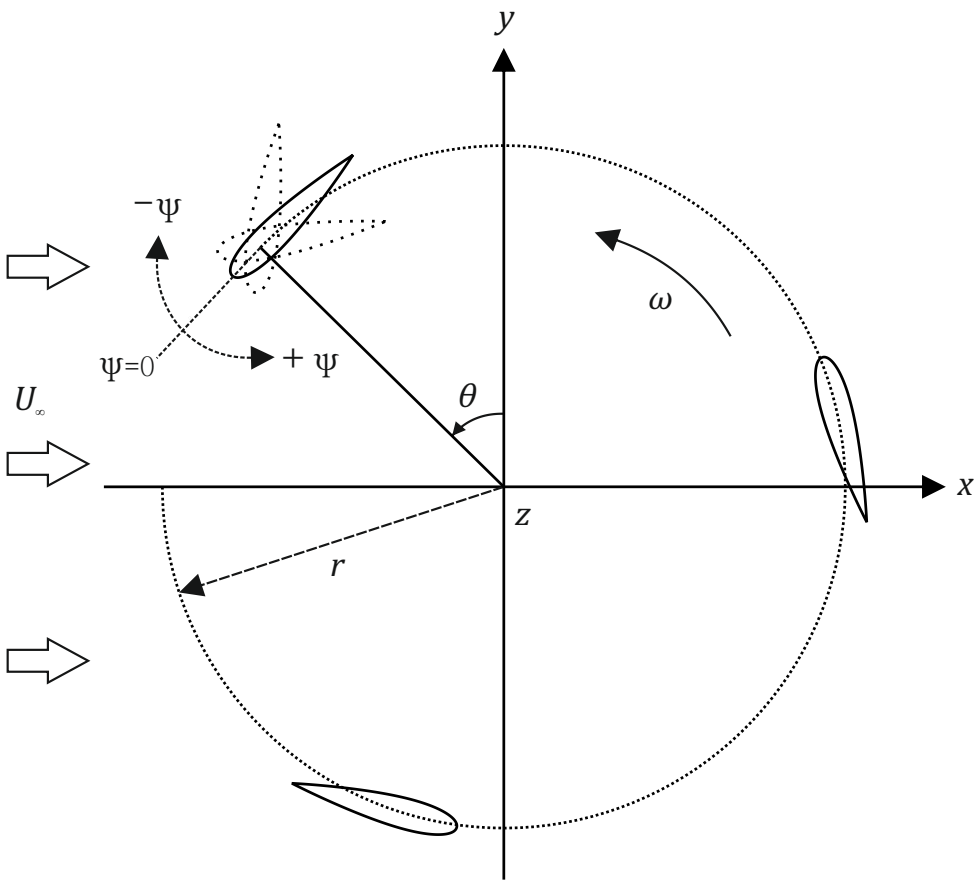

Figure 7-1: Diagram of active blade pitching sign convention

7.2 Active Pitch Regimes

7.2.1 Testing: Sinusoidal

A simple sinusoidal pitching motion aims to eliminate stall by pitching the blades towards the flow at both upstream and downstream locations. Although a gross simplification, the motion is easy to implement providing a suitable test scenario for developing and verifying the success of the numerical environment. The sinusoidal pitching regime was implemented using an equation directly in the solver equation language. A maximum pitch is set, ψ_{max}, resulting in a sinusoidal action calculated by equation 7.1.

$$\psi = sin\theta(-\psi_{max}) \tag{7.1}$$

7.2.2 α-limit

The principle of the α-limit method is to employ pitch control to achieve a limited maximum angle of attack perceived by the turbine blade at all positions on its orbit. Pitch control is calculated as the difference between a stall limit angle of attack, α_{lim}, and the derived angle of attack, α, for all azimuthal positions. The calculation is applied only to predicted angles above the stall limit with the remainder being set to zero. The calculation has to adapt to upstream and downstream positions where angle of attack switches from positive to negative. The calculation is given in equations 7.2 and 7.3, where the blade actuation demand angle is denoted ψ and the stall limit angle is α_{lim} (Matlab code available in appendix D.1). For this study α is assumed to be ideal and hence calculated by equation 3.4. Subtracting the predicted angle from the initial estimation results in a prediction of the effective angle, ξ, see equation 7.4.

$$Upstream: \ \psi = \alpha_{lim} - \alpha, \ for: \ \alpha > \alpha_{lim}, \ else: \psi = 0 \tag{7.2}$$

$$Downstream: \ \psi = -\alpha_{lim} - \alpha, \ for: \ \alpha < -\alpha_{lim}, \ else: \psi = 0 \tag{7.3}$$

$$\xi = \alpha - \psi \tag{7.4}$$

7.2.2.1 Downstream Loss

Chapter 6 highlighted the significance of the momentum loss between upstream and downstream blade paths. In order to account for this feature a reduced downstream flow is included by means of a percentage loss, designated by the symbol ϕ. The loss correction is implemented as a loss to the upstream velocity, i.e. if the upstream velocity is 2m/s, a ϕ of 40% would result in a downstream velocity of 1.2m/s ($2 \times (1 - 0.4)$). Equations 7.5 and 7.6 give the corrected angle of attack and resultant corrective demand angle respectively.

$$\alpha_\phi = tan^{-1} \frac{U_\infty(1-\phi)sin\theta}{U_\infty(1-\phi)cos\theta + U_t} \tag{7.5}$$

$$Downstream(loss): \ \psi = -\alpha_{lim} - \alpha_\phi, \ for: \ \alpha_\phi < -\alpha_{lim}, \ else: \psi = 0 \tag{7.6}$$

7.2.2.2 Smoothing

During a series of preliminary tests at pitch control in the numerical model it was discovered that the instantaneous acceleration of the blades at the start and end of pitching caused large power spikes, shown in Figure 7-2. The source of the issue was found to be sharp change in demand angle which was a characteristic of calculating the pitch directly in the solver equation language. To counter the problem a mathematical smoothing of the demand angle had to be included in the process, this resulted in the demand angles being pre-calculated in Matlab. The method of smoothing chosen was a moving average method; an example of the boundary handing is given in equation 7.7 for a value span of 5.

$$\begin{aligned}
&\psi_s(1) = \psi(1) \\
&\psi_s(2) = (\psi(1) + \psi(2) + \psi 3))/3 \\
&\psi_s(3) = (\psi(1) + \psi(2) + \psi(3) + \psi(4) + \psi(5))/5 \\
&\psi_s(4) = (\psi(2) + \psi(3) + \psi(4) + \psi(5) + \psi(6))/5 \\
&....
\end{aligned} \tag{7.7}$$

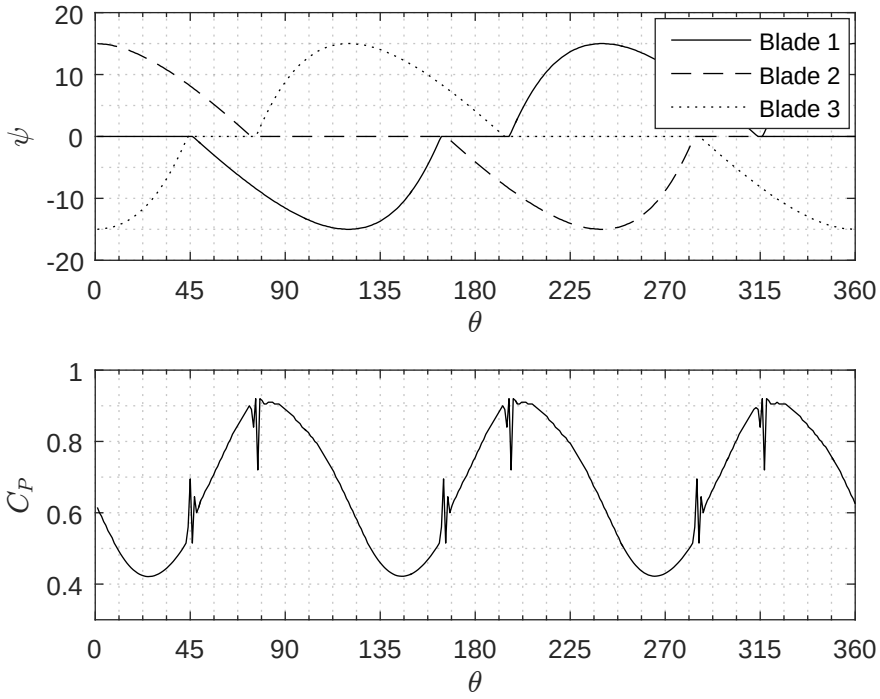

Figure 7-2: Graphs showing blade demand angle and coefficient of power spikes versus azimuth angle

7.2.2.3 Summary

Adding downstream loss to the α-limit method results in a number of predicted behaviours which are demonstrated in Figure 7-3. The plots show the effects of implementing a limit on angle of attack, governed by α_{lim}, and adding a downstream loss factor, ϕ. Three cases are presented, the first, included as a reference, is an unaltered prediction of α previously shown in Section 3.2 where zero pitch is demanded, $\psi = 0$, and therefore the resultant angles, ξ, are the same as α. For the second case α_{lim} has been set to 15°, note how blade pitch demand ψ is equal for both upstream and downstream ranges. The bottom plot, effective angle ξ, confirms the blade is now limited to the defined α_{lim} of 15° both upstream and downstream. The final pitching regime example adds a downstream loss of 30%. The effect is that a reduced α is predicted, resulting in a smaller demand ψ, and finally a narrowed peak on the resultant angle ξ. The number of combinations of these two factors, plus the variance of angle of attack, makes plotting all possibilities prohibitively excessive for illustration purposes. Instead, these relationships will be plotted just for specific instances in the results. Note that the mathematical smoothing of the demand angle has been implemented. The effect can be identified by the curved start and end to the demand angle plots which are not present in Figure 7-2.

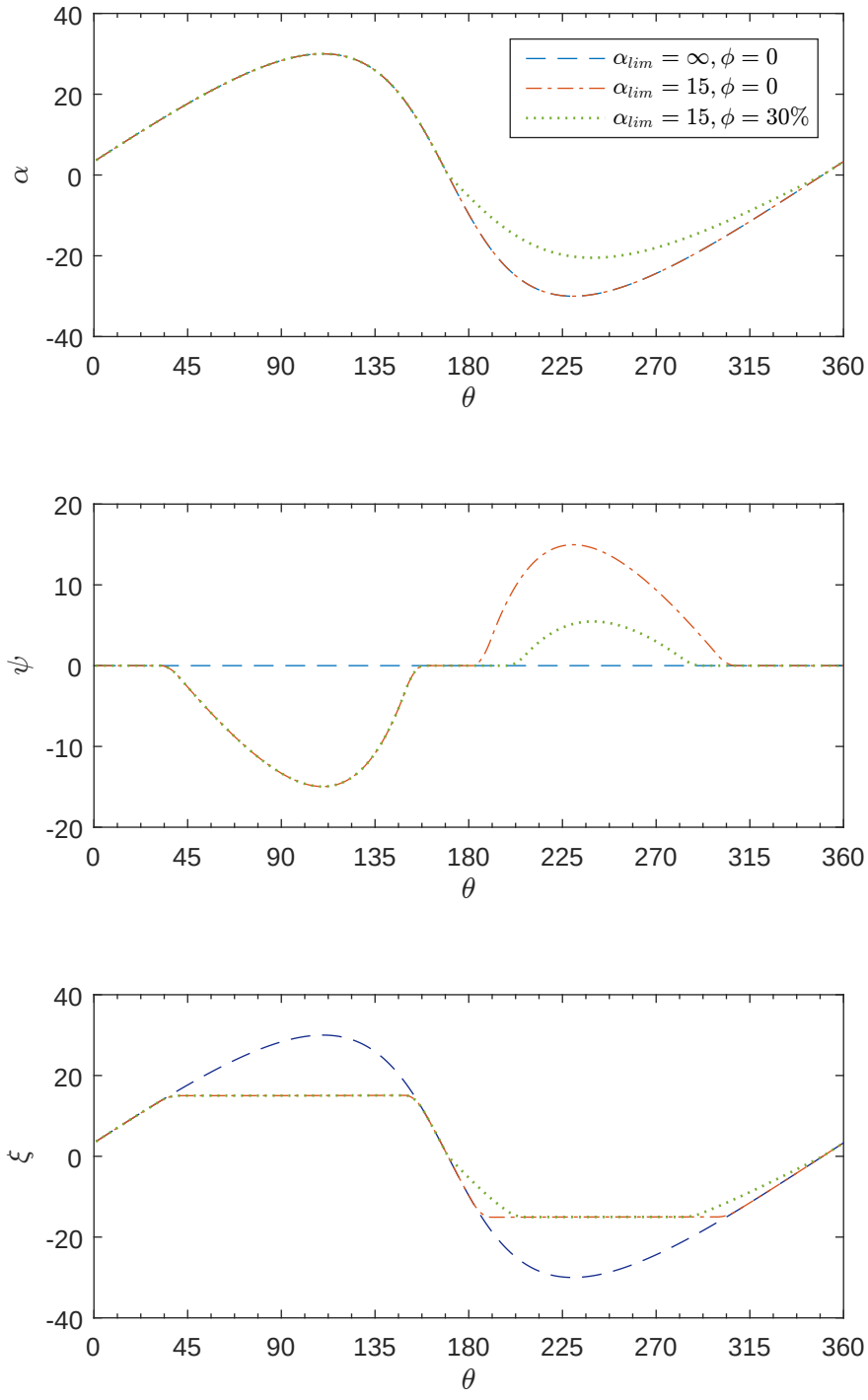

Figure 7-3: Graph of α-limit variables versus rotational position; top: zero loss angle of attack, middle: active blade pitch, bottom: resultant angle of attack

7.2.3 α_{local}- limit

As the name suggests, the proposed method is conceptually the same as the α-limit model, however, predicted angle α is replaced with the numerically sampled angle α_{local} which has been collected from the fixed pitch case. Mathematically, α is replaced with α_{local} in equations 7.2, 7.3 and 7.4. Downstream loss is not required as this is already included in the sampled angle, however, the demand angle still undergoes smoothing to avoid torque spikes. Figure 7-4 shows the generation of demand angles, ψ, from α_{local} taken from sample point 'd' (sample locations shown in Figure 6-4) . The example calculation is set to an α_{lim} of 17° which is reflected in the effective blade angle of attack, ξ. Notice that the plots are limited to a maximum TSR of 3.5, this is because above this ratio α_{local} does not exceed 17° and therefore pitching is not necessary to prevent stall.

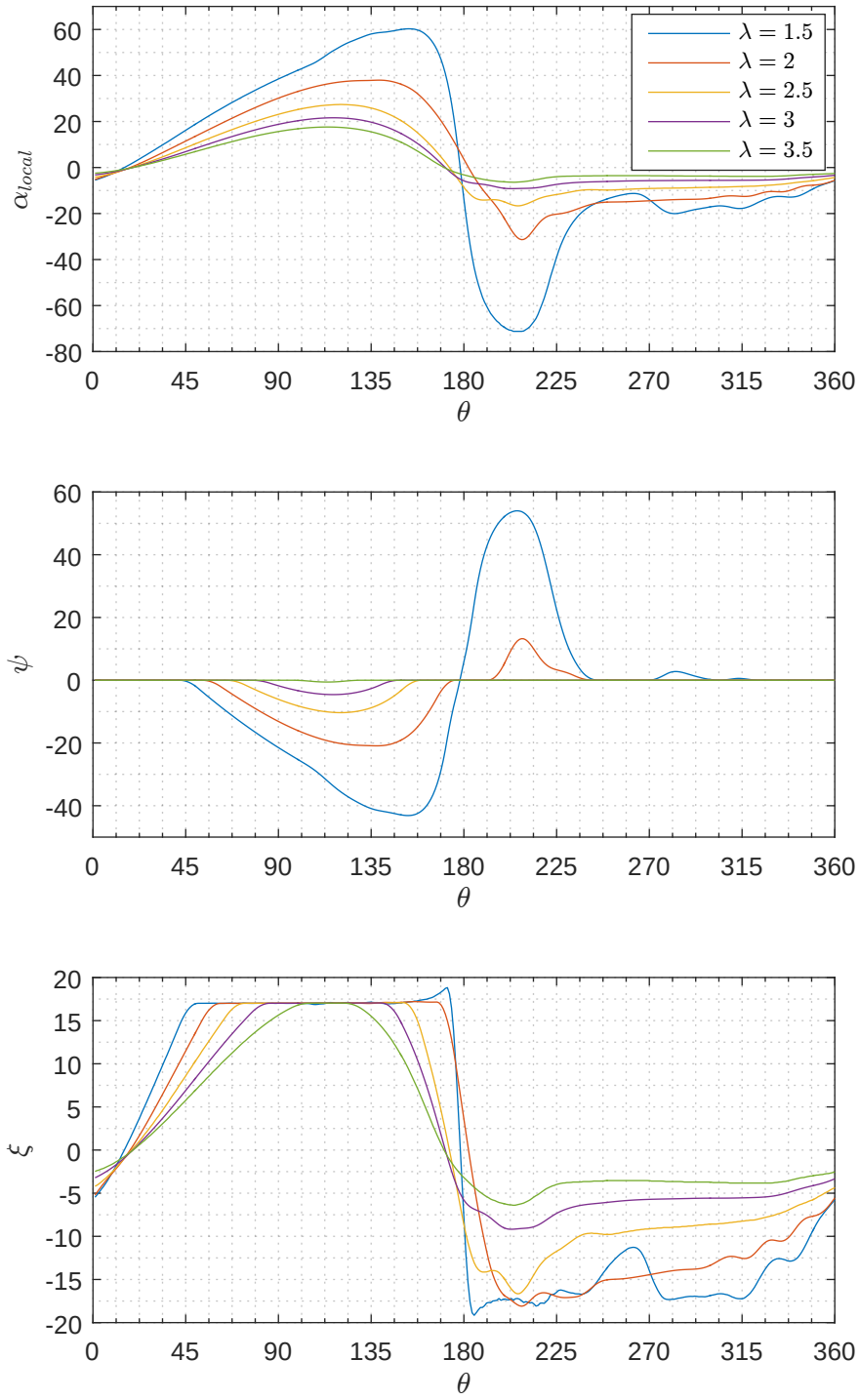

Figure 7-4: Graph of α_{local}-limit variables versus rotational position; top: zero loss angle of attack, middle: active blade pitch, bottom: resultant angle of attack

7.3 Numerical Model Setup

The numerical model is identical to the large scale turbine model described in Section 6.2 with the addition of active pitching. Pitch augmentation was achieved by assembling a mesh motion control in the solver. The method was activated by assigning the 'blade domains' as 'subdomains', this opens up the ability in ANSYS CFX to apply a mesh motion. Mesh motion allows the mesh nodes of a selected region to be moved in any direction by providing components of displacement. In the same manner as the rotating domain, the interface between the moving mesh and the adjoining domain is handled by a GGI interface. The software options required to implement mesh motion in ANSYS CFX (now version 17.0) include:

- Blade Domain
  - Mesh Deformation - Option: Regions of Motion Specified
  - Mesh Deformation - Displacement Rel. To: Previous Mesh
- Subdomain
  - Basic Settings - Location: Blade Domain
  - Basic Settings - Coordinate Frame: Blade Axis (custom axis at the centre of each blade)
  - Mesh Motion - Option: Specified Displacement
  - Mesh Motion - Displacement - Option: Cartesian Components
  - Mesh Motion - Displacement - X Component: User CEL equations (repeated for Y Component)

With the solver settings in place, the challenge is to provide Cartesian components of displacement to the subdomain mesh motion. To simplify the method of control, the integrated equation language was used to convert a simple actuation angle into the desired components of motion (x' and y'), shown by equations 7.8 and 7.9, where x and y are components of current position, δx and δy are components of total mesh displacement and ψ is the pitch demand angle.

$$x' = ((x - \delta x)\, cos\psi - (y - \delta y)\, sin\psi) - (x - \delta x) \tag{7.8}$$

$$y' = ((x - \delta x)\, sin\psi + (y - \delta y)\, cos\psi) - (y - \delta y) \tag{7.9}$$

Equations 7.8 and 7.9 are repeated for each of the three blades requiring a demand pitch angle ψ for each. Again, the CEL language is used to simplify the required input by phase shifting a single value of ψ by 120° and 240° to provide individual demand angles for the second and third blades respectively.

The process of implementing and processing the data for each active pitch model is summarised in Figure 7-5. At the time of starting this study a new high performance computing (HPC) facility (University of Bath's 'Balena' HPC) became available. The HPC enabled solutions to be solved on 48 cores, taking 6 hours and reaching an average of 22500 iterations to complete 7 turbine rotations. All solutions were checked for convergence using the same method presented in Section 6.3, all solutions reached <1% error within 7 rotations.

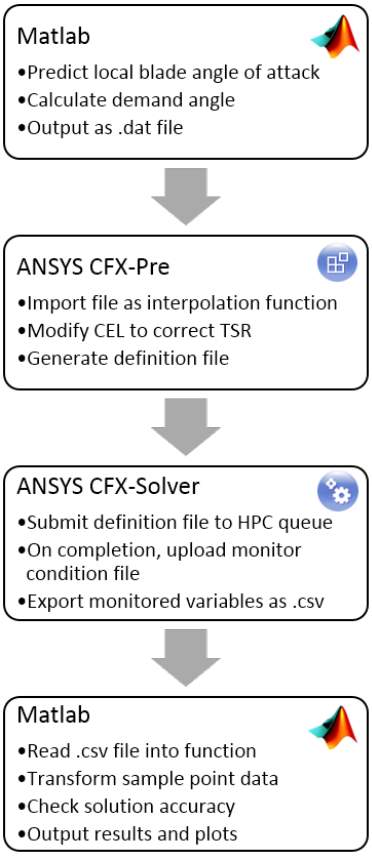

Figure 7-5: Flow chart summarising the process involved to implement active pitching

7.4 Test Plan

To keep the number of permutations in line with the available computational resource a testing strategy was devised for the three pitching schemes. To start, all initial development was chosen to be conducted at a TSR of 2, this was selected

due to the challenging nature of the case, suffering from stall at both upstream and downstream blade paths. Further details of the order and manner of the devised testing are described as follows:

1. Sinusoidal tests:

   (a) The case was initially used to develop and verify the functionality of the numerical method.

   (b) The peak sinusoidal deflection, ψ_{max}, was varied from 4° to 20° in increments of 2°.

2. α-limit:

   (a) An initial study was conducted without downstream loss for α_{lim} values of 12° to 28° at a TSR of 2. Other TSRs were not explored at this stage as the matrix of testing would be prohibitively large, therefore an assumption had to made that a TSR of 2 is representative of other TSRs for peak performance trends.

   (b) The two highest performing α_{lim} cases were then explored over a full range of downstream loss factor, ϕ, from 10% up the point where downstream loss meant that α was just below α_{lim} and therefore no pitching was taking place downstream. The aim of the tests is to establish which downstream loss factor gives the highest performance.

   (c) With α_{lim} and ϕ for peak performance established, the values are applied to all TSRs to create a curve of maximum turbine performance.

3. α_{local}-limit:

   (a) Firstly, the isolated blade testing in Chapter 4 predicted that peak lift for the blade at high Reynolds number is achieved at an angle of attack of 17°, therefore α_{lim} is set to this value for the study. In addition, based on the analysis in Chapter 6 sample point 'd' is predicted to provide peak performance. Therefore, the study focusses on these limits for TSRs of 1.5, 2, 2.5 and 3.

   (b) A 2nd iteration of the method was conducted, where α_{local} is updated based on the result from the first test, denoted α'_{local}, such that a new prediction of ψ is made for the new case. The approach has the effect of iterative convergence on idealising the pitch control in order to achieve the original α_{lim}.

7.5 Results

7.5.1 Sinusoidal, TSR=2

The sinusoidal tests were mainly included as a method development case, therefore the analysis is kept to a minimum in the form of Figure 7-6. $\overline{C_P}$ can be seen reaching a maximum at a peak pitching angle of 8°, at a value of ∼0.65. For reference, the fixed pitch turbine achieves a $\overline{C_P}$ of 0.43 at a TSR of 2, therefore, the sinusoidal motion exhibits an increase in performance of 51%.

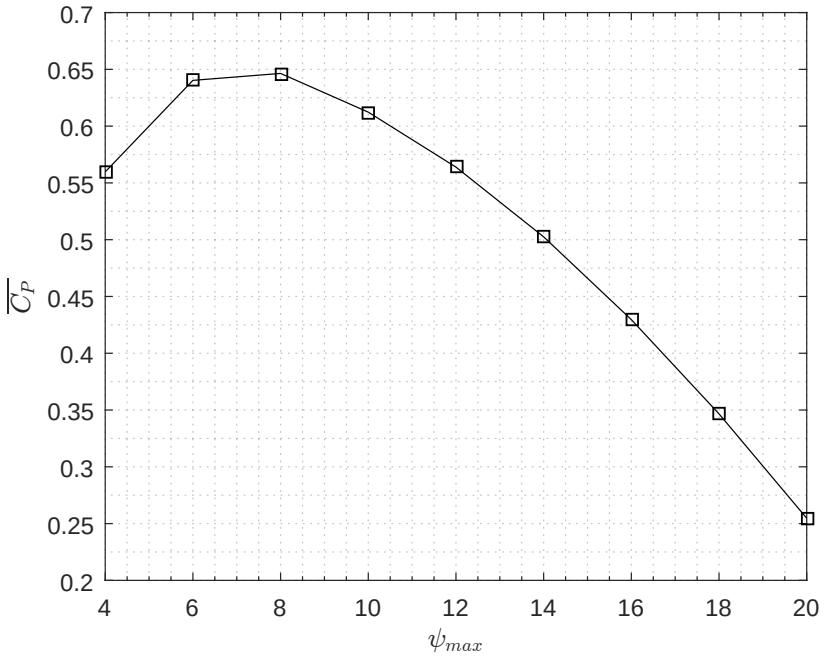

Figure 7-6: Mean coefficient of power for a range of sinusoidal blade pitching motions reaching maximum angles of 4° to 20° at a TSR of 2

7.5.2 α-limit

7.5.2.1 Without Downstream Loss, TSR=2

The first stage of the study is to establish turbine performance for a range of α_{lim}. In this case, blade pitch occurs both upstream and downstream equally as zero losses are assumed. The result, shown in Figure 7-7, predicts a peak performance at an α_{lim} of 18°. At a peak of 0.7, the performance is 63% higher than the fixed pitch turbine. In addition, the thrust has also been reduced by 18% making the turbine significantly more hydrodynamically efficient. The contributions of a single blade from upstream and downstream arcs can be examined for improvement by

comparing Figure 7-8 with the fixed pitch results in Figure 6-11. The comparison reveals that at the maximum power output, at an α_{lim} of 18°, performance can be attributed to the upstream sweep in the turbine, with the downstream remaining roughly equal. Interestingly, the peak is currently very close the 17° stall point predicted in Chapter 4 for the single blade at high Reynolds number.

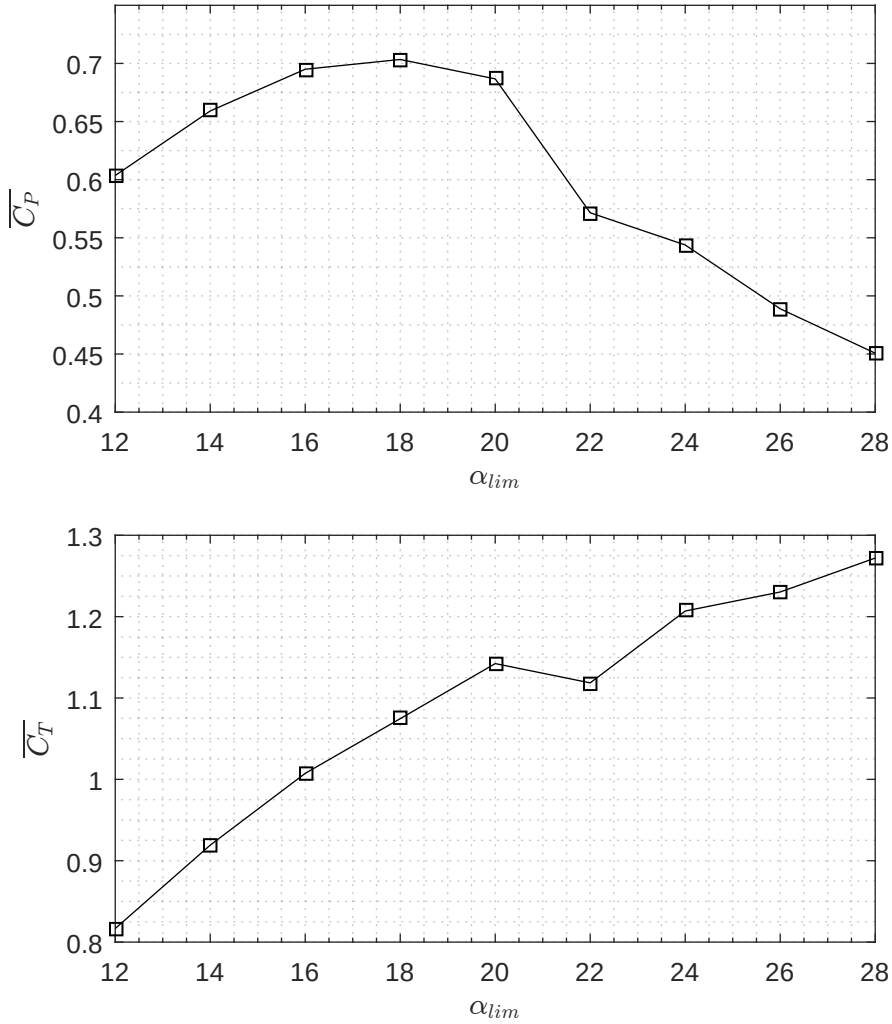

Figure 7-7: Graphs showing the α-limit mean coefficients for a range of angle of attack limits; top: power, bottom: thrust

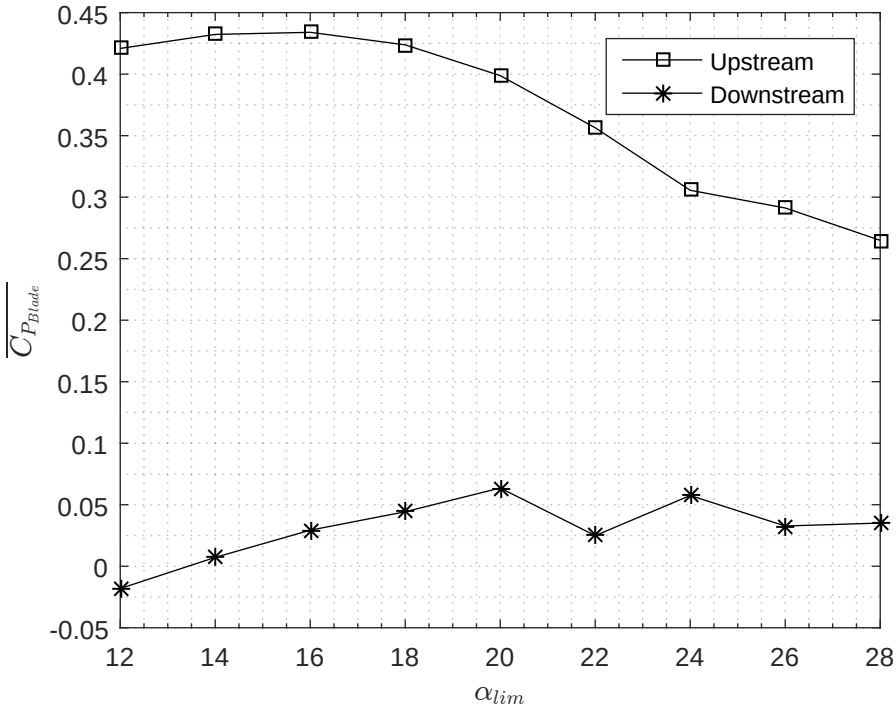

Figure 7-8: Graph showing the α-limit single blade mean power coefficient for upstream and downstream positions versus angle of attack limits of 12 to 28

7.5.2.2 With Downstream Loss, TSR=2

The highest two performers from the first stage of testing, an α_{lim} of 16° and 18°, were tested for all values of downstream loss at increments of 10% until zero downstream pitching was required. The results for $\overline{C_P}$ are shown in Figure 7-9 where the 16° case visibly outperforms 18° peaking at a ϕ of 50%. To ensure a maximum had been found the study was extended to include 14° and 12° although only a few cases we tested close to the know maximum. The 14° case almost exactly matches the 16° at a ϕ of 50% with both achieving a $\overline{C_P}$ of 0.81, while the 12° gives a poorer result confirming that the peak has been passed. The second plot, Figure 7-10 displays the coefficient of thrust for all cases. Most significantly, at a ϕ of 50% the thrust of the α_{lim}=14° produces a lower thrust than the 18° case despite producing an equal amount of power and therefore has a greater hydrodynamic efficiency.

Evaluating the upstream and downstream contributions to power, plotted in Figure 7-11, the upstream plot (top) shows a gradual decline in power generation as ϕ is increased, conversely, the downstream (bottom) increases with ϕ and at a higher rate. The result is conclusive evidence that sacrificing some energy extraction from the upstream half of the rotation and allowing the flow to propagate through the

turbine for extraction at the downward half can result in a greater overall power extraction. It may be possible to exploit this behaviour to reduce peak structural forces on the blades while maintaining a high efficiency. With both 14° and 16° achieving an equally high peak $\overline{C_P}$ at $\phi = 50\%$ both cases are progressed into a study of all TSRs to determine if an optimum can be found.

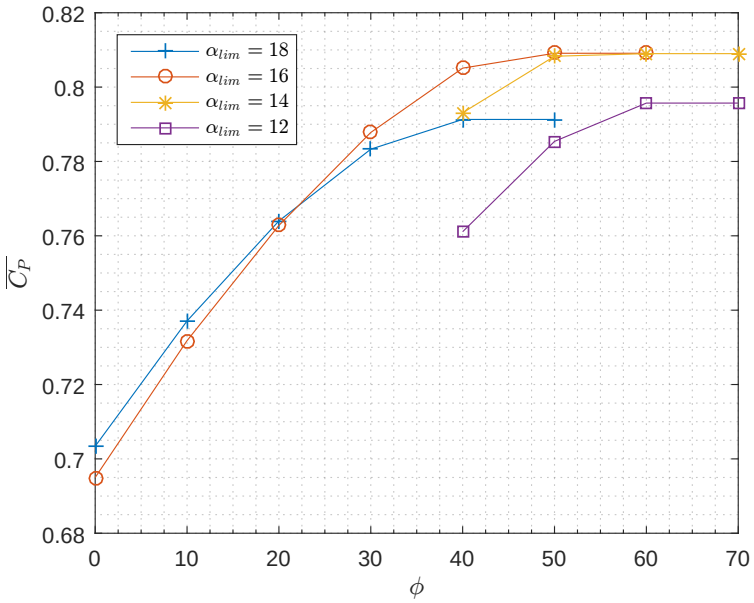

Figure 7-9: Graph showing the α-limit mean power coefficient versus downstream loss percentage for multiple blade pitch limits

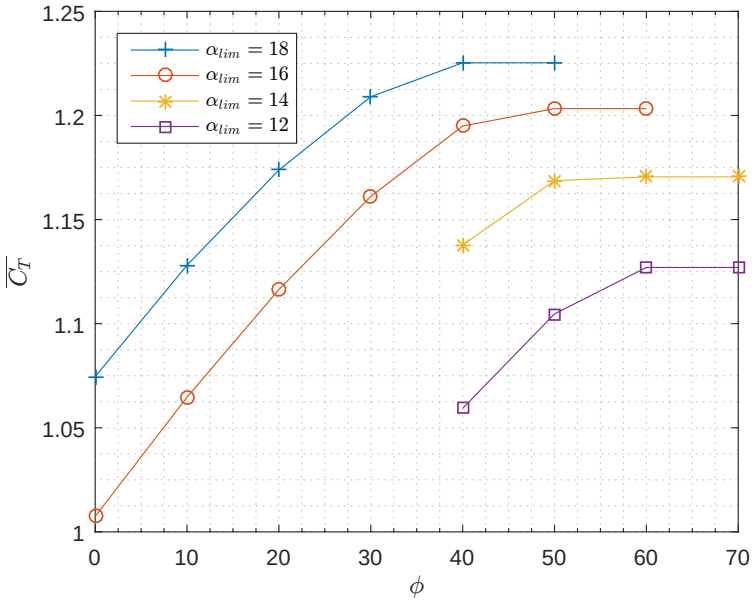

Figure 7-10: Graph showing the α-limit mean thrust coefficient versus downstream loss percentage for multiple blade pitch limits

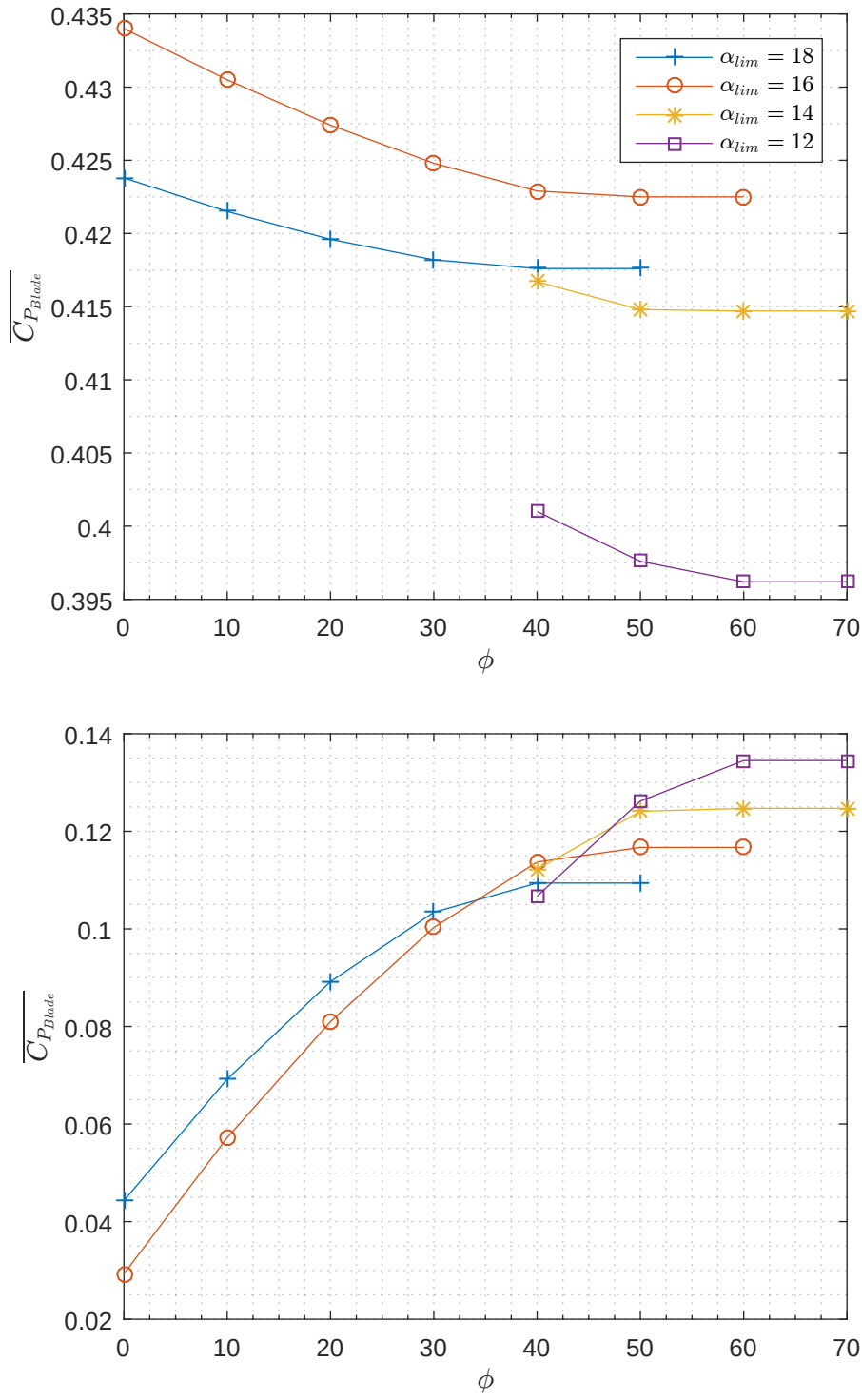

Figure 7-11: Graphs showing the α-limit single blade mean coefficient of power versus downstream loss percentage for multiple blade pitch limits; top: upstream, bottom: downstream

7.5.2.3 Performance: All TSRs

The values of α_{lim} and ϕ established at a TSR of 2 as the highest performing, are applied and numerically computed for all TSRs up to 3.5; above this value the local flow angle does not exceed the specified α_{lim} and hence no pitching is required. The results are plotted in Figure 7-12 for mean coefficients of power, torque and thrust. The performance curves in the plot of $\overline{C_P}$ show that an α_{lim} of 14° has a slight advantage over the 16° result having produced marginally more torque across the TSRs that utilise active pitching. Peak performance occurs at a TSR of 2.5 where $\overline{C_P}$ reaches 0.91, an 18% improvement over the fixed pitch equivalent. The source of the improvement can be examined in Figure 7-13 where plots of angle of attack and velocity have been captured for the TSR=2 case using local sampling at sample points 'c' and 'd'. The plot of C_P also includes un-pitched angle prediction α and pitch demand angle ψ. It is immediately apparent that while the case is aimed at limiting the peak angle of attack to 14°, the difference between to zero loss prediction of α and the actual value, could have resulted in an upstream sample angle straddling the originally predicted 17° stall point if sample point 'd' is taken to be correct. Downstream the situation is quite different with the sampled angle peaking closer to 25°. With stall expected around 17° it is unexpected that an optimum power be found at a ϕ of 50%. Examining $\overline{C_Q}$, the high downstream peak appears to cause no perceivable detriment to torque output. A possible explanation is that the increased angle of attack is being used, in part, to cancel out a virtual camber effect which was shown highly influential in Section 6.4.2.2 of the fixed pitch study. A combination of active pitching and the virtual camber effect is yet to be extensively understood, with the results here suggesting that pitching outwards on the upstream flight path could have a different influence on virtual camber than pitching inwards for the downstream flight path.

The result for U_{local}, given in the bottom plot of Figure 7-13, displays a velocity trace much closer the zero loss prediction (dashed line). The change is particularly prevalent around a θ of 180° where a velocity dip followed by a rapid increase found in the fixed pitch case (Figure 6-19) has been eliminated, this suggests that the flow through the turbine is much more stable than the fixed pitch turbine case.

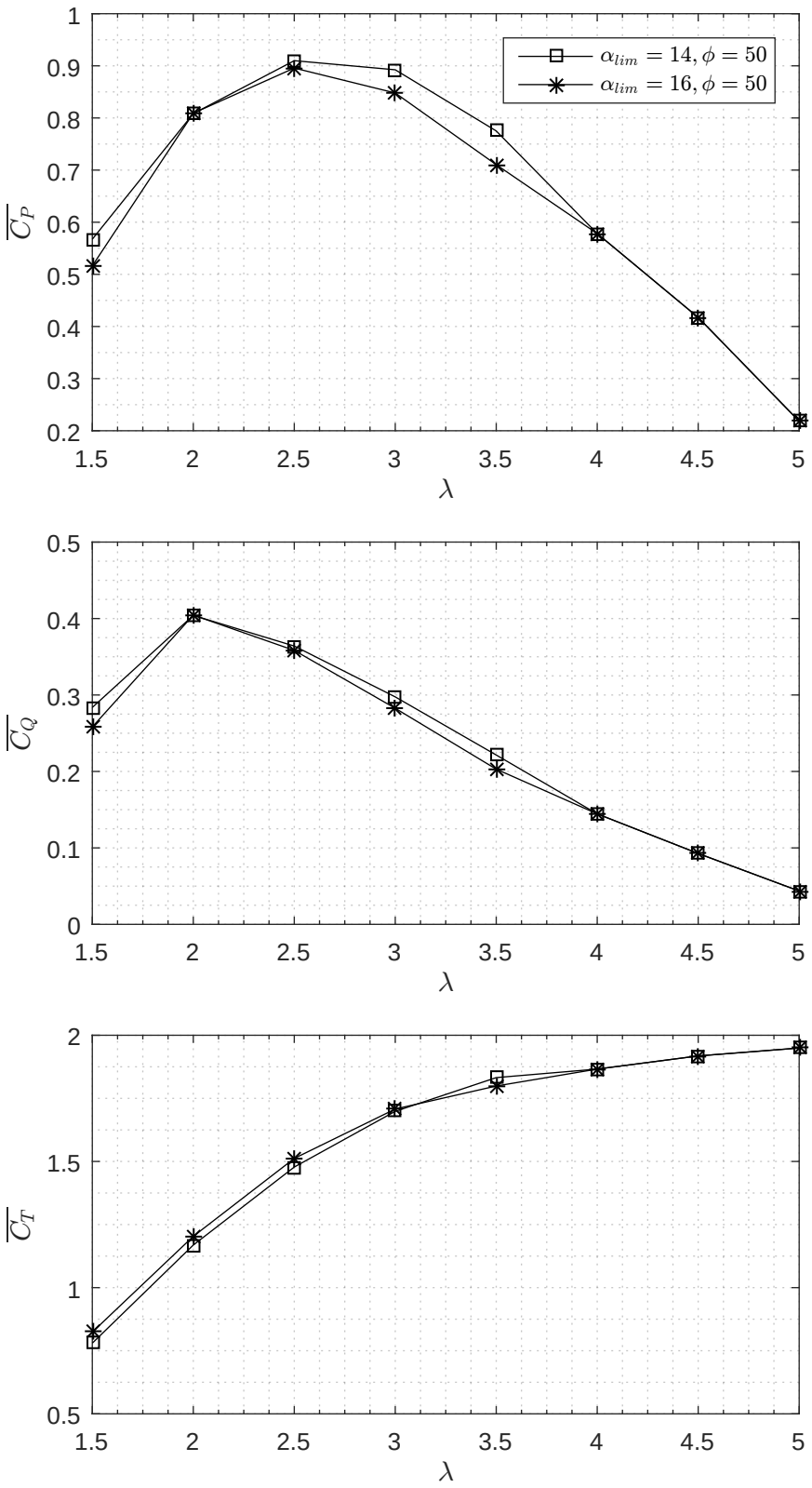

Figure 7-12: Graphs showing the α-limit performance mean coefficients versus azimuth angle; top: power, middle: torque, bottom: thrust

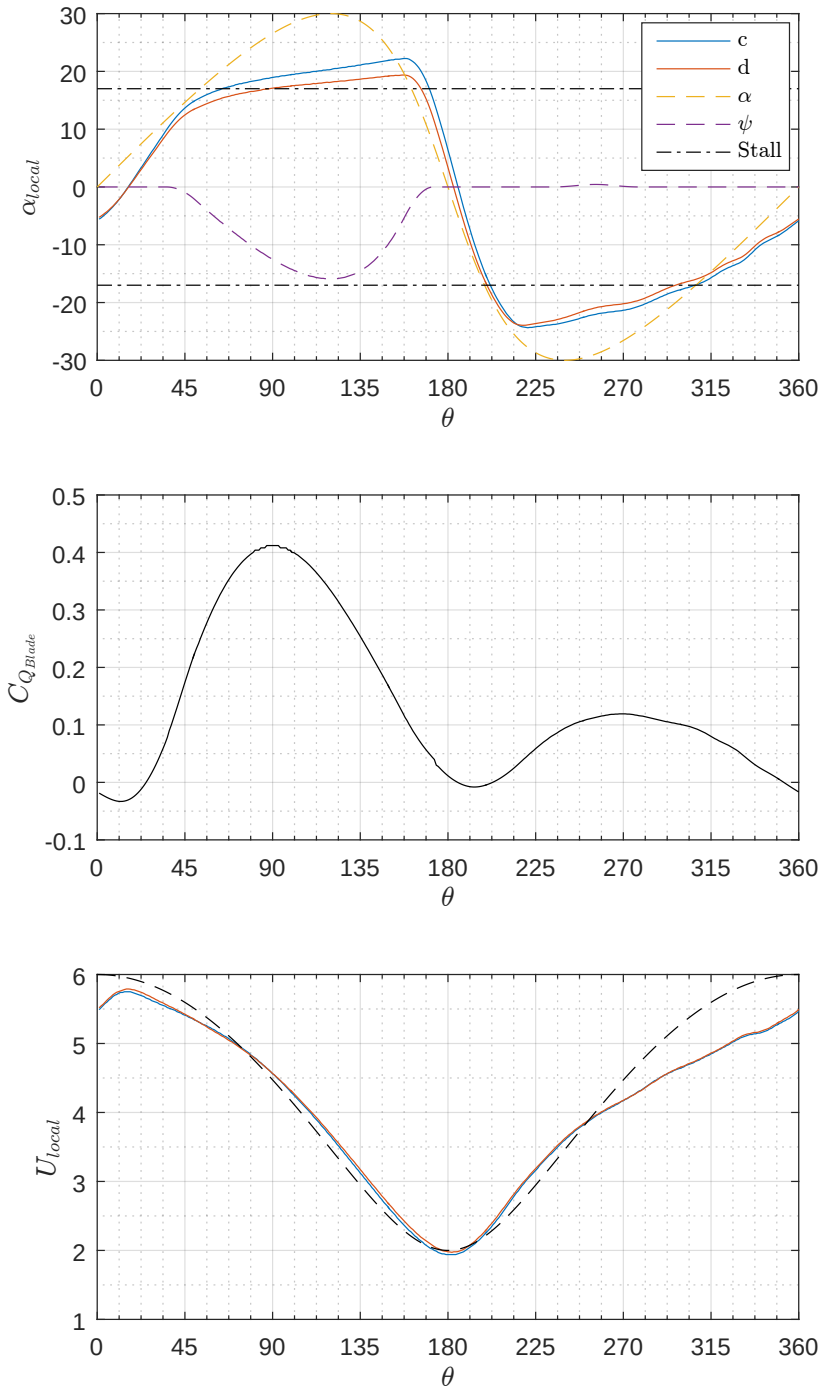

Figure 7-13: For the case TSR=2, α_{lim}=14° and ϕ=50%, graphs are plotted of the sample point parameters versus azimuth angle for a single blade, including; top: local angle, middle: coefficient of torque, bottom: local velocity

7.5.3 α_{local}-limit

The α-limit study predicted peak performance where sample point 'd' achieves an approximate value of 17° on the upstream stroke of the turbine. The result confirms that the proposed values for the sample point based pitching were robust approximations. Accordingly, testing is conducted as planned using the point 'd' sample data to calculate a pitching regime with an α_{lim} of 17° for the two iterations proposed in Section 7.4, part 3b. The philosophy behind the iterative approach is that after correcting for stall from the fixed pitch case sampling, it is rational that the resultant turbine performance, and hence flow conditions, will be altered, and therefore the original correction becomes invalidated. Using the new α_{local}, termed α'_{local}, as the initial condition and re-correcting ψ, an effective second iteration can be completed reducing the error between desired and achieved blade angles of attack. Theoretically this process can be repeated until the sampled local pitch is fully representative of the influence of the turbine on the flow field and a state of convergence is reached.

Summaries of local conditions sampled by point 'd' for iteration 1 and 2 are presented in Figures 7-14 and 7-15 respectively. The plots of α_{local} display the iterative convergence in action. Figure 7-14 shows that after a single correction sample point 'd' returns a perceived angle of attack that is significantly truncated from its original peak of ∼40° (see Figure 6-19) down to values straddling the 17° target. However, its path is erratic with a number of fluctuations, particularly either side of the transition between upstream and downstream positions. The fluctuation has a visible effect on blade torque in the same region, although local velocity is significantly improved compared to the fixed pitch case. Moving on to the second iteration, shown in Figure 7-15, sample point 'd' is significantly improved achieving upstream and downstream target peak α_{local} angles with low quantitative error. In addition, the upstream blade torque appears wider and the transition smoothed, the effect of these changes will be examined later in the analysis.

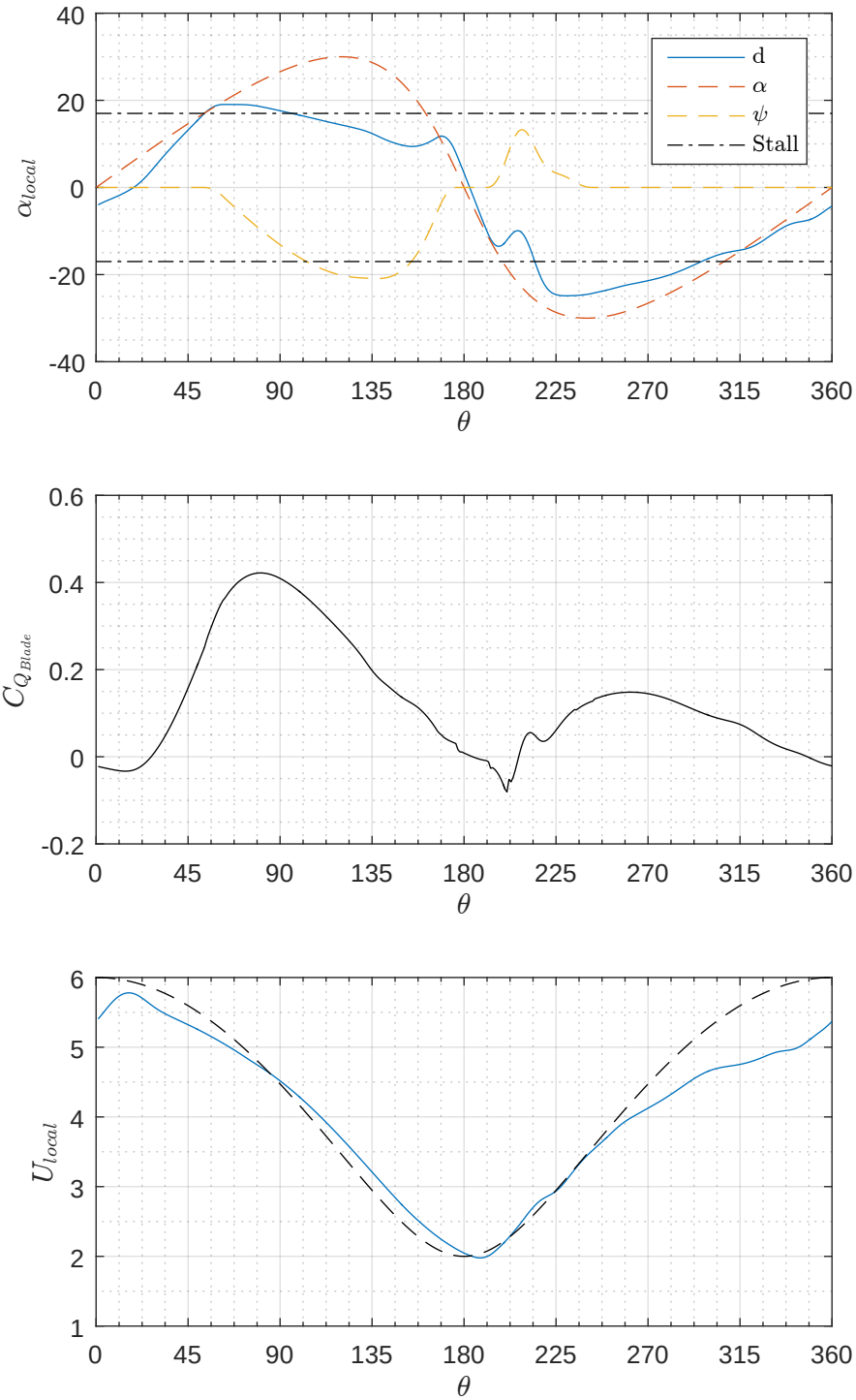

Figure 7-14: For the case TSR=2, α_{lim}=17°, iteration 1, graphs are plotted of the sample point parameters versus azimuth angle for a single blade, including; top: local angle, middle: coefficient of torque, bottom: local velocity

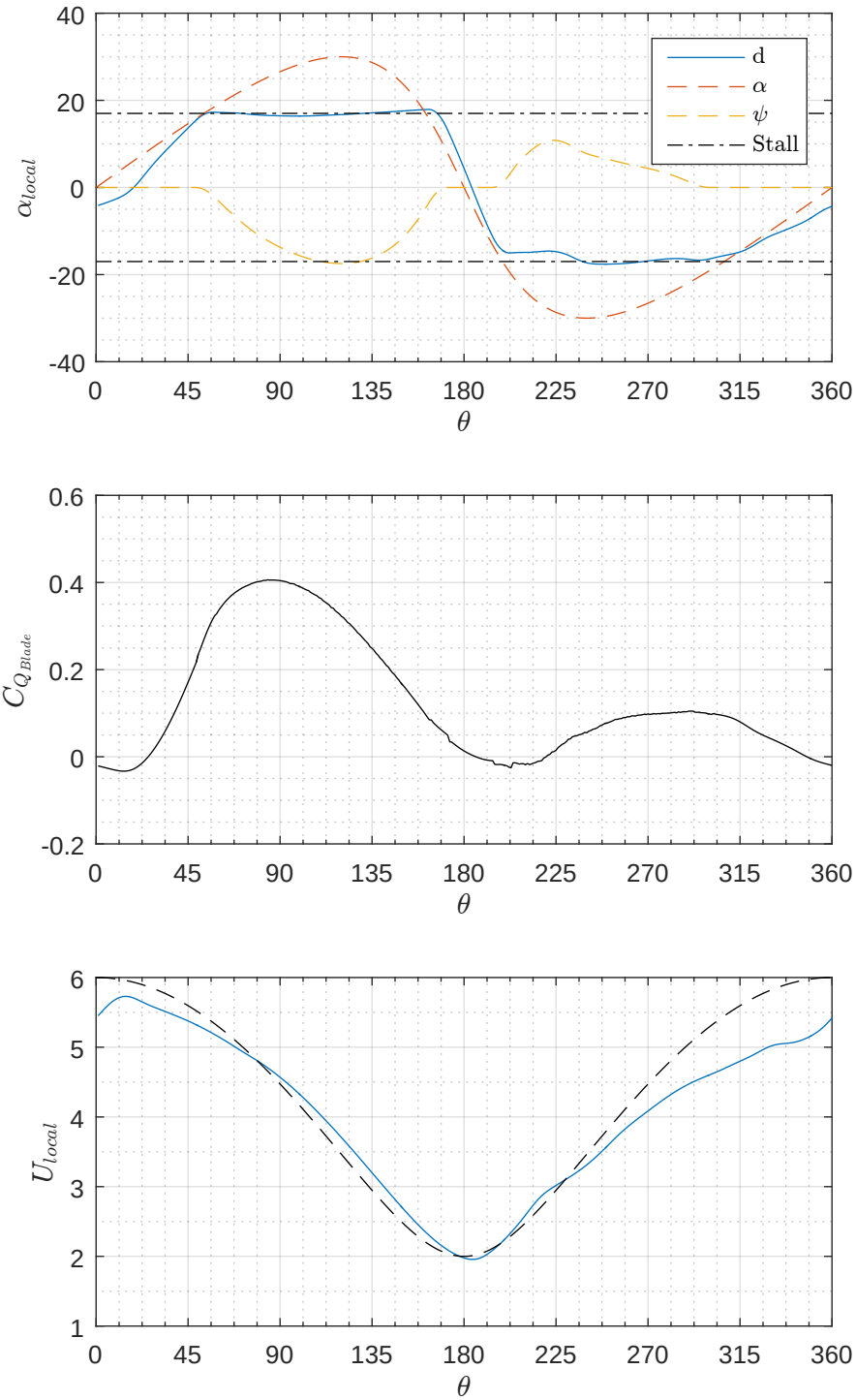

Figure 7-15: For the case TSR=2, α_{lim}=17°, iteration 2, graphs are plotted of the sample point parameters versus azimuth angle for a single blade, including; top: local angle, middle: coefficient of torque, bottom: local velocity

The performance of the turbine after iterations 1 and 2 are plotted in Figure 7-16 for mean coefficients of power, torque and thrust. The peak power occurs at a TSR of 2.5 and reaches a value of 0.913, an almost identical output to the α-limit optimisation. Comparing the two iterations in terms of power, both results are quantitatively close, although the 2nd iteration generates more power in three of the four TSRs tested. The differences between the two are better seen in the plot of $\overline{C_Q}$ where the biggest improvement occurs at a TSR of 1.5 with a $\sim$12% increase over the 1st iteration. Finally, the thrust is lower across all TSRs for the 2nd iteration, with both iterations producing similar power the result is a marginally higher hydrodynamic efficiency. The only point to challenge the trend is that the first iteration produced higher $\overline{C_P}$ than the 2nd iteration at a TSR of 2. The source of this outlier can be located in Figure 7-17 which shows that the downstream contribution is higher for the first iteration. Comparing 'd' on Figure 7-14 with the 2nd iteration result on Figure 7-15 over the downstream section, α_{local} can be seen reaching a higher angle of attack $\sim$25°, versus the 2nd iteration where it is corrected to peak at a limit of 17°. This additional performance from the higher angle of attack on the downstream sweep is consistent with the findings in the α-limit case and discussed in Section 7.5.2.3. The evidence again points towards allowing the turbine to reach a higher angle of attack on the downstream path to maximise performance.

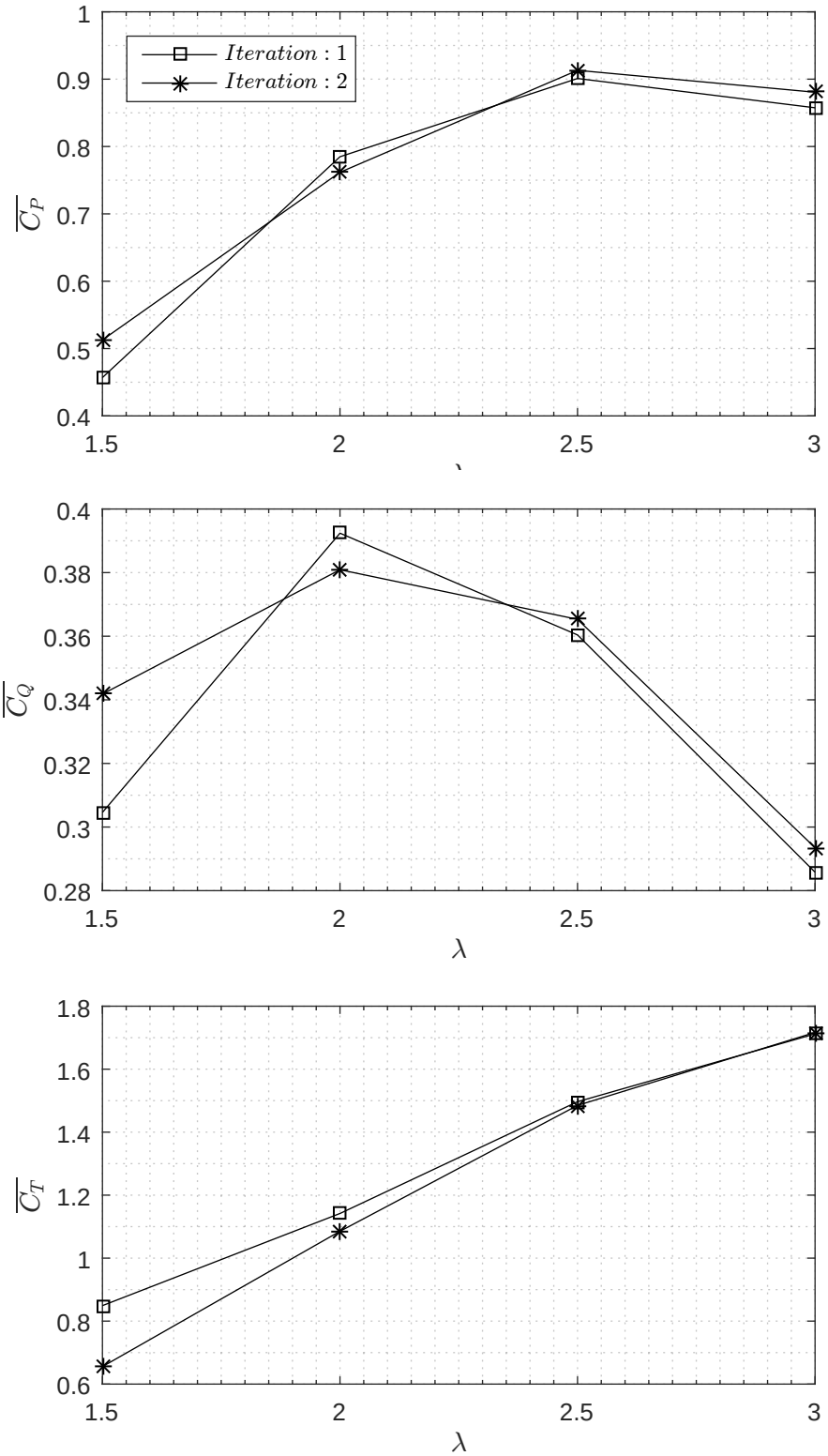

Figure 7-16: Graphs showing the α_{local}-limit performance mean coefficients versus azimuth angle; top: power, middle: torque, bottom: thrust

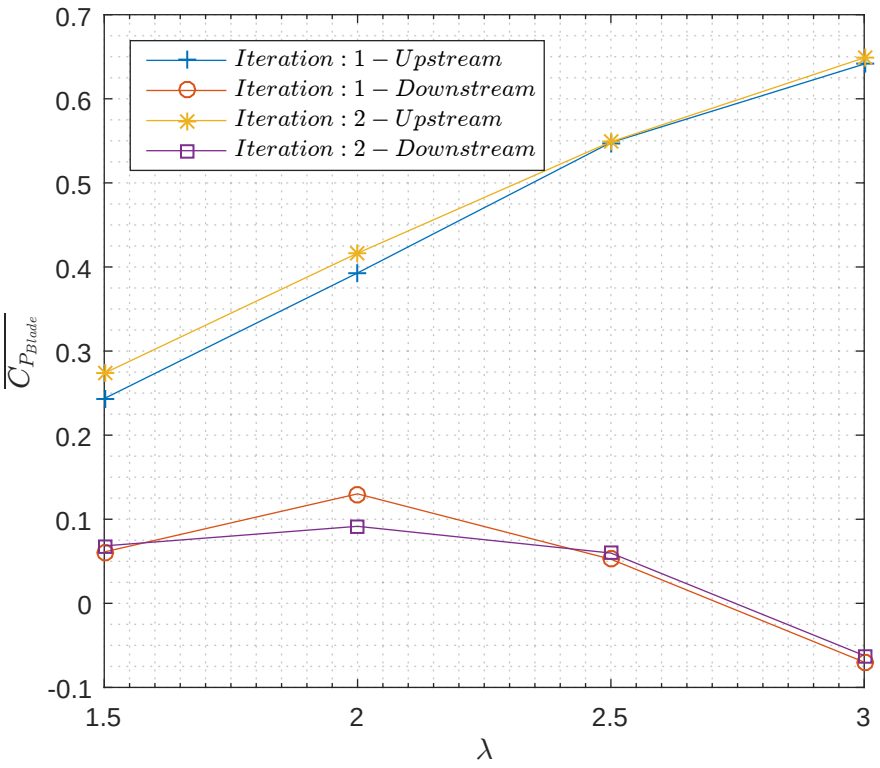

Figure 7-17: Graphs showing the α_{local}-limit single blade coefficient of power versus downstream loss percentage for multiple blade pitch limits; top: upstream, bottom: downstream

7.6 Comparison

The results for fixed pitch, α-limit and α_{local}-limit are bought together is this section and compared to highlight any performance enhancement achieved. To begin, the optimal versions of pitching motion, where α-limit is set to values of α_{lim}=14° and ϕ=50%, and the α_{local}-limit is set α_{lim}=17°, are plotted in Figure 7-18. Examining the blade pitch demand ψ, optimisation of the two methods has resulted in a very similar upstream regime. This convergence on a similar pitching scheme was achieved despite the α-limit expecting to realise an α_{lim}=14° when in fact, due to the error of assuming zero losses, the pitching regime actually resulted in a 17°-18° maximum. The convergence of the two techniques on a closely matching active blade pitching path adds some validity to the optimum found. The main variance between the two is that the α-limit peaked with a downstream loss of 50%, resulting in almost zero downstream pitching. In contrast, with the α_{local}-limit it was assumed that the stall limit of 17° should be applied at all times and therefore the downstream is limited to this value by the input of blade pitching visible on the lower plot. Examining α_{local}, captured by sample point 'd', the upper graph shows how both methods limit the blade angle of attack close to the originally predicted stall point of the blade identified in Chapter 4, while the fixed pitch continues up to 41° and hence well beyond the stall point of the blade.

A comparison of turbine performance metrics for all pitching cases is presented in Figure 7-19. The performance enhancement of torque output, and hence power, is similar for both pitching methods versus the fixed pitch. The increase in mean power coefficient is highest at the lowest TSR, gradually reducing until zero pitching at a TSR of 4. The plot of $\overline{C_P}$ also reveals that the α-limit method slightly outperforms the α_{local}-limit at the lowest two TSRs, a behaviour previously identified as having a propensity to prefer a higher α_{lim} that upstream. A summary of the performance increases is included in Table 7.1.

In the lower graph of Figure 7-19 displays the coefficient of thrust for the three cases. The result shows that the blade pitching cases reduce the thrust across the lower TSR range despite the large increase in power extraction from the flow. As a result, the hydrodynamic efficiency, a measure of power extracted for the amount of thrust placed on the incoming flow, is significantly increased. A comparison of hydrodynamic efficiency is presented in Figure 7-20 for the three pithing regimes identified.

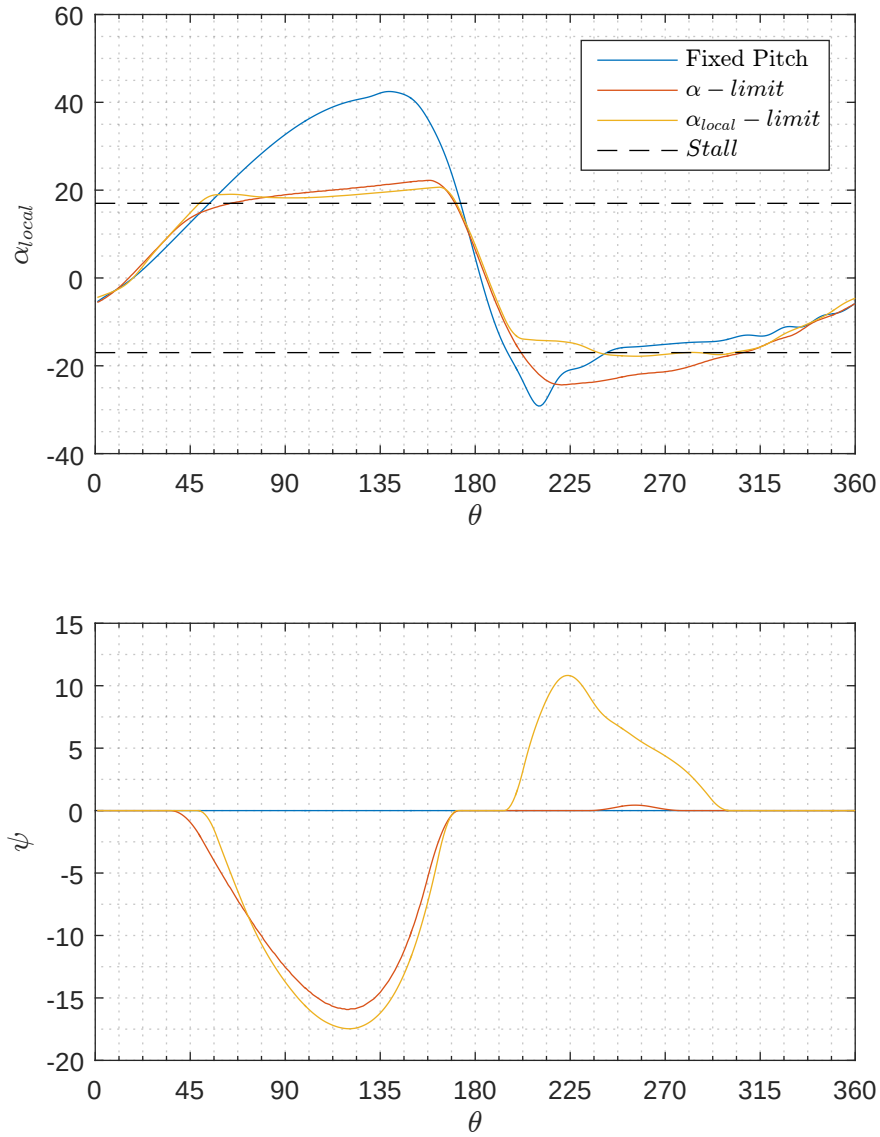

Figure 7-18: Graphs showing (top) blade angle α_{local} sampled from point 'd' and (bottom) blade pitch demand angle ψ versus azimuth angle, for pitching regimes including fixed pitch, α-limit and α_{local}-limit at a TSR=2

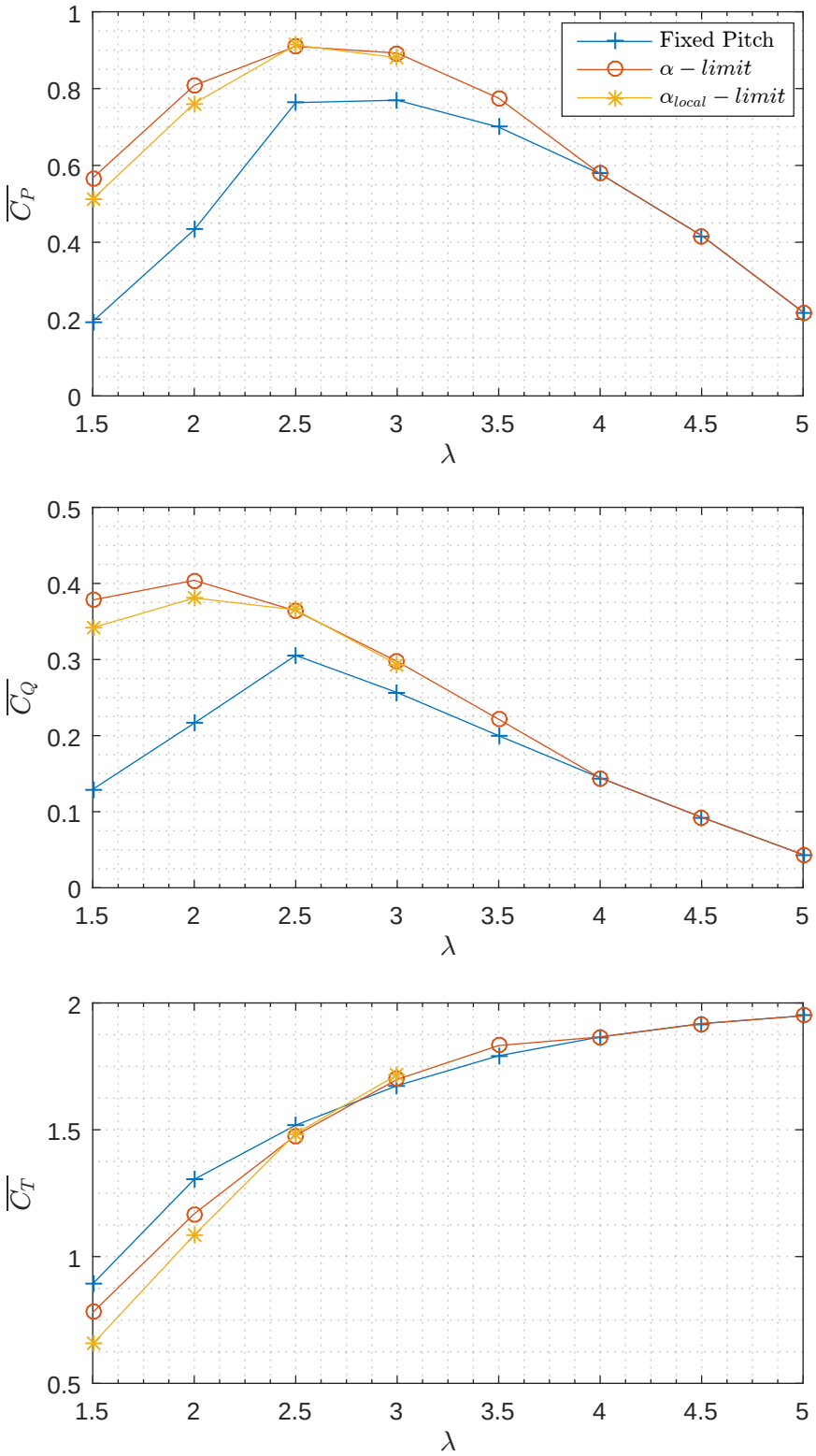

Figure 7-19: Comparison of three pitching regimes for performance coefficients versus azimuth angle; top: power, middle: torque, bottom: thrust

TSR	1.5	2	2.5	3	3.5
α-limit	+192%	+87%	+19%	+16%	+11%
α_{local}-limit	+164%	+76%	+20%	+14%	n/a

Table 7.1: Percentage increase in turbine $\overline{C_P}$ for active pitching methods

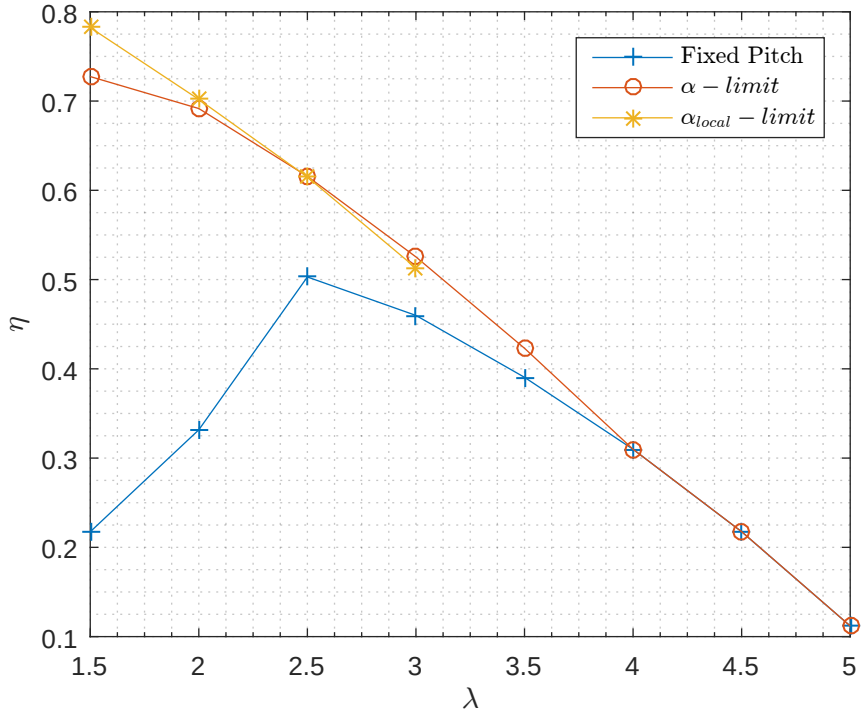

Figure 7-20: Hydrodynamic efficiency versus TSR for three pitching regimes

7.7 Discussion

In this chapter two methods of optimising an active pitch scheme have been proposed and tested in an attempt to improve the power output of a large scale cross-flow turbine. The α-limit method required a series of optimisation tests which eventually led to a peak performance at an estimated angle of attack limit of 14°. However, further scrutiny showed that the blade was reaching 17° - 18°, the difference being the error from using α, an idealised angle, as the basis of the estimation. The α-limit method also required a parameter analysis of velocity loss to establish an appropriate downstream corrector. Despite these limitations, the final performance was the highest achieved at the lowest tip speed ratios. This was mainly due to the downstream performance where a higher angle of attack than the upstream was found to be preferable. The main drawback of the method is

that an extensive parameter study is required to find the optimum, a process that would need to be repeated for alternative turbines. More cases and geometries are required to validate and establish any empirical relationships, in particular the loss coefficient which is known to vary with TSR from the analysis in Chapter 6.

The second method, α_{local}-limit, is based on the large scale numerical model where sample point 'd', one chord length ahead of the leading edge of the blade, was used to monitor local angles of attack and velocity. The monitored data is used as a baseline against which an active pitch sequence was calculated. After two iterations of the method, the performance of the turbine achieved a maximum $\overline{C_P}$, at a TSR of 2.5, just above the α-limit method. The advantage of the method is that a performance improvement was possible with only two numerical solves per tip speed ratio beyond the original fixed pitch baseline. In addition, the method has huge potential to optimise any turbine configuration, velocity profile, and blade profile, with equal effectiveness.

7.8 Conclusion

The study conducted in this chapter can be summarised to the following points:

- An angle of attack limiting based pitching mechanism is an effective method to increase turbine performance.
- The active pitching methods explored achieved a 20% increase in peak performance and significantly extend the range of operational tip speed ratios
- The α-limit method highlighted that there is a potential advantage to allowing the turbine blades to reach a higher angle of attack across the downstream sweep, further work is required to fully explore this effect
- The α_{local}-limit method achieved an equal peak power to the parameter study method, requiring only two model iterations

The methods developed and tested in this chapter are two potential methods of optimising a cross-flow tidal turbine. In particular, the novel sampling and optimisation method could have a significant impact on active pitch turbine technology once its capabilities have been fully explored and exploited.

Chapter 8

Conclusions

The original motivation for the research conducted in this thesis was the ever increasing risk to life that human activity driven climate change poses. As part of the solution, the widespread adoption of renewable energy by governments, industry and individuals has been gaining traction over the last two decades. However, the diverse climates and topologies throughout the world mean that a equally diverse selection of technologies are required to fulfil this potential. While tidal streams are prevalent in many parts of the globe, the UK in particularly well positioned to exploit this source of energy with the Pentland Firth being identified as one of the world's best site for tidal power (Carrington, 2013). This potential, and the fact that the technology is still in its infancy, made tidal technology a fitting topic for the research conducted in this thesis.

From the outset, the research philosophy adopted in this thesis has been to arrive at computational methods and technical solutions through robust analysis and independent investigation. This process began when the direction of the research was still falling into place and the circular cylinder case was conceived as a challenge that truly tested the limits of the CFD options at hand. The circular cylinder case was used to compare two prevalent solvers, ANSYS CFX and OpenFOAM, develop modelling strategies and assess suitability for planned future studies. The considered aspects included user interaction, functional capability, modelling options, numerical stability, and finally, quantitative accuracy. The study presented in Chapter 2 represents just part of a larger investigation where alternative turbulence models were trialled but a sufficient quality of results was not possible to form a report. The use of the $k - \omega$ SST turbulence closure model was ultimately chosen for the study as a compromise between accuracy and computational resource. The simulations were tightly controlled, adhering to $y^+ \sim 1$, cell aspect ratio treatment, Courant control and turbulence specification. The results conclusively demonstrated that the unsteady RANS method was

remarkably accurate at low Re, quantitatively matching experimental drag forces and shedding frequencies. The limits of applicability were also presented in which drag could be reasonably predicted up to an $Re \sim 1{\times}10^6$. In contrast, lift displayed different behaviours between the two solvers, but could only be relied upon up to $Re \sim 100$. The outcome of the study was the selection of CFX as the solver for the ongoing research due to the infancy of OpenFOAM and hence its limited capabilities. The chapter was published with the aim of providing a guide to the capabilities and pitfalls of using unsteady RANS models for cylindrical structures in offshore tidal flows, or indeed any application.

In Chapter 3 the cross-flow turbine was introduced in detail. The chapter set out the fundamentals of the turbine and the parameters by which turbine performance is judged throughout the rest of the thesis. A review of numerically focussed cross-flow literature revealed a number of common numerical methodologies, both prior to, and during, the work conducted in this thesis, were in prominent use by researchers in the field. The 2D multi-domain simplification of the cross-flow turbine was shown to be a promising numerical method by a number of authors. Provided the turbine blades do not heavily stall, RANS methods displayed an equal capability to accurately predict turbine performance, when compared with higher order methods. In addition, the use of active blade pitching is highlighted as a credible approach to significantly increase turbine performance. A combination of these elements influenced the methodology and direction of the research thereon.

The objective of Chapter 4 was to validate the accuracy of a chosen numerical method on a single blade so that the accuracy of the full turbine would also be validated, at least in part, by association. The first step was to independently re-evaluate the suitability of a number of numerical methods for the prediction of a single turbine blade. A review of literature confirmed that the $k-\omega$ SST turbulence model was very capable at high Reynolds numbers, but that careful attention should be paid to y^+ in low Re conditions. A series of numerical investigations allowed tuning of the mesh discretisation and identification of the limits of applicability of the method for a number of Reynolds numbers equivalent to turbines at various scales. The result of the study was that meshes adhering to y^+ values between 5 and 15 produced the most stable and accurate results. This range of y^+ is traditionally seen as unfavourable, however, the special wall treatment algorithm in ANSYS CFX afforded a favourable compromise between accuracy and mesh density in the boundary layer. All of the numerical models were built with a circular domain containing the turbine blade profile. The approach ensured all developed meshing strategies could be directly transferred to the full turbine model under assembly in the next phase of the research.

In Chapter 5 a laboratory tested cross-flow turbine was used as a basis to construct a numerical cross-flow turbine model with the aim of validating the methodology.

Once a strategy was developed to convert the 3-dimensional experimental case into a representative 2D simplification, a multi-domain model was constructed in the same fashion as research identified in Chapter 3. A preliminary round of parameter studies were conducted on the numerical setup in order to optimise spatial and temporal discretisation. The study suggested a maximum angle of 1° of motion per timestep and a total of 5-6 rotations to reach a relative error of $\overline{Cp} < 1\%$. The resultant numerical environment was then used to replicate the experimental turbine over a range of operational tip speed ratios. An exact qualitative match was achieved, plus a substantial quantitative accuracy with average and peak errors for all coefficients (power, torque and thrust) of <2% and ∼10% respectively. Following this, three alternative flow conditions were selected to test the scalability of turbine performance with mean blade chord Reynolds number. The hypothesis for the study was that Reynolds number was critical to the behaviour of the turbine and that performance would not scale equally for different cases. The assumption was proven to be correct with the results showing that the lowest performing case at an $Re < 200 \times 10^3$ became the second best performing at values of $Re > 300 \times 10^3$. All thee cases increase in performance at equal rates once mean blade chord Reynolds number reached $\sim 350 \times 10^3$, a value which is proposed as an aspirational minimum for future cross-flow tidal turbine development activities in order to ensure behavioural scalability.

With novel methods of increasing cross-flow turbine performance being an objective of the research, the findings of Chapter 5 were heeded, and a larger sized turbine in which all cases fall above a mean blade chord Reynolds number of 350×10^3 was constructed for evaluation in Chapter 6. In addition to the detailed hydrodynamic evaluation of the turbine, the study was also used to trial a novel flow sampling method devised to aid the understanding of the local conditions of the turbine blade. The problem identified was that past research has typically relied on momentum based models or extensive parameter studies to predict and optimise turbine yield, by sampling velocities in-situ it was postulated that angle of attack could be determined and optimised directly. The sampling proved very effective, confirming earlier findings which highlighted the difference between the upstream and downstream blade pass contributions and the contribution of the virtual camber effect on blade bending forces and pitching moment. The information amassed in the chapter suggested that an active pitch scheme would be an effective way to maximise performance.

In Chapter 7 two active pitching strategies are proposed and studied using the developed numerical method. The first strategy is to arrive at an optimised performance using an iterative parametric study based on idealised vector resolution and a loss factor. The second strategy uses the sampled local flow condition data from Chapter 6 to directly compute blade pitching to idealise stall avoidance. Both

methods result in increases in peak coefficient of power of ∼20%, with lower tip speed ratios of 1.5 and 2 increasing by margins of >160% and 75% respectively. Most significantly, the optimisation using the sampled local flow data, referred to as α_{local}-limit, required only the original CFD result, plus two additional solution iterations to converge on the specified stall-limited optimum. This convergence on an idealised pitching function is the fastest and most effective seen by the author, which is made possible by a novel sampling method that provides a new insight into the hydrodynamics of the cross-flow turbine.

8.1 Further Work

The local sampling and optimisation method developed in this thesis is a new concept that requires further validation to prove its capability versus existing optimisation methods. Furthermore, the work completed represents one possible interpretation of the local flow sampling methodology and resulting pitching function and therefore both have an extensive scope of potential improvements. Potential routes of investigation and optimisation include:

- minimising drag where angles of attack are low
- understanding the identified increase in performance at higher stall angle limits along the downstream flight path
- understanding and maximising the relationship between blade camber, which may be added to relieve the virtual camber effect, and the pitching function
- refinement and optimisation of the sample point distance, currently suggested to be 1 chord length ahead of the blade
- a study of the sample point correction angle, currently set to the pivot of the blade ($\psi + \phi$), an alternative being the leading edge of the blade
- creation of an experimental turbine with local flow sampling instrumentation to validate the CFD

Beyond the refinement of the optimisation method, the use of the optimisation method can be trialled in more challenging and potentially realistic cases. Examples include flows with higher turbulence, measured flow streams such as the 1/7th power law or indeed a location specific measured flow distribution, with a free surface included and expansion into 3D to explore local flow variance at blade ends. In these types of conditions the optimisation method is expected to excel because it does not require any assumptions in terms of flow conditions, the

main challenge being to ensure the CFD is as representative as possible of the physical turbine.

Active pitch cross-flow turbines have the potential to not only achieve efficiencies that challenge conventional axial turbines, but offer an array of additional advantages over the fixed pitch variant. The work in this thesis provides a robust basis to develop novel solutions for active pitch cross-flow turbines.

8.2 List of Publications

- Stringer, R. M., Hillis, A. & Zang, J., Numerical investigation of laboratory tested cross-flow tidal turbines and Reynolds number scaling, *Renewable Energy*, 2016, 85, 1316 - 1327
- Stringer, R. M., Zang, J. & Hillis. A., Unsteady RANS computations of flow around a circular cylinder for a wide range of Reynolds numbers, *Ocean Engineering*, 2014, 87, 1 - 9

Conference Papers

- Stringer, R. M., Zang, J. & Hillis, A., Prediction of Lab Scale Cross-Flow Tidal Turbine Performance Using Unsteady RANS, *Proceedings of the 10th European Wave and Tidal Energy Conference*, 2-5 September 2013, Aalborg, Denmark.
- Stringer, R. M., Zang, J. & Hillis, A., Numerical Modelling of a Laboratory Scale Tidal Turbine, *Proceedings of the 2nd Oxford Tidal Energy Workshop*, 18-19 March 2013, Oxford, UK.
- Stringer, R. M., J. Zang., Evaluation of URANS Solvers for Cylindrical Structures in Tidal Flow, *Proceedings of the 22nd International Offshore and Polar Engineering Conference (ISOPE)*, June 22, 2012.
- Stringer, R. M., J. Zang., Evaluation of FVNS Solvers for Structures in Tidal Flow, *Proceedings of the Oxford Tidal Energy Workshop*, 29-30 March 2012, Oxford, UK.
- Zang, J., Taylor, P. H., Morgan, G., Stringer, R., Orszaghova, J., Grice, J. and Tello, M., 2010. Steep Wave and Breaking Wave Impact On Offshore Wind Turbine Foundations - Ringing Revisited, *25th International Workshop on Water Waves and Floating Bodies*, Harbin, May 12, 2010.

References

Abbott, I. H. A. and Von Doenhoff, A. E. (1959). *Theory of wing sections, including a summary of airfoil data,*. Dover Publications, New York.

ABP Marine Environmental Research (2008). Atlas of uk marine renewable energy resources. [online] http://www.renewables-atlas.info/. [Accessed September 2017].

Achenbach, E. (1968). Distribution of local pressure and skin friction around a circular cylinder in cross-flow up to $Re = 5 \times 10^6$. *Journal of Fluid Mechanics*, 34:625.

Achenbach, E. and Heinecke, E. (1981). On vortex shedding from smooth and rough cylinders in the range of reynolds-numbers 6×10^3 to 5×10^6. *Journal of Fluid Mechanics*, 109(Aug):239–251.

Adam, D. (2008). I underestimated the threat, says stern. *The Guardian*.

Alam, M. and Sandham, N. D. (2000). Direct numerical simulation of 'short' laminar separation bubbles with turbulent reattachment. *Journal of Fluid Mechanics*, 410:1–28.

Anderson, J. D. (1995). *Computational Fluid Dynamics: The basics with applications*. McGraw-Hill, Inc, University of Maryland.

ANSYS® (2010). Academic research, release 13.0, help system, cfx reference guide, 6.3.4.1.5.2. integration to the wall (low-reynolds number formulaton).

ANSYS® (2011a). Academic research, release 14.0, help system, theory guide, 2. turbulence and wall function theory, 2.8. modeling flow near the wall, 2.8.1. mathematical formulation.

ANSYS® (2011b). Academic research, release 14.0, help system, theory guide, 3. ggi and mfr theory.

Arup Energy (2005). Oscillating water column wave energy converter evaluation report. Technical report, The Carbon Trust.

Babinsky, H. (2003). How do wings work? *Physics Education*, 38(6):497.

Bachant, P. and Wosnik, M. (2016). Effects of reynolds number on the energy conversion and near-wake dynamics of a high solidity vertical-axis cross-flow turbine. *Energies*, 9(2):–.

Bardina, J. E., Huang, P., and Coakley, T. (1997). Turbulence modeling validation testing and development. Technical report, NASA.

Barth, T. and Jesperson, D. (1989). The design and application of upwind schemes on unstructured meshes. Technical report, AIAA Paper 89-0366.

Benim, A. C., Cagan, M., Nahavandi, A., and Pasqualotto, E. (2007). Rans predictions of turbulent flow past a circular cylinder over the critical regime. In *Proceedings of the 5th Iasme/Wseas International Conference on Fluid Mechanics and Aerodynamics (Fma '07)*, pages 235–240.

Beri, H. and Yao, Y. (2011). Double multiple streamtube model and numerical analysis of vertical axis wind turbine. *Energy and Power Engineering*, Vol.03No.03:9.

Betz, A. (1920). Das maximum der theoretisch moeglichen ausnutzung des windes durch windmotoren. *Zeitschrift fuer das gesamte Turbinenwesen*, 26:307–309.

Bianchini, A., Carnevale, E. A., and Ferrari, L. (2011). A model to account for the virtual camber effect in the performance prediction of a h-darrieus vawt using momentum models. *Wind Engineering*, 35(4):465–482.

Black & Veatch (2005a). Phase ii uk tidal stream energy resource assessment marine energy challenge. [online] www.carbontrust.com/media/174041/phaseiitidalstreamresourcereport2005.pdf. [Accessed September 2017].

Black & Veatch (2005b). Tidal stream energy resource and technology summary. [online] www.carbontrust.com/media/174045/uk-tidal-stream-resource-and-technology.pdf. [Accessed September 2017].

Blazek, J. (2005). *Computational Fluid Dynamics: Principles and Applications*. Elsevier, St Augustin.

Bogateanu, R., Dumitrache, A., Dumitrescu, H., and Stoica, C. I. (2014). Reynolds number effects on the aerodynamic performance of small vawts. *UPB Scientific Bulletin, Series D: Mechanical Engineering*, 76(1):25–36.

Brinkerhoff, J. R. and Yaras, M. I. (2011). Interaction of viscous and inviscid instability modes in separation-bubble transition. *Physics of Fluids*, 23(124102):–.

Brochier, G., Fraunie, P., Beguier, C., and Paraschivoiu, I. (1986). Water channel experiments of dynamic stall on darrieus wind turbine blades. *Journal of Propulsion and Power*, 2(5):445–449.

Callaghan, J. and Boud, R. (2006). Future marine energy. Technical report, The Carbon Trust.

Carrington, D. (2013). Tidal power from pentland firth 'could provide half of scotland's electricity'. [online] https://www.theguardian.com/environment/2013/jul/10/tidal-power-penland-firth-scotland-electricity/. [Accessed 6 September 2017].

Catalano, P. and Tognaccini, R. (2011). Large eddy simulations of the flow around the sd 7003 airfoil. In *AIMETA Conference*.

CBC News (2009). Fundy tidal power demonstration approved. [online] http://www.cbc.ca/news/canada/nova-scotia/fundy-tidal-power-demonstration-approved-1.783307. [Accessed September 2017].

Coleman, G. N. and Sandberg, R. D. (2010). A primer on direct numerical simulation of turbulence - methods, procedures and guidelines. Technical report, Aerodynamics & Flight Mechanics Research Group, School of Engineering Sciences. University of Southampton.

Consul, C. A. (2008). Design and analysis of the aerofoil sections for thawt. Transfer report, University of Oxford.

Consul, C. A. (2011). *Hydrodynamic Analysis of a Tidal Cross-Flow Turbine*. Phd, University of Oxford.

Consul, C. A. and Willden, R. H. J. (2011). An investigation of the influence of free surface effects on the hydrodynamic performance of marine cross-flow turbines. In *9th European Wave and Tidal Energy Conference*.

Consul, C. A., Willden, R. H. J., and McIntosh, S. C. (2013). Blockage effects on the hydrodynamic performance of a marine cross-flow turbine. In *Philosophical Transactions of the Royal Society of London A: Mathematical, Physical and Engineering Sciences*, volume 371. The Royal Society.

Counsil, J. N. N. and Boulama, K. G. (2012). Validating the urans shear stress transport gamma - re-theta model for low-reynolds-number external aerodynamics. *International Journal for Numerical Methods in Fluids*, 69(8):1411–1432.

Coutanceau, M. and Bouard, R. (1977). Experimental determination of the main features of the viscous flow in the wake of a circular cylinder in uniform translation. part 2. unsteady flow. *Journal of Fluid Mechanics*, 79(Feb22):257.

Dai, Y. M., Gardiner, N., Sutton, R., and Dyson, P. K. (2011). Hydrodynamic analysis models for the design of darrieus-type vertical-axis marine current turbines. *Proceedings of the Institution of Mechanical Engineers, Part M: Journal of Engineering for the Maritime Environment*, 225(3):295–307.

Dai, Y. M. and Lam, W. (2009). Numerical study of straight-bladed darrieus-type tidal turbine. *Proceedings of the Institution of Civil Engineers - Energy*, 162(2):67–76.

Darrieus, G. J. M. (1931). Turbine having its rotating shaft transverse to the flow of the current. Patent. US 1,835,018.

de O.Falcao, A. F. (2010). Wave energy utilization: A review of the technologies. *Renewable and Sustainable Energy Reviews*, 14(3):899 – 918.

Dehkordi, B. G. and Jafari, H. H. (2009). Numerical simulation of flow through tube bundles in in-line square and general staggered arrangements. *International Journal of Numerical Methods for Heat and Fluid Flow*, 19(8):1038–1062.

Dennis, S. C. R. and Chang, G. Z. (1970). Numerical solutions for steady flow past a circular cylinder at reynolds numbers up to 100. *Journal of Fluid Mechanics*, 42:471.

Department for Business, Energy & Industrial Strategy (2017). Digest of united kingdom energy statistics 2017. [online] https://www.gov.uk/government/collections/digest-of-uk-energy-statistics-dukes. [Accessed September 2017].

Devinant, P., Laverne, T., and Hureau, J. (2002). Experimental study of wind-turbine airfoil aerodynamics in high turbulence. *Journal of Wind Engineering and Industrial Aerodynamics*, 90(6):689–707.

Dodge, D. (2001). An illustrated history of wind power development. Online.

Douvi, E. C., Tsavalos, A. I., and Margaris, D. P. (2012). Evaluation of the turbulence models for the simulation of the flow over a national advisory committee for aeronautics (naca) 0012 airfoil. *Journal of Mechanical Engineering Research*, 4(3):100–111.

Drela, M. (1989). *XFOIL: An Analysis and Design System for Low Reynolds Number Airfoils*, pages 1–12. Springer Berlin Heidelberg, Berlin, Heidelberg.

Drew, B., Plummer, A. R., and Sahinkaya, M. N. (2009). A review of wave energy converter technology. *Journal of Power and Energy*, 223 Part A:887–902.

Duckers, L. (1994). Climate change energy and the environment. wave energy; crests and troughs. *Renewable Energy*, 5(5):1444 – 1452.

Embley Energy Ltd (n.d.). Sperboy - history. [online] http://www.sperboy.com/page001.html. [Accessed September 2017].

EMEC (n.d.a). Pelamis wave power. [online] http://www.emec.org.uk/about-us/wave-clients/pelamis-wave-power/. [Accessed September 2017].

EMEC (n.d.b). Wave energy devices. [online] http://www.emec.org.uk/marine-energy/wave-devices/. [Accessed September 2017].

Engineering Business Ltd. (n.d.). Marine power project: Oscillating hydrofoil. [online] http://www.esru.strath.ac.uk/EandE/Web_sites/05-06/marine_renewables/technology/oschydro.htm. [Accessed September 2017].

ESDU (1980). Esdu 80025: Mean forces, pressures and flow field velocities for circular cylindrical structures: single cylinder with two-dimensional flow. [online] https://www.esdu.com/.

ETSU (1985). *Wave energy: the Department of Energy's R&D programme, 1974-1983, ETSU Report Number R-26*. Energy Technology Support Unit, AERE for the Department of Energy.

FERC (2010). Reedsport opt wave park settlement agreement. [online] https://elibrary.ferc.gov/idmws/File_list.asp?document_id=13836497. [Accessed September 2017].

Ferreira, C. J. S., Bijl, H., van Bussel, G., and van Kuik, G. (2007). Simulating dynamic stall in a 2d vawt: Modeling strategy, verification and validation with particle image velocimetry data. *Journal of Physics: Conference Series*, 75(1):12–23.

Ferro, B. D. (2006). Wave and tidal energy: Its emergence and the challenges it faces. *Refocus*, 7(3):46–48.

Fischer, A., de Almeida, L. E. B., and Beluco, A. (2016). Coverting energy from ocean currents. *International Journal of Research in Engineering and Technology*, 5(3):220–227.

Fraenkel, P. L. (2010). Development and testing of marine current turbine's seagen 1.2mw tidal stream turbine. In *3rd International Conference on Ocean Energy*. Marine Current Turbines Ltd.

Galpin, P. F., Broberg, R. B., and Hutchinson, B. R. (1995). Three-dimensional navier-stokes predictions of steady state rotor/stator interaction with pitch change.

Garrett, C. and Cummins, P. (2007). The efficiency of a turbine in a tidal channel. *Journal of Fluid Mechanics*, 588:243–251.

Gebreslassie, M. G., Sanchez, S. O., Tabor, G. R., Belmont, M. R., Bruce, T., Payne, G. S., and Moon, I. (2016). Experimental and cfd analysis of the wake characteristics of tidal turbines. *International Journal of Marine Energy*, 16:209 – 219.

Gorle, J. M. R., Chatellier, L., Pons, F., and Ba, M. (2014). Numerical analysis of hydrodynamics and circulation controlled blades for darrieus turbine. In *14èmes Journées de l'Hydrodynamique*, Chaussée du Vexin, 27105 Val de Reuil. DGA Techniques hydrodynamiques.

Gretton, G. (2009). *Hydrodynamic analysis of a vertical axis tidal current turbine*. Phd thesis, The University of Edinburgh.

Grove, A. S., Shair, F. H., Petersen, E. E., and Acrivos, A. (1964). An experimental investigation of the steady separated flow past a circular cylinder. *Journal of Fluid Mechanics*, 19(1):60.

Grylls, W., Dale, B., and Sarr, P. (1978). A theoretical and experimental investigation into the variable pitch vertical axis wind turbine. In *International Symposial on Wind Energy Systems*, volume 2, pages E–9.

Hain, R., Kahler, C. J., and Radespiel, R. (2009). Dynamics of laminar separation bubbles at low-reynolds-number aerofoils. *Journal of Fluid Mechanics*, 630:129–153.

Harris, M. (2016). Aws, trident sign agreement for wave energy tech development. [online] https://www.hydroworld.com/articles/2016/10/aws-trident-sign-agreement-for-wave-energy-tech-development.html. [Accessed September 2017].

Hill, C., Neary, V., Gunawan, B., Guala, M., and Sotiropoulos, F. (2014). U.s. department of energy reference model program rm2: Experimental results. Technical report, University of Minnesota, St. Anthony Falls Laboratory, College of Science & Engineering, University of Minnesota, Minneapolis, MN.

Hirsch, H. and Mandal, A. C. (1987). A cascade theory for the aerodynamic performance of darrieus wind turbines. *Wind Engineering*, 4(2):49–55.

Honji, H. and Taneda, S. (1969). Unsteady flow past a circular cylinder. *Journal of the Physical Society of Japan*, 27(6):1668.

Hwang, I. S., Lee, Y. H., and Kim, S. J. (2009). Optimization of cycloidal water turbine and the performance improvement by individual blade control. *Applied Energy*, 86(9):1532 – 1540.

Iaccarino, G., Ooi, A., Durbin, P. A., and Behnia, M. (2003). Reynolds averaged simulation of unsteady separated flow. *International Journal of Heat and Fluid Flow*, 24(2):147–156.

IPCC (2014). *Climate Change 2014: Synthesis Report. Contribution of Working Groups I, II and III to the Fifth Assessment Report of the Intergovernmental Panel on Climate Change.* IPCC, Geneva, Switzerland.

Issa, R. I. (1986). Solution of the implicitly discretized fluid-flow equations by operator-splitting. *Journal of Computational Physics*, 62(1):40–65.

Jacobs, E. and Sherman, A. (1937). *Report No. 586: Airfoil Section Characteristics as Affected by Variations of the Reynolds Number*. National Advisory Committee for Aeronautics: Report. NACA.

Jacobs, E. N., Ward, K. E., and Pinkerton, R. M. (1933). Report no. 460: The characteristics of 78 related airfoil sections from tests in the variable-density wind tunnel. Technical report, NACA, Washington DC.

Jagadeesh, P. and Murali, K. (2009). Application of low-re turbulence models for flow simulations past underwater vehicle hull forms. *Journal of Naval Architecture and Marine Engineering*, 2(1):41–54.

Jimenez, J. (2010). The contributions of a. n. kolmogorov to the theory of turbulence. *Arbor*, (704):589–606.

Kalitzin, G., Medic, G., Iaccarino, G., and Durbin, P. (2005). Near-wall behavior of rans turbulence models and implications for wall functions. *Journal of Computational Physics*, 204(1):265–291.

Karin, J. (2009). Hydropower from vortex induced vibrations. [online] Available at: http://thefutureofthings.com/3889-hydropower-from-vortex-induced-vibrations/. [Accessed September 2017].

Katofsky, R. (2008). Ocean energy: technology basics. *Renewable Energy Focus*, 9(3):34 – 36.

Kepler Energy (n.d.). About us. [online] http://www.keplerenergy.co.uk/about-html.php. [Accessed September 2017].

Khammas, A. A. W. (2007). Buch der synergie. [online] Available at: http://www.wavedragon.net/. [Accessed September 2017].

Kim, Y. and Xie, Z. (2016). Modelling the effect of freestream turbulence on dynamic stall of wind turbine blades. *Computers and Fluids*, 129:53–66.

Kirk, W. T., Capece, V. R., Pechlivanoglou, G., Nayeri, C. N., and Paschereit, C. O. (2014). Comparative study of cfd solver models for modeling of flow over wind turbine airfoils.

Lain, S. and Osorio, C. (2010). Simulation and evaluation of a straight-bladed darrieus-type cross flow marine turbine. *Journal of Scientific and Industrial Research (JSIR)*, 69:906–912.

Lain, S., Quintero, B., Trujillo, D., and Ulianov, Y. (2012). Simulation of vertical axis water turbines. In *Alternative Energies and Energy Quality (SIFAE)*. IEEE.

Langtry, R. B., Menter, F. R., Likki, S. R., Suzen, Y. B., Huang, P. G., and Volker, S. (2006). A correlation-based transition model using local variables - part ii: Test cases and industrial applications. *Journal of Turbomachinery-Transactions of the Asme*, 128(3):423–434.

Lanzafame, R., Mauro, S., and Messina, M. (2014). 2d cfd modeling of h-darrieus wind turbines using a transition turbulence model. *Energy Procedia*, 45(Supplement C):131 – 140. ATI 2013 - 68th Conference of the Italian Thermal Machines Engineering Association.

Lienhard, J. (1966). *Synopsis of Lift, Drag, and Vortex Frequency Data for Rigid Circular Cylinders*. Bulletin (Washington State University. College of Engineering. Research Division). Technical Extension Service, Washington State University.

Lin, J. C. M. and Pauley, L. L. (1996). Low-reynolds-number separation on an airfoil. *Aiaa Journal*, 34(8):1570–1577.

Lunar Energy Power Ltd. (n.d.). History and developement. [online] http://www.lunarenergy.co.uk/history.htm. [Accessed September 2017].

Lynn, P. A. (2013). *Electricity from Wave and Tide: An Introduction to Marine Energy*. John Wiley & Sons Ltd.

Malan, P. (2009). Calibrating the gamma-re theta transition model for commercial cfd. In *47th AIAA Aerospace Sciences Meeting Including The New Horizons Forum and Aerospace Exposition*, number 1142. AIAA.

Marine Current Turbine Ltd (2016). Marine current turbines. [online] http://www.lunarenergy.co.uk/history.htm. [Accessed September 2017].

Massey, B. S. (1989). *Mechanics of fluids*. Van Nostrand Reinhold, 6th ed. edition.

Maître, T., Amet, E., and Pellone, C. (2013). Modeling of the flow in a darrieus water turbine: Wall grid refinement analysis and comparison with experiments. *Renewable Energy*, 51:497–512.

Matyushenko, A. A. and Garbaruk, A. V. (2016). Adjustment of the k-w sst turbulence model for prediction of airfoil characteristics near stall. *Journal of Physics: Conference Series*, 769(1):012082.

McAdam, R. A., Houlsby, G. T., and Oldfield, M. L. G. (2013a). Experimental measurements of the hydrodynamic performance and structural loading of the transverse horizontal axis water turbine: Part 1. *Renewable Energy*, 59(0):105–114.

McAdam, R. A., Houlsby, G. T., and Oldfield, M. L. G. (2013b). Experimental measurements of the hydrodynamic performance and structural loading of the transverse horizontal axis water turbine: Part 2. *Renewable Energy*, 59:141–149.

McAdam, R. A., Houlsby, G. T., and Oldfield, M. L. G. (2013c). Experimental measurements of the hydrodynamic performance and structural loading of the transverse horizontal axis water turbine: Part 3. *Renewable Energy*, 59:82–91.

Mcmasters, J. H. and Henderson, M. L. (1979). Low-speed single element airfoil synthesis. *Technical Soaring*, 4(2):1–21.

Menter, F. R. (1994). 2-equation eddy-viscosity turbulence models for engineering applications. *Aiaa Journal*, 32(8):1598–1605.

Menter, F. R., Langtry, R., and Volker, S. (2006a). Transition modelling for general purpose cfd codes. *Flow Turbulence and Combustion*, 77(1-4):277–303.

Menter, F. R., Langtry, R. B., Likki, S. R., Suzen, Y. B., Huang, P. G., and Volker, S. (2006b). A correlation-based transition model using local variables - part i: Model formulation. *Journal of Turbomachinery-Transactions of the Asme*, 128(3):413–422.

Migliore, P. G., Wolfe, W. P., and Fanucci, J. B. (1980). Flow curvature effects on darrieus turbine blade aerodynamics. *Journal of Energy*, 4(2):49–55.

Miller, R. (2009). Scottish server farms team on tidal power. [online] http://www.datacenterknowledge.com/archives/2009/01/28/scottish-server-farms-team-on-tidal-power.htm. [Accessed September 2017].

Miller, R. P. (n.d.). Development of a proposal for a technology assessment report: Wave energy devices. [online] http://rosspmiller.weebly.com/wave-devices.html. [Accessed September 2017].

Morgado, J., Vizinho, R., Silvestre, M., and PÃ¡scoa, J. (2016). Xfoil vs cfd performance predictions for high lift low reynolds number airfoils. *Aerospace Science and Technology*, 52:207 – 214.

NASA (2017). Sp-367 introduction to the aerodynamics of flight. Online. Accessed 08/01/17.

Neptune Renewable Energy (2010). Tidal technology - the neptune proteus mark iii. [online] http://www.neptunerenewableenergy.com/tidal-technology-the-neptune-proteus-mark-iii/. [Accessed September 2017].

New Energy Corporation Inc. (n.d.). New energy - photo gallery. [online] http://www.newenergycorp.ca/gallery.html. [Accessed September 2017].

Norberg, C. (2003). Fluctuating lift on a circular cylinder: review and new measurements. *Journal of Fluids and Structures*, 17(1):57–96.

Ocean Flow Energy (nd). Evopod tidal turbine technology. [online] http://www.oceanflowenergy.com/index.html. [Accessed September 2017].

Ong, M. C., Utnes, T., Holmedal, L. E., Myrhaug, D., and Pettersen, B. (2009). Numerical simulation of flow around a smooth circular cylinder at very high reynolds numbers. *Marine Structures*, 22(2):142–153.

Paillard, B., Astolfi, J., and Hauville, F. (2015). Uranse simulation of an active variable-pitch cross-flow darrieus tidal turbine: Sinusoidal pitch function investigation. *International Journal of Marine Energy*, 11:9–26.

Paraschivoiu, I. (1988). Double-multiple streamtube model for studying vertical-axis wind turbines. *Journal of Propulsion and Power*, 4(4):370–377.

Park, J., Kwon, K., and Choi, H. (1998). Numerical solutions of flow past a circular cylinder at reynolds numbers up to 160. *Journal of Mechanical Science and Technology*, 12(6):1200–1205.

Patel, S. (2011). Changing winds: The evolving wind turbine. [online] http://www.powermag.com/changing-winds-the-evolving-wind-turbine/. [Accessed September 2009].

Peyret, R. (1996). *Handbook of Computational Fluid Mechanics*. Academic Press Ltd, Nice.

QinetiQ Ltd. (1994). Cycloidal power generation - phase 2. Technical report, QinetiQ Ltd. T/06/00229/00/REP/2.

Raghavan, K. and Bernitsas, M. M. (2011). Experimental investigation of reynolds number effect on vortex induced vibration of rigid circular cylinder on elastic supports. *Ocean Engineering*, 38(5-6):719–731.

Rahman, M. M., Karim, M. M., and Alim, M. A. (2008). Numerical investigation of unsteady flow past a circular cylinder using 2-d finite volume method. *Journal of Naval Architecture and Marine Engineering*, 4:27–42.

ReNew (2007). Unconventional wind turbines. *ReNew: Technology for a Sustainable Future*, (101):32–35.

reNews (2016). Atlantis to decommission seagen. [online] http://renews.biz/101295/atlantis-to-decommission-seagen/. [Accessed September 2017].

Rosenfeld, M. and Kwak, D. (1988). Numerical simulation of unsteady incompressible viscous flows in generalized coordinate systems. Technical report, NASA Technical Memorandum 101016.

Roshko, A. (1955). On the wake and drag of bluff bodies. *Journal of the Aeronautical Sciences*, 22(2):124–132.

Ross, D. (1995). *Power from the waves*. Oxford University Press.

Rumsey, C. L. and Spalart, P. R. (2009). Turbulence model behavior in low reynolds number regions of aerodynamic flowfields. *Aiaa Journal*, 47(4):982–993.

Salter, S. H. (1975). Apparatus and method for extracting wave energy. Patent. US 3,928,967.

Santhanakrishnan, A., Pern, N., Ramakumar, K., and Jacob, J. (2005). Enabling flow control technology for low speed uavs. In *Infotech@Aerospace Conferences*. American Institute of Aeronautics and Astronautics.

Savonius, S. J. (1929). Rotor adapted to be driven by wind or flowing water. Patent. US 1,697,574.

Scheider, E., Ehrhart, J., and Kreitner, J. (1931). Blade wheel with moveable blade. Patent. US 1,823,169.

Schlichting, H. and Gersten, K. (2016). *Boundary-Layer Theory*. Springer Berlin Heidelberg.

Schluntz, J. and Willden, R. (2015). The effect of blockage on tidal turbine rotor design and performance. *Renewable Energy*, 81(Supplement C):432 – 441.

Selig, M. (2003). Low reynolds number airfoil design lecture notes. In *VKI Lecture Series, Applied Vehicle Technology Panel*, pages 24–28.

Selig, M., Guglielmo, J., Broeren, A., and Giguere, P. (1996). Experiments on airfoils at low reynolds numbers. In *Aerospace Sciences Meetings*. American Institute of Aeronautics and Astronautics.

Shan, H., Jiang, L., and Liu, C. Q. (2005). Direct numerical simulation of flow separation around a naca 0012 airfoil. *Computers & Fluids*, 34(9):1096–1114.

Shih, W. C. L., Wang, C., Coles, D., and Roshko, A. (1993). Experiments on flow past rough circular-cylinders at large reynolds-numbers. *Journal of Wind Engineering and Industrial Aerodynamics*, 49(1-3):351–368.

Soraghan, C. E., Leithead, W. E., Feuchtwang, J., and Yue, H. (2013). Double multiple streamtube model for variable pitch vertical axis wind turbines. In *Fluid Dynamics and Co-located Conferences*, pages –. American Institute of Aeronautics and Astronautics.

South, P. and Rangi, R. S. (1971). Preliminary tests of a high speed vertical axis wind mill model. Technical Report Report No. LTR-LA-74, National Research Council of Canada.

Spalding, D. B. (1961). A single formula for the law of the wall. *Trans ASME Series A, J. Appl. Mech.*, 28(3):444–458.

Stern, N. (2007). *The Economics of Climate Change: The Stern Review*. Cambridge University Press.

Strickland, J. and Department, S. L. A. E. P. (1975). *The Darrieus Turbine: A Performance Prediction Model Using Multiple Streamtubes*. SAND. Sandia Laboratories.

Strickland, J., Webster, B., and Nyugen, T. (1981). Vortex model of the darrieus turbine: An analytical and experimental study. technical report, sand81-7017. Technical report, Sandia National Laboratories, U.S.

Taneda, S. (1956). Experimental investigation of the wakes behind cylinders and plates at low reynolds numbers. *Journal of the Physical Society of Japan*, 11(3):302–307.

Tang, L. (2008). Reynolds-averaged navier-stokes simulation of low-reynolds-number airfoil aerodynamics. *Journal of Aircraft*, 45(3):848–856.

Templin, R. (1974). *Aerodynamic Performance Theory for the NRC Vertical-axis Wind Turbine*. Laboratory technical report - National Research Council Canada, National Aeronautical Establishment. National Research Council Canada, National Aeronautical Establishment.

The Met Office (2014). Cop20 - climate risk- an update on the science. [online] Available from: https://www.metoffice.gov.uk. [Accessed September 2017].

The Watt Committee on Energy (2005). *Renewable Energy Sources*. Number Report 22. Elsevier Applied Science.

Timmer, W. (2008). Two-dimensional low-reynolds number wind tunnel results for airfoil naca 0018. *Wind Engineering*, 32(6):525–537.

Todkar, V., Shinde, G., Kamble, S., and Gunavant, P. (2017). An overviewof wind mills. In *National Conference on Design, Manufacturing, Energy&Thermal Engineering(NCDMETE-2017)*, volume 4.

Tritton, D. J. (1959). Experiments on the flow past a circular cylinder at low reynolds numbers. *Journal of Fluid Mechanics*, 6(4):547.

Tutar, M. and Holdo, A. E. (2001). Computational modelling of flow around a circular cylinder in sub-critical flow regime with various turbulence models. *International Journal for Numerical Methods in Fluids*, 35(7):763–784.

Uranga Cabrera, A. (2010). *Investigation of transition to turbulence at low Reynolds numbers using Implicit Large Eddy Simulations with a Discontinuous Galerkin method*. Phd, Massachusetts Institute of Technology.

Wang, S. Y., Ingham, D. B., Ma, L., Pourkashanian, M., and Tao, Z. (2010). Numerical investigations on dynamic stall of low reynolds number flow around oscillating airfoils. *Computers & Fluids*, 39(9):1529–1541.

Wave Dragon (n.d.). Wave dragon energy converter. [online] Available at: http://www.wavedragon.net/. [Accessed September 2017].

Westwood, A. (2004). Ocean power: Wave and tidal energy review. *Refocus*, 5(5):50–55.

Whelan, J., Graham, J. M. R., and Peiro, J. (2009). A free-surface and blockage correction for tidal turbines. *Journal of Fluid Mechanics*, 624:281–291.

Whelan, J. and Stallard, T. (2011). Arguments for modifying the geometry of a scale model rotor. In Bahaj, A. E., editor, *Proceedings of the 8th European Wave and Tidal Energy Conference*, number 50, Southampton, UK,.

Wieselsberger, C., Betz, A., and Prandtl, L. (1923). *Ergebnisse der aerodynamischen Versuchsanstalt zu Gottingen I.[-II.] Lieferung*. Muchen u. Berlin.

Wilcox, D. C. (1993). A two-equation turbulence model for wall-bounded and free-shear flows.

Williamson, C. H. K. (1996). Vortex dynamics in the cylinder wake. *Annual Review of Fluid Mechanics*, 28:477–539.

Windte, J., Scholz, U., and Radespiel, R. (2006). Validation of the rans-simulation of laminar separation bubbles on airfoils. *Aerospace Science and Technology*, 10(6):484–494.

Xia, J. Q., Falconer, R. A., and Lin, B. L. (2010). Impact of different operating modes for a severn barrage on the tidal power and flood inundation in the severn estuary, uk. *Applied Energy*, 87(7):2374–2391.

Yarusevych, S., Sullivan, P. E., and Kawall, J. G. (2009). On vortex shedding from an airfoil in low-reynolds-number flows. *Journal of Fluid Mechanics*, 632:245–271.

Yuan, W., Xu, H., Khalid, M., and Radespiel, R. (2006). A parametric study of les on laminar-turbulent transitional flows past an airfoil. *International Journal of Computational Fluid Dynamics*, 20(1):45–54.

Zdravkovich, M. M. (1990). Conceptual overview of laminar and turbulent flows past smooth and rough circular-cylinders. *Journal of Wind Engineering and Industrial Aerodynamics*, 33(1-2):53–62.

Zhang, L., Wang, L.-B., Li, F.-L., and Zhang, G.-X. (2004). Streamtube models for performance prediction of vertical-axis variable-pitch turbine for tidal current energy conversion. *J Harbin Eng Univ*, 25:261–266.

Appendix A

Isolated Blade Data

A.1 Matlab blade profile generation

Blade profiles used in the research were based on the NACA four-digit series. Matlab was used to generate point clouds that could be interpolated in CAD to form 2D and 3D solids. The matlab code is given below, note that the blade is defined, located and scaled as required by the code (see annotations). The resultant point clouds include the straight blade and circumferentially wrapped versions.

```
function [] = FoilCoords()

clc;
p = 25; %position of pivot, % from leading edge
t = 18; %thickness, % relative to chord
c = 65.45; %chord length, mm
r = 250; %radius of blade pivot from turbine center, mm
i = 100; %number of points for each surface (upper & lower
x0 = 1.0089304113651427093; %exact value of x, where y=0 at trailing edge
ix = [1:1:i-1]; %index of x points
x = 1-cos(degtorad((ix-1).*(90/(i-2)))); %cosine distribution of x
x = [x x0]; %addition of trailing edge x coordinate to the array

%generation of x & y coordinates
yu = (t/100/0.2)*(0.2969*x.^0.5-0.126*x-0.3516*x.^2+0.2843*x.^3-0.1015*x.^4);
xx = x-(p/100); %reposition of x coordinates to pivot position
yl = -yu; %symmetrical aerofoil therefore y lower equal y uppper

%scale straight blade coordinates to correct chord length
xu1 = xx.*c;
yu1 = r+ (yu.*c);
xl1 = xx.*c;
yl1 = r+ (yl.*c);
```

```
%scale and transform wrapped blades (experimental geometry)
xu2 = (r+(yu.*c)).*(sin((xx.*c)/r));
yu2 = (r+(yu.*c)).*(cos((xx.*c)/r));
xl2 = (r+(yl.*c)).*(sin((xx.*c)/r));
yl2 = (r+(yl.*c)).*(cos((xx.*c)/r));

end
```

A.2 Mesh parameter study data - CFD

All data is calculated for an isolated blade at $Re = 3.15 \times 10^6$. Each test case is calculated at 0, 4, 8, 12, 16 and 20 degrees angle of attack (α); named AoA in the table below. The accuracy of each test group (identified in first column) is calculated as a mean error of cases tested at 4, 8, 12 and 16 AoA (highlighted in grey) from experimental data given in appendix section A.3.

Test Group	Name	AoA	Inflation First Layer Height (y1)	Number of Layers	Layer Growth Ratio	Surface Divisions	Surface Bias	Mesh Growth Ratio	Max Element Size	CL	CD	y+ Max	y+ Min	CM	Blade Domain Nodes	Fixed Domain Nodes	CL % error	CD % error	abs CL % error	abs CD % error	Group Avg % error	Group Max CL % error	Group Max CD % error
1	1	0	1E-6	30	1.2	250	1	1.05	2.5E-3	0.001	0.010	2.34	0.03	5.5E-6	69860	47668	-494.5%	6.9%	494.5%	6.9%			
	2	4	1E-6	30	1.2	250	1	1.05	2.5E-3	0.411	0.011	2.86	0.07	-5.6E-4	69860	47668	-2.4%	1.7%	2.4%	1.7%			
	3	8	1E-6	30	1.2	250	1	1.05	2.5E-3	0.810	0.014	3.55	0.15	-1.1E-3	69860	47668	-1.9%	-0.4%	1.9%	0.4%			
	4	12	1E-6	30	1.2	250	1	1.05	2.5E-3	1.163	0.019	4.37	0.04	-1.9E-3	69860	47668	-0.1%	0.3%	0.1%	0.3%			
	5	16	1E-6	30	1.2	250	1	1.05	2.5E-3	1.408	0.033	5.14	0.04	-2.6E-3	69860	47668	2.9%	3.1%	2.9%	3.1%			
	6	20	1E-6	30	1.2	250	1	1.05	2.5E-3	1.115	0.113	5.09	0.06	-3.4E-4	69860	47668	13.0%	35.6%	13.0%	35.6%	1.60%	2.86%	3.08%
2	7	0	5E-5	30	1.2	250	1	1.05	2.5E-3	0.000	0.010	110.4	0.74	2.2E-6	56326	47668	-153.9%	7.6%	153.9%	7.6%			
	8	4	5E-5	30	1.2	250	1	1.05	2.5E-3	0.418	0.011	130.7	1.52	-4.6E-4	56326	47668	-4.2%	2.9%	4.2%	2.9%			
	9	8	5E-5	30	1.2	250	1	1.05	2.5E-3	0.824	0.013	158.0	1.39	-9.5E-4	56326	47668	-3.7%	1.8%	3.7%	1.8%			
	10	12	5E-5	30	1.2	250	1	1.05	2.5E-3	1.198	0.018	189.0	1.50	-1.6E-3	56326	47668	-3.2%	7.2%	3.2%	7.2%			
	11	16	5E-5	30	1.2	250	1	1.05	2.5E-3	1.490	0.027	218.3	1.87	-2.4E-3	56326	47668	-2.8%	19.4%	2.8%	19.4%			
	12	20	5E-5	30	1.2	250	1	1.05	2.5E-3	1.549	0.059	235.5	2.26	-2.4E-3	56326	47668	-20.9%	66.3%	20.9%	66.3%	5.66%	4.19%	19.37%
3	13	0	1E-5	30	1.2	250	1	1.05	2.5E-3	0.000	0.011	23.65	0.35	4.6E-6	62768	47668	-186.4%	2.5%	186.4%	2.5%			
	14	4	1E-5	30	1.2	250	1	1.05	2.5E-3	0.411	0.012	28.25	1.01	-5.7E-4	62768	47668	-2.4%	-2.0%	2.4%	2.0%			
	15	8	1E-5	30	1.2	250	1	1.05	2.5E-3	0.809	0.014	35.12	1.23	-1.2E-3	62768	47668	-1.7%	-3.4%	1.7%	3.4%			
	16	12	1E-5	30	1.2	250	1	1.05	2.5E-3	1.166	0.019	42.70	0.14	-1.9E-3	62768	47668	-0.4%	-0.7%	0.4%	0.7%			
	17	16	1E-5	30	1.2	250	1	1.05	2.5E-3	1.402	0.033	48.85	0.79	-2.6E-3	62768	47668	3.3%	2.5%	3.3%	2.5%			
	18	20	1E-5	30	1.2	250	1	1.05	2.5E-3	1.129	0.105	47.92	0.77	-1.0E-3	62768	47668	11.9%	40.4%	11.9%	40.4%	2.05%	3.26%	3.39%
4	19	0	5E-6	30	1.2	250	1	1.05	2.5E-3	0.001	0.011	12.13	0.09	9.3E-6	64756	47668	-462.3%	0.8%	462.3%	0.8%			
	20	4	5E-6	30	1.2	250	1	1.05	2.5E-3	0.409	0.012	14.56	0.50	-5.9E-4	64756	47668	-1.9%	-3.9%	1.9%	3.9%			
	21	8	5E-6	30	1.2	250	1	1.05	2.5E-3	0.801	0.014	17.99	0.40	-1.2E-3	64756	47668	-0.8%	-6.8%	0.8%	6.8%			
	22	12	5E-6	30	1.2	250	1	1.05	2.5E-3	1.158	0.020	21.81	0.27	-1.9E-3	64756	47668	0.3%	-5.2%	0.3%	5.2%			
	23	16	5E-6	30	1.2	250	1	1.05	2.5E-3	1.383	0.035	25.09	0.23	-2.7E-3	64756	47668	4.6%	-2.3%	4.6%	2.3%			
	24	20	5E-6	30	1.2	250	1	1.05	2.5E-3	1.022	0.122	23.67	0.67	-1.6E-4	64756	47668	20.3%	30.2%	20.3%	30.2%	3.24%	4.58%	6.84%
5	25	0	5E-7	30	1.2	250	1	1.05	2.5E-3	0.000	0.010	1.18	0.03	3.4E-6	71440	47668	-84.7%	5.6%	84.7%	5.6%			
	26	4	5E-7	30	1.2	250	1	1.05	2.5E-3	0.409	0.011	1.44	0.02	-5.9E-4	71440	47668	-2.1%	1.2%	2.1%	1.2%			
	27	8	5E-7	30	1.2	250	1	1.05	2.5E-3	0.806	0.014	1.77	0.02	-1.2E-3	71440	47668	-1.5%	-1.2%	1.5%	1.2%			
	28	12	5E-7	30	1.2	250	1	1.05	2.5E-3	1.162	0.019	2.16	0.02	-1.9E-3	71440	47668	-0.1%	1.6%	0.1%	1.6%			
	29	16	5E-7	30	1.2	250	1	1.05	2.5E-3	1.425	0.031	2.50	0.02	-2.7E-3	71440	47668	1.7%	8.0%	1.7%	8.0%			
	30	20	5E-7	30	1.2	250	1	1.05	2.5E-3	1.379	0.078	2.65	0.02	-1.9E-3	71440	47668	-7.6%	55.5%	7.6%	55.5%	2.16%	2.08%	7.96%
6	31	0	1E-5	10	1.2	250	1	1.05	2.5E-3	0.000	0.011	23.65	0.35	4.6E-6	62768	47668	-186.4%	2.5%	186.4%	2.5%			
	32	4	1E-5	10	1.2	250	1	1.05	2.5E-3	0.411	0.012	28.25	1.01	-5.7E-4	62768	47668	-2.4%	-2.0%	2.4%	2.0%			
	33	8	1E-5	10	1.2	250	1	1.05	2.5E-3	0.809	0.014	35.12	1.23	-1.2E-3	62768	47668	-1.7%	-3.4%	1.7%	3.4%			
	34	12	1E-5	10	1.2	250	1	1.05	2.5E-3	1.166	0.019	42.70	0.14	-1.9E-3	62768	47668	-0.4%	-0.7%	0.4%	0.7%			
	35	16	1E-5	10	1.2	250	1	1.05	2.5E-3	1.402	0.033	48.85	0.79	-2.6E-3	62768	47668	3.3%	2.5%	3.3%	2.5%			
	36	20	1E-5	10	1.2	250	1	1.05	2.5E-3	1.129	0.105	47.92	0.77	-1.0E-3	62768	47668	11.9%	40.4%	11.9%	40.4%	2.05%	3.26%	3.39%
7	37	0	1E-5	20	1.2	250	1	1.05	2.5E-3	0.000	0.011	23.65	0.35	4.6E-6	62768	47668	-186.4%	2.5%	186.4%	2.5%			
	38	4	1E-5	20	1.2	250	1	1.05	2.5E-3	0.411	0.012	28.25	1.01	-5.7E-4	62768	47668	-2.4%	-2.0%	2.4%	2.0%			
	39	8	1E-5	20	1.2	250	1	1.05	2.5E-3	0.809	0.014	35.12	1.23	-1.2E-3	62768	47668	-1.7%	-3.4%	1.7%	3.4%			
	40	12	1E-5	20	1.2	250	1	1.05	2.5E-3	1.166	0.019	42.70	0.14	-1.9E-3	62768	47668	-0.4%	-0.7%	0.4%	0.7%			
	41	16	1E-5	20	1.2	250	1	1.05	2.5E-3	1.402	0.033	48.85	0.79	-2.6E-3	62768	47668	3.3%	2.5%	3.3%	2.5%			
	42	20	1E-5	20	1.2	250	1	1.05	2.5E-3	1.129	0.105	47.92	0.77	-1.0E-3	62768	47668	11.9%	40.4%	11.9%	40.4%	2.05%	3.26%	3.39%
8	43	0	1E-5	40	1.2	250	1	1.05	2.5E-3	0.000	0.011	23.65	0.35	4.6E-6	62768	47668	-186.4%	2.5%	186.4%	2.5%			
	44	4	1E-5	40	1.2	250	1	1.05	2.5E-3	0.411	0.012	28.25	1.01	-5.7E-4	62768	47668	-2.4%	-2.0%	2.4%	2.0%			
	45	8	1E-5	40	1.2	250	1	1.05	2.5E-3	0.809	0.014	35.12	1.23	-1.2E-3	62768	47668	-1.7%	-3.4%	1.7%	3.4%			
	46	12	1E-5	40	1.2	250	1	1.05	2.5E-3	1.166	0.019	42.70	0.14	-1.9E-3	62768	47668	-0.4%	-0.7%	0.4%	0.7%			
	47	16	1E-5	40	1.2	250	1	1.05	2.5E-3	1.402	0.033	48.85	0.79	-2.6E-3	62768	47668	3.3%	2.5%	3.3%	2.5%			
	48	20	1E-5	40	1.2	250	1	1.05	2.5E-3	1.129	0.105	47.92	0.77	-1.0E-3	62768	47668	11.9%	40.4%	11.9%	40.4%	2.05%	3.26%	3.39%
9	49	0	1E-5	30	1.1	250	1	1.05	2.5E-3	0.000	0.011	23.63	0.49	5.3E-6	68488	47668	-227.5%	2.8%	227.5%	2.8%			
	50	4	1E-5	30	1.1	250	1	1.05	2.5E-3	0.412	0.011	28.19	1.02	-5.5E-4	68488	47668	-2.7%	-1.6%	2.7%	1.6%			
	51	8	1E-5	30	1.1	250	1	1.05	2.5E-3	0.811	0.014	35.10	1.23	-1.1E-3	68488	47668	-2.0%	-3.2%	2.0%	3.2%			
	52	12	1E-5	30	1.1	250	1	1.05	2.5E-3	1.172	0.020	42.59	0.48	-1.8E-3	68488	47668	-1.0%	-1.6%	1.0%	1.6%			
	53	16	1E-5	30	1.1	250	1	1.05	2.5E-3	1.416	0.032	49.00	0.58	-2.6E-3	68488	47668	2.3%	5.3%	2.3%	5.3%			
	54	20	1E-5	30	1.1	250	1	1.05	2.5E-3	1.129	0.104	47.84	0.99	-1.0E-3	68488	47668	11.9%	40.5%	11.9%	40.5%	2.46%	2.69%	5.27%
10	55	0	1E-5	30	1.3	250	1	1.05	2.5E-3	0.000	0.011	23.70	0.23	4.4E-6	60794	47668	-176.0%	2.1%	176.0%	2.1%			
	56	4	1E-5	30	1.3	250	1	1.05	2.5E-3	0.410	0.012	28.34	1.01	-5.8E-4	60794	47668	-2.1%	-2.5%	2.1%	2.5%			
	57	8	1E-5	30	1.3	250	1	1.05	2.5E-3	0.806	0.014	35.15	1.23	-1.2E-3	60794	47668	-1.4%	-4.0%	1.4%	4.0%			
	58	12	1E-5	30	1.3	250	1	1.05	2.5E-3	1.161	0.020	42.63	0.37	-1.9E-3	60794	47668	0.0%	-1.6%	0.0%	1.6%			
	59	16	1E-5	30	1.3	250	1	1.05	2.5E-3	1.387	0.034	48.80	0.67	-2.7E-3	60794	47668	4.3%	-0.7%	4.3%	0.7%			
	60	20	1E-5	30	1.3	250	1	1.05	2.5E-3	1.187	0.100	48.83	0.86	-1.2E-3	60794	47668	7.4%	43.1%	7.4%	43.1%	2.08%	4.32%	3.97%

11	61	0	1E-5	30	1.2	150	1	1.05	2.5E-3	-0.001	0.011	23.53	0.56	-1.2E-5	45990	47668	874.7%	2.7%	874.7%	2.7%			
	62	4	1E-5	30	1.2	150	1	1.05	2.5E-3	0.411	0.011	28.07	3.43	-5.6E-4	45990	47668	-2.6%	-1.8%	2.6%	1.8%			
	63	8	1E-5	30	1.2	150	1	1.05	2.5E-3	0.807	0.014	36.32	0.40	-1.1E-3	45990	47668	-1.6%	-5.1%	1.6%	5.1%			
	64	12	1E-5	30	1.2	150	1	1.05	2.5E-3	1.168	0.020	44.32	0.64	-1.8E-3	45990	47668	-0.6%	-1.3%	0.6%	1.3%			
	65	16	1E-5	30	1.2	150	1	1.05	2.5E-3	1.406	0.033	51.92	0.24	-2.6E-3	45990	47668	3.0%	1.7%	3.0%	1.7%			
	66	20	1E-5	30	1.2	150	1	1.05	2.5E-3	1.150	0.103	61.24	1.51	-1.0E-3	45990	47668	10.3%	41.1%	10.3%	41.1%	2.22%	3.02%	5.07%
12	67	0	1E-5	30	1.2	200	1	1.05	2.5E-3	0.000	0.011	23.59	0.41	3.4E-6	54552	47668	-115.8%	2.6%	115.8%	2.6%			
	68	4	1E-5	30	1.2	200	1	1.05	2.5E-3	0.411	0.011	28.07	1.26	-5.7E-4	54552	47668	-2.4%	-1.8%	2.4%	1.8%			
	69	8	1E-5	30	1.2	200	1	1.05	2.5E-3	0.808	0.014	35.11	1.39	-1.2E-3	54552	47668	-1.7%	-3.6%	1.7%	3.6%			
	70	12	1E-5	30	1.2	200	1	1.05	2.5E-3	1.167	0.020	42.54	0.43	-1.9E-3	54552	47668	-0.5%	-1.2%	0.5%	1.2%			
	71	16	1E-5	30	1.2	200	1	1.05	2.5E-3	1.405	0.033	48.83	1.13	-2.6E-3	54552	47668	3.1%	2.3%	3.1%	2.3%			
	72	20	1E-5	30	1.2	200	1	1.05	2.5E-3	1.128	0.106	47.69	0.38	-9.0E-4	54552	47668	12.0%	39.6%	12.0%	39.6%	2.07%	3.08%	3.59%
13	73	0	1E-5	30	1.2	300	1	1.05	2.5E-3	0.000	0.011	23.60	0.27	2.6E-6	67998	47668	-66.8%	2.5%	66.8%	2.5%			
	74	4	1E-5	30	1.2	300	1	1.05	2.5E-3	0.410	0.012	28.32	0.68	-5.8E-4	67998	47668	-2.3%	-2.0%	2.3%	2.0%			
	75	8	1E-5	30	1.2	300	1	1.05	2.5E-3	0.808	0.014	35.17	0.86	-1.2E-3	67998	47668	-1.7%	-3.4%	1.7%	3.4%			
	76	12	1E-5	30	1.2	300	1	1.05	2.5E-3	1.166	0.019	42.69	0.45	-1.9E-3	67998	47668	-0.4%	-0.9%	0.4%	0.9%			
	77	16	1E-5	30	1.2	300	1	1.05	2.5E-3	1.404	0.033	48.95	0.71	-2.6E-3	67998	47668	3.1%	3.0%	3.1%	3.0%			
	78	20	1E-5	30	1.2	300	1	1.05	2.5E-3	1.119	0.106	47.79	0.84	-9.9E-4	67998	47668	12.7%	39.8%	12.7%	39.8%	2.11%	3.11%	3.37%
14	79	0	1E-5	30	1.2	350	1	1.05	2.5E-3	0.000	0.011	23.68	0.09	5.3E-7	76188	47668	84.8%	2.4%	84.8%	2.4%			
	80	4	1E-5	30	1.2	350	1	1.05	2.5E-3	0.410	0.012	28.39	0.59	-5.8E-4	76188	47668	-2.3%	-2.1%	2.3%	2.1%			
	81	8	1E-5	30	1.2	350	1	1.05	2.5E-3	0.809	0.014	35.26	0.75	-1.2E-3	76188	47668	-1.7%	-3.5%	1.7%	3.5%			
	82	12	1E-5	30	1.2	350	1	1.05	2.5E-3	1.167	0.020	42.73	0.18	-1.8E-3	76188	47668	-0.5%	-1.6%	0.5%	1.6%			
	83	16	1E-5	30	1.2	350	1	1.05	2.5E-3	1.404	0.033	48.98	0.56	-2.6E-3	76188	47668	3.2%	2.9%	3.2%	2.9%			
	84	20	1E-5	30	1.2	350	1	1.05	2.5E-3	1.124	0.105	47.99	0.66	-1.1E-3	76188	47668	12.3%	40.2%	12.3%	40.2%	2.22%	3.15%	3.46%
15	85	0	1E-5	30	1.2	250	2	1.05	2.5E-3	0.000	0.011	23.63	0.31	1.1E-6	60284	47668	9.2%	2.5%	9.2%	2.5%			
	86	4	1E-5	30	1.2	250	2	1.05	2.5E-3	0.410	0.012	28.37	0.57	-5.8E-4	60284	47668	-2.3%	-2.1%	2.3%	2.1%			
	87	8	1E-5	30	1.2	250	2	1.05	2.5E-3	0.809	0.014	35.20	0.72	-1.2E-3	60284	47668	-1.8%	-3.2%	1.8%	3.2%			
	88	12	1E-5	30	1.2	250	2	1.05	2.5E-3	1.166	0.019	42.74	0.31	-1.9E-3	60284	47668	-0.4%	-0.6%	0.4%	0.6%			
	89	16	1E-5	30	1.2	250	2	1.05	2.5E-3	1.401	0.033	48.97	0.98	-2.7E-3	60284	47668	3.3%	2.9%	3.3%	2.9%			
	90	20	1E-5	30	1.2	250	2	1.05	2.5E-3	1.144	0.103	48.26	0.48	-1.1E-3	60284	47668	10.8%	41.2%	10.8%	41.2%	2.07%	3.34%	3.18%
16	91	0	1E-5	30	1.2	250	3	1.05	2.5E-3	0.000	0.011	23.67	0.12	2.5E-7	60854	47668	76.6%	2.5%	76.6%	2.5%			
	92	4	1E-5	30	1.2	250	3	1.05	2.5E-3	0.410	0.012	28.42	0.48	-5.8E-4	60854	47668	-2.3%	-2.1%	2.3%	2.1%			
	93	8	1E-5	30	1.2	250	3	1.05	2.5E-3	0.809	0.014	35.26	0.58	-1.2E-3	60854	47668	-1.8%	-3.2%	1.8%	3.2%			
	94	12	1E-5	30	1.2	250	3	1.05	2.5E-3	1.166	0.019	42.80	0.28	-1.9E-3	60854	47668	-0.5%	-0.5%	0.5%	0.5%			
	95	16	1E-5	30	1.2	250	3	1.05	2.5E-3	1.400	0.033	48.99	0.29	-2.7E-3	60854	47668	3.4%	2.9%	3.4%	2.9%			
	96	20	1E-5	30	1.2	250	3	1.05	2.5E-3	1.117	0.106	47.82	1.19	-9.3E-4	60854	47668	12.8%	39.4%	12.8%	39.4%	2.08%	3.41%	3.16%
17	97	0	1E-5	30	1.2	250	1	1.025	2.5E-3	0.000	0.011	23.57	0.03	2.2E-6	107504	47668	-46.1%	3.3%	46.1%	3.3%			
	98	4	1E-5	30	1.2	250	1	1.025	2.5E-3	0.411	0.011	28.24	1.22	-5.6E-4	107504	47668	-2.5%	-1.1%	2.5%	1.1%			
	99	8	1E-5	30	1.2	250	1	1.025	2.5E-3	0.807	0.014	35.16	1.35	-1.2E-3	107504	47668	-1.5%	-3.5%	1.5%	3.5%			
	100	12	1E-5	30	1.2	250	1	1.025	2.5E-3	1.164	0.020	42.59	0.41	-1.9E-3	107504	47668	-0.3%	-1.3%	0.3%	1.3%			
	101	16	1E-5	30	1.2	250	1	1.025	2.5E-3	1.392	0.033	48.75	0.30	-2.7E-3	107504	47668	4.0%	3.7%	4.0%	3.7%	2.23%	3.96%	3.69%
18	103	0	1E-5	30	1.2	250	1	1.075	2.5E-3	0.000	0.011	23.64	0.22	1.8E-6	52980	47668	-12.1%	1.6%	12.1%	1.6%			
	104	4	1E-5	30	1.2	250	1	1.075	2.5E-3	0.412	0.012	28.27	0.97	-5.6E-4	52980	47668	-2.6%	-3.1%	2.6%	3.1%			
	105	8	1E-5	30	1.2	250	1	1.075	2.5E-3	0.812	0.014	35.13	1.21	-1.1E-3	52980	47668	-2.1%	-4.8%	2.1%	4.8%			
	106	12	1E-5	30	1.2	250	1	1.075	2.5E-3	1.173	0.020	42.74	0.13	-1.8E-3	52980	47668	-1.0%	-2.2%	1.0%	2.2%			
	107	16	1E-5	30	1.2	250	1	1.075	2.5E-3	1.420	0.033	49.12	0.40	-2.5E-3	52980	47668	2.1%	1.6%	2.1%	1.6%			
	108	20	1E-5	30	1.2	250	1	1.075	2.5E-3	1.156	0.105	48.23	1.06	-8.5E-4	52980	47668	9.8%	39.8%	9.8%	39.8%	2.44%	2.63%	4.79%
19	109	0	1E-5	30	1.2	250	1	1.1	2.5E-3	0.000	0.011	23.68	0.38	2.2E-6	49606	47668	9.5%	0.6%	9.5%	0.6%			
	110	4	1E-5	30	1.2	250	1	1.1	2.5E-3	0.412	0.012	28.29	1.03	-5.4E-4	49606	47668	-2.8%	-4.4%	2.8%	4.4%			
	111	8	1E-5	30	1.2	250	1	1.1	2.5E-3	0.814	0.014	35.09	1.27	-1.1E-3	49606	47668	-2.4%	-6.3%	2.4%	6.3%			
	112	12	1E-5	30	1.2	250	1	1.1	2.5E-3	1.177	0.020	42.72	0.33	-1.7E-3	49606	47668	-1.4%	-4.2%	1.4%	4.2%			
	113	16	1E-5	30	1.2	250	1	1.1	2.5E-3	1.431	0.034	49.25	0.43	-2.4E-3	49606	47668	1.3%	0.8%	1.3%	0.8%			
	114	20	1E-5	30	1.2	250	1	1.1	2.5E-3	1.164	0.108	48.22	0.68	-4.9E-4	49606	47668	9.2%	38.4%	9.2%	38.4%	2.95%	2.85%	6.34%
20	115	0	1E-5	30	1.2	250	1	1.2	2.5E-3	0.000	0.012	23.71	0.61	8.3E-6	46096	47668	-400.0%	-4.5%	400.0%	4.5%			
	116	4	1E-5	30	1.2	250	1	1.2	2.5E-3	0.415	0.012	28.31	1.12	-4.9E-4	46096	47668	-3.6%	-10.2%	3.6%	10.2%			
	117	8	1E-5	30	1.2	250	1	1.2	2.5E-3	0.822	0.015	35.16	1.34	-9.4E-4	46096	47668	-3.4%	-13.6%	3.4%	13.6%			
	118	12	1E-5	30	1.2	250	1	1.2	2.5E-3	1.195	0.022	42.88	0.30	-1.4E-3	46096	47668	-3.0%	-12.5%	3.0%	12.5%			
	119	16	1E-5	30	1.2	250	1	1.2	2.5E-3	1.470	0.036	49.59	0.65	-1.9E-3	46096	47668	-1.4%	-5.0%	1.4%	5.0%			
	120	20	1E-5	30	1.2	250	1	1.2	2.5E-3	1.159	0.115	47.98	0.66	-1.6E-4	46096	47668	9.5%	34.6%	9.5%	34.6%	6.58%	3.59%	13.58%
21	121	0	1E-5	30	1.2	250	1	1.05	1.5E-3	0.000	0.011	23.63	0.20	2.1E-6	83642	47668	-26.1%	2.7%	26.1%	2.7%			
	122	4	1E-5	30	1.2	250	1	1.05	1.5E-3	0.410	0.011	28.27	0.97	-5.7E-4	83642	47668	-2.3%	-1.8%	2.3%	1.8%			
	123	8	1E-5	30	1.2	250	1	1.05	1.5E-3	0.808	0.014	35.15	1.18	-1.2E-3	83642	47668	-1.7%	-3.3%	1.7%	3.3%			
	124	12	1E-5	30	1.2	250	1	1.05	1.5E-3	1.165	0.020	42.58	0.46	-1.8E-3	83642	47668	-0.3%	-2.6%	0.3%	2.6%			
	125	16	1E-5	30	1.2	250	1	1.05	1.5E-3	1.403	0.033	48.98	0.98	-2.6E-3	83642	47668	3.2%	3.2%	3.2%	3.2%			
	126	20	1E-5	30	1.2	250	1	1.05	1.5E-3	1.152	0.102	48.29	0.79	-1.2E-3	83642	47668	10.1%	41.9%	10.1%	41.9%	2.31%	3.24%	3.27%
22	127	0	1E-5	30	1.2	250	1	1.05	2.0E-3	0.000	0.011	23.77	0.19	5.7E-7	70056	47668	68.4%	2.7%	68.4%	2.7%			
	128	4	1E-5	30	1.2	250	1	1.05	2.0E-3	0.410	0.011	28.25	0.97	-5.7E-4	70056	47668	-2.4%	-1.9%	2.4%	1.9%			
	129	8	1E-5	30	1.2	250	1	1.05	2.0E-3	0.808	0.014	35.13	1.21	-1.2E-3	70056	47668	-1.7%	-3.3%	1.7%	3.3%			
	130	12	1E-5	30	1.2	250	1	1.05	2.0E-3	1.166	0.019	42.62	0.48	-1.9E-3	70056	47668	-0.4%	-0.9%	0.4%	0.9%			
	131	16	1E-5	30	1.2	250	1	1.05	2.0E-3	1.404	0.033	48.90	1.04	-2.6E-3	70056	47668	3.2%	3.3%	3.2%	3.3%			
	132	20	1E-5	30	1.2	250	1	1.05	2.0E-3	1.121	0.105	47.78	0.50	-9.9E-4	70056	47668	12.5%	39.9%	12.5%	39.9%	2.13%	3.17%	3.30%

23	133	0	1E-5	30	1.2	250	1	1.05	3.0E-3	0.000	0.011	23.65	0.28	1.6E-6	60406	47668	10.0%	2.5%	10.0%	2.5%			
	134	4	1E-5	30	1.2	250	1	1.05	3.0E-3	0.411	0.012	28.25	0.97	-5.7E-4	60406	47668	-2.4%	-2.0%	2.4%	2.0%			
	135	8	1E-5	30	1.2	250	1	1.05	3.0E-3	0.808	0.014	35.10	1.18	-1.2E-3	60406	47668	-1.7%	-3.3%	1.7%	3.3%			
	136	12	1E-5	30	1.2	250	1	1.05	3.0E-3	1.166	0.019	42.67	0.15	-1.9E-3	60406	47668	-0.4%	-0.9%	0.4%	0.9%			
	137	16	1E-5	30	1.2	250	1	1.05	3.0E-3	1.405	0.033	49.03	0.95	-2.6E-3	60406	47668	3.1%	3.1%	3.1%	3.1%			
	138	20	1E-5	30	1.2	250	1	1.05	3.0E-3	1.123	0.105	47.75	0.60	-9.7E-4	60406	47668	12.4%	39.9%	12.4%	39.9%	2.12%	3.08%	3.34%
24	139	0	1E-6	10	1.2	250	1	1.05	2.5E-3	0.001	0.010	2.34	0.03	5.5E-6	69860	47668	-494.5%	6.9%	494.5%	6.9%			
	140	4	1E-6	10	1.2	250	1	1.05	2.5E-3	0.411	0.011	2.86	0.07	-5.6E-4	69860	47668	-2.4%	1.7%	2.4%	1.7%			
	141	8	1E-6	10	1.2	250	1	1.05	2.5E-3	0.810	0.014	3.55	0.15	-1.1E-3	69860	47668	-1.9%	-0.4%	1.9%	0.4%			
	142	12	1E-6	10	1.2	250	1	1.05	2.5E-3	1.163	0.019	4.37	0.04	-1.9E-3	69860	47668	-0.1%	0.3%	0.1%	0.3%			
	143	16	1E-6	10	1.2	250	1	1.05	2.5E-3	1.408	0.033	5.14	0.04	-2.6E-3	69860	47668	2.9%	3.1%	2.9%	3.1%			
	144	20	1E-6	10	1.2	250	1	1.05	2.5E-3	1.115	0.113	5.09	0.06	-3.4E-4	69860	47668	13.0%	35.6%	13.0%	35.6%	1.60%	2.86%	3.08%
25	145	0	1E-6	20	1.2	250	1	1.05	2.5E-3	0.001	0.010	2.34	0.03	5.5E-6	69860	47668	-494.5%	6.9%	494.5%	6.9%			
	146	4	1E-6	20	1.2	250	1	1.05	2.5E-3	0.411	0.011	2.86	0.07	-5.6E-4	69860	47668	-2.4%	1.7%	2.4%	1.7%			
	147	8	1E-6	20	1.2	250	1	1.05	2.5E-3	0.810	0.014	3.55	0.15	-1.1E-3	69860	47668	-1.9%	-0.4%	1.9%	0.4%			
	148	12	1E-6	20	1.2	250	1	1.05	2.5E-3	1.163	0.019	4.37	0.04	-1.9E-3	69860	47668	-0.1%	0.3%	0.1%	0.3%			
	149	16	1E-6	20	1.2	250	1	1.05	2.5E-3	1.408	0.033	5.14	0.04	-2.6E-3	69860	47668	2.9%	3.1%	2.9%	3.1%			
	150	20	1E-6	20	1.2	250	1	1.05	2.5E-3	1.115	0.113	5.09	0.06	-3.4E-4	69860	47668	13.0%	35.6%	13.0%	35.6%	1.60%	2.86%	3.08%
26	151	0	1E-6	40	1.2	250	1	1.05	2.5E-3	0.001	0.010	2.34	0.03	5.5E-6	69860	47668	-494.5%	6.9%	494.5%	6.9%			
	152	4	1E-6	40	1.2	250	1	1.05	2.5E-3	0.411	0.011	2.86	0.07	-5.6E-4	69860	47668	-2.4%	1.7%	2.4%	1.7%			
	153	8	1E-6	40	1.2	250	1	1.05	2.5E-3	0.810	0.014	3.55	0.15	-1.1E-3	69860	47668	-1.9%	-0.4%	1.9%	0.4%			
	154	12	1E-6	40	1.2	250	1	1.05	2.5E-3	1.163	0.019	4.37	0.04	-1.9E-3	69860	47668	-0.1%	0.3%	0.1%	0.3%			
	155	16	1E-6	40	1.2	250	1	1.05	2.5E-3	1.408	0.033	5.14	0.04	-2.6E-3	69860	47668	2.9%	3.1%	2.9%	3.1%			
	156	20	1E-6	40	1.2	250	1	1.05	2.5E-3	1.115	0.113	5.09	0.06	-3.4E-4	69860	47668	13.0%	35.6%	13.0%	35.6%	1.60%	2.86%	3.08%
27	157	0	1E-6	30	1.1	250	1	1.05	2.5E-3	0.000	0.010	2.34	0.11	-7.6E-6	72482	47668	577.8%	10.4%	577.8%	10.4%			
	158	4	1E-6	30	1.1	250	1	1.05	2.5E-3	0.399	0.011	2.86	0.09	-7.9E-4	72482	47668	0.4%	6.5%	0.4%	6.5%			
	159	8	1E-6	30	1.1	250	1	1.05	2.5E-3	0.784	0.013	3.55	0.01	-1.6E-3	72482	47668	1.4%	6.3%	1.4%	6.3%			
	160	12	1E-6	30	1.1	250	1	1.05	2.5E-3	1.119	0.018	4.41	0.03	-2.5E-3	72482	47668	3.7%	7.2%	3.7%	7.2%			
	161	16	1E-6	30	1.1	250	1	1.05	2.5E-3	1.355	0.032	5.09	0.12	-3.2E-3	72482	47668	6.5%	7.3%	6.5%	7.3%			
	162	20	1E-6	30	1.1	250	1	1.05	2.5E-3	1.395	0.069	5.53	0.14	-2.4E-3	72482	47668	-8.9%	60.7%	8.9%	60.7%	4.91%	6.51%	7.26%
28	163	0	1E-6	30	1.3	250	1	1.05	2.5E-3	0.000	0.010	2.36	0.02	5.0E-6	65326	47668	-193.5%	6.4%	193.5%	6.4%			
	164	4	1E-6	30	1.3	250	1	1.05	2.5E-3	0.411	0.011	2.87	0.09	-5.6E-4	65326	47668	-2.4%	1.0%	2.4%	1.0%			
	165	8	1E-6	30	1.3	250	1	1.05	2.5E-3	0.809	0.014	3.58	0.16	-1.1E-3	65326	47668	-1.8%	-1.3%	1.8%	1.3%			
	166	12	1E-6	30	1.3	250	1	1.05	2.5E-3	1.166	0.019	4.40	0.02	-1.8E-3	65326	47668	-0.4%	-0.7%	0.4%	0.7%			
	167	16	1E-6	30	1.3	250	1	1.05	2.5E-3	1.383	0.035	5.15	0.02	-2.6E-3	65326	47668	4.6%	-1.9%	4.6%	1.9%			
	168	20	1E-6	30	1.3	250	1	1.05	2.5E-3	1.053	0.118	4.97	0.05	-2.7E-4	65326	47668	17.8%	32.5%	17.8%	32.5%	1.76%	4.56%	1.92%
29	169	0	1E-6	30	1.2	150	1	1.05	2.5E-3	-0.001	0.010	2.33	0.07	-2.4E-5	50384	47668	1592%	6.6%	1592%	6.6%			
	170	4	1E-6	30	1.2	150	1	1.05	2.5E-3	0.411	0.011	2.81	0.51	-5.5E-4	50384	47668	-2.5%	1.3%	2.5%	1.3%			
	171	8	1E-6	30	1.2	150	1	1.05	2.5E-3	0.811	0.014	3.43	0.16	-1.1E-3	50384	47668	-2.0%	-0.8%	2.0%	0.8%			
	172	12	1E-6	30	1.2	150	1	1.05	2.5E-3	1.171	0.019	4.17	0.04	-1.8E-3	50384	47668	-0.8%	0.6%	0.8%	0.6%			
	173	16	1E-6	30	1.2	150	1	1.05	2.5E-3	1.422	0.032	5.01	0.08	-2.5E-3	50384	47668	1.9%	4.7%	1.9%	4.7%			
	174	20	1E-6	30	1.2	150	1	1.05	2.5E-3	1.227	0.100	5.12	0.05	-6.1E-4	50384	47668	4.2%	43.2%	4.2%	43.2%	1.84%	2.54%	4.73%
30	175	0	1E-6	30	1.2	200	1	1.05	2.5E-3	-0.001	0.010	2.34	0.01	-1.6E-5	60290	47668	896.2%	6.8%	896.2%	6.8%			
	176	4	1E-6	30	1.2	200	1	1.05	2.5E-3	0.410	0.011	2.84	0.25	-5.7E-4	60290	47668	-2.3%	1.5%	2.3%	1.5%			
	177	8	1E-6	30	1.2	200	1	1.05	2.5E-3	0.811	0.014	3.52	0.19	-1.1E-3	60290	47668	-2.0%	-0.6%	2.0%	0.6%			
	178	12	1E-6	30	1.2	200	1	1.05	2.5E-3	1.164	0.019	4.31	0.02	-1.9E-3	60290	47668	-0.2%	-0.3%	0.2%	0.3%			
	179	16	1E-6	30	1.2	200	1	1.05	2.5E-3	1.412	0.033	5.14	0.04	-2.5E-3	60290	47668	2.6%	3.4%	2.6%	3.4%			
	180	20	1E-6	30	1.2	200	1	1.05	2.5E-3	1.145	0.107	5.13	0.13	-7.2E-4	60290	47668	10.6%	39.2%	10.6%	39.2%	1.62%	2.57%	3.42%
31	181	0	1E-6	30	1.2	300	1	1.05	2.5E-3	0.000	0.010	2.34	0.07	-2.2E-6	78938	47668	-238.1%	6.9%	238.1%	6.9%			
	182	4	1E-6	30	1.2	300	1	1.05	2.5E-3	0.410	0.011	2.87	0.19	-5.7E-4	78938	47668	-2.3%	1.8%	2.3%	1.8%			
	183	8	1E-6	30	1.2	300	1	1.05	2.5E-3	0.809	0.014	3.57	0.15	-1.1E-3	78938	47668	-1.8%	-0.3%	1.8%	0.3%			
	184	12	1E-6	30	1.2	300	1	1.05	2.5E-3	1.163	0.019	4.41	0.04	-1.9E-3	78938	47668	-0.2%	-0.3%	0.2%	0.3%			
	185	16	1E-6	30	1.2	300	1	1.05	2.5E-3	1.388	0.034	5.19	0.02	-2.6E-3	78938	47668	4.2%	0.2%	4.2%	0.2%			
	186	20	1E-6	30	1.2	300	1	1.05	2.5E-3	1.104	0.115	5.07	0.06	-2.6E-4	78938	47668	13.8%	34.7%	13.8%	34.7%	1.39%	4.22%	1.78%
32	187	0	1E-6	30	1.2	350	1	1.05	2.5E-3	0.000	0.010	2.34	0.01	1.2E-7	87570	47668	136.0%	7.1%	136.0%	7.1%			
	188	4	1E-6	30	1.2	350	1	1.05	2.5E-3	0.410	0.011	2.87	0.18	-5.7E-4	87570	47668	-2.3%	1.6%	2.3%	1.6%			
	189	8	1E-6	30	1.2	350	1	1.05	2.5E-3	0.810	0.014	3.59	0.17	-1.1E-3	87570	47668	-1.9%	-0.4%	1.9%	0.4%			
	190	12	1E-6	30	1.2	350	1	1.05	2.5E-3	1.164	0.019	4.43	0.04	-1.9E-3	87570	47668	-0.2%	-0.5%	0.2%	0.5%			
	191	16	1E-6	30	1.2	350	1	1.05	2.5E-3	1.387	0.034	5.18	0.04	-2.6E-3	87570	47668	4.3%	0.1%	4.3%	0.1%			
	192	20	1E-6	30	1.2	350	1	1.05	2.5E-3	1.090	0.114	5.09	0.05	-3.8E-4	87570	47668	14.9%	35.1%	14.9%	35.1%	1.41%	4.31%	1.62%
33	193	0	1E-6	30	1.2	250	2	1.05	2.5E-3	0.000	0.010	2.35	0.06	1.5E-6	70156	47668	-197.2%	6.8%	197.2%	6.8%			
	194	4	1E-6	30	1.2	250	2	1.05	2.5E-3	0.410	0.011	2.87	0.19	-5.8E-4	70156	47668	-2.2%	1.9%	2.2%	1.9%			
	195	8	1E-6	30	1.2	250	2	1.05	2.5E-3	0.806	0.014	3.59	0.19	-1.2E-3	70156	47668	-1.5%	-0.2%	1.5%	0.2%			
	196	12	1E-6	30	1.2	250	2	1.05	2.5E-3	1.155	0.019	4.42	0.01	-2.0E-3	70156	47668	0.5%	-0.1%	0.5%	0.1%			
	197	16	1E-6	30	1.2	250	2	1.05	2.5E-3	1.399	0.033	5.21	0.04	-2.6E-3	70156	47668	3.5%	2.7%	3.5%	2.7%			
	198	20	1E-6	30	1.2	250	2	1.05	2.5E-3	1.236	0.097	5.37	0.13	-8.4E-4	70156	47668	3.6%	44.6%	3.6%	44.6%	1.58%	3.51%	2.71%
34	199	0	1E-6	30	1.2	250	3	1.05	2.5E-3	0.000	0.010	2.35	0.06	1.6E-6	69750	47668	-1.7%	7.0%	1.7%	7.0%			
	200	4	1E-6	30	1.2	250	3	1.05	2.5E-3	0.409	0.011	2.88	0.22	-6.0E-4	69750	47668	-1.9%	1.9%	1.9%	1.9%			
	201	8	1E-6	30	1.2	250	3	1.05	2.5E-3	0.807	0.014	3.60	0.04	-1.2E-3	69750	47668	-1.5%	-0.2%	1.5%	0.2%			
	202	12	1E-6	30	1.2	250	3	1.05	2.5E-3	1.157	0.019	4.43	0.03	-2.0E-3	69750	47668	0.3%	0.3%	0.3%	0.3%			
	203	16	1E-6	30	1.2	250	3	1.05	2.5E-3	1.413	0.032	5.23	0.05	-2.6E-3	69750	47668	2.5%	4.7%	2.5%	4.7%			
	204	20	1E-6	30	1.2	250	3	1.05	2.5E-3	1.252	0.095	5.50	0.02	-9.4E-4	69750	47668	2.3%	46.0%	2.3%	46.0%	1.66%	2.54%	4.66%

35	205	0	1E-6	30	1.2	250	1	1.025	2.5E-3	0.000	0.010	2.34	0.02	7.1E-7	119238	47668	48.2%	7.8%	48.2%	7.8%			
	206	4	1E-6	30	1.2	250	1	1.025	2.5E-3	0.412	0.011	2.86	0.11	-5.3E-4	119238	47668	-2.7%	2.7%	2.7%	2.7%			
	207	8	1E-6	30	1.2	250	1	1.025	2.5E-3	0.808	0.014	3.55	0.16	-1.1E-3	119238	47668	-1.7%	0.2%	1.7%	0.2%			
	208	12	1E-6	30	1.2	250	1	1.025	2.5E-3	1.166	0.019	4.38	0.04	-1.9E-3	119238	47668	-0.5%	3.0%	0.5%	3.0%			
	209	16	1E-6	30	1.2	250	1	1.025	2.5E-3	1.387	0.033	5.13	0.08	-2.7E-3	119238	47668	4.3%	2.5%	4.3%	2.5%			
	210	20	1E-6	30	1.2	250	1	1.025	2.5E-3	1.188	0.101	5.21	0.02	-5.7E-4	119238	47668	7.3%	42.5%	7.3%	42.5%	2.21%	4.34%	3.02%
36	211	0	1E-6	30	1.2	250	1	1.075	2.5E-3	0.000	0.010	2.34	0.05	-7.0E-6	57970	47668	444.8%	5.7%	444.8%	5.7%			
	212	4	1E-6	30	1.2	250	1	1.075	2.5E-3	0.412	0.011	2.86	0.07	-5.5E-4	57970	47668	-2.7%	0.4%	2.7%	0.4%			
	213	8	1E-6	30	1.2	250	1	1.075	2.5E-3	0.813	0.014	3.56	0.17	-1.1E-3	57970	47668	-2.3%	-2.5%	2.3%	2.5%			
	214	12	1E-6	30	1.2	250	1	1.075	2.5E-3	1.172	0.020	4.37	0.04	-1.8E-3	57970	47668	-0.9%	-1.5%	0.9%	1.5%			
	215	16	1E-6	30	1.2	250	1	1.075	2.5E-3	1.415	0.034	5.19	0.05	-2.4E-3	57970	47668	2.4%	0.7%	2.4%	0.7%			
	216	20	1E-6	30	1.2	250	1	1.075	2.5E-3	1.170	0.107	5.17	0.06	-4.4E-4	57970	47668	8.7%	39.0%	8.7%	39.0%	1.67%	2.68%	2.50%
37	217	0	1E-6	30	1.2	250	1	1.1	2.5E-3	0.001	0.011	2.35	0.09	1.3E-5	53512	47668	-855.2%	4.6%	855.2%	4.6%			
	218	4	1E-6	30	1.2	250	1	1.1	2.5E-3	0.413	0.011	2.86	0.11	-5.2E-4	53512	47668	-3.0%	-1.2%	3.0%	1.2%			
	219	8	1E-6	30	1.2	250	1	1.1	2.5E-3	0.813	0.014	3.55	0.21	-1.1E-3	53512	47668	-2.3%	-4.5%	2.3%	4.5%			
	220	12	1E-6	30	1.2	250	1	1.1	2.5E-3	1.173	0.020	4.35	0.04	-1.8E-3	53512	47668	-1.0%	-4.0%	1.0%	4.0%			
	221	16	1E-6	30	1.2	250	1	1.1	2.5E-3	1.426	0.034	5.17	0.05	-2.4E-3	53512	47668	1.6%	-0.4%	1.6%	0.4%			
	222	20	1E-6	30	1.2	250	1	1.1	2.5E-3	1.353	0.087	5.38	0.06	-1.0E-3	53512	47668	-5.6%	50.2%	5.6%	50.2%	2.25%	3.02%	4.50%
38	223	0	1E-6	30	1.2	250	1	1.2	2.5E-3	-0.001	0.011	2.36	0.07	-5.1E-6	48174	47668	791.7%	-1.3%	791.7%	1.3%			
	224	4	1E-6	30	1.2	250	1	1.2	2.5E-3	0.414	0.012	2.90	0.04	-4.9E-4	48174	47668	-3.2%	-8.1%	3.2%	8.1%			
	225	8	1E-6	30	1.2	250	1	1.2	2.5E-3	0.819	0.015	3.58	0.14	-9.6E-4	48174	47668	-3.1%	-12.9%	3.1%	12.9%			
	226	12	1E-6	30	1.2	250	1	1.2	2.5E-3	1.191	0.022	4.39	0.02	-1.5E-3	48174	47668	-2.5%	-13.3%	2.5%	13.3%			
	227	16	1E-6	30	1.2	250	1	1.2	2.5E-3	1.459	0.037	5.18	0.06	-1.9E-3	48174	47668	-0.7%	-8.2%	0.7%	8.2%			
	228	20	1E-6	30	1.2	250	1	1.2	2.5E-3	1.411	0.087	5.54	0.12	-7.8E-4	48174	47668	-10.1%	50.6%	10.1%	50.6%	6.51%	3.21%	13.31%
39	229	0	1E-6	30	1.2	250	1	1.05	1.5E-3	0.000	0.010	2.34	0.04	-5.1E-7	90852	47668	-43.4%	7.3%	43.4%	7.3%			
	230	4	1E-6	30	1.2	250	1	1.05	1.5E-3	0.410	0.011	2.85	0.11	-5.7E-4	90852	47668	-2.3%	2.0%	2.3%	2.0%			
	231	8	1E-6	30	1.2	250	1	1.05	1.5E-3	0.809	0.014	3.55	0.16	-1.1E-3	90852	47668	-1.8%	-0.2%	1.8%	0.2%			
	232	12	1E-6	30	1.2	250	1	1.05	1.5E-3	1.158	0.019	4.38	0.03	-1.9E-3	90852	47668	0.3%	-0.2%	0.3%	0.2%			
	233	16	1E-6	30	1.2	250	1	1.05	1.5E-3	1.401	0.033	5.19	0.04	-2.6E-3	90852	47668	3.4%	2.6%	3.4%	2.6%			
	234	20	1E-6	30	1.2	250	1	1.05	1.5E-3	1.111	0.112	5.07	0.06	-4.3E-4	90852	47668	13.3%	36.3%	13.3%	36.3%	1.59%	3.38%	2.64%
40	235	0	1E-6	30	1.2	250	1	1.05	2.0E-3	0.000	0.010	2.34	0.06	1.4E-6	77206	47668	193.2%	7.1%	193.2%	7.1%			
	236	4	1E-6	30	1.2	250	1	1.05	2.0E-3	0.411	0.011	2.87	0.07	-5.6E-4	77206	47668	-2.5%	1.8%	2.5%	1.8%			
	237	8	1E-6	30	1.2	250	1	1.05	2.0E-3	0.810	0.014	3.57	0.11	-1.1E-3	77206	47668	-1.9%	-0.3%	1.9%	0.3%			
	238	12	1E-6	30	1.2	250	1	1.05	2.0E-3	1.163	0.019	4.37	0.04	-1.9E-3	77206	47668	-0.1%	0.3%	0.1%	0.3%			
	239	16	1E-6	30	1.2	250	1	1.05	2.0E-3	1.405	0.033	5.17	0.03	-2.6E-3	77206	47668	3.0%	3.0%	3.0%	3.0%			
	240	20	1E-6	30	1.2	250	1	1.05	2.0E-3	1.098	0.114	5.04	0.05	-3.5E-4	77206	47668	14.3%	35.2%	14.3%	35.2%	1.62%	3.04%	2.98%
41	241	0	1E-6	30	1.2	250	1	1.05	3.0E-3	0.001	0.010	2.34	0.03	1.1E-5	67420	47668	-809.3%	6.8%	809.3%	6.8%			
	242	4	1E-6	30	1.2	250	1	1.05	3.0E-3	0.411	0.011	2.86	0.07	-5.5E-4	67420	47668	-2.6%	1.6%	2.6%	1.6%			
	243	8	1E-6	30	1.2	250	1	1.05	3.0E-3	0.809	0.014	3.56	0.14	-1.1E-3	67420	47668	-1.8%	-0.4%	1.8%	0.4%			
	244	12	1E-6	30	1.2	250	1	1.05	3.0E-3	1.164	0.019	4.38	0.05	-1.9E-3	67420	47668	-0.3%	0.4%	0.3%	0.4%			
	245	16	1E-6	30	1.2	250	1	1.05	3.0E-3	1.396	0.034	5.14	0.04	-2.6E-3	67420	47668	3.7%	1.4%	3.7%	1.4%			
	246	20	1E-6	30	1.2	250	1	1.05	3.0E-3	1.102	0.114	5.02	0.05	-3.1E-4	67420	47668	14.0%	35.0%	14.0%	35.0%	1.52%	3.67%	1.62%
42	247	0	1E-6	30	1.2	250	1	1.05	2.5E-3	0.001	0.010	2.34	0.03	5.5E-6	69860	47668	-494.5%	6.9%	494.5%	6.9%			
	248	4	1E-6	30	1.2	250	1	1.05	2.5E-3	0.411	0.011	2.86	0.07	-5.6E-4	69860	47668	-2.4%	1.7%	2.4%	1.7%			
	249	8	1E-6	30	1.2	250	1	1.05	2.5E-3	0.810	0.014	3.55	0.15	-1.1E-3	69860	47668	-1.9%	-0.4%	1.9%	0.4%			
	250	12	1E-6	30	1.2	250	1	1.05	2.5E-3	1.163	0.019	4.37	0.04	-1.9E-3	69860	47668	-0.1%	0.3%	0.1%	0.3%			
	251	16	1E-6	30	1.2	250	1	1.05	2.5E-3	1.408	0.033	5.14	0.04	-2.6E-3	69860	47668	2.9%	3.1%	2.9%	3.1%			
	252	20	1E-6	30	1.2	250	1	1.05	2.5E-3	1.115	0.113	5.09	0.06	-3.4E-4	69860	47668	13.0%	35.6%	13.0%	35.6%	1.60%	2.86%	3.08%
43	274	0	1E-6	30	1.2	250	1	1.075	3.0E-3	-0.001	0.010	2.34	0.06	-9.0E-6	54702	47668	840.3%	5.8%	840.3%	5.8%			
	275	1	1E-6	30	1.2	250	1	1.075	3.0E-3	0.102	0.010	2.45	0.29	-1.5E-4	54702	47668	-1.4%	5.0%	1.4%	5.0%			
	276	2	1E-6	30	1.2	250	1	1.075	3.0E-3	0.206	0.011	2.58	0.37	-2.8E-4	54702	47668	-2.0%	4.7%	2.0%	4.7%			
	277	3	1E-6	30	1.2	250	1	1.075	3.0E-3	0.309	0.011	2.71	0.31	-4.2E-4	54702	47668	-2.1%	2.3%	2.1%	2.3%			
	278	4	1E-6	30	1.2	250	1	1.075	3.0E-3	0.411	0.011	2.86	0.09	-5.5E-4	54702	47668	-2.5%	0.4%	2.5%	0.4%			
	279	5	1E-6	30	1.2	250	1	1.075	3.0E-3	0.513	0.012	3.03	0.27	-6.8E-4	54702	47668	-2.8%	0.4%	2.8%	0.4%			
	280	6	1E-6	30	1.2	250	1	1.075	3.0E-3	0.614	0.012	3.20	0.28	-8.2E-4	54702	47668	-2.7%	-0.3%	2.7%	0.3%			
	281	7	1E-6	30	1.2	250	1	1.075	3.0E-3	0.714	0.013	3.37	0.20	-9.6E-4	54702	47668	-2.5%	-1.9%	2.5%	1.9%			
	282	8	1E-6	30	1.2	250	1	1.075	3.0E-3	0.811	0.014	3.56	0.17	-1.1E-3	54702	47668	-2.1%	-2.2%	2.1%	2.2%			
	283	9	1E-6	30	1.2	250	1	1.075	3.0E-3	0.906	0.015	3.76	0.04	-1.3E-3	54702	47668	-1.5%	-2.1%	1.5%	2.1%			
	284	10	1E-6	30	1.2	250	1	1.075	3.0E-3	0.998	0.016	3.96	0.01	-1.4E-3	54702	47668	-1.6%	-2.4%	1.6%	2.4%			
	285	11	1E-6	30	1.2	250	1	1.075	3.0E-3	1.086	0.018	4.16	0.02	-1.6E-3	54702	47668	-1.3%	-2.3%	1.3%	2.3%			
	286	12	1E-6	30	1.2	250	1	1.075	3.0E-3	1.169	0.020	4.37	0.04	-1.8E-3	54702	47668	-0.7%	-1.3%	0.7%	1.3%			
	287	13	1E-6	30	1.2	250	1	1.075	3.0E-3	1.249	0.022	4.58	0.05	-2.0E-3	54702	47668	-0.2%	0.3%	0.2%	0.3%			
	288	14	1E-6	30	1.2	250	1	1.075	3.0E-3	1.318	0.025	4.78	0.01	-2.2E-3	54702	47668	0.6%	2.1%	0.6%	2.1%			
	289	15	1E-6	30	1.2	250	1	1.075	3.0E-3	1.373	0.028	4.97	0.08	-2.3E-3	54702	47668	1.6%	2.2%	1.6%	2.2%			
	290	16	1E-6	30	1.2	250	1	1.075	3.0E-3	1.410	0.034	5.21	0.01	-2.5E-3	54702	47668	2.7%	-0.1%	2.7%	0.1%			
	291	17	1E-6	30	1.2	250	1	1.075	3.0E-3	1.421	0.043	5.37	0.09	-2.5E-3	54702	47668	4.2%	2.1%	4.2%	2.1%			
	292	18	1E-6	30	1.2	250	1	1.075	3.0E-3	1.398	0.055	5.42	0.05	-2.3E-3	54702	47668	2.7%	36.7%	2.7%	36.7%			
	293	19	1E-6	30	1.2	250	1	1.075	3.0E-3	1.295	0.077	5.36	0.06	-1.7E-3	54702	47668	3.4%	45.9%	3.4%	45.9%			
	294	20	1E-6	30	1.2	250	1	1.075	3.0E-3	1.161	0.109	5.23	0.06	-3.8E-4	54702	47668	9.4%	37.6%	9.4%	37.6%	1.90%	4.24%	4.98%

A.3 Mesh parameter study data - Experimental

The following table contains digitally extracted profile (infinite wing) coefficients of lift and drag for a NACA 0018 from Jacobs et al. (1933), page 305.

α	C_L	C_D
0	0.0001	0.0111
1	0.1009	0.0110
2	0.2017	0.0112
3	0.3025	0.0111
4	0.4010	0.0113
5	0.4996	0.0117
6	0.5981	0.0122
7	0.6965	0.0127
8	0.7948	0.0135
9	0.8929	0.0146
10	0.9827	0.0158
11	1.0719	0.0173
12	1.1611	0.0193
13	1.2462	0.0219
14	1.3264	0.0251
15	1.3960	0.0291
16	1.4495	0.0340
17	1.4835	0.0434
18	1.4375	0.0870
19	1.3407	0.1418
20	1.2815	0.1753
21	1.2325	0.2031
22	1.1835	0.2308
23	1.1347	0.2585
24	1.0917	0.2828
25	1.0490	0.3070
26	1.0063	0.3312
27	0.9635	0.3554

Appendix B

Experimental Details

B.1 Dimensions of experimental flume partitions

The flume constriction consists of two partitions running the entire depth of the flume included to isolate drive and instrumentation systems from the surrounding water. The shape of entry and exit of the partitions is a Bezier spline, this was discrtised into coordinates for the numberical simulation, see Table B.1 for the values.

x (mm)	y (mm)
0	0
14.585	0.689
28.116	2.660
40.712	5.771
52.488	9.880
63.563	14.844
74.052	20.520
84.074	26.766
93.744	33.440
103.181	40.399
112.500	47.500
121.820	54.601
131.256	61.560
140.927	68.234
150.948	74.480
161.438	80.156
172.512	85.120
184.289	89.229
196.884	92.340
210.416	94.311
225.000	95.000

Table B.1: Dimensions of partition spline

The partition spline is mirrored and spaced by a 0.25m straight section to form one of the partitions. An complete partition profile is shown in Figure B-1. Note that the turbine axis is aligned with the centre of the partition.

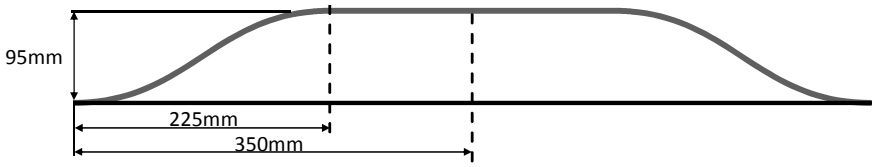

Figure B-1: Diagram of partition shape

B.2 Current Profile

The experimental and numerical velocity profiles are given in Table B.2. The numerical has been corrected by a factor of b_C/b_T (1.8/1.61) to compensate for the constriction of the experimental channel, details are given in Section 5.3.3.1.

Depth (mm)	Experimental U_∞ (m/s)	Numerical U_∞ (m/s)
0	0.0005	0.0006
10	0.2386	0.2668
20	0.2679	0.2995
30	0.2866	0.3204
40	0.3007	0.3361
50	0.3120	0.3489
100	0.3462	0.3871
150	0.3562	0.3982
200	0.3626	0.4054
250	0.3619	0.4046
300	0.3620	0.4048
350	0.3580	0.4002
400	0.3471	0.3880
450	0.3388	0.3788
500	0.3233	0.3614
550	0.3001	0.3356
600	0.2796	0.3126
650	0.2759	0.3084
700	0.2674	0.2990
750	0.2505	0.2800
800	0.2438	0.2726
850	0.2340	0.2616
900	0.2242	0.2506
950	0.2143	0.2396
1000	0.2045	0.2286

Table B.2: Velocity profiles of experimental and numerical flumes

B.3 Experimental Turbine Data

The experimental data in the table below was provided by Ross McAdam, University of Oxford, and Kepler Energy Ltd. The experimental procedure is described in detail in Section 5.2.5. The experimental procedure included ramping the turbine rotation speed gradually upward and downward while capturing torque and thrust in realtime. Averaging and smoothing of the data by the original author resulted in the values of $\overline{Q}$ and $\overline{T}$ given in the table below. Subscripts $\uparrow$ and $\downarrow$ denote the turbine speed rising and falling respectively, the average of which is calculated in the 'Corrected' column where the original blade length, L_b (1.528), is also corrected for giving a value per unit length (1m). Coefficients are calculated as specified by equations 3.11, 3.12 and 3.13, see Table 5.1 for parameter values.

Turbine Speed		Torque (Nm)		Thrust (Nm)		Corrected		Coefficients		
ω	λ	$\overline{Q_\uparrow}$	$\overline{Q_\downarrow}$	$\overline{T_\uparrow}$	$\overline{T_\downarrow}$	$\frac{\overline{Q_\uparrow}+\overline{Q_\downarrow}}{2L_b}$	$\frac{\overline{T_\uparrow}+\overline{T_\downarrow}}{2L_b}$	$\overline{C_P}$	$\overline{C_Q}$	$\overline{C_T}$
0.000	0.000	0.288	0.090	15.720	21.978	0.124	12.336	0.000	0.000	0.361
0.067	0.056	0.112	-0.018	21.474	21.278	0.031	13.989	0.000	0.003	0.409
0.133	0.112	0.157	0.049	22.069	20.198	0.067	13.831	0.001	0.006	0.405
0.200	0.168	0.175	0.090	19.937	19.338	0.087	12.852	0.001	0.008	0.376
0.267	0.224	0.256	0.090	20.295	22.872	0.113	14.125	0.002	0.011	0.413
0.333	0.280	0.257	0.223	21.345	20.019	0.157	13.535	0.004	0.015	0.396
0.400	0.335	0.201	0.144	21.595	21.700	0.113	14.167	0.004	0.011	0.414
0.467	0.391	0.201	0.264	23.239	20.013	0.152	14.153	0.006	0.014	0.414
0.533	0.447	0.031	0.377	25.951	20.989	0.134	15.360	0.006	0.013	0.449
0.600	0.503	0.365	0.100	21.784	23.635	0.152	14.862	0.007	0.014	0.435
0.667	0.559	0.100	0.231	26.197	25.257	0.108	16.837	0.006	0.010	0.492
0.734	0.615	0.088	0.246	26.634	24.433	0.109	16.710	0.006	0.010	0.489
0.800	0.671	0.396	0.187	23.247	25.085	0.191	15.815	0.012	0.018	0.463
0.867	0.727	0.100	0.196	26.593	26.744	0.097	17.453	0.007	0.009	0.511
0.934	0.783	0.192	0.108	25.717	30.785	0.098	18.489	0.007	0.009	0.541
1.000	0.839	0.267	0.392	29.613	27.810	0.216	18.790	0.017	0.020	0.550
1.067	0.894	0.301	0.087	27.283	29.914	0.127	18.716	0.011	0.012	0.547
1.134	0.950	0.216	0.271	31.385	30.191	0.159	20.149	0.014	0.015	0.589
1.200	1.006	0.106	0.034	31.213	31.799	0.046	20.619	0.004	0.004	0.603
1.267	1.062	0.275	0.132	29.025	28.707	0.133	18.891	0.013	0.013	0.553
1.334	1.118	0.050	0.226	34.717	28.411	0.090	20.657	0.010	0.009	0.604
1.400	1.174	0.181	0.243	34.400	31.504	0.139	21.565	0.015	0.013	0.631
1.467	1.230	0.269	0.161	29.770	33.399	0.141	20.670	0.016	0.013	0.605
1.534	1.286	0.169	0.288	34.631	37.832	0.149	23.712	0.018	0.014	0.694
1.600	1.342	0.076	0.305	33.512	34.374	0.125	22.214	0.016	0.012	0.650

1.667	1.398	0.286	0.317	41.138	40.854	0.197	26.830	0.026	0.019	0.785
1.734	1.453	0.171	0.278	35.536	37.856	0.147	24.016	0.020	0.014	0.702
1.800	1.509	0.385	0.394	49.102	47.932	0.255	31.752	0.036	0.024	0.929
1.867	1.565	0.261	0.520	47.157	42.274	0.256	29.264	0.038	0.024	0.856
1.934	1.621	0.267	0.432	49.000	44.957	0.228	30.745	0.035	0.022	0.899
2.001	1.677	0.387	0.490	46.752	41.109	0.287	28.750	0.045	0.027	0.841
2.067	1.733	0.465	0.594	47.180	41.022	0.347	28.862	0.057	0.033	0.844
2.134	1.789	0.493	0.666	40.232	37.573	0.379	25.460	0.064	0.036	0.745
2.201	1.845	0.628	0.811	51.736	40.095	0.471	30.049	0.082	0.044	0.879
2.334	1.957	0.681	0.886	44.918	48.272	0.513	30.494	0.095	0.048	0.892
2.467	2.068	0.983	1.185	73.193	50.722	0.710	40.548	0.138	0.067	1.186
2.601	2.180	1.119	1.315	56.393	59.650	0.796	37.972	0.164	0.075	1.111
2.667	2.236	1.231	1.454	67.225	60.410	0.878	41.765	0.185	0.083	1.222
2.734	2.292	1.235	1.541	57.688	47.503	0.908	34.421	0.196	0.086	1.007
2.867	2.404	1.424	1.849	60.701	68.513	1.071	42.282	0.243	0.101	1.237
2.934	2.460	1.672	1.874	78.293	67.469	1.160	47.697	0.269	0.109	1.395
3.001	2.516	1.640	1.877	70.205	69.204	1.151	45.618	0.273	0.109	1.334
3.201	2.683	2.023	2.180	82.886	70.020	1.375	50.034	0.348	0.130	1.464
3.334	2.795	2.115	2.348	67.685	73.311	1.460	46.137	0.385	0.138	1.350
3.401	2.851	2.221	2.393	67.401	71.773	1.510	45.541	0.406	0.142	1.332
3.468	2.907	2.344	2.399	74.730	76.627	1.552	49.528	0.426	0.146	1.449
3.534	2.963	2.410	2.538	79.096	85.076	1.619	53.721	0.453	0.153	1.571
3.601	3.019	2.474	2.500	79.185	79.512	1.627	51.930	0.464	0.154	1.519
3.668	3.075	2.457	2.569	81.340	77.396	1.645	51.943	0.477	0.155	1.519
3.734	3.130	2.566	2.587	81.288	80.900	1.686	53.072	0.498	0.159	1.552
3.801	3.186	2.592	2.566	84.586	83.330	1.688	54.946	0.507	0.159	1.607
3.868	3.242	2.610	2.619	84.040	82.427	1.711	54.472	0.523	0.161	1.593
3.934	3.298	2.621	2.709	85.302	85.111	1.744	55.763	0.543	0.165	1.631
4.001	3.354	2.690	2.637	87.064	85.112	1.743	56.340	0.552	0.164	1.648
4.068	3.410	2.676	2.613	87.573	83.712	1.731	56.049	0.557	0.163	1.639
4.134	3.466	2.735	2.711	89.161	86.971	1.782	57.635	0.583	0.168	1.686
4.201	3.522	2.735	2.616	89.675	83.298	1.751	56.601	0.582	0.165	1.656
4.268	3.578	2.703	2.641	89.329	89.886	1.749	58.644	0.590	0.165	1.715
4.334	3.634	2.662	2.703	92.233	89.992	1.755	59.628	0.602	0.166	1.744
4.401	3.689	2.716	2.673	90.477	87.052	1.764	58.092	0.614	0.166	1.699
4.468	3.745	2.687	2.757	91.714	92.637	1.781	60.324	0.630	0.168	1.764
4.535	3.801	2.735	2.706	93.437	91.863	1.781	60.635	0.639	0.168	1.774
4.601	3.857	2.719	2.646	92.865	90.636	1.756	60.046	0.639	0.166	1.756
4.668	3.913	2.586	2.654	92.914	95.121	1.715	61.530	0.633	0.162	1.800

4.735	3.969	2.513	2.660	94.336	94.416	1.693	61.764	0.634	0.160	1.807
4.801	4.025	2.591	2.452	94.575	90.690	1.650	60.624	0.627	0.156	1.773
4.868	4.081	2.537	2.453	93.989	93.699	1.633	61.416	0.629	0.154	1.796
4.935	4.137	2.436	2.424	94.426	92.233	1.590	61.080	0.621	0.150	1.787
5.001	4.193	2.381	2.230	96.816	90.558	1.509	61.313	0.597	0.142	1.793
5.068	4.248	2.446	2.218	95.270	95.109	1.526	62.297	0.612	0.144	1.822
5.135	4.304	2.277	2.377	99.493	97.033	1.523	64.308	0.618	0.144	1.881
5.201	4.360	2.248	1.987	99.023	95.146	1.386	63.537	0.570	0.131	1.858
5.268	4.416	2.144	2.065	96.235	94.935	1.377	62.555	0.574	0.130	1.830
5.335	4.472	2.049	2.155	97.144	97.960	1.376	63.843	0.580	0.130	1.867
5.401	4.528	1.980	1.927	93.989	97.199	1.279	62.562	0.546	0.121	1.830
5.468	4.584	1.827	1.840	99.697	96.323	1.200	64.143	0.519	0.113	1.876
5.535	4.640	1.796	1.890	96.538	102.061	1.206	64.987	0.528	0.114	1.901
5.601	4.696	1.685	1.813	100.302	99.180	1.145	65.276	0.507	0.108	1.909
5.668	4.752	1.610	1.582	98.657	96.801	1.044	63.959	0.468	0.099	1.871
5.735	4.807	1.570	1.590	96.365	97.193	1.034	63.337	0.469	0.098	1.853
5.802	4.863	1.556	1.573	99.503	100.162	1.024	65.335	0.470	0.097	1.911
5.868	4.919	1.508	1.511	101.307	100.310	0.988	65.974	0.458	0.093	1.930
5.935	4.975	1.568	1.397	94.769	100.380	0.970	63.858	0.455	0.092	1.868

Appendix C

Large Scale Turbine Data

C.1 Channel Velocity

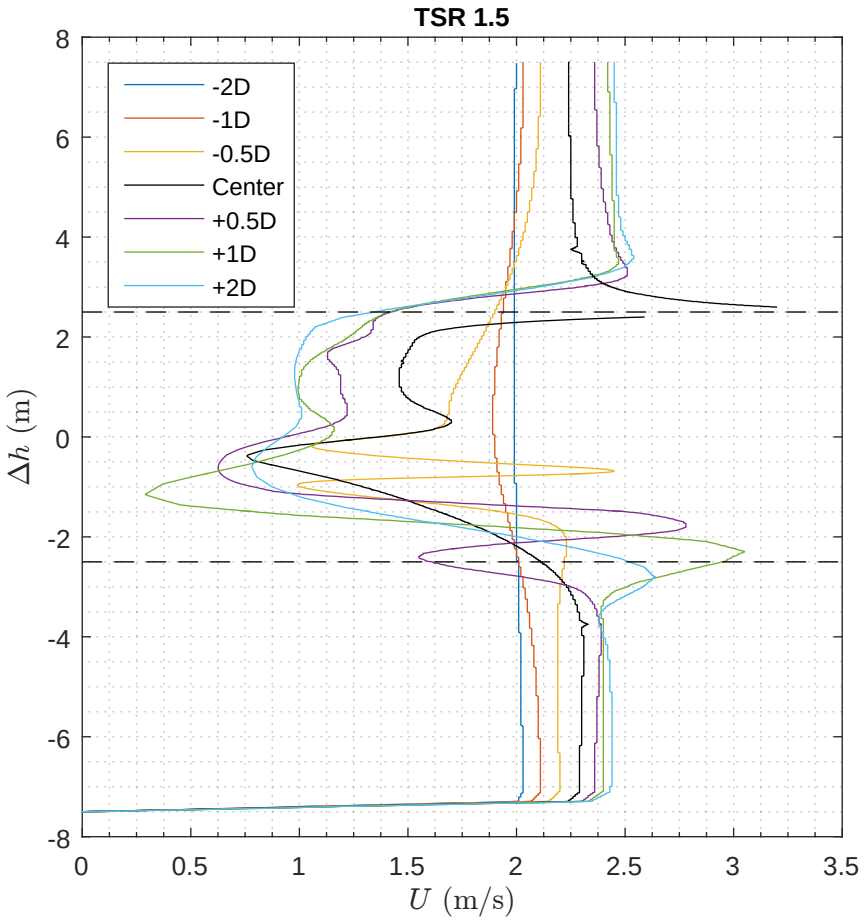

Figure C-1: Numerical flume velocity profiles with depth at a TSR of 1.5

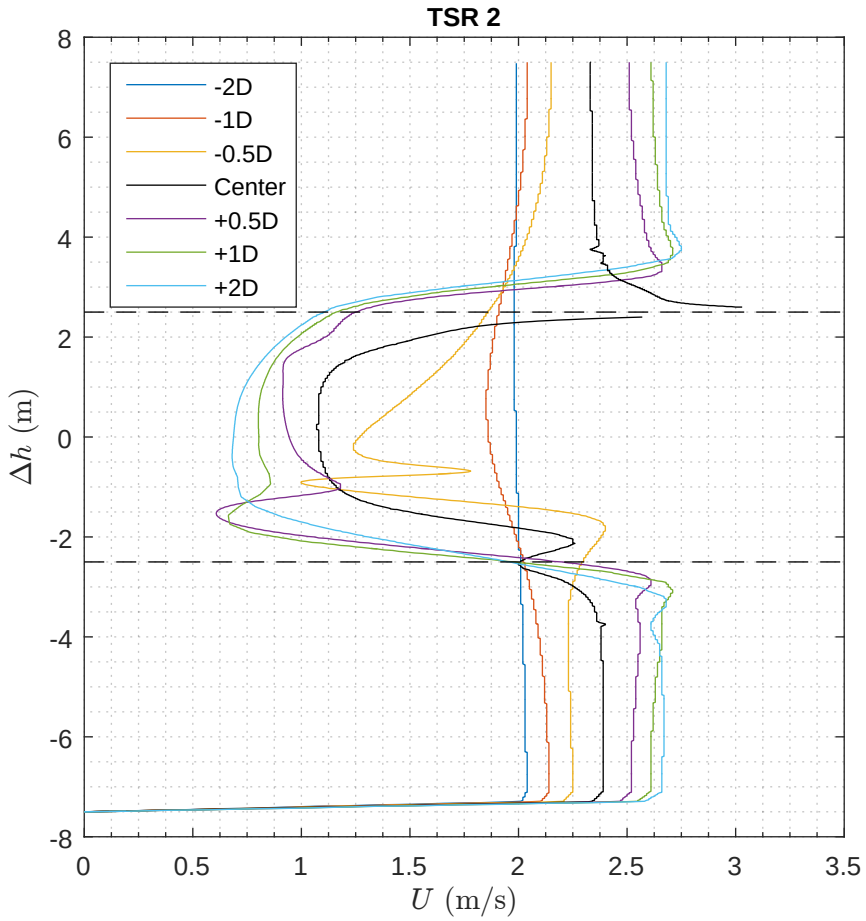

Figure C-2: Numerical flume velocity profiles with depth at a TSR of 2

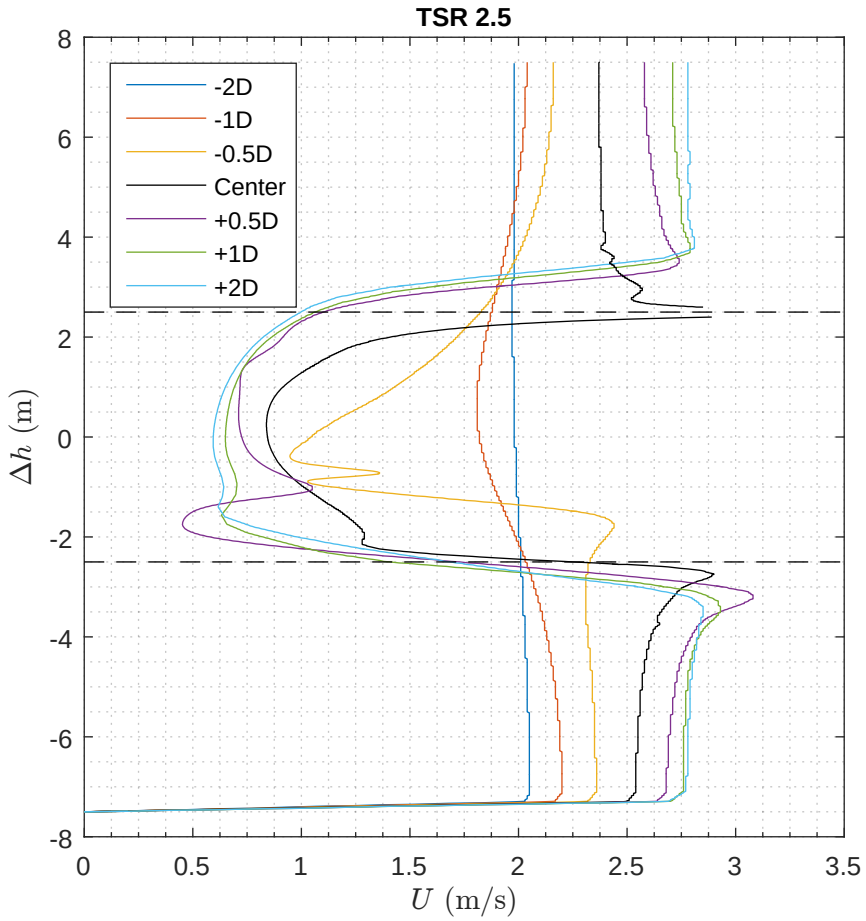

Figure C-3: Numerical flume velocity profiles with depth at a TSR of 2.5

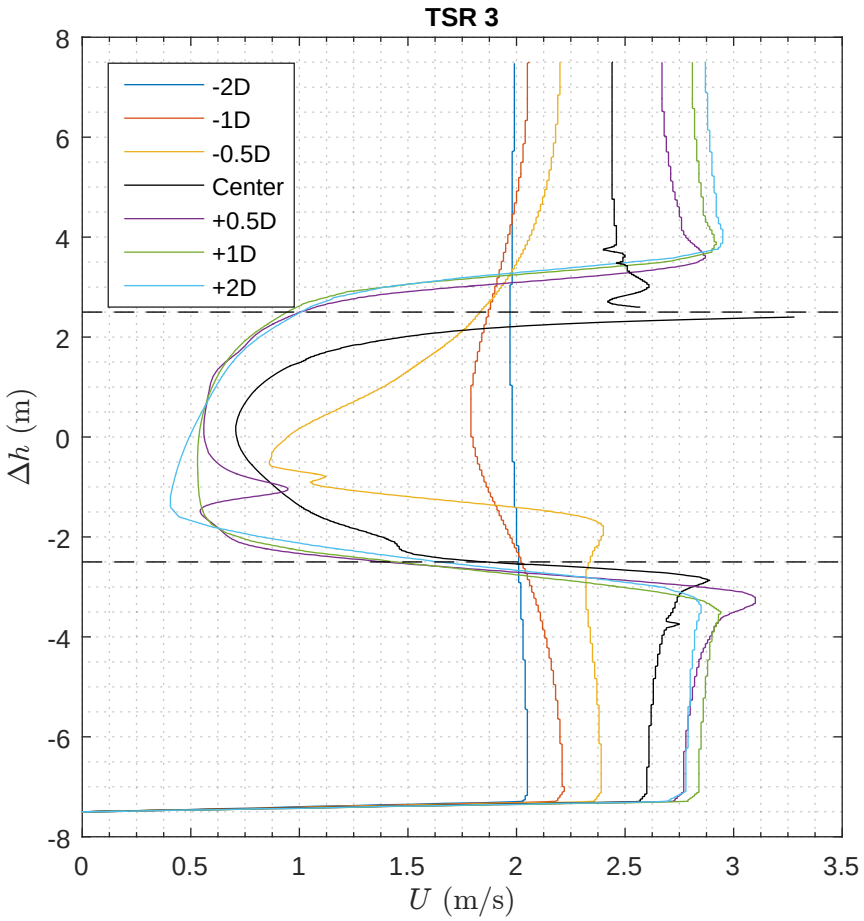

Figure C-4: Numerical flume velocity profiles with depth at a TSR of 3

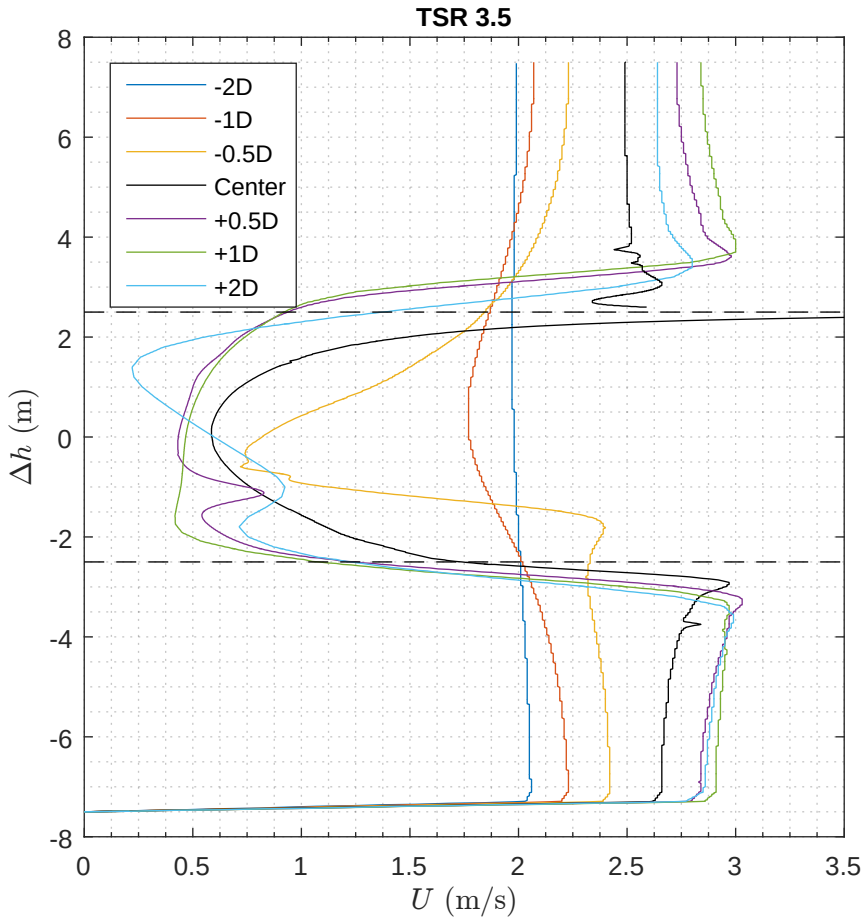

Figure C-5: Numerical flume velocity profiles with depth at a TSR of 3.5

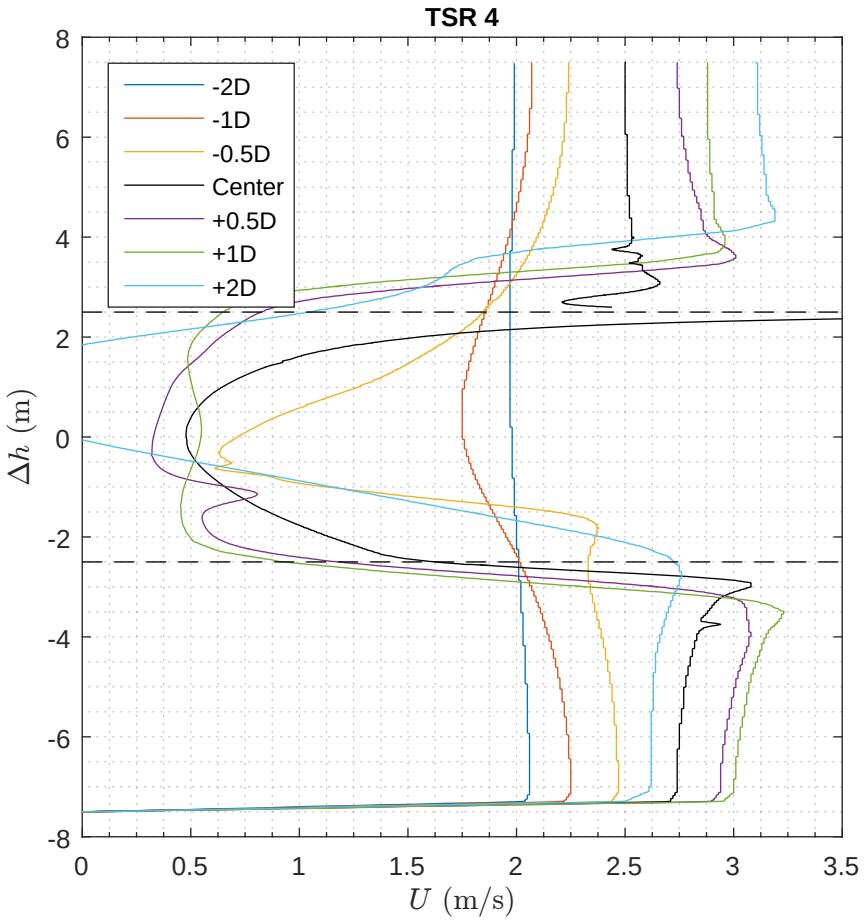

Figure C-6: Numerical flume velocity profiles with depth at a TSR of 4

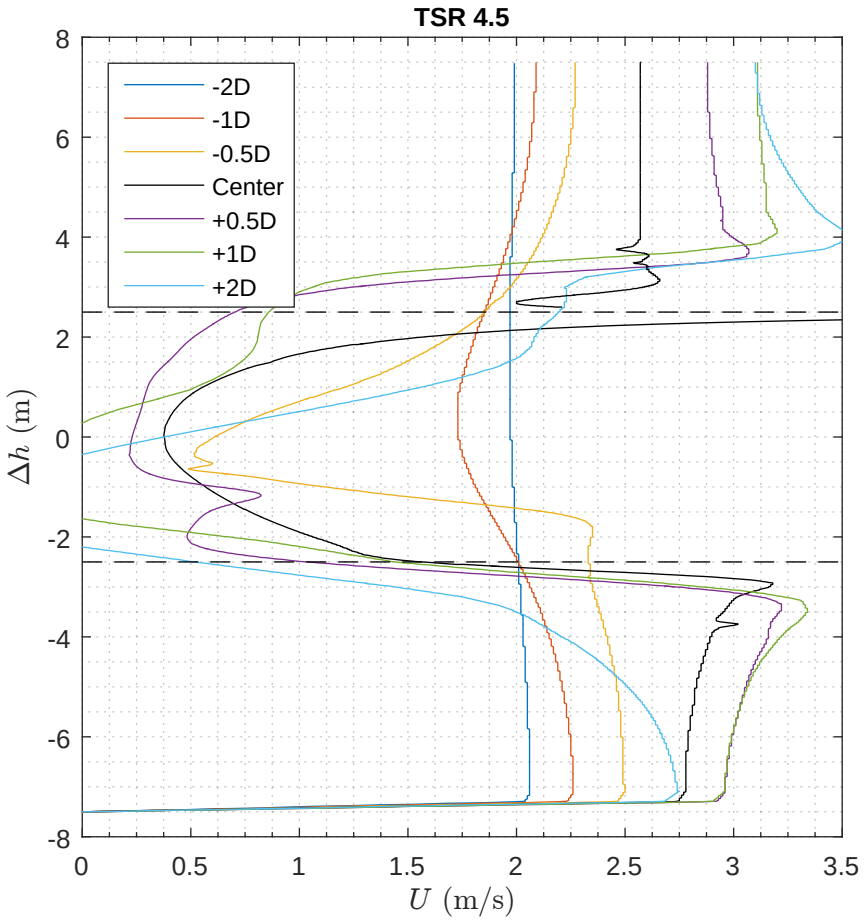

Figure C-7: Numerical flume velocity profiles with depth at a TSR of 4.5

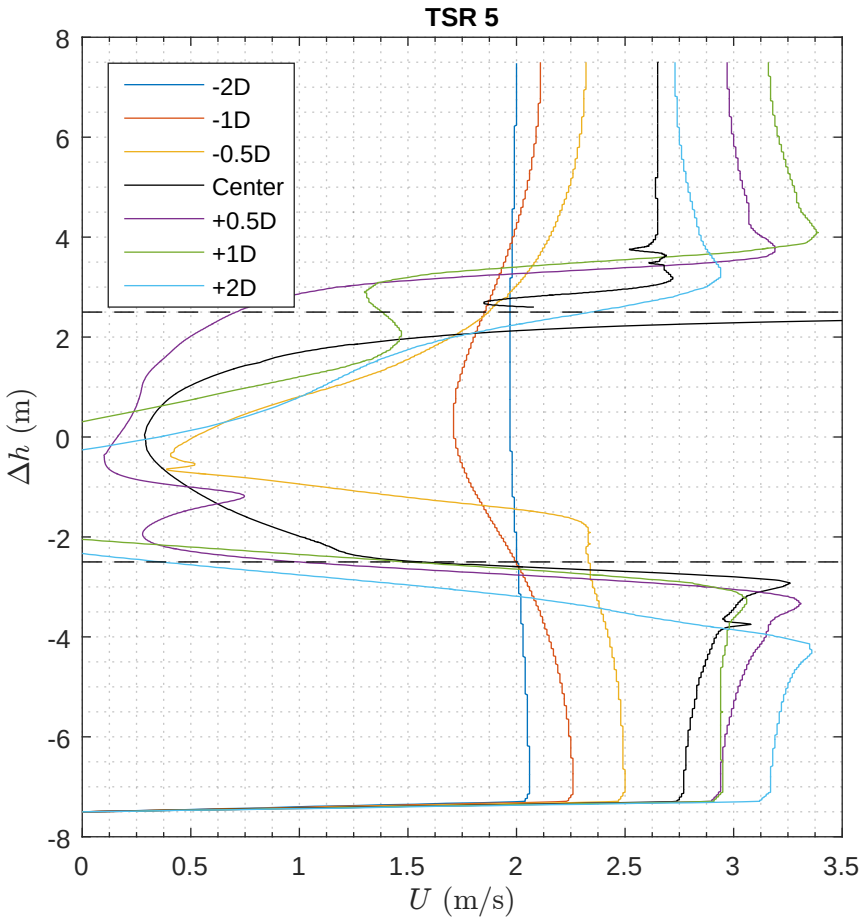

Figure C-8: Numerical flume velocity profiles with depth at a TSR of 5

C.2 Local sampling

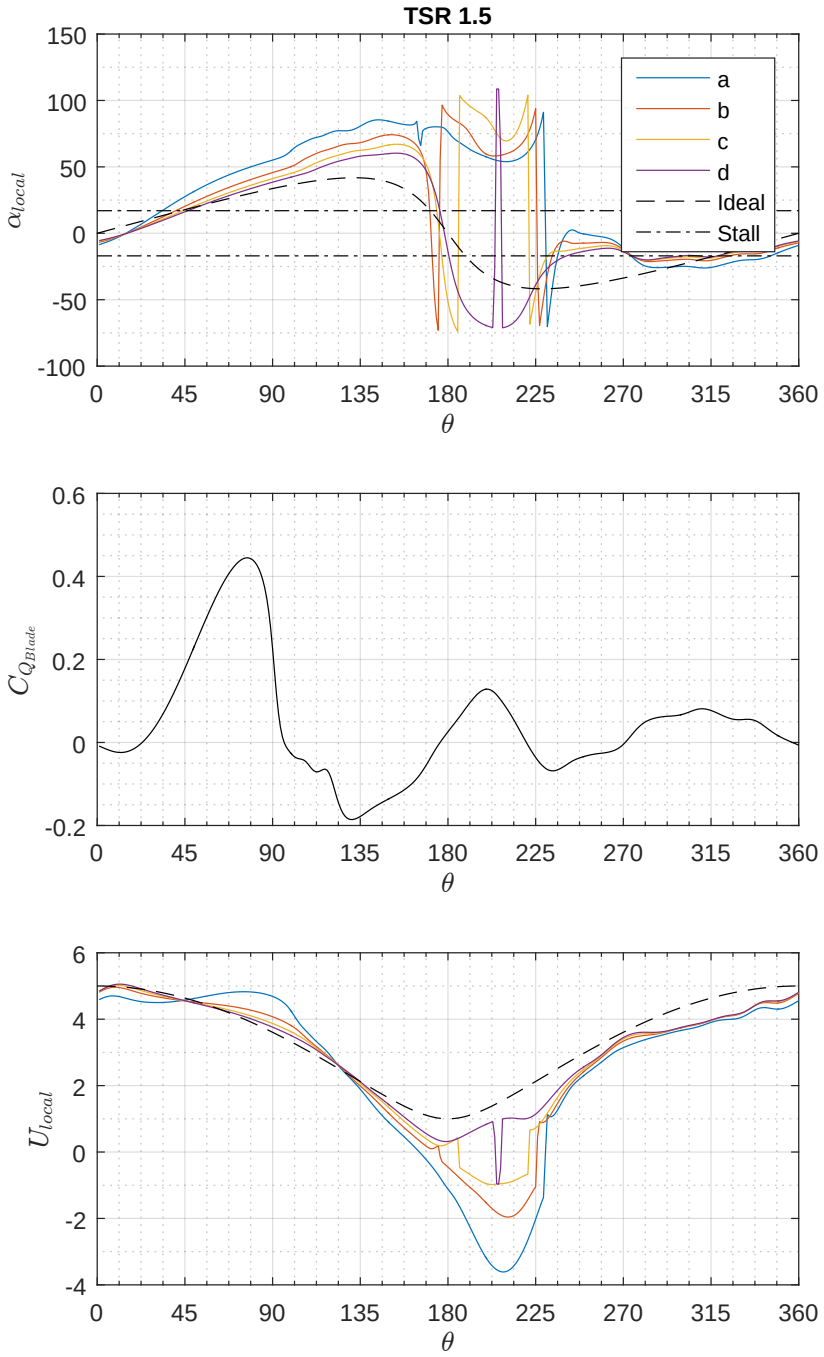

Figure C-9: Graphs of sample point parameters versus azimuth angle for a single blade, including; top: local angle, middle: coefficient of torque, bottom: local velocity. TSR=1.5

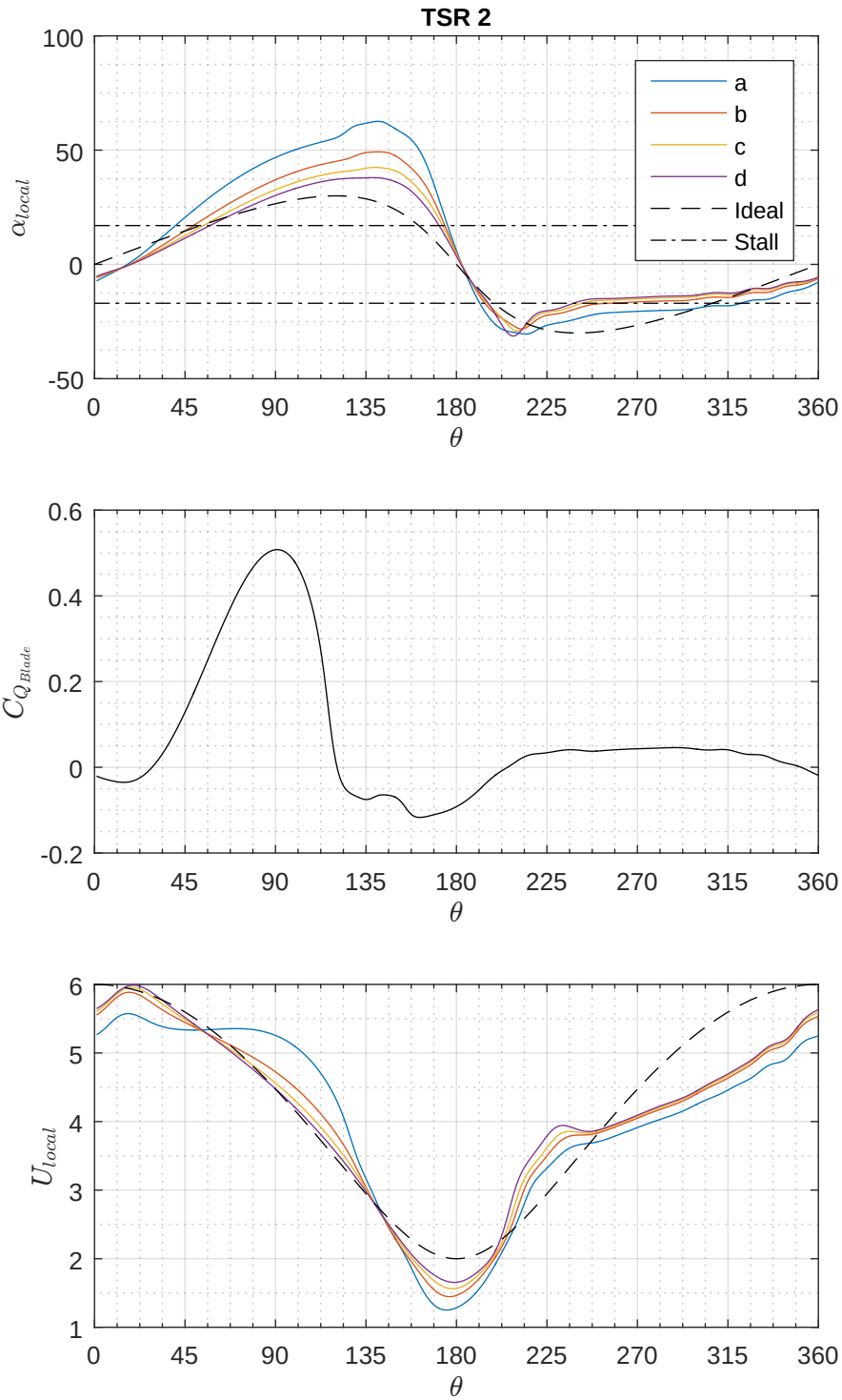

Figure C-10: Graphs of sample point parameters versus azimuth angle for a single blade, including; top: local angle, middle: coefficient of torque, bottom: local velocity. TSR=2

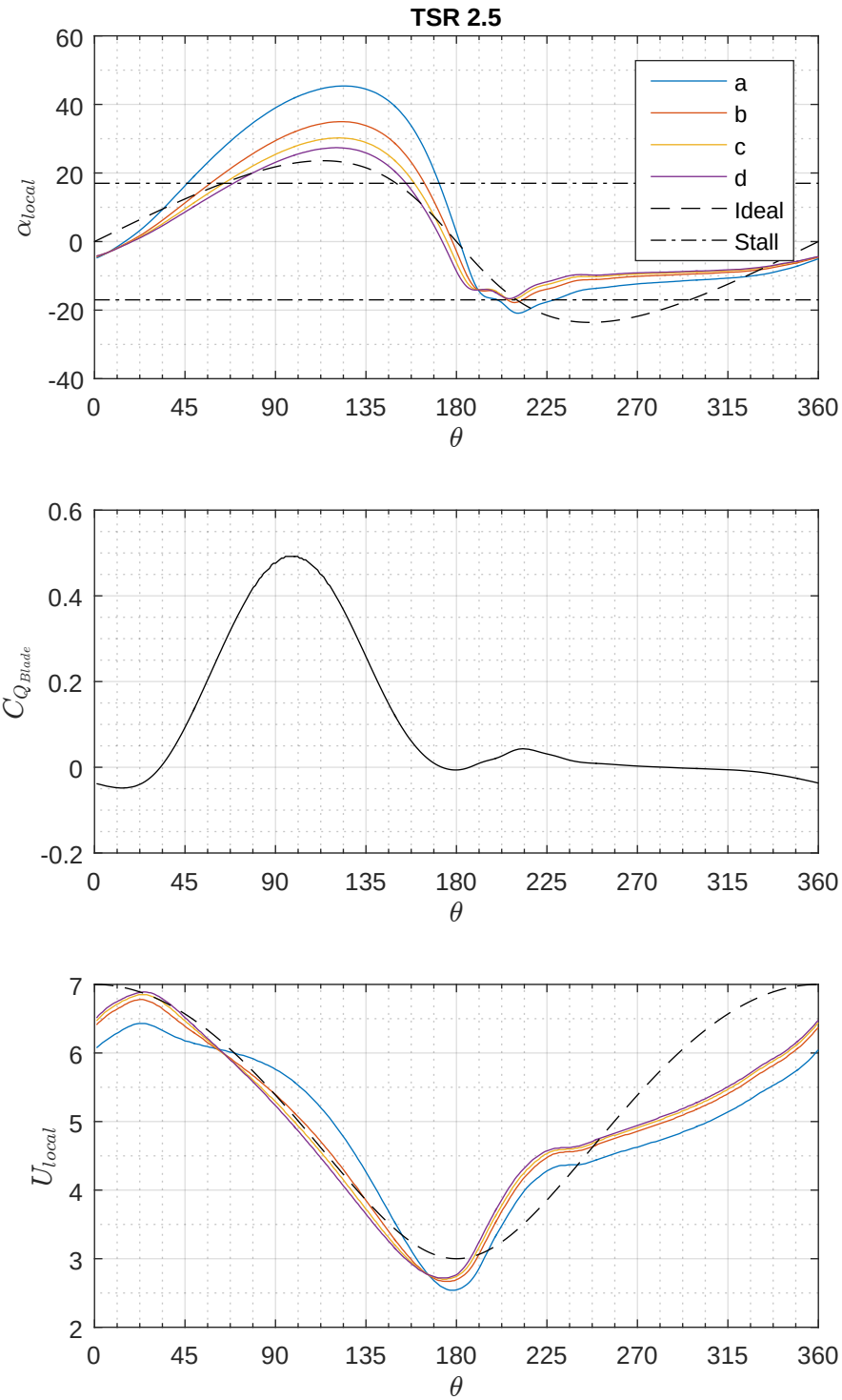

Figure C-11: Graphs of sample point parameters versus azimuth angle for a single blade, including; top: local angle, middle: coefficient of torque, bottom: local velocity. TSR=2.5

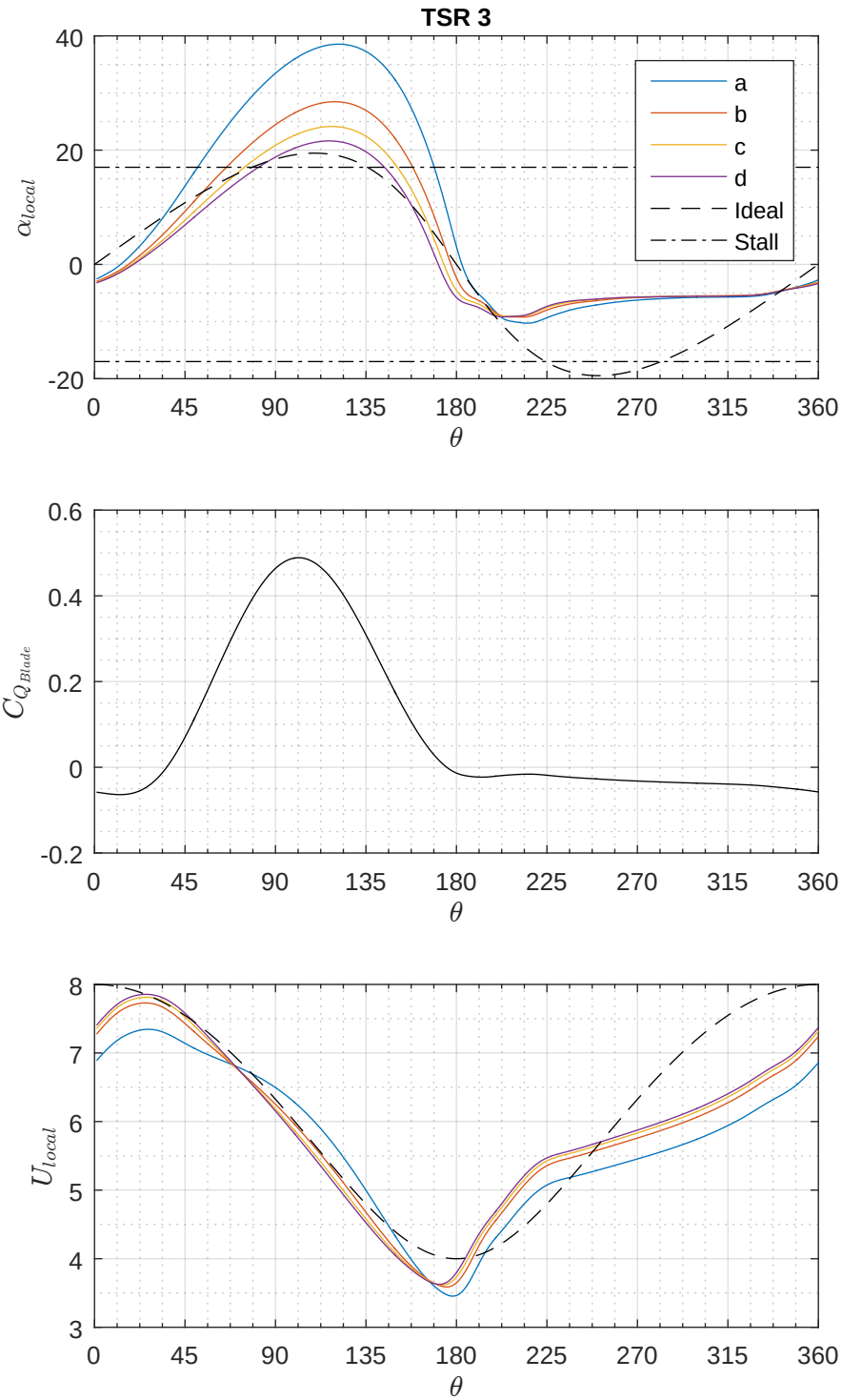

Figure C-12: Graphs of sample point parameters versus azimuth angle for a single blade, including; top: local angle, middle: coefficient of torque, bottom: local velocity. TSR=3

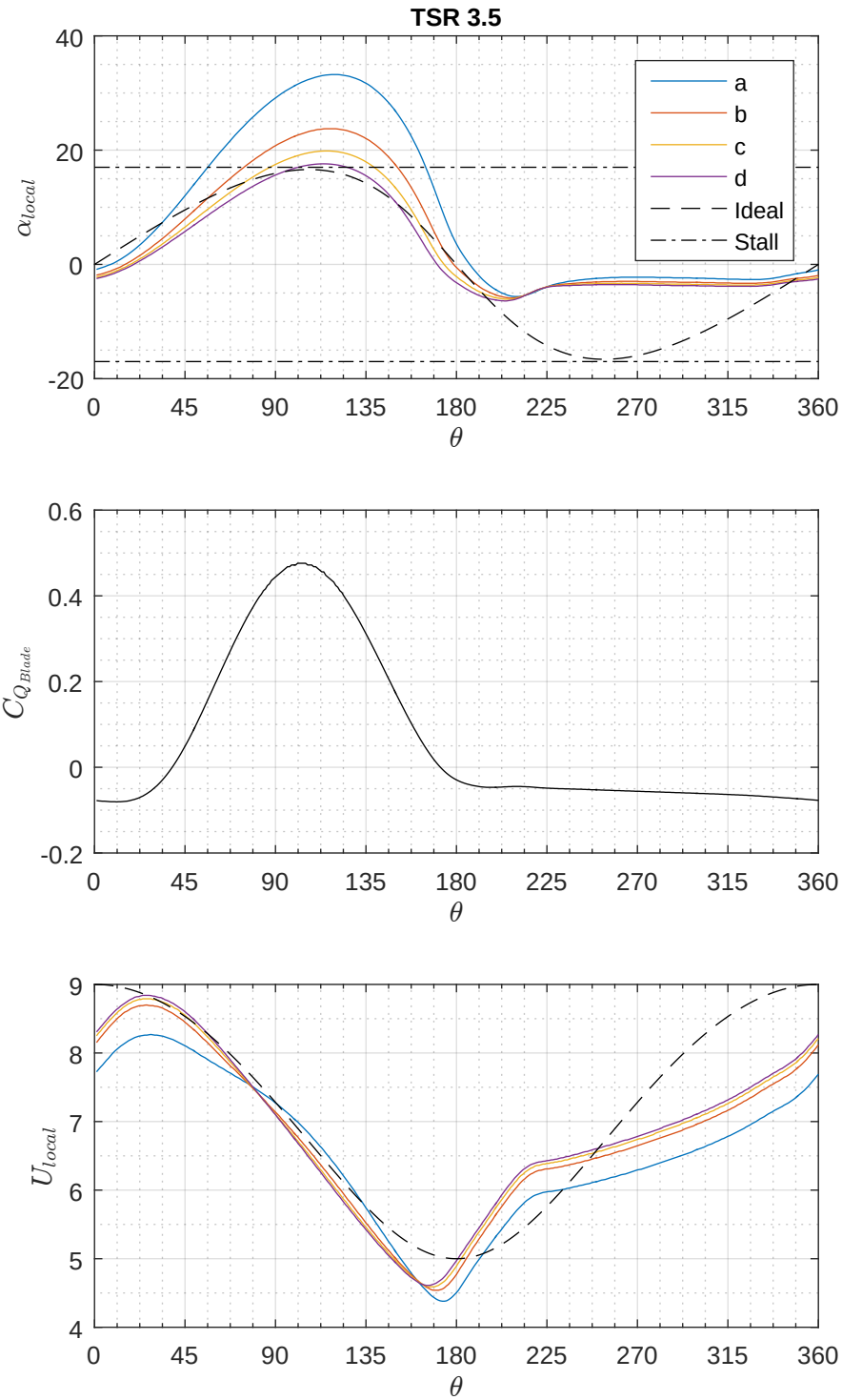

Figure C-13: Graphs of sample point parameters versus azimuth angle for a single blade, including; top: local angle, middle: coefficient of torque, bottom: local velocity. TSR=3.5

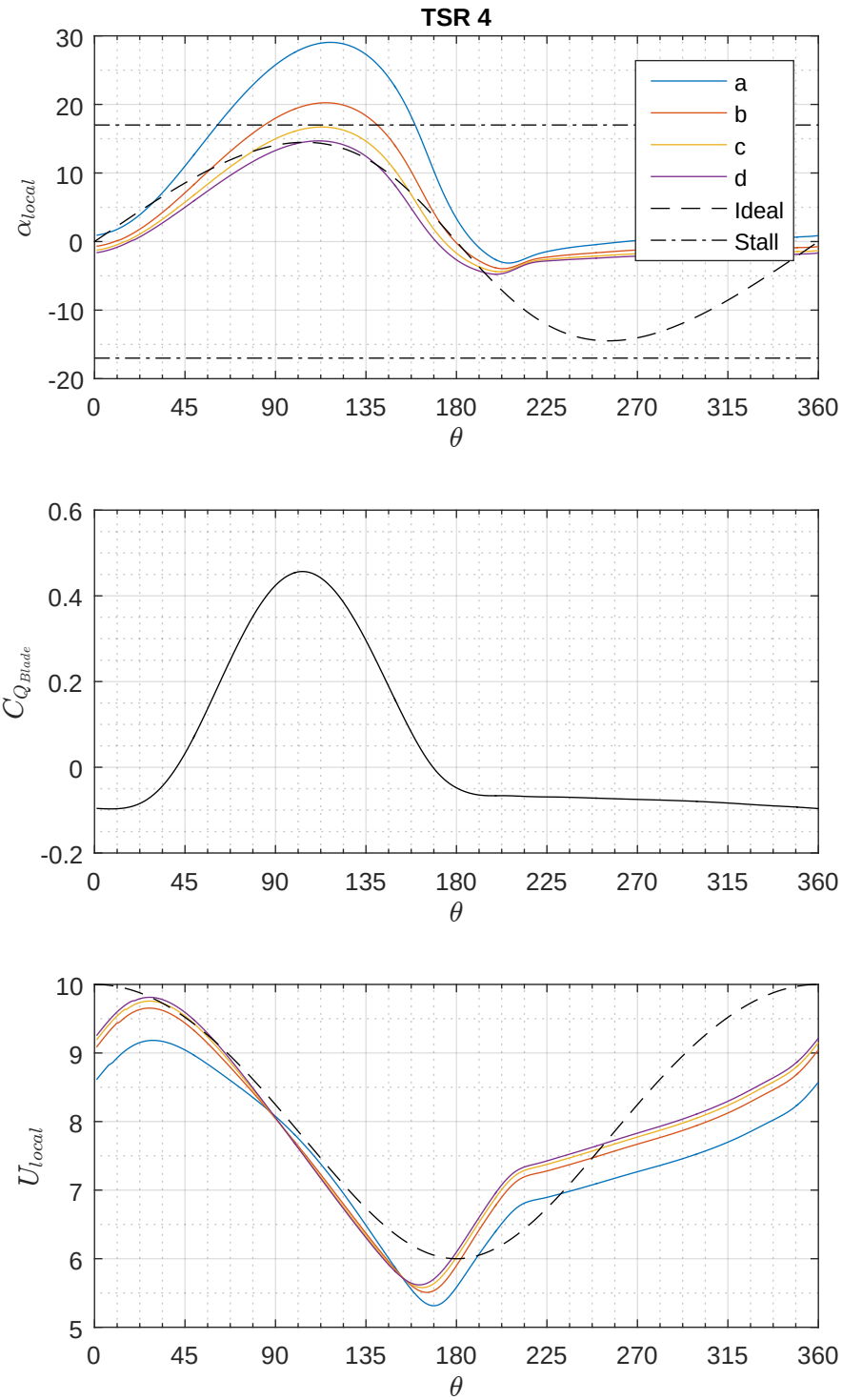

Figure C-14: Graphs of sample point parameters versus azimuth angle for a single blade, including; top: local angle, middle: coefficient of torque, bottom: local velocity. TSR=4

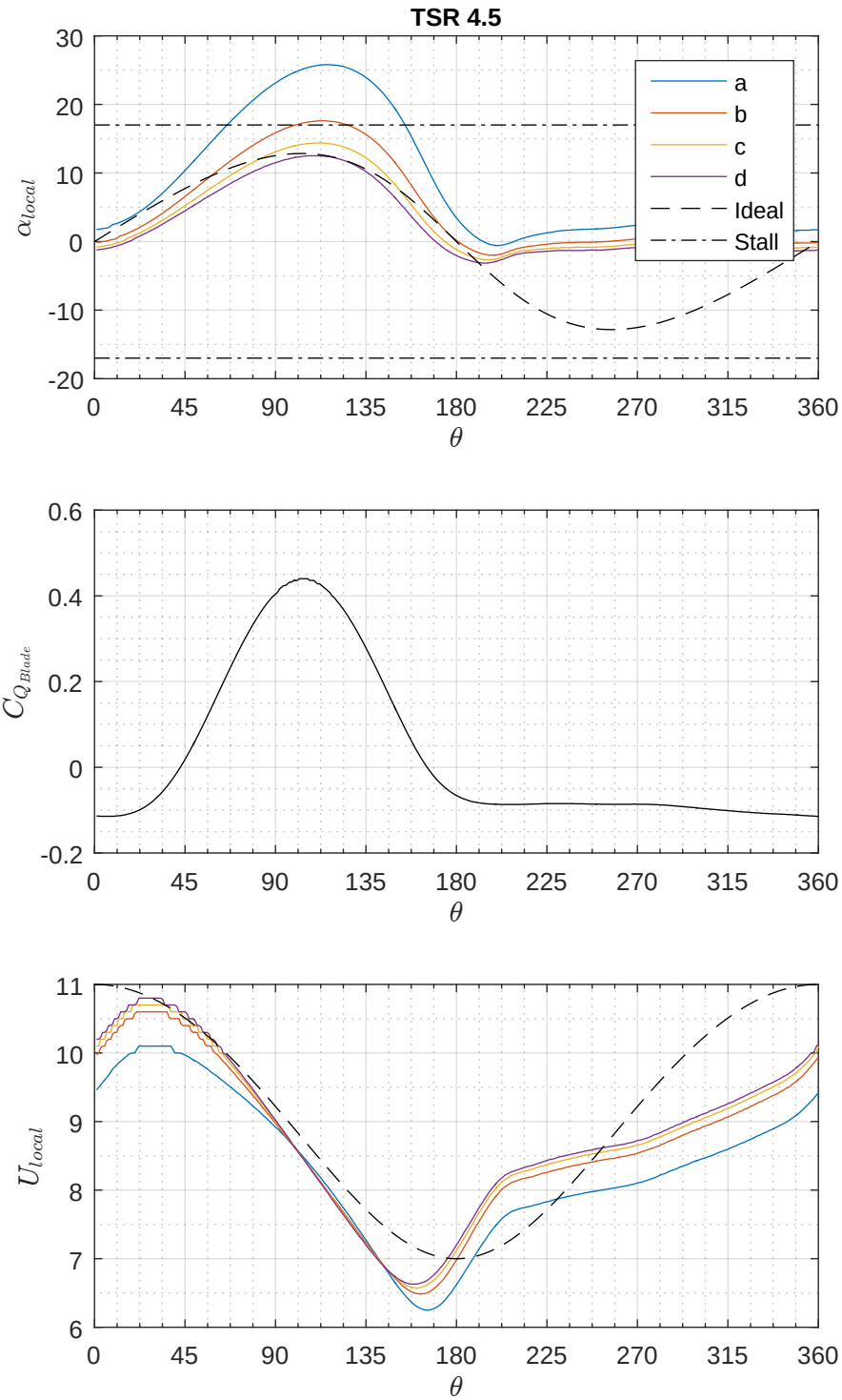

Figure C-15: Graphs of sample point parameters versus azimuth angle for a single blade, including; top: local angle, middle: coefficient of torque, bottom: local velocity. TSR=4.5

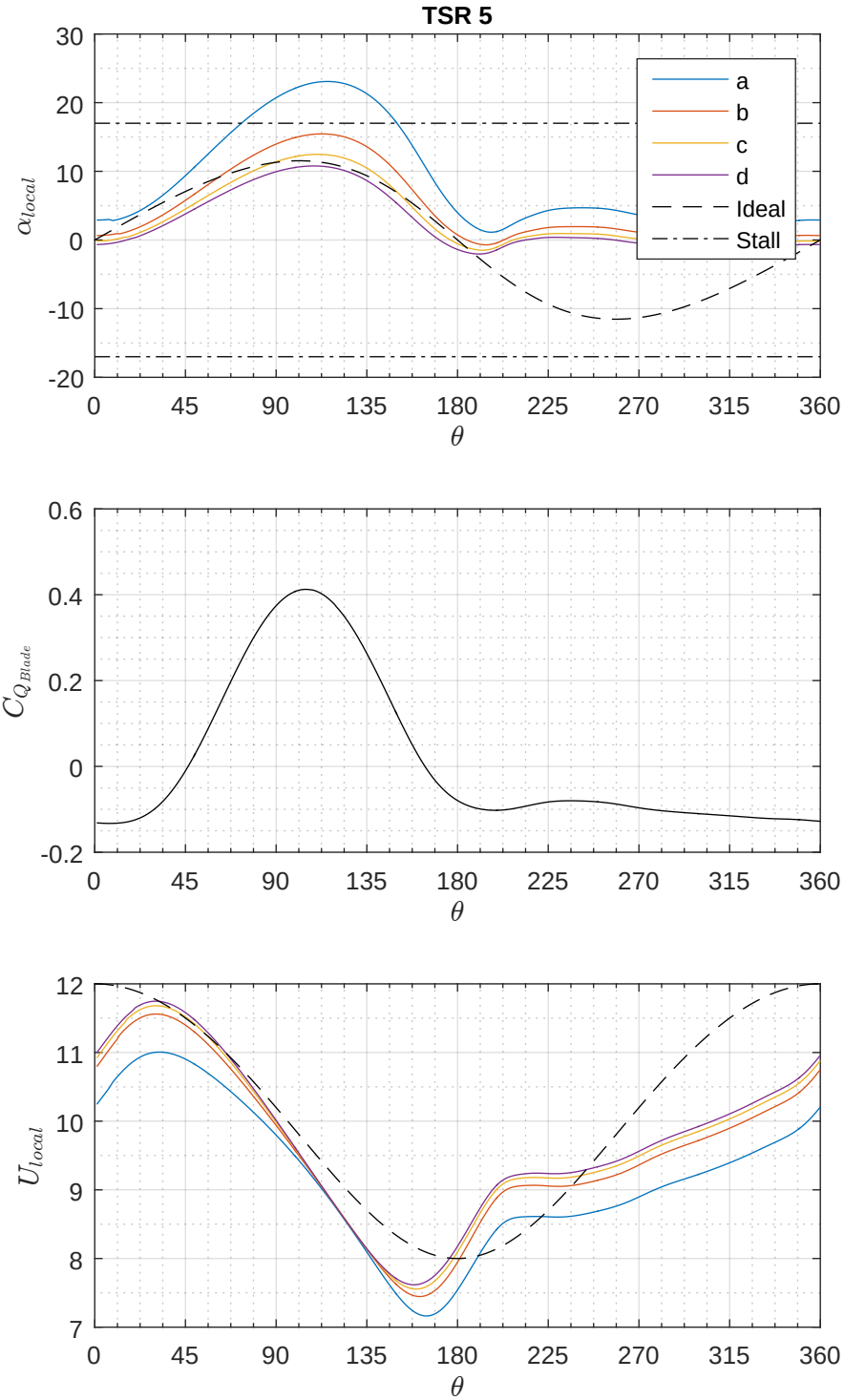

Figure C-16: Graphs of sample point parameters versus azimuth angle for a single blade, including; top: local angle, middle: coefficient of torque, bottom: local velocity. TSR=5

Appendix D

Active Pitch Control

D.1 Demand Angle Calculation

The matlab code used to calculate the demand angle is included below:

```
function [] = StallPitchAppx()

clf;
clc;

% Variables
MeanTSR = 2;
Radius= 2.5;
LossFactor = 0.5;
AoAmax1 = 14;
Phase = 0;
Uhigh = 2;
Ulow =2;
Smoothing = 15;
Uprof = [Uhigh,Ulow];
Xref = [Radius,(Radius*-1)];
MeanFlow = (Uhigh+Ulow)/2;

Phase = degtorad(Phase);
AoAmax = degtorad(AoAmax1);
xx = 1:1:360;

count = 1; %loop through all angles
for TurbAng = 2*pi/360+Phase:2*pi/360:2*pi+Phase
    TurbAng1 = mod(TurbAng,2*pi);
    Uloc1 = interp1(Xref,Uprof,(cos(TurbAng1)*Radius),'linear');
    TSR1 = (MeanFlow*MeanTSR)/Uloc1;
      % Calculate ideal AoA based on local TSR
```

```
      if(TurbAng1 < pi)
          AoAres1 = atan(sin(TurbAng1)/(cos(TurbAng1)+TSR1)); else
          AoAres1 = atan(sin(TurbAng1)*LossFactor/(cos(TurbAng1)*LossFactor+TSR1));
      end
      % Calculate difference between ideal and required
      if(TurbAng1 < pi); if(AoAres1 < AoAmax); AoA1 = 0; else AoA1 = AoAmax-AoAres1; end
      else if(AoAres1 > AoAmax*-1); AoA1 = 0; else AoA1 = AoAmax*-1-AoAres1; end
      end
      % Collect values
      Resolved1(count)=radtodeg(AoAres1);
      Actuated1(count)=radtodeg(AoA1);
      Loc1(count)=(TurbAng1);
      count=count+1;
end
   %Summarise and smooth
   Resolved1 = Resolved1; %alpha prediction
   Smoothed1 = smooth(Actuated1, Smoothing, 'moving')'; %demand angles
   Effective1 =(Resolved1+Smoothed1); %perceived angles
end
```